Effect of recombinant mouse sclerostin proteins on bone formation *in vitro* and in a murine model of sclerosteosis

by

Timothy James Dreyer

Submitted in partial fulfilment in accordance with the requirements for the degree of

Doctor of Philosophy

Department of Paraclinical Sciences

Faculty of Veterinary Science

University of Pretoria

December 2020

UNIVERSITEIT VAN PRETORIA
UNIVERSITY OF PRETORIA
YUNIBESITHI YA PRETORIA

Supervisor: Prof. Vinny Naidoo

Co-supervisor: Prof. Lyndy McGaw

Dedicated to

Dr Herman Hamersma (1930-2019),

my physician, friend, and a paragon of medicine.

Declaration

The studies presented in this thesis were performed by the author whilst a member of the Department of Paraclinical Sciences, Faculty of Veterinary Science, University of Pretoria, South Africa.

This is my original work, except where acknowledgment is made, and it has not previously been submitted for any other degree in this or any other institution of higher learning. All sources cited or quoted in this research paper are indicated and acknowledged with a comprehensive reference list.

_____

Timothy James Dreyer

December 2020

Abstract

Sclerosteosis is a severe autosomal recessive sclerosing skeletal dysplasia with no available treatment. It is characterised by excessive bone formation and is caused by mutations in the *SOST* gene that lead to loss of expression of sclerostin, a protein that acts as a negative regulator of bone formation by binding to low-density lipoprotein receptor-related proteins 5 and 6 (LRP5/6) Wnt co-receptors to inhibit the canonical Wnt/β-catenin signalling pathway. This study investigated the effectiveness of sclerostin replacement therapy in a mouse model of sclerosteosis. Recombinant wild type mouse sclerostin (mScl) and two novel mScl fusion proteins containing a C-terminal human immunoglobulin G1 (IgG1) antibody fraction crystallisable (mScl hFc), or C-terminal human Fc with a poly-aspartate motif (mScl hFc PD), to increase serum half-life and promote localisation to bone, respectively, were produced and purified using mammalian expression and standard chromatography techniques. These recombinant mScl proteins bound to LRP6 with high affinity (nM range) and completely inhibited matrix mineralisation in an *in vitro* bone nodule formation assay. Pharmacokinetic assessment following a single dose administered to wild type (WT) or SOST knock out (SOST$^{-/-}$) mice indicated that the presence of the hFc increased protein half-life from less than 5 minutes to at least 1.5 days. The effect of a 6-week treatment with these proteins on the skeletal phenotype of young SOST$^{-/-}$ mice revealed that mScl hFc PD treatment resulted in a modest but significant reduction in trabecular bone volume compared with the vehicle control. There was no marked effect on cortical bone indices assessed by μCT, whole body areal bone mineral density by DXA, or terminal levels of the bone formation marker procollagen type 1 N-terminal propeptide (P1NP) in any of the SOST$^{-/-}$ or WT treatment groups, possibly due to insufficient exposure. Administration of recombinant mScl hFc PD protein partially corrected the high bone mass phenotype of the SOST$^{-/-}$ mouse, suggesting that bone-targeting of sclerostin engineered to improve half-life was able to negatively regulate bone formation in the SOST$^{-/-}$ mouse model of sclerosteosis. However, the modest efficacy indicates that sclerostin replacement may not be an optimal strategy to mitigate excessive bone formation in sclerosteosis, hence alternative approaches should be explored.

Peer reviewed papers

— Manuscript under revision for Scientific Reports: "Recombinant sclerostin inhibits bone formation *in vitro* and in a mouse model of sclerosteosis."

Research output and awards

— Oral presentation at the 2019 University of Pretoria Faculty day.

— Oral presentation at the UCB annual PhD day 2019.

— Invited speaker at 8th International Workshop on Advances in the Molecular Pharmacology and Therapeutics of Bone and other Musculoskeletal Diseases/Cancer and Bone Society 2018 Meeting at St Catherine's College, Oxford, UK. https://molpharmworkshop.org/

— Oral presentation at the Bloomsbury Centre for Skeletal Research 2018. https://bloomsbury-skeletal-research.org/

— Poster presented at the UCB annual PhD day 2018.

— Won Best Generator of Patient Insights at UCB NewMeds Science Congress 2017.

— Poster presented and a live interview at the UCB NewMeds Science Congress 2017.

Acknowledgments

helped me put things back into perspective. Thank you to Mr Carl Doyle for many hours of music and game talk that made lengthy protein purification afternoons much more enjoyable. I owe him and Mr Prashant Mori much. A very special thank you to Dr Mike Wright for being a top-class friend and host, imparting valuable wisdom and advice on life and such over many Flaming Cow burgers.

Further gratitude is extended to Prof. Jacques Theron and Ms Andalé Conradie at the Department of Microbiology and Plant Pathology, and Prof. Lyndy McGaw (co-supervisor) and Ms Annette Venter at the Department of Paraclinical Science, University of Pretoria, for their support and assistance.

Thank you to all the sclerosteosis families for trusting in me and motivating me with their kind words of support. Thank you also to my friends and family for supporting and believing in me while I gallivanted across the pond. Lastly, I'd like to share my utmost appreciation for my parents, who provided encouragement, comfort, and support from afar and ensured that I never lose my faith, and a very special thank you to my brother for keeping me company when home felt especially far away.

Abbreviations

°C	degree Celsius
μA	micro Ampere
μcal	micro calories
μCT	micro Computed Tomography
μg	micro gram
μL	micro Litre
μM	micro Molar
aa	amino acid
Ab	Anti-body
aBMD	areal Bone Mineral Density
ADA	Anti-Drug Antibody
ALP	Alkaline Phosphatase
ANOVA	Analysis of variance
AP-1	Activator Protein 1
AUC	Area Under Curve
B.Ar	Bone Area
BMD	Bone Mineral Density
BMP	Bone Morphogenetic Protein
BMU	Basic Multicellular Unit
bp	base pair
B.Pm	Bone Perimeter
BRC	Bone Remodelling Compartment
BSA	Bovine Serum Albumin
BSP	Bone Sialoprotein
BV/TV	Bone Volume as percentage of Total Volume scanned
Ca	calcium
CEC	Cation Exchange Chromatography
CK1	Casein Kinase 1
Cl	Chloride
ClC-7	Chloride Channel 7
cm	centimetre
Cmax	maximum concentration
CM-dextran	Carboxymethyl-dextran
CMV	Cytomegalovirus
CO_2	Carbon Dioxide
Col1A	Collagen type 1A
CPC	Cetylpyridinium Chloride
Cs.Th	Cross-sectional Thickness
CTR	Calcitonin Receptor
DA	Degree of Anisotropy
DC-STAMP	Dendrocyte expressed Seven Transmembrane Protein
dH_2O	distilled water
Dlx5	Distal-less homeobox-5
DMP-1	Dentin Matrix Protein-1
DNA	Deoxyribonucleic Acid
DOL	Degree Of Labelling

DPBS	Dulbecco's Phosphate-buffered Saline
DVL	Dishevelled
DXA	Dual X-ray Absorptiometry
ECL	Electrochemiluminescence
ECM	Extracellular Matrix
EDC	Ethyl(dimethylaminopropyl)-carbodiimide
EDTA	Ethylenediaminetetraacetic Acid
EMA	European Medicines Agency
ER	Endoplasmic Reticulum
ETS	Erythroblast Transformation Specific
EU	Endotoxin Unit
FA	Formic Acid
Fab	Fragment antigen binding
FBS	Foetal Bovine Serum
Fc	Fragment crystallisable
FDA	U.S. Food and Drug Administration
FGF	Fibroblast Growth Factor
Fzd	Frizzled
g	gravity
GAG	Glycosaminoglycans
GH	Growth Hormone
GSK3β	Glycogen Synthase Kinase 3β
H	Hydrogen
HEK	Human Embryonic Kidney
HEPES	4-(2-hydroxyethyl)-1-piperazineethanesulfonic acid
hFc	human Fragment crystallisable
HCl	Hydrochloric acid
HPLC	High Pressure Liquid Chromatography
HSC	Haematopoietic Stem Cell
IAA	Iodoacetamide
IGF	Insulin-like Growth Factor
IgG	Immunoglobulin G
IHH	Indian Hedgehog
IL	Interleukin
IR	Infrared
ITC	Isothermal Titration Calorimetry
IV	Intravenous
Kb	kilo base
KD	Dissociation constant
kDa	kilodalton
kg	kilogram
kV	kilovolt
L	Litre
LB	Luria-Bertani
LC-MS	Liquid Chromatography Mass Spectrometry

LED	Light-emitting Diode	PNGase F	Peptide-N-glycosidase F
M	Molar	PTH	Parathyroid Hormone
Ma.Ar	Medullary Area	PTHrP	cytokine Parathyroid Hormone related
mAU	milli-Absorbance Units		
M-CSF	Macrophage Colony Stimulating Factor	PVDF	Polyvinylidene Fluoride
		RANK	Receptor Activator of Nuclear factor κB
MEPE	Matrix Extracellular Phosphoglycoprotein		
		RANKL	Receptor Activator of Nuclear factor κB Ligand
MES	2-(N-morpholino)ethanesulfonic acid		
mg	milligram	rhTNALP	recombinant human Tissue-Nonspecific Alkaline Phosphatase
min	minute		
MITF	Microphthalmia-associated Transcriptor Factor		
		ROI	Region Of Interest
mL	millilitre	rpm	revolutions per minute
mm	millimetre	RSA	Rat Serum Albumin
mM	millimolar	RU	Resonance Unit
MMI	Moment of Inertia	Runx2	Runt-related transcription factor-2
MMP9	Matrix Metalloproteinase-9	s	second
ms	millisecond	SC	Subcutaneous
MSC	Mesenchymal Stem Cell	Scl	Sclerostin
mScl	mouse Sclerostin	SD	Standard Deviation
MST	Microscale Thermophoresis	SDS-PAGE	Sodium Dodecyl-sulfate Polyacrylamide Gel Electrophoresis
Msx2	Msh homeobox homologue-2		
MW	Molecular Weight		
MWCO	Molecular Weight Cut-Off	SEC	Size Exclusion Chromatography
NaCl	Sodium Chloride	SMI	Structural Model Index
NaOH	Sodium Hydroxide	SPR	Surface Plasmon Resonance
NBF	Neutral Buffered Formalin	TAE	Tris-acetate-EDTA
NCA	Non-Compartmental Analyses	T.Ar	Tissue Area
ND	Not Determined	Tb.N	Trabecular Number
NFATc1	Nuclear Factor of Activated T cells calcineurin dependent 1	Tb.Pf	Trabecular bone Pattern factor
		T.Pm	Tissue Perimeter
		Tb.Th	Trabecular Thickness
NHS	N-hydroxysuccinimide	Tb.Sp	Trabecular Space
nm	nanometer	TCEP	Tris(2-carboxyethyl)- phosphine
nmol	nanomolar	TCF/LEF	T-cell factor/Lymphoid Enhancer Factor
ns	non-significant		
OCN	Osteocalcin		
OI	Osteogenesis Imperfecta	TGF-β	Transforming Growth Factor-beta
OPG	Osteoprotegerin	TRAP	Tartrate-resistant Acid Phosphatase
OPN	Osteopontin		
Osx	Osterix	UV	Ultraviolet
P1NP	Procollagen type I N-terminal Propeptide	V	Volt
		vBMD	volumetric Bone Mineral Density
PBS	Phosphate-buffered Saline	VEGF	Vascular Endothelial Growth Factor
PD	Poly-aspartate	Vss	Volume of distribution
PDGF	Platelet Derived Growth Factor	Wnt	Wingless int
PES	Polyethersulfone	WT	Wild Type
pg	picogram	YT	Yeast extract Tryptone
PHEX	Phosphate-regulating Neutral Endopeptidase, X-linked		
pI	Isoelectric point		

Table of Contents

List of Figures

List of Tables

Chapter 1: Introduction

1.1. Overview

Sclerosteosis is a rare, autosomal recessive, high bone mass condition with no known treatment (Beighton and Hamersma, 1979; van Lierop et al., 2017). It is associated with increased bone formation and disease management is limited to difficult and protracted surgical decompression of entrapped cranial nerves and elevated intracranial pressure (du Plessis, 1993; Hamersma and Hofmeyr, 2007). Sclerosteosis is caused by mutations in the *SOST* gene that result in loss of functional sclerostin, a protein that regulates the canonical Wnt/β-catenin pathway, a signalling pathway that plays an essential role in developmental regulation and adult bone homeostasis (Balemans et al., 2001, 1999; Brunkow et al., 2001; Nusse and Clevers, 2017). Loss of sclerostin thus leads to enhanced canonical Wnt signalling in the skeleton, resulting in the excessive bone formation characteristic of sclerosteosis (Lin et al., 2009).

1.2. Hypothesis

Sclerosteosis can be treated by administering exogenous sclerostin, thereby antagonising the canonical Wnt signalling pathway and subsequently reducing abnormal bone formation.

1.3. Aim and objectives

The aim of this project was to investigate whether novel exogenous sclerostin constructs can slow down excess bone formation in a sclerosteosis mouse model.

Objective 1:   Design and clone novel sclerostin constructs fused with human Fc and an octa-aspartic motif.

Objective 2:   Express and purify the recombinant sclerostin-Fc fusion proteins.

Objective 3: Demonstrate *in vitro* functionality and effectivity through biophysical techniques and a bone nodule formation assay.

Objective 4: Demonstrate *in vivo* functionality, effectivity, and safety in SOST knockout and wild-type mice by administering recombinant sclerostin fusion constructs, completing pharmacokinetic and pharmacodynamic assays, and analysing bone formation parameters.

Chapter 2: Literature review

2.1. Bone: an introduction

One of the differentiating features of vertebrates is the presence of an internal skeleton onto which the muscles and ligaments are attached (Clarke, 2008). The skeleton is made of numerous individual bones that vary between species by size and shape. In addition to being an internal scaffold that supports the body and movement, bone is a highly adaptable endocrine organ consisting of living cells and mineralised connective tissue that affords physical support and protection to the body's soft tissue, permits movement and locomotion, and in most vertebrates harbours bone marrow for haematopoiesis (Zapata and Amemiya, 2000; Han et al., 2018). It is capable of adapting to changing requirements by altering its structure and mass, and acts as an important reservoir of numerous minerals, including phosphate, calcium, magnesium and organic molecules, to maintain mineral homeostasis and acid base balance (Clarke, 2008; Florencio-Silva et al., 2015).

2.1.1. Bone structure and composition

There are four general categories of bone in the human skeleton: long (humeri, radii, femurs and tibiae), short (carpal and tarsal bones), irregular (vertebrae) and flat bones (skull, mandible and ribs). Mammalian long bones, such as the femurs, consist of a hollow, cylindrical diaphysis, composed of a thick cortical bone shell, that is capped at both ends by expanded and rounded, articular cartilage covered epiphyses, with developing regions, known as metaphyses, in between (Figure 2.1) (Clarke, 2008; Fuchs et al., 2019). The diaphysis is lined with the endosteum, a thin cover consisting of a single sheath of bone lining cells and osteoblasts, which surrounds the medullary cavity that contains bone marrow or yellow fatty tissue and interspersed endosteum-covered trabecular bone (Islam et al., 1990). In contrast, the metaphyses and epiphyses at the ends of the diaphysis mainly consist of porous trabecular bone (also known as cancellous bone) that is surrounded by a thin cortical bone shell (Gurevitch et al., 2007). To separate the cortical bone from overlying soft tissue or musculature, the outer cortical bone surface is covered with the periosteum, an intermediate connective tissue sheath composed of collagen and elastin fibres, fibroblasts,

microvasculature, nerve networks, osteoblasts, chondrocytes and mesenchymal stem cells (MSCs) that can differentiate into bone cells and aid in bone healing (Ito et al., 2001; Dwek, 2010; Duchamp de Lageneste et al., 2018).

2.1.1.1. Cortical bone

Cortical bone accounts for approximately 80% of skeletal tissue mass and significantly contributes to the mechanical role of bone. It is compact, with low porosity that results in great compressive strength, and consists of osteons. Osteons consist of a central blood vessel-containing Haversian canal enveloped by concentric walls of lamellae with uniformly spaced osteocyte-containing lacunae (Figure 2.1) (Stout et al., 1999). Branching canaliculae radiate from each lacuna, penetrate the lamellae, and forms a network of interconnecting cavities by linking to the canaliculae of nearby lacunae. These osteons form branching networks within the cortical bone and regions between them are filled with interstitial bone. Volkmann's canals allow blood vessels to come into contact with the medullary space and trabecular bone for delivery of nutrients and oxygen (Figure 2.1).

2.1.1.2. Trabecular bone

In contrast to cortical bone, trabecular bone consists of saucer-shaped bone packets composed of layers of lamellae (Figure 2.1). Trabecular bone has high porosity (>50% of total trabecular bone volume) and comprises of a honeycomb-like network of horizontal and vertical rod- and plate-like structural components (trabeculae), giving trabecular bone its sponge-like appearance (Figure 2.1) (Fuchs et al., 2019). This allows for even distribution of load and absorption of energy. The porous structure further provides a larger surface area for increased contact between bone and blood vessels, connective tissues, and red bone marrow, thereby facilitating bone's role in mineral homeostasis and haematopoiesis.
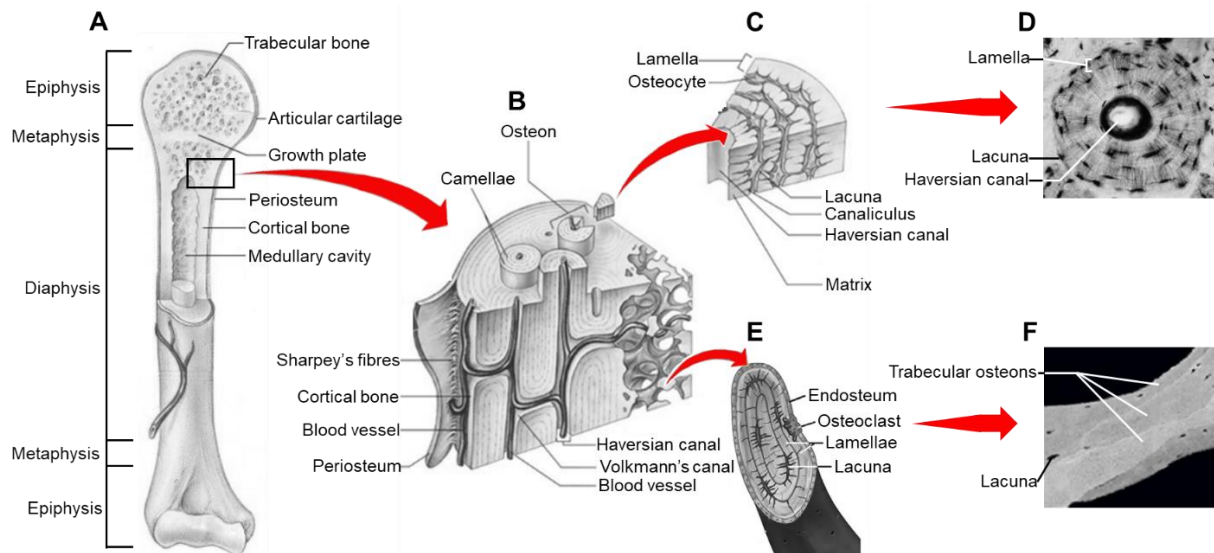
Figure 2.1: Schematic illustration of bone structure and organisation. A) Representation of a long bone consisting of a cylindrical diaphysis and two articular surfaces (epiphyses) separated from the diaphysis by developing regions (metaphyses) that contain the growth plates. B) Microstructure and organisation of cortical and trabecular bone, with visible osteons (Haversian systems) and central Haversian canals. C) A section of a cortical bone osteon showing the lamellae, osteocytes, lacunae, canaliculus, and central Haversian canal. D) Cross section of cortical osteon viewed by light microscope. E) A cross section of trabecular bone showing the lamellae, lacunae, and outer endosteum cover. F) Trabecular osteons viewed by backscattered electron imaging. Figure adapted from Fuchs et al., 2019; Marieb and Hoehn, 2012; Roschger et al., 2008.

2.1.1.3. Bone matrix

The intercellular substance of cortical and trabecular bone, known as the bone matrix, consists of both organic and inorganic (approximately 70% of total bone mass) components. The organic matrix is mainly composed of collagen (approximately 90% collagen type I), a key structural element that gives bone its flexibility. Collagen is produced within osteoblasts and is a rope-like fibrous protein composed of many collagen fibrils, each fibril consisting of a single α2 and two α1 polypeptide chains (Brodsky and Persikov, 2005; Bou-Gharios and de Crombrugghe, 2008). Other organic components consist of non-collagenous protein: proteoglycans, osteocalcin (OCN), osteopontin (OPN), fibronectin and bone sialoprotein (BSP), and are essential for growth, differentiation of osteoblasts, osteoclasts and osteocytes, cell adhesion, tissue mineralisation and bone remodelling (Young et al., 1992; Gehron Robey, 2008). The inorganic bone matrix serves as an ion reservoir for calcium, phosphorus, sodium and magnesium. These ions form calcium hydroxyapatite, the most abundant mineral in the skeleton, which gives bone most of its stiffness (Fuchs et al., 2019).

2.1.2. Bone cells

The functional integrity of bone is maintained primarily by osteoblasts, osteocytes and osteoclasts embedded in the bone matrix, and contribute only a small mass to the skeleton (Robey et al., 1993). Populations of these cells build on the extensive bone extracellular matrix which, in turn, controls their ability to resorb and deposit bone (Karaplis, 2008).

2.1.2.1. Osteoblasts

Osteoblasts are mainly known for their bone forming function and make up 4-6% of total resident bone cells. They are cuboidal cells that are located on bone formation surfaces and originate from local proliferating undifferentiated pluripotent MSCs (Figure 2.2) (Capulli et al., 2014). The MSCs are present in the periosteum and bone marrow stroma, and their differentiation into osteoblasts is regulated by expression of specific genes and transcription factors such as runt-related transcription factor-2 (Runx2), osterix (Osx, also known as Sp7), distal-less homeobox-5 (Dlx5), and msh homeobox homologue-2 (Msx2) that play key roles in committing MSCs to the preosteoblast lineage instead of adipocyte, myocyte or chondrocyte lineages (Ichida et al., 2004; Samee et al., 2008; Kawane et al., 2018; Komori, 2019). Osteoblast progenitors proliferate and become committed to the osteoblast lineage through direct regulation of numerous genes by Runx2, causing Runx2 expressing MSCs to segregate from the osteochondroprogenitors to form preosteoblasts (Sinha and Zhou, 2013; Komori, 2019). Runx2 expressed by preosteoblasts induces expression of Osx, which acts downstream from Runx2 and induces formation of immature osteoblasts by interacting with phosphatase calcineurin activated nuclear factor of activated T cells calcineurin dependent 1 (NFATc1) (Figure 2.2) (Koga et al., 2005; Sinha and Zhou, 2013). Expression of Runx2 and Osx can be regulated by members of the wingless (Wnt) and Indian hedgehog (IHH) signalling pathways as well as growth and transcription factors such as bone morphogenetic proteins (BMP), which can induce bone formation by activating Runx2 and Osx expression. Expression is further regulated by transforming growth factor-beta (TGF-β), which can either inhibit late stage osteoblastic maturation or induce osteoblastic differentiation through regulation of Runx2 expression (Komori, 2019).

Once Runx2 and collagen type 1A (Col1A) expressing osteoblast progenitors are established, a proliferation step follows, during which osteoblast progenitors highly express proliferative genes (c-Fos and histone H4) and alkaline phosphatase (ALP), a key enzyme in bone mineralisation (Figure 2.2) (Sunters et al., 2004; Capulli et al., 2014; Khani et al., 2017). The new preosteoblasts express Col1A, insulin-like growth factors (IGFs), fibroblast growth factors (FGFs), TGF-β, cell adhesion proteins (such as fibronectin), and BSP. However, for cells to further differentiate into mature, bone-forming osteoblasts, Runx2, Osx, β-catenin and other Wnt signalling pathway components need to be expressed (Hu et al., 2005; Sinha and Zhou, 2013; Komori, 2019). There is also evidence that other factors, such as microRNAs and connexin 43, are required for osteoblast differentiation: microRNAs play regulatory roles in gene expression and can stimulate or prevent osteoblast differentiation, whilst mutations in the connexin 43 gene, the main connexin in bone, impairs osteoblast differentiation (Zhang et al., 2011; Plotkin and Bellido, 2013).

Receptor activator of nuclear factor κB ligand (RANKL) and numerous growth and transcription factors (such as Runx2, BSP, Osx, ALP, FGFs, IGFs and TGF-β) are expressed during transition from preosteoblasts to mature osteoblasts (Figure 2.2) (Hu et al., 2005; Sinha and Zhou, 2013; Komori, 2019; Tobeiha et al., 2020). Cells undergo morphological changes and become cuboidal cells with a single nucleus, abundant rough ER, prominent Golgi apparatus, various secretory vesicles, and basophilic cytoplasm (Capulli et al., 2014). Osx expression is increased and collagen proteins (collagen type 1), non-collagen proteins, osteonectin, BSP and OPN and proteoglycans (decorin and biglycan) are secreted to form the organic matrix. Mineralisation of the matrix then occurs in two phases: the vesicular phase, followed by the fibrillar phase. During the vesicular phase, matrix vesicles that were released into the organic matrix by osteoblasts bind to proteoglycans and other matrix organic elements (Golub, 2009; Hasegawa et al., 2017). Proteoglycans are then degraded by osteoblast-secreted enzymes to release immobilised calcium ions (Ca^+) from the matrix vesicles, allowing the Ca^+ to cross the vesicle membrane via calcium channels (annexins). Osteoblast-secreted ALP degrades phosphate containing compounds within the matrix vesicle, thereby releasing phosphate ions (PO_4^{3-}). Hydroxyapatite crystals are formed when the released Ca^+ and PO_4^{3-} nucleate. During the fibrillar phase, hydroxyapatite crystals are released when the matrix vesicle ruptures due to oversaturation with Ca^+ and PO_4^{3-}, and

spread to the surrounding matrix to form mineralised bone (Golub, 2009; Hasegawa et al., 2017).

Upon completion of bone formation, mature osteoblasts become either osteocytes, bone lining cells, or undergo apoptosis (Figure 2.2) (Jilka et al., 2008; Capulli et al., 2014). Osteoblasts also possess receptors for sex steroids, vitamin D3, parathyroid hormone (PTH), insulin, neuronal targets and cytokines, demonstrating that diverse local and systemic influences can mediate osteoblast function (Zaidi, 2007).
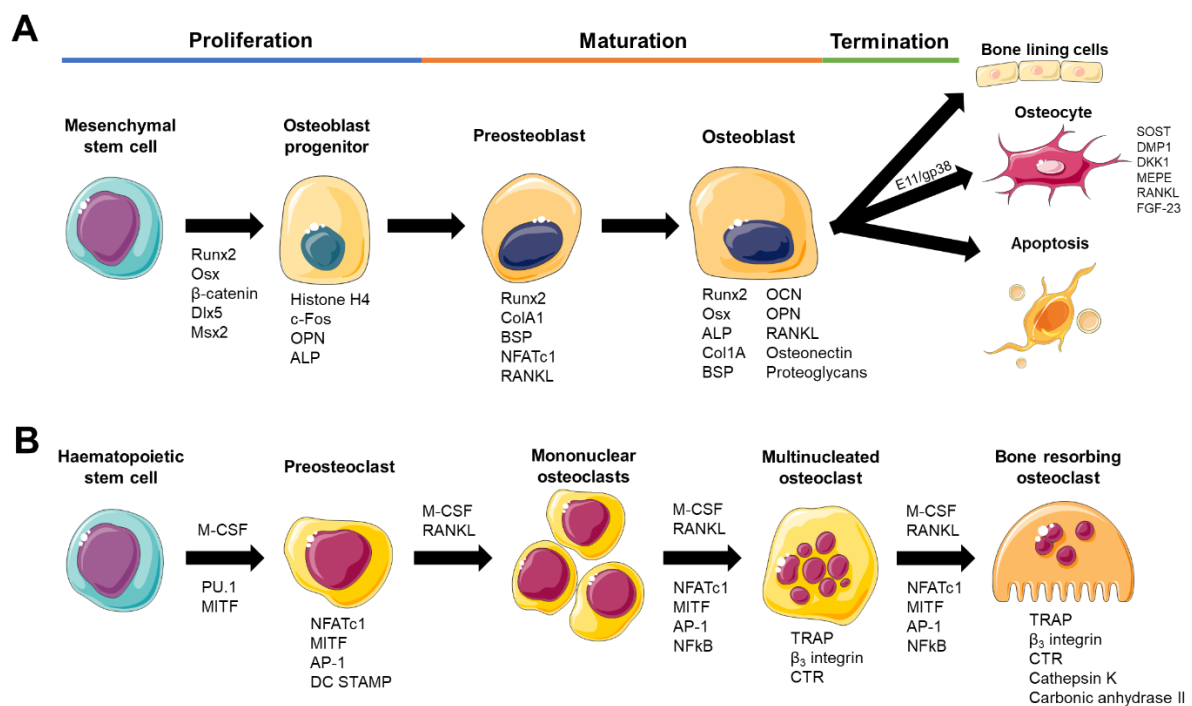
Figure 2.2: Osteoblast and osteoclast lineages. A) Osteoblast proliferation and differentiation from mesenchymal stem cells, as well as genes and factors regulating osteoblastogenesis. Different stages of osteoblastogenesis are indicated by the coloured top line. B) Osteoclast proliferation and differentiation from haematopoietic stem cells, and genes and factors that regulate osteoclastogenesis. Figure produced using Servier Medical Art.

2.1.2.2. Osteocytes

At the end of the bone formation cycle, most mature osteoblasts are dispersed across the bone matrix and, through continued differentiation, become osteocytes, the most abundant (approximately 90% of the total number bone cells) and long lived (up to 25 years) bone cells (Goldring, 2015; Robling and Bonewald, 2020). During the transition from osteoblasts to

osteocytes, long cytoplasmic processes start to emerge and become integrated into the bone matrix to allow the cells to communicate with neighbouring cells and upregulate E11/gp38 (podoplanin, an early osteocyte dendrite formation marker) expression (Zhang et al., 2006; Capulli et al., 2014). As the bone matrix mineralises, the dispersed immature osteocytes become trapped and begin to mature and highly express new osteocyte markers (matrix extracellular phosphoglycoprotein (MEPE), FGF-23 and dentin matrix protein-1 (DMP-1)) that cooperatively control calcium and phosphate regulation (Feng et al., 2003; Nampei et al., 2004; Ubaidus et al., 2009; Robling and Bonewald, 2020). In contrast, expression of OCN, BSP, Col1 and ALP is downregulated.

Mature osteocytes fixed in the bone matrix are an essential source of receptor activator of nuclear factor κB ligand (RANKL) and may direct both the spatial and temporal recruitment of bone cells during bone remodelling (Xiong et al., 2015). Furthermore, osteocytes selectively express sclerostin (Scl), a secreted glycoprotein that antagonises the canonical Wnt and BMP signalling pathways, thereby inhibiting bone formation (Poole et al., 2005; van Bezooijen et al., 2005). Maturing osteocytes undergo morphological and structural changes that correspond with a decrease in protein production and secretion: the round osteoblast size and number of cytoplasmic organelles are reduced, whilst the nucleus to cytoplasm ratio is increased (Schaffler et al., 2014). Mature osteocytes occupy lacunae surrounded by mineralised bone matrix, but form osteocyte lacunocanalicular systems by passing cytoplasmic or dendric processes through canaliculi interconnecting the lacunae (Bozal et al., 2012; Wittig et al., 2019). These systems reach the vascular supply and provide cells with oxygen and nutrients (Thompson et al., 2011). The cytoplasmic processes also connect to neighbouring osteocytes, osteoblasts, and bone lining cell processes by gap junctions to facilitate intercellular nutrients and signalling molecule transport. Osteocytes further enable intercellular communication by releasing signalling molecules, such as prostaglandins and nitric oxide, into the interstitial fluid flowing through lacunocanalicular systems (Yellowley et al., 2000; Wang et al., 2005; Civitelli, 2008).

This interconnectivity and distribution, as well as the abundance of osteocytes in the bone matrix, enable osteocytes to perform their primary role: convert mechanical stimuli to biochemical signals (potentially via the piezoelectric effect). This allows bone, possibly through a process known as Wolff's law, to adapt to daily mechanical forces by changing its

shape (Frost, 1994; Bonewald, 2006; Santos et al., 2009; Bakker and Klein-Nulend, 2010). Bone deposition and resorption is finely controlled under mechanical load. For instance, under mechanical stress, osteocyte expression of Scl, a protein that inhibits the canonical Wnt/β-catenin signalling pathway to down regulate bone formation, decreases, which, in conjunction with other osteoclastogenic factors, is thought to promote osteoclast activity and suppress osteoblast activity (Robling et al., 2008). In addition to modulating bone remodelling, embedded osteocytes can also control mineral metabolism, regulate the function of other organs by secreting endocrine signals, and modify the properties of the surrounding bone matrix (Dallas et al., 2013; Robling and Bonewald, 2020). Ultimately, osteocytes die by apoptosis due to old age or mechanical damage. This process can however act as a signal for osteoclasts to initiate bone resorption by osteoclasts (Plotkin, 2014; Robling and Bonewald, 2020).

2.1.2.3. Bone lining cells

Bone lining cells are quiescent osteoblasts that have a flat shape, few cytoplasmic organelles, a flat and narrow nucleus, and cytoplasm that extends down the bone surface. The cells cover bone surfaces where no bone formation or resorption occur, and sometimes extend cytoplasmic processes into the canaliculi to form gap junctions between neighbouring bone lining cells and osteocytes (Miller et al., 1989; Wein, 2017). Their function is not fully understood, but, when osteoclastic bone resorption should not occur, bone lining cells have been shown to inhibit direct interaction between the bone matrix and osteoclasts (Andersen et al., 2009). Osteoblastic secretory activity (see 2.1.2.1) can be reacquired, depending on the physiological status of bone, and bone lining cells can express OPG and RANKL to facilitate osteoclast differentiation. Lastly, during the bone remodelling cycle, bone lining cells form a key element of the temporary basic multicellular unit (BMU) (Everts et al., 2002; Wein, 2017).

2.1.2.4. Osteoclasts

Osteoclasts are large, terminally differentiated single or multinucleated cells that are responsible for bone resorption (Figure 2.2). They are derived from haematopoietic stem cells

(HSCs) in the liver, spleen and bone marrow that are stimulated by macrophage colony stimulating factor (M-CSF) to generate mononuclear cells that become osteoclast precursor cells. These precursor cells are introduced into the blood circulation to exit at resorption sites and fuse and form immature multinucleated osteoclasts (Teitelbaum, 2000). Development of mature osteoclasts occurs within the local bone microenvironment and requires a multitude of transcription factors and other proteins secreted by osteoprogenitor mesenchymal cells, osteocytes, osteoblasts and mesenchymal stromal cells that promote transcription factor activation and gene expression in osteoclast precursor cells to drive cells into a mature osteoclast phenotype (Crockett et al., 2011; Yavropoulou and Yovos, 2008).

Osteoclastogenesis commences when RANKL binds to receptor activator of nuclear factor κB (RANK) by physical contact with osteoclast precursors (Jimi et al., 1996; Asagiri and Takayanagi, 2007; Soltanoff et al., 2009). When both M-CSF and RANKL, two crucial cytokines, are present, the preosteoclasts fuse together into a multinucleated osteoclast associated with initiation of β3 integrin, tartrate-resistant acid phosphatase (TRAP) (assists with bone resorption in mature osteoclasts) and calcitonin receptor (CTR) expression (Suda et al., 1999). Other osteoclastogenic factors, such as dendrocyte expressed seven transmembrane protein (DC-STAMP) and NFATc1, are also expressed when RANKL binds to RANK (Takayanagi et al., 2002; Miyamoto, 2006). NFATc1 interacts with ETS-family transcription factor PU.1, c-Fos, a member of AP-1, and microphthalmia-associated transcriptor factor (MITF) to regulate cathepsin K and TRAP, both genes that are critical for osteoclast activity (Wang et al., 1992; Matsuo et al., 2004; Partington et al., 2004; Costa et al., 2011). Combined expression of these factors promotes immature osteoclast differentiation into mature osteoclasts (Figure 2.2) (Boyle et al., 2003). Low extracellular pH likely increases the expression of the osteoclastogenic and bone-resorption regulatory factors (such as NFATc1, OPN and cathepsin K), resulting in increased osteoclast differentiation, survival and resorptive activity (Brandao-Burch et al., 2005; Yuan et al., 2016). Osteoclastogenesis can be inhibited by osteoprotegerin (OPG), which acts as a soluble decoy for RANKL and occupies stromal RANKL binding sites on osteoclast precursor cells and differentiated osteoclasts to prevent binding between RANKL and RANK. The RANKL/RANK/OPG process is essential for osteoclastogenesis and osteoblastic modulation of the RANKL/OPG ratio is another example of the intimate functional coupling between osteoblasts and osteoclasts (Simonet et al., 1997; Boyce and Xing, 2008).

Mature osteoclasts can have 4-5 nuclei and form a highly dynamic podosome that is, through mediation by $\alpha v\beta 3$-integrin (transmits signals that polarises osteoclast) and CD44, attached to the bone surface where it establishes a microenvironment that is separated from the surrounding extracellular space, allowing bone resorption to proceed solely under the ruffled podosome border (Figure 2.2) (Chabadel et al., 2007; Luxenburg et al., 2007). Chloride channel 7 (ClC-7) and vacuolar-type H^+-ATPase pumps (V-ATPase) transports Cl^- anions and H^+ cations through the ruffled border plasma membrane to, together with the action of carbonic anhydrase II, acidify the compartment between the osteoclast and bone matrix. This acidification results in dissolution of hydroxyapatite crystals to form the characteristic Howship's lacunae (shallow bone concavities) and exposes the organic matrix (Riihonen et al., 2007; Qin et al., 2012). Matrix metalloproteinase-9 (MMP9), TRAP and cathepsin K are transported to the Howship's lacuna and degrades the exposed collagenous matrix. The degradation products are then transported through the ruffled border via endocytosis and moved, by transcytosis, to the functional secretory domain located opposite from the ruffled border for secretion (Nesbitt and Horton, 1997; Henriksen et al., 2006; Teitelbaum, 2007; Wilson et al., 2009).

Osteoclasts also display various other functions, such as participation in immune responses, influencing bone formation by secreting factors that act on osteoblasts and osteoclasts, hormone secretion, and movement of hematopoietic stem cells from bone marrow to the bloodstream, thus functioning as more than just bone resorption cells (Boyce et al., 2009; Charles and Aliprantis, 2014; Han et al., 2018).

2.1.3. Bone physiology

Bone is a dynamic organ that can alter its structure and mass to adapt to shifting needs. It accomplishes this through bone growth, modelling, remodelling and other activities, each with their own functions and mediator mechanisms.

2.1.3.1. Bone growth

Skeletal bones are formed by two processes: intramembranous and endochondral ossification. Flat bones, such as the cranium and medial clavicles, are formed by intramembranous ossification, whilst irregular and long bones from the axial (mandible and vertebrae) and appendicular (humeri, radii, femurs and tibiae) skeleton are formed by endochondral ossification (Yamaguchi et al., 2000; Nakashima and de Crombrugghe, 2003).

Intramembranous ossification

Condensation of mesenchymal cells initiates the intramembranous ossification process. The condensed cells then differentiate into osteoblasts and, due to the absence of a cartilaginous framework known as anlagen, deposits bone matrix (osteoid) directly to form ossification centres (Figure 2.3) (Karaplis, 2008, p. 3). Plates that expand are formed during development. However, to regulate the expansive growth of the cranium, flat bones formed by this process do not fuse with other bones and are separated by junctions known as sutures (Hall and Miyake, 1992).

Endochondral ossification

To begin the endochondral ossification process, condensed mesenchymal cells in the central diaphysis produce a growing population of collagen type II expressing chondrocytes (Figure 2.3) (Kosher et al., 1986; Karaplis, 2008). The chondrocytes produce a collagen type II containing extracellular matrix (ECM) and form cartilaginous anlagen that act as templates for developing bone. Chondrocytes then become hypertrophic and signal peripherally localised perichondral cells to direct differentiation into osteoblasts. The anlagen at the centre of the extended cartilaginous template becomes vascularised when vascular endothelial growth factor (VEGF) is expressed by the hypertrophic chondrocytes, forming the ossification centre (Karaplis, 2008; Berendsen and Olsen, 2015). Vascularisation enables osteoblast precursor cells to infiltrate the template, develop into mature osteoblasts, and begin secretion and mineralisation of an collagen type I-containing ECM, thereby producing anlagen through endochondral ossification (Figure 2.3) (Nakashima and de Crombrugghe, 2003; Berendsen and Olsen, 2015). The ossification centre propagates towards the two epiphyseal growth

plates which, through chondrocyte proliferation at the proximal end and differentiation to hypertrophy and apoptosis at the distal end, facilitates continuous linear bone growth in long bones (Karaplis, 2008).
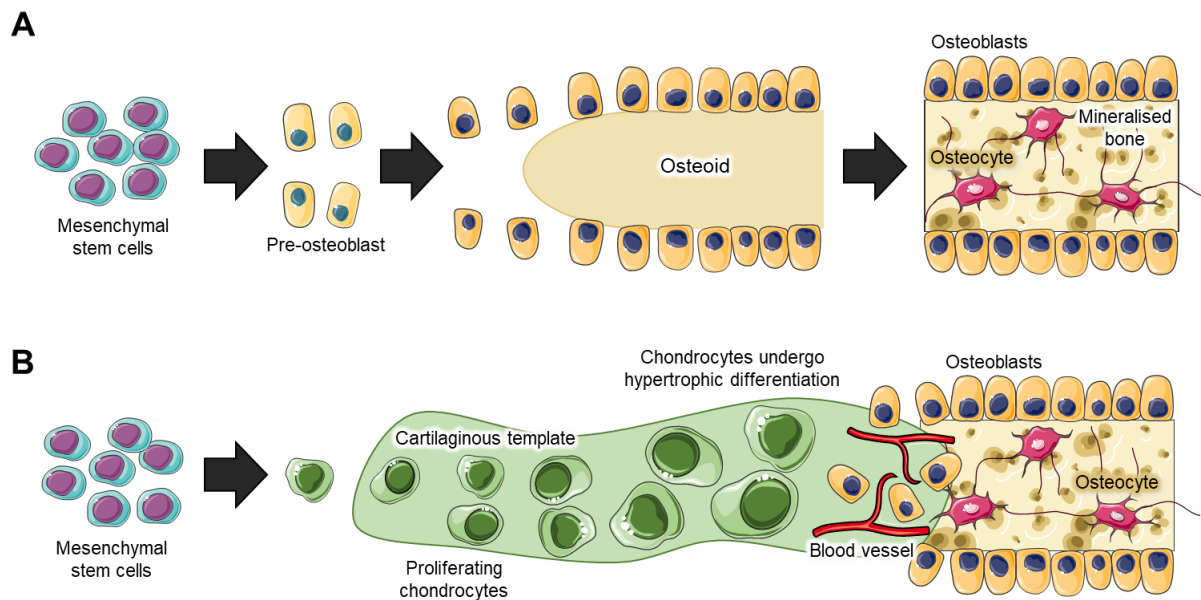
Figure 2.3: Intramembranous and endochondral ossification. A) Intramembranous ossification. Mesenchymal stem cells (MSCs) differentiate into preosteoblasts, which in turn differentiate into osteoblasts. Osteoblasts lay down Col1-rich osteoid that mineralises to form an ossification centre. Upon completion of bone formation, some osteoblasts terminally differentiate into osteocytes. B) Endochondral ossification. MSCs differentiate into chondrocytes and produces a cartilaginous template for endochondral bone formation. Chondrocytes become hypertrophic and signal for vascularisation of the template, allowing osteoblasts to transport to the site and form osteoid on the template. Figure produced using Servier Medical Art and adapted from Kenkre and Bassett, 2018.

The canonical Wnt pathway determines whether MSCs differentiate into osteoblasts or chondrocytes for intramembranous or endochondral bone formation respectively (Hartmann, 2007; Houschyar et al., 2019). Sonic hedgehog morphogen partially induces Wnt signalling in the intramembranous bone formation area, resulting in elevated MSC β-catenin levels (Hu et al., 2005). This inhibits expression of genes required for chondrogenesis, whilst increasing transcription of genes required for osteoblastogenesis. In contrast, low β-catenin levels are present in endochondral bone formation, resulting in upregulation of transcription factors that drives MSCs to differentiate into chondrocytes (Akiyama et al., 2002). Endochondral ossification is negatively regulated by local FGF, which inhibits chondrocyte proliferation, and chondrocyte differentiation to hypertrophy is inhibited by cytokine parathyroid hormone

related peptide (PTHrP) (Vortkamp et al., 1996; Ornitz, 2005). In addition, glucocorticoids, growth hormone (GH), IGFs, thyroid hormone, oestrogen, androgen, vitamin D and leptin are all involved in chondrocyte proliferation, maturation, differentiation, hypertrophy, and subsequent bone growth (reviewed by Nilsson et al., 2005).

2.1.3.2. Bone modelling

The purpose of bone modelling is bone growth, and optimisation and minimisation of bone strength and mass by maintaining or changing the size, shape and mass of pre-existing bone. Bone modelling mainly happens during skeletal growth and enables bone adaptation in response to rapidly changing growth-related mechanical strain (Robling et al., 2006; Seeman, 2009; Allen and Burr, 2014). Once signals for change are detected, bones can be shaped or reshaped by the selective independent or coordinated actions of osteoblasts (formation modelling) and osteoclasts (resorption modelling) (Figure 2.4) (Allen and Burr, 2014; Langdahl et al., 2016).

During growth, the proper shape of long bones and radial growth is maintained by highly coordinated bone apposition and resorption on spatially independent bone surfaces (Figure 2.4) (Allen and Burr, 2014; Langdahl et al., 2016). As the long bone lengthens, periosteal resorption modelling is accompanied by formation modelling on the endocortical surface of the metaphyseal region (Ominsky et al., 2015). During radial growth, bone apposition on the periosteal surface is usually countered by resorption modelling on the endocortical surface, allowing the medullary area to increase without significantly impacting bone strength (Ruff and Hayes, 1982; Zebaze et al., 2007). Modelling drift, a process during which bone is formed and resorbed on opposite cortices, is mainly associated with radial growth, but also occurs in adult skeletons. These drifts enable the skeleton to adapt to changes in the direction of an applied mechanical load and are, for example, responsible for changes in orientation of the axis of an aging hip joint, orthodontic tooth movements and modified humerus shape and size in a tennis player's playing arm (Haapasalo et al., 2000; Kontulainen et al., 2003; Gasser and Kneissel, 2017).

Bone modelling decreases significantly once skeletal maturity is reached. However, other factors such as mechanical loading, PTH, oestrogen and sclerostin play major roles in directing radial bone growth through bone modelling and can result in renewed modelling in the adult skeleton (Hodsman and Steer, 1993; Lindsay et al., 2006; Ominsky et al., 2014).

2.1.3.3. Bone remodelling

Bone remodelling is a coupled reconstruction process that replaces aged and damaged bone with new bone throughout life, thus maintaining mechanical integrity and renewing the entire adult skeleton approximately every 10 years, with trabecular remodelling occurring at a much faster rate than cortical remodelling (Julie C. Crockett et al., 2011; Kenkre and Bassett, 2018). The process can release growth factors (such as TGF-β, IGFs and FGF) embedded in bone and is the sole mechanism that replaces aged, dying or dead osteocytes (Seeman, 2013; Raubenheimer et al., 2017).

Bone remodelling is characterised by sequential bone resorption and formation, mediated by osteoclasts and osteoblasts respectively, that occur in a coupled manner in a bone remodelling unit (BMU) on a given bone surface (Figure 2.4) (Crockett et al., 2011; Hattner et al., 1965; Seeman, 2008). The BMU functions in a special bone remodelling compartment (BRC) with a roof of bone lining cells on the marrow side and the remodelling bone surface on the osseous side (Figure 2.4) (Crockett et al., 2011). The whole BMU moves as a unit, with osteoblasts following behind osteoclasts, allowing the resorption and formation processes to occur in a controlled, coupled manner that ensures new bone is deposited where bone has been removed by osteoclasts. New BMUs are initiated from within bone marrow, periosteum or vasculature within existing osteons (Parfitt, 2000; Allen and Burr, 2014). Osteons are the final products of cortical bone remodelling (described in 2.1.1 Bone structure and composition). Bone remodelling on trabecular, endocortical and sometimes subperiosteal surfaces forms hemiosteons, which are osteons with no incorporated blood vessels. During intracortical remodelling, osteoclasts drill through cortical bone in a cone-shaped formation, leaving a rod-like void that is filled by following osteoblasts in a closing cone (Dempster and Lindsay, 1993; Parfitt, 1994).

Remodelling in intracortical, endocortical and trabecular surfaces is common during growth, development and adulthood, whilst remodelling on the periosteal surface occurs far less frequently. The remodelling rate is high during growth and then slowly decreases until peak bone mass is reached. Bone mass is then stable for 1-2 decades until age related bone loss resulting from increased bone resorption and decreased bone formation begins (Dempster and Lindsay, 1993). The bone remodelling rate varies in adults and is influenced by genetics, age and modifiable factors such as physical activity, hormonal status, nutrition and medication. The process increases progressively after onset of menopause, due to loss of circulating oestrogen, resulting in increased osteoclast formation, decreased osteoclast apoptosis, and subsequent suppression of remodelling (Allen and Burr, 2014). The remodelling process is classified as either targeted (30%) or non-targeted (70%) remodelling (Parfitt, 2002). Non-targeted remodelling is considered a random process during which osteoclast resorption is triggered by a systemic initiating event and is believed to be more involved in mineral homeostasis and the fulfilment of bone metabolic requirements by storing and releasing minerals such as phosphorous and calcium. In contrast, targeted remodelling plays a role in maintaining skeletal mechanical integrity and initiates osteoclast-mediated resorption by directing osteoclasts to a given location via specific local signals (Burr, 2002). Targeted remodelling repairs sections of bone in response to mechanical forces, microscopic damage and osteocyte apoptosis (Mori and Burr, 1993; Burr, 2002). Microscopic damage disrupts the osteocyte network by physically breaking cytoplasmic connections between cells. These osteocytes that are cut off undergo apoptosis and produce RANKL, a crucial element in the recruitment and development of osteoclasts (Verborgt et al., 2000). In addition, nearby healthy osteocytes produce OPG, an apoptotic signal for osteoclasts. It is possible that this signalling pattern serves as a target for osteoclasts to initiate remodelling activity at the breakage site. Osteocyte apoptosis is induced by an excess of glucocorticoid, oestrogen deficiency and mechanical disuse, which are all linked to increased remodelling, further supporting the vital part played by osteocyte apoptosis in bone remodelling (Kennedy et al., 2012). Furthermore, inhibition of osteocyte apoptosis results in inhibition of bone remodelling.

The remodelling cycle is characterised by activation, resorption, reversal, formation and resting phases (Figure 2.4) (Allen and Burr, 2014). These five stages are not coordinated with

each other and at any given time occur at approximately one million remodelling sites throughout the skeleton. In humans, each cycle takes approximately 4-6 months (this time is highly altered by disease) and matrix mineralisation continues for months after production (Kenkre and Bassett, 2018).

Activation

The activation phase is triggered by systemic hormones, microscopic bone damage and mechanical forces and starts with digestion of an unmineralised matrix layer by bone lining cell-produced collagenase to expose the bone matrix. Osteoclast precursor cells are then recruited to the exposed surface where they, due to a decrease in pH and an increase in osteoclastogenic and bone-resorption regulatory factors, differentiate into preosteoclasts that merge to become multinucleated mature osteoclasts (Figure 2.4) (Chambers and Fuller, 1985; Raggatt and Partridge, 2010; Kenkre and Bassett, 2018).

Resorption

During the resorption phase, bone lining cells withdraw from the bone surface, making it possible for the multinucleated mature osteoclasts to attach to the exposed matrix (Figure 2.4). The attached osteoclasts actively dissolve the bone hydroxyapatite, thereby liberating the collagen fibres, which are useful biomarkers for bone resorption. New osteoclasts are recruited to the site as resorption proceeds to either support existing osteoclasts or replace dead osteoclasts. Osteoclasts resorb for 3-6 weeks at a given site (Kenkre and Bassett, 2018).
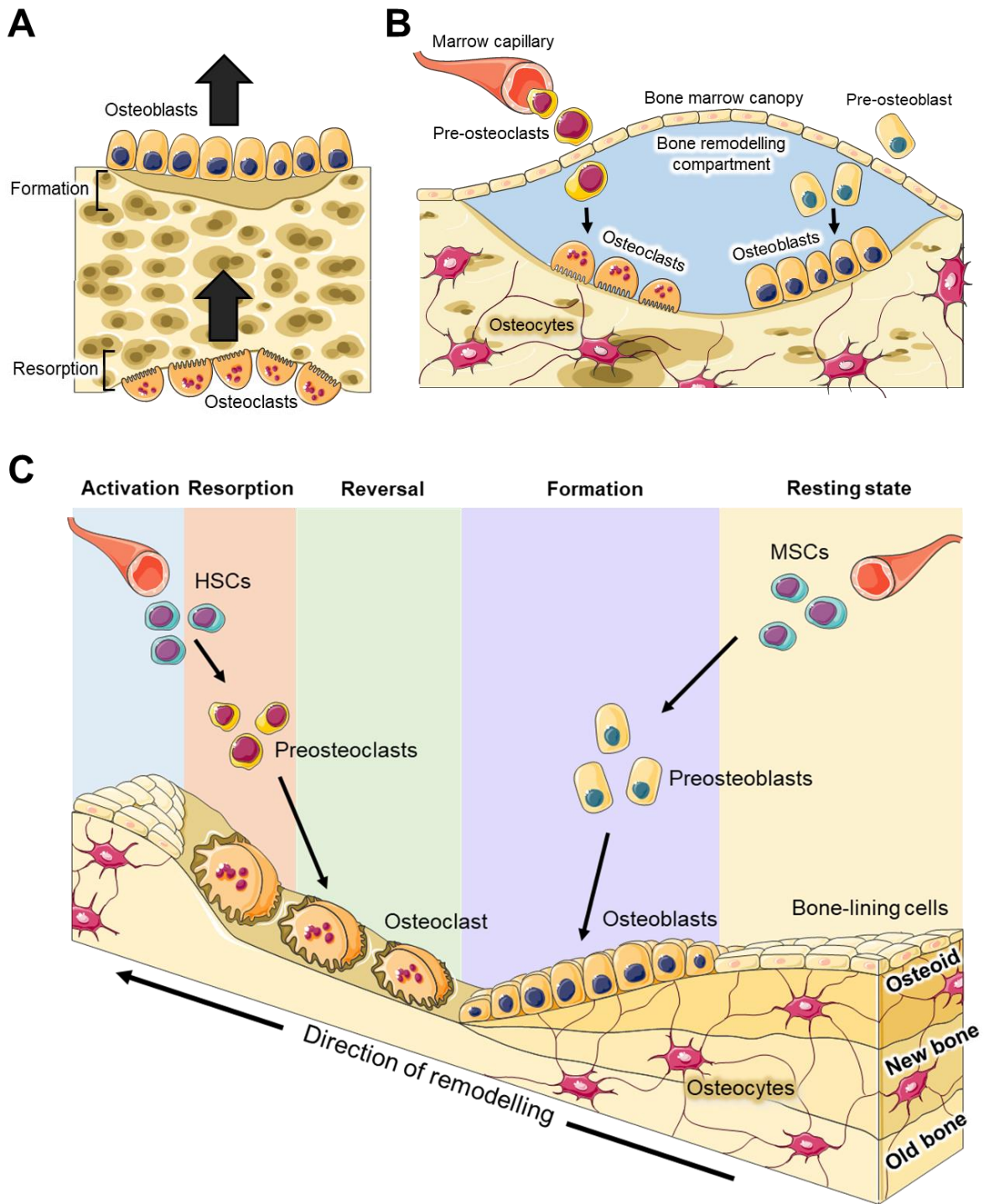
Figure 2.4: Bone modelling and remodelling. A) Modelling: Once signals for change are detected in bone, bones can be shaped or reshaped by the selective independent or coordinated actions of osteoblasts (formation modelling) and osteoclasts (resorption modelling). Formation and resorption modelling occur on different surfaces. B) Bone remodelling compartment (BRC): When remodelling is required, a roof of bone lining cells is formed on the marrow side allowing remodelling in C) to occur on the osseous side within the BRC. C) Bone remodelling by a basic multicellular unit (BMU). The remodelling cycle consists of activation, resorption, reversal, formation, and resting phases. Haematopoietic stem cells (HSCs) are activated by a stimulus (e.g. microdamage) and differentiates into preosteoclasts, which then differentiate into mature osteoclasts that actively resorb bone at the stimulus site. As osteoclasts move on, mesenchymal stem cell (MSC) derived preosteoblasts differentiate into osteoblasts that form osteoid at the resorption sites. Upon completion of bone formation, osteoblasts either die or differentiate into bone lining cells or osteocytes. Figure produced using Servier Medical Art.

Reversal

Osteoclast resorption is ceased during the reversal phase and osteoblast precursors differentiate to initiate bone formation (Figure 2.4). The presence of extracellular ephrin-B4 on osteoblasts and ephrin-B2 on osteoclast cell membranes suggest that reversal could be initiated by direct cell-to-cell interaction between osteoclasts and osteoblasts or osteoblast precursors, thus inducing cessation for one and activation for the other (Zhao et al., 2006). It is also possible that osteoblast recruitment, migration and differentiation are stimulated by topographical changes that are sensed by osteocytes, factors secreted by osteocytes (CTHRC1, Wnt10b, cardiotrophin-1, sphingosine-1-phosphate, BMP6, and complement factor3a) and bone matrix released factors, such as platelet derived growth factor (PDGF), TGF-β, IGFs, and BMPs, from the resorption phase (McNamara et al., 2006; Julie C. Crockett et al., 2011; Sims and Martin, 2015; Sims et al., 2016). For osteoblasts to proceed, remaining collagen fragments on the exposed surface are removed by little defined specialised cells that deposit a thin layer of new bone matrix (reversal line) that is rich in proteoglycans such as OPN. This proteoglycan rich reversal line inhibits crack propagation, provides fibre matrix bonding to enhance bone's resistance to fractures, and delineates boundaries of osteons and hemiosteons from surrounding old matrix (Sroga and Vashishth, 2012; Kenkre and Bassett, 2018).

Formation

Mature osteoblasts deposit osteoid, primarily composed of collagen type 1 fibres, that serves as a template for the hydroxyapatite crystals (Figure 2.4). Primary mineralisation, where calcium and phosphate ions are incorporated into the matrix, takes approximately 2-3 weeks. This is followed by secondary mineralisation, where the final addition and mineralisation of hydroxyapatite crystals occur, a process that can take up to a year or longer to complete (Raggatt and Partridge, 2010; Gasser and Kneissel, 2017).

Resting

After forming new bone, osteoblasts either undergo apoptosis, are replaced by new osteoblasts if more bone formation is still required or are integrated into the bone matrix to

differentiate into osteocytes. Finally, to conclude the bone remodelling cycle, remaining osteoblasts become inactive bone lining cells that cover the new bone surface and the new matrix continues to mineralise over time (Kenkre and Bassett, 2018).

The bone remodelling balance or bone balance is the net quantity of old bone resorbed and new bone deposited in each bone remodelling cycle. In young adults, bone mass is stable and bone remodelling is balanced for one to two decades after reaching peak bone mass (Langdahl et al., 2016). Once age-related bone loss begins, the balance becomes is slightly negative in healthy adults (Kiberstis et al., 2000; Langdahl et al., 2016). Any imbalance or dysregulation of this balance results in many pathological conditions.

2.1.4. Metabolic bone disorders

In mature, healthy bone, bone remodelling ensures that bone mass or quality is not altered during the remodelling cycles. Maintaining this proper bone balance necessitates balanced coupling of bone resorption and bone formation, processes that involve numerous coordinated signalling mechanisms. This fine balance can be disrupted by age-related factors, hormonal imbalances, medication, secondary diseases and changes in physical activity, resulting in abnormal bone remodelling and development of bone disorders.

2.1.4.1. Osteoporosis

Osteoporosis, the most common metabolic bone disorder, affects approximately 30% of women and 20% of men older than 50 years of age (Cooper and Ferrari, 2017). The condition is characterised by low bone mass and reduced structural integrity, and resulting bone fragility and increased susceptibility to fractures ("Consensus development conference," 1993; NIH Consensus Development Panel on Osteoporosis Prevention, Diagnosis, and Therapy, 2001). Postmenopausal osteoporosis affects postmenopausal women and is characterised by an accelerated phase of bone loss resulting from a decrease in oestrogen levels associated with menopause.

Oestrogen maintains bone formation and antiresorptive effects by directly and indirectly promoting osteoclast apoptosis, whilst also promoting the differentiation of bone marrow stromal cells towards the osteoblast lineage, increasing differentiation of preosteoblasts to osteoblasts, and restricting osteoblast and osteocyte apoptosis (Chow et al., 1992; Qu et al., 1998). It does this by increasing procollagen synthesis and production of growth factors (TGFα and IGF-1) by osteoblasts, and suppressing expression of sclerostin, a potent Wnt signalling inhibitor (Oursler et al., 1991; Mirza et al., 2010; Mödder et al., 2011; Farr et al., 2015). It also suppresses RANKL (key factor in osteoclast development) production and some cytokines (interleukin 1 and 6 (IL-1 and -6), TNFα and M-CSF), and increases OPG production by osteoblast lineage cells (Hofbauer et al., 1999; Eghbali-Fatourechi et al., 2003; Drake and Khosla, 2018). Oestrogen also plays a dominant part in maintaining skeletal integrity in aging men (Falahati-Nini et al., 2000; Finkelstein et al., 2016). A decrease in oestrogen at onset of menopause and during aging thus mainly results in an extended bone resorption and shortened bone formation period, and an increased BMU activation frequency rate, resulting in decreased total bone mass (seen as a negative bone balance) and structural weakening of bone (Hughes et al., 1996; Manolagas, 2000; McClung et al., 2018). In men, trabecular bone formation by osteoblasts and osteocyte related prevention of trabecular bone loss is stimulated by testosterone signalling (Golds et al., 2017; Shin et al., 2018). Bone is also indirectly affected by testosterone through aromatisation of testosterone to oestrogen by aromatase. Testosterone deficiency in elderly men and men with both primary and secondary hypogonadism thus results in osteoporosis, with decreased BMD and increased risk of fractures (Golds et al., 2017; Shin et al., 2018). Osteoporosis is also caused by glucocorticoid treatment and lack of physical movement (Takata and Yasui, 2001; Smith et al., 2005; Kim et al., 2007).

2.1.4.2. Osteogenesis imperfecta

Osteogenesis imperfecta (OI), or "brittle bone disease", is a group of heritable conditions that are characterised by variable degrees in bone fragility and consequent bone fractures. It is the most common bone disease caused by a variable single gene mutation that results in defects in collagen type 1 fibrils or defective production of collagen type 1 by osteoblasts,

resulting in reduction in bone strength that can vary from a modest increase in fracture risk to a lethal form (Peel, 2009). Defective or insufficient collagen type 1 results in a significant decrease in cortical and trabecular bone quality or quantity, with consequent shortened and deformed limbs, scoliosis, and vertebral compressions that often present with multiple fractures (Shapiro et al., 1989; Engelbert et al., 2003). In addition, respiration function can be limited by defective thoracic musculoskeletal development, and hydrocephalus and hearing loss (conductive, sensorineural or mixed) may occur (Kuurila et al., 2003; Kovero et al., 2006; Vitale et al., 2007).

2.1.4.3. Paget's disease of bone

Paget's disease of bone is the second most common metabolic bone disorder. It is characterised by the presence of giant multinucleated osteoclasts, with as many as 100 nuclei, that cause a dramatic increase in bone resorption, and a subsequent increase in formation of new bone by an increased number of osteoblasts near the resorption areas to compensate for bone loss (Mills and Singer, 1976; Rebel et al., 1976; Gherardi et al., 1980). Pagetic osteoclast precursors' hyperresponsiveness to RANKL further contributes to the significant increase in bone resorption (Menaa et al., 2000). Due to this disordered resorption and formation, a disorganised mixture of woven and lamellar bone is developed at the affected skeletal sites. The disorganised bone is characterised by decreased bone density, increased vascularisation and expanded size, resulting in bone that is weaker and more prone to deformities or fractures than healthy bone (Peel, 2009; Charles et al., 2018). These bone changes cause bone deformities, bone related pain, secondary arthritis, and associated neurological complications (Feng and McDonald, 2011).

2.1.4.4. Rickets

Rickets occurs prior to epiphyseal closure in children and is characterised by hypomineralisation of the bone matrix associated with a directly inhibited mineralisation process and/or severe nutritional calcium (Ca), vitamin D and phosphate deficiency. Related growth plate cartilage accumulates as hypertrophic chondrocytes fail to undergo apoptosis (a

process dependent on phosphorylation of caspase-9) due to hypophosphatasia, thereby preventing vascularisation and subsequent osteoblastic mineralisation of the cartilaginous template (Demay et al., 2007; Munns et al., 2016). This hypomineralisation results in abnormal growth plate development, painful swelling around metaphyseal zones, stunted growth and bone deformities (Pettifor et al., 2018). In addition, symptoms are further enhanced by heightened bone resorption and increased bone turnover caused by inhibition of osteoblast progenitors, decreased OPG and increased RANKL (Lips et al., 2013).

2.1.4.5. Osteomalacia

Osteomalacia is a metabolic bone disorder that is characterised by hyperosteoidosis and impaired or altered bone mineralisation that results in low BMD and accumulation of unmineralised osteoid in the skeleton (Francis and Selby, 1997; Gifre et al., 2011; Bilezikian, 2019). Clinical features include muscle weakness, musculoskeletal pain, skeletal fractures and deformity, raised serum ALP and is often accompanied by rickets (widening of epiphyses and impaired skeletal growth) in childhood. As with rickets, the major cause of osteomalacia is a severe deficiency in vitamin D, phosphate, Ca and/or direct inhibition of the mineralisation process, resulting from limited sun exposure and disorders in vitamin D and phosphate metabolism (Francis and Selby, 1997; Bilezikian, 2019). Vitamin D is metabolised in the liver to produce 25-hydroxyvitamin D, followed by renal production of 1,25-dihydroxyvitamin D, the hormonally active metabolite of vitamin D, which promotes mineralisation by osteoblasts and stimulates intestinal Ca uptake to maintain plasma Ca concentrations (Francis and Selby, 1997; Need et al., 2008; Christakos et al., 2016). Lack of vitamin D results in decreased phosphate and Ca uptake, as well as secondary hyperparathyroidism, which increases bone resorption but reduces mineralisation. Calciotropic hormones, such as PTH, thus maintain plasma Ca concentrations at the expense of skeletal integrity to prevent dysregulation of vital Ca-dependent physiological functions like neuromuscular and cardiac excitation and blood coagulation (Need et al., 2008).

2.1.4.6. Osteopetrosis

Osteopetrosis, also known as "marble bone disease", is a heterogenous group of rare heritable bone-remodelling disorders that, in contrast to the metabolic bone disorders discussed above, are characterised by increased bone mass (Stark and Savarirayan, 2009; Sobacchi et al., 2013). These changes are caused by autosomal recessive or autosomal dominant mutations that affect osteoclast formation or function, resulting in defective osteoclast mediated bone resorption during skeletal growth and bone modelling and remodelling (Feng and McDonald, 2011; Bilezikian, 2019). Osteopetrosis is a rare condition and presents as two distinctive clinical forms: the more common autosomal dominant adult type (approximately 1 in 20 000), which presents relatively few symptoms, and the rarer autosomal recessive infantile type (approximately 1 in 250 000), which is usually fatal in early childhood if left untreated (Johnston et al., 1968; Loría-Cortés et al., 1977; Stark and Savarirayan, 2009).

2.1.4.7. Van Buchem disease

Van Buchem disease (previously known as hyperostosis corticalis generalisata) is a rare (<40 reported cases), autosomal recessive, sclerosing bone dysplasia (van Buchem et al., 1955; Fosmoe et al., 1968; Van Hul et al., 1998). The condition is characterised by progressive generalised hyperostosis (increased bone formation) throughout life, primarily in the skull, mandible, ribs, clavicles and diaphysis of the long bones. Excess bone in the skull often entrap the cranial nerves and may result in facial nerve palsy, sensorineural hearing loss, visual complications and neuralgic pain (Fosmoe et al., 1968; van Buchem et al., 1976). Van Buchem disease is caused by deletion of a 52 kb homozygous, non-coding segment in the 17q12-q21 chromosomal region (Balemans et al., 2002; Van Hul et al., 1998). The deletion occurs 35 kb downstream from the *SOST* gene and removes an enhancer element that is essential for directing the expression of sclerostin, a negative regulator of bone formation, in the adult skeleton, resulting in defective sclerostin synthesis (Loots et al., 2005). The condition is allelic to sclerosteosis, another rare bone disorder with a similar, but more severe phenotype.

2.2. Sclerosteosis

Sclerosteosis (OMIM accession number 269500) is an autosomal recessive, high bone mass condition that was first described in 1958 (Truswell, 1958). It is a rare condition with approximately 100 cases reported worldwide, of which two thirds are of Afrikaner descent from South Africa, where the sclerosteosis phenotype was delineated (Beighton et al., 1976, 1977; Beighton and Hamersma, 1979; Beighton, 1988). Other cases are from the US (Higinbotham and Alexander, 1941; Kelley and Lawlah, 1946; Stein et al., 1983), Germany (Pietruschka, 1958), Japan (Sugiura and Yasuhara, 1975), Spain (Bueno et al., 1994), Senegal (Tacconi et al., 1998), Greek Cypriot (Itin et al., 2001), Brazil (Kim et al., 2008), Turkey (Piters et al., 2010) and China (He et al., 2016). Sclerosteosis has been linked to loss of function mutations in *LRP4* as well as absence of sclerostin expression caused by mutations within the *SOST* gene and is, in contrast to many osteopetrotic high bone mass conditions, associated with increased bone formation (hyperostosis), instead of defects in bone resorption (Balemans et al., 2001; Balemans et al., 2002; Beighton et al., 1984; Fijalkowski et al., 2016). Variable cutaneous or bony syndactyly (fusion of the digits) and dysplastic or absent nails are absent from van Buchem disease, but are the earliest post-natal indicators of sclerosteosis (Figure 2.5) (Beighton et al., 1976; Hamersma et al., 2003). Further clinical features include increased bone mineral density (BMD) throughout the skeleton, thicker than normal trabeculae and cortices, and widespread skeletal overgrowth during the early decades of life. Bone overgrowth is more prominent in the skull, mandible, and long bones, resulting in gross distortion of the facies and a tall stature (Figure 2.5) (Hamersma et al., 2003; Gardner et al., 2005). As with van Buchem, the facial nerve is often entrapped as a result of hyperostosis of the skull, causing recurring facial palsy that results in impaired facial movement later in life. During early childhood, patients experience conductive hearing loss, which is usually followed by sensorineural hearing loss in adulthood when the vestibulocochlear nerve becomes entrapped and the round and oval windows of the inner ear starts to close due to excessive bone growth (Hamersma and Hofmeyr, 2007). Furthermore, thickening of calvarium can result in a potentially fatal increase in intracranial pressure in the early decades of life (du Plessis, 1993; Hamersma et al., 2003). The condition is currently managed through complex decompression surgery, whilst hearing loss can be corrected through middle ear surgery, use of hearing aids, and brain stem implantation of electrodes if the auditory nerves are damaged

(du Plessis, 1993; Hamersma and Hofmeyr, 2007). Nonetheless, treatment of the pathological changes of sclerosteosis remains difficult due to the thickness and density of the bone. Surgical intervention is lengthy and difficult, and typical neurosurgical instruments are often inadequate (du Plessis, 1993). Furthermore, symptoms often recur due to post-surgical bone regrowth. Remarkably, the disease is not linked to elevated risk of fractures, regardless of increased BMD and bone mass. The mutated *SOST* gene does not appear to have extensive pleiotropic effects, as suggested by an otherwise normal endocrine system and no noticeable effects on non-skeletal tissue (Brunkow et al., 2001). In contrast to sclerosteosis patients, disease carriers, with only a single mutated allele, have lower circulating sclerostin levels (approximately 60%) and increased BMD compared to non-disease carrying controls (van Lierop et al., 2017).

Causative mutations have been mapped to the q12-q21 location on chromosome 17, the same location as the van Buchem disease causing mutations (see 2.1.4.6), and two independent research groups reported mutations in the *SOST* gene, where a premature amino-terminal (N-terminal) stop codon results in loss of sclerostin expression (Van Hul et al., 1998; Balemans et al., 1999, 2001; Brunkow et al., 2001). Additional *SOST* mutations, one of which alters the processing of the *SOST* transcript, have subsequently been identified (Balemans et al., 2002; van Lierop et al., 2017). More recently, mutations in *LRP4*, located at p11.2 on chromosome 11, were shown to effect changes in the extra cellular β-propeller of LRP4, a region that is crucial for sclerostin interaction with LRP4 (Leupin et al., 2011; Chang et al., 2014; Fijalkowski et al., 2016). All of these reported mutations result in loss of functional sclerostin or sclerostin-LRP4 interaction, and subsequent disruption of the canonical Wnt signalling pathway (Fijalkowski et al., 2016; van Lierop et al., 2017).
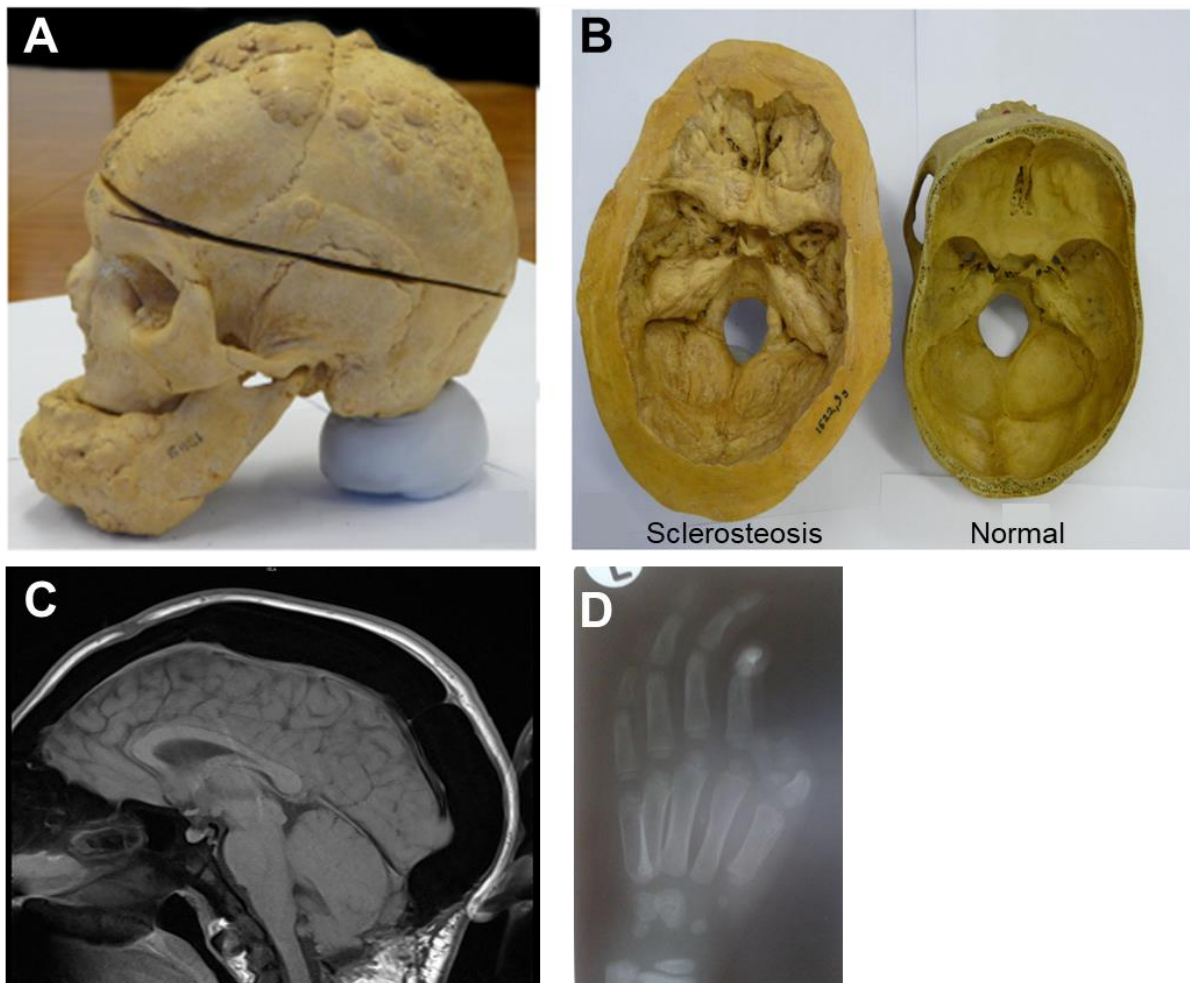
Figure 2.5: Skull and hand of a sclerosteosis patient. A) and B) Photos of the skull of a patient with sclerosteosis (A) and (B), and an individual without the bone disorder (B). C) MRI of the skull of a sclerosteosis patient, with the black region around the brain representative of excessive bone. D) X-ray image of the hand of a sclerosteosis patient with syndactyly. *From the collection of the University of Pretoria, South Africa (van Lierop et al., 2017).*

2.3. Wnt signalling

The wingless-related integration site (Wnt) signalling pathway is an evolutionarily conserved pathway that is essential for regulation of embryogenesis and maintenance of adult tissue homeostasis. In response to Wnt stimulus, direct signalling can occur along one of three distinct intracellular pathways: one is a canonical Wnt/β-catenin signalling pathway, whilst the others are non-canonical pathways. The canonical Wnt/β-catenin signalling pathway is the most extensively-studied of the three and is essential for bone formation (reviewed by Niehrs, 2012; Baron and Kneissel, 2013; Nusse and Clevers, 2017).

The canonical Wnt signalling pathway is activated once Wnt, a secreted glycoprotein, binds to the seven-transmembrane-spanning receptors from the frizzled family of receptors (Fzd) and the low-density lipoprotein receptor-related proteins 5 and 6 (LRP5/6) Wnt co-receptors, forming an LRP5/6-Wnt-Fzd ternary complex (Figure 2.6). Fzd then interacts intracellularly with dishevelled (DVL), whilst the phosphorylated cytoplasmic domain of LRP5/6 recruits AXIN, subsequently disrupting the activity of the β-catenin containing destruction complex. Activated non-phosphorylated β-catenin accumulates in the cytoplasm, from where it is translocated to the cell nucleus and initiates expression of the *Wnt* target genes by associating with T-cell factor/lymphoid enhancer factor (TCF/LEF) transcription factors bound to nuclear DNA (Figure 2.6) (Nusse and Clevers, 2017; Holdsworth et al., 2019).

Wnt pathway activation is tightly controlled by secreted antagonists, such as sclerostin (Scl), that either binds to Wnt ligands or Wnt co-receptors. Sclerostin antagonises the canonical Wnt signalling pathway by binding to the LRP4 Scl co-receptor and the LRP5/6 Wnt co-receptors, thus preventing interaction between Wnt and LRP5/6, and the consequent development of the LRP5/6-Wnt-Fzd complex and its activation of the Wnt signalling cascade (Figure 2.6) (Fijalkowski et al., 2016; Holdsworth et al., 2019). During this inhibited state, cytosolic β-catenin is phosphorylated by glycogen synthase kinase 3 beta (GSK3β) and casein kinase 1 (CK1) (part of the destruction complex), labelling β-catenin for ubiquitination and subsequent degradation by the proteasome. This prevents β-catenin accumulation and translocation to the nucleus, allowing Groucho, a transcriptional repressor, to associate with the TCF/LEF transcription factors and keep it in an inactive state, thereby inhibiting expression of Wnt target genes (Figure 2.6) (Angers and Moon, 2009; Nusse and Clevers, 2017; Holdsworth et al., 2019).

Among numerous roles, canonical Wnt signalling promotes MSC differentiation to the osteoblast lineage, whilst inhibiting osteoclastogenesis and MSC commitment to adipogenic and chondrogenic lineages (Day et al., 2005; Glass et al., 2005; Hill et al., 2005; Lerner and Ohlsson, 2015).
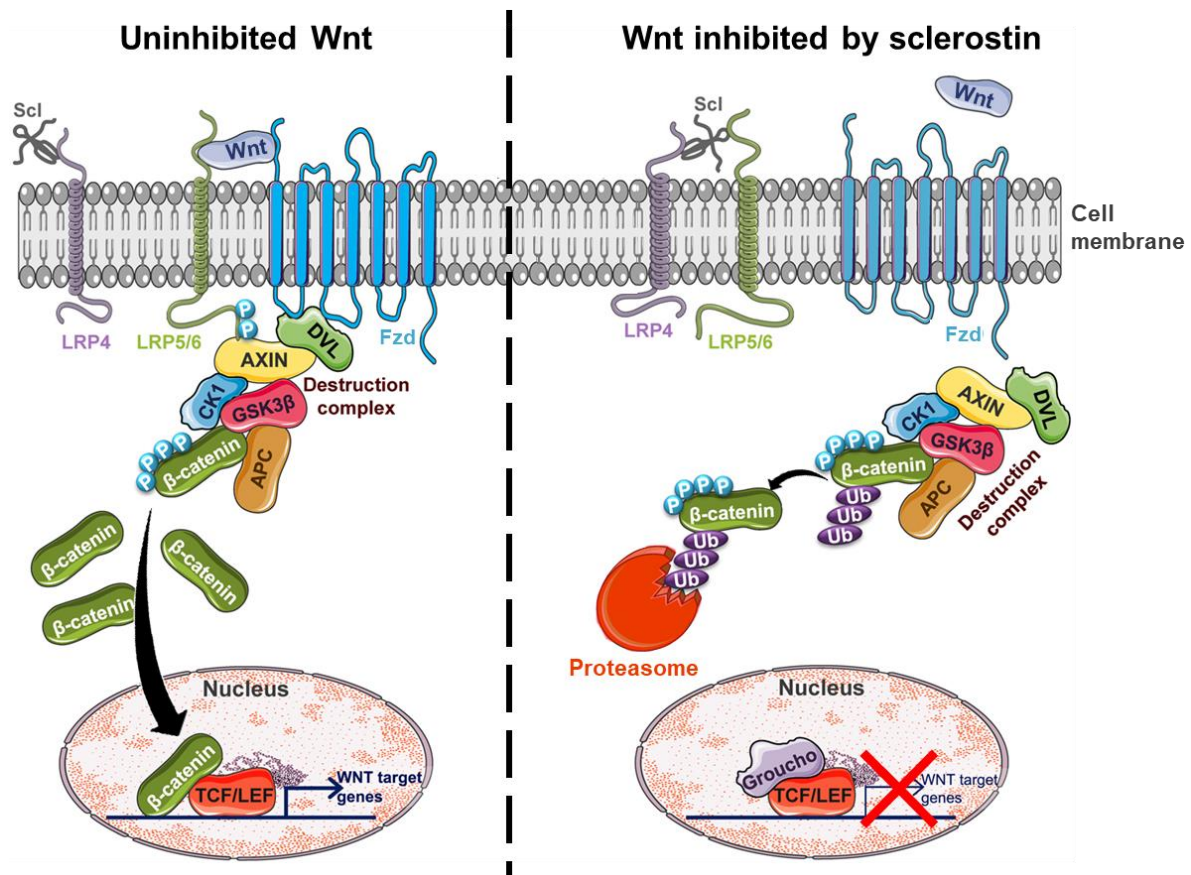
Figure 2.6: A simple illustration of the uninhibited and sclerostin inhibited canonical Wnt signalling pathway. Uninhibited extracellular Wnt binds to a frizzled (Fzd) family and the LRP5/6 cell-surface receptors to form a ternary complex. The intracellular region of LRP5/6 is phosphorylated, followed by AXIN recruitment, resulting in disruption of destruction complex activity. Transcription of Wnt target genes is initiated once non-phosphorylated β-catenin binds the TCF/LEF transcription factors in the cell nucleus. The canonical Wnt signalling pathway is inhibited when sclerostin binds to LRP4 and LRP5/6 *Wnt* co-receptors. This prevents Wnt from interacting with LRP5/6 and inhibits LRP5/6–Wnt–Fzd complex formation and subsequent AXIN recruitment. The destruction complex tags phosphorylated β-catenin with ubiquitin, targeting it for proteasomal degradation. In the cell nucleus, transcription of *Wnt* target genes is repressed when Groucho associates with DNA-bound TCF/LEF transcription factors. Figure adapted from Holdsworth *et al.*, 2019.

2.4. Sclerostin

Sclerostin (Scl), a potent Wnt antagonist, was originally identified in genetic screens of sclerosteosis and van Buchem disease, and is expressed in mouse skeletal anlagen and limb buds, where it plays a role in limb patterning (Loots et al., 2005; Collette et al., 2016). Through early development and adulthood, Scl expression is primarily expressed by mature osteocytes in the skeleton. However, lesser amounts of Scl are also produced by cementocytes, hypertrophic and articular chondrocytes, synovial fibroblasts, and other cells linked with mineralised matrix (Poole et al., 2005; Chouinard et al., 2016; Wehmeyer et al., 2016).

Sclerostin is also present in non-mineralising tissues, such as the kidney and human aorta, where it is upregulated during vascular calcifications, acting as a potential regulator of mineralisation. During embryogenesis and neonatal development, Scl is expressed in developing heart and the smooth muscle cells of the great arteries (Bezooijen et al., 2007; Zhu et al., 2011; Murali et al., 2017). Remarkably, there are no apparent effects on non-skeletal tissue in sclerosteosis patients, suggesting that Scl does not have widespread pleiotropic effects (Brunkow et al., 2001).

Sclerostin is present in the circulation of non-diseased adults and serum levels increase with age, whilst no Scl is detected in sclerosteosis patients (Roforth et al., 2014; van Lierop et al.,2017). The circulating Scl appears to be relevant to the skeleton, as systemically overexpression of Scl (up to two-fold) in mice caused a modest reduction in femoral and trabecular bone fractions, but its role is not yet completely understood (Zhang et al., 2016; Kim et al., 2017). Sclerostin activity within the skeleton appears to occur at a local level where it is produced by local osteocytes (Poole et al., 2005). This is corroborated by an increase in both circulating Scl and bone mass when Scl binding to LRP4, a co-receptor that plays an important role in retaining and facilitating local Scl action, is impaired, suggesting that the circulating Scl does not always correlate with bone density (Fijalkowski et al., 2016).

A range of approaches, such as Scl deletion in SOST knockout animals, overexpression of Scl in transgenic animals, administration of recombinant Scl protein and neutralisation of endogenous Scl using Scl antibodies in mouse, rat, monkey and human genetic, preclinical and clinical studies, have been applied to demonstrate that Scl plays a crucial role in bone homeostasis by regulating bone resorption and inhibiting bone formation (Li et al., 2009; Krause et al., 2010; Ominsky et al., 2010; Holdsworth et al., 2019).
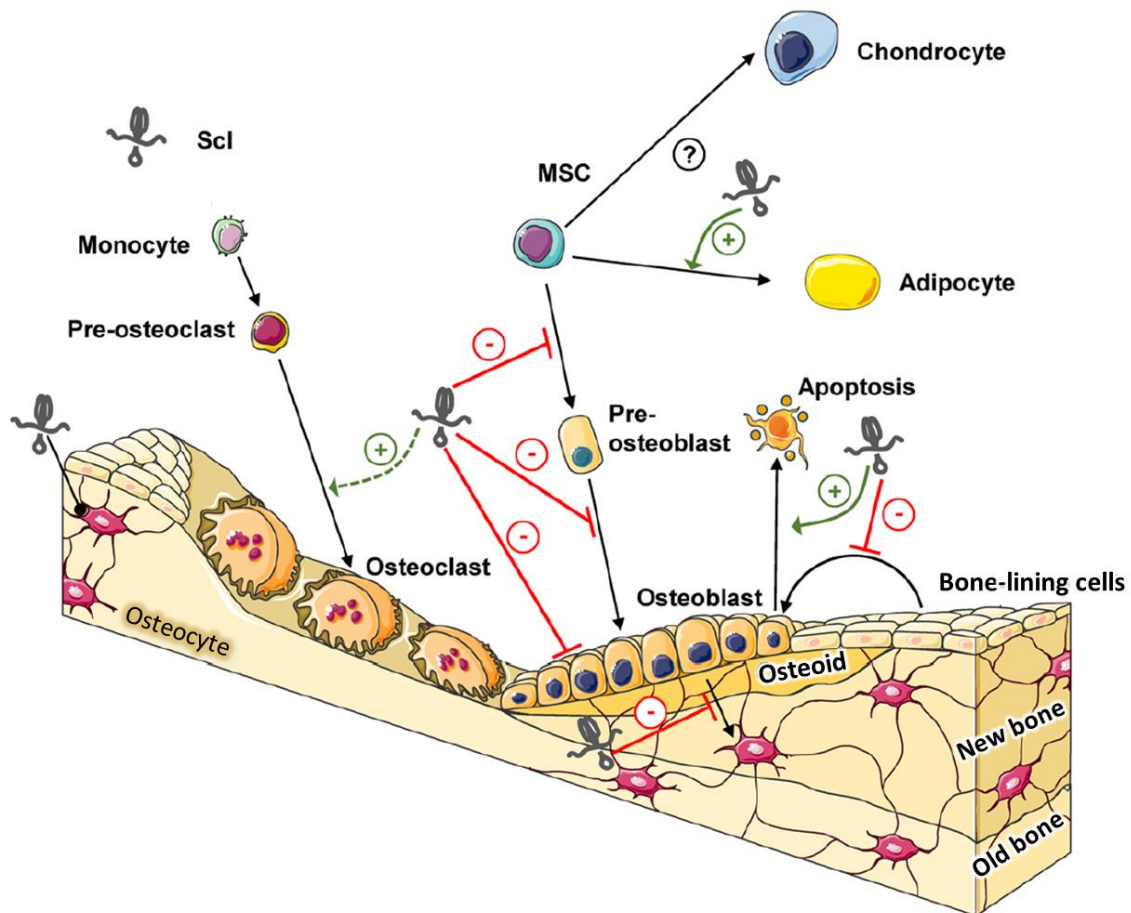
Figure 2.7: Effects of sclerostin on bone formation and resorption. Sclerostin (Scl) inhibits bone formation by inhibiting the canonical Wnt signalling pathway and exerts its function by: restricting MSC differentiation towards the osteoblast lineage; promoting adipogenic differentiation; inhibiting pre-osteoblasts from differentiating into osteoblasts; preventing quiescent bone lining cells from reverting to their osteoblastic state; promoting osteoblast apoptosis; decreasing osteoblast-mediated bone matrix formation; inhibiting osteoblast differentiation into osteocytes. Scl further enhances osteoclast differentiation by controlling osteoblast expressed osteoclast regulators, thereby promoting bone resorption indirectly. Figure adapted from Holdsworth et al., 2019.

2.4.1. Cellular level actions of sclerostin

2.4.1.1. Osteoblast lineage

Sclerostin exerts its function as a bone formation inhibitor in various ways throughout the osteoblast lineage (Figure 2.7). It decreases osteoblast proliferation and osteoprogenitor recruitment to the active bone surface, whilst increasing osteoblast apoptosis, thereby regulating the function of the osteoblast linage and population of osteoprogenitor cells directly, causing a decrease in osteoblast numbers and subsequent bone formation (Ominsky et al., 2015; Taylor et al., 2016; Greenbaum et al., 2017; Boyce et al., 2018). In addition, ALP activity is decreased by Scl, resulting in decreased mineralisation, which is also linked to

upregulation of MEPE and associated reduction in phosphate-regulating neutral endopeptidase, X-linked (PHEX), a pro-mineralisation enzyme, expression in human primary cells (Winkler et al., 2003; Sutherland et al., 2004; Atkins et al., 2011; Kogawa et al., 2017). Post bone formation, Scl plays a role in regulation of osteocyte maturation by inhibiting transition of late osteoblasts to osteocytes (Atkins et al., 2011). Moreover, restoration of Wnt signalling, enhanced osteogenesis and decreased osteocyte apoptosis, is associated with Scl inhibition, demonstrating Scl's role as a regulator of osteocyte apoptosis (Lin et al., 2009; Veverka et al., 2009; Krause et al., 2010; Shahnazari et al., 2012b). Sclerostin may also be involved with perilacunar mineral regulation by local osteocytes and plays a key role in maintaining osteocyte morphology, connectivity, number and orientation, and bone lining cell quiescence (Chandra et al., 2017; Kim et al., 2017; Qing and Bonewald, 2009; Ren et al., 2015). In addition, osteocyte Scl expression is decreased in bone under mechanical load, whilst increased in bone under no load, consistent with the proposed skeletal mechanosensory role of osteocytes (Robling et al., 2008; Kogawa et al., 2017).

2.4.1.2. Osteoclasts

In contrast to the osteoblast lineage, Scl has no direct influence on osteoclasts and indirectly enhances and increases osteoclastogenesis and bone resorption in manner that depends on RANKL (Figure 2.7) (Wijenayaka et al., 2011). This is done by regulating the Wnt signalling pathway in osteoblasts and osteocytes, and subsequently exerting an effect on the RANKL:OPG ratio, which plays a key role in osteoclastogenesis, a process that is promoted by RANKL binding to RANK (Glass et al., 2005; Tu et al., 2015). There is also evidence that Scl could regulate osteoclastogenesis by affecting expression of other regulators, such as Csf1 and WNT1-induced secretion protein (Wisp1) (Taylor et al., 2016; Holdsworth et al., 2018).

2.4.1.3. Chondrocytes

Activated Wnt signalling inhibits MSC differentiation into chondrocytes and, in response, articular chondrocytes and growth plate hypertrophic chondrocytes express Scl to inhibit the canonical Wnt/β-catenin pathway. However, the effect of Scl on chondrocyte differentiation

has not been studied in depth (Figure 2.7) (Winkler et al., 2003; Bezooijen et al., 2009). *In vitro* studies have however shown that Scl increases anabolic gene expression and decreases catabolic proteases expression to inhibit chondrocyte apoptosis (Chan et al., 2011; Bouaziz et al., 2015).

2.4.1.4. Adipocytes

Sclerostin promotes MSC differentiation towards the adipogenic lineage and enhances adipogenesis in white adipose tissue, thus acting as an endocrine factor and contributing to cross communication between the skeleton and adipose tissue (Figure 2.7). This regulation of adipose tissue could demonstrate a link between Scl and energy metabolism. However, Scl-mediated inhibition of adipogenesis and regulation of fat deposits in humans is currently not well studied and understood (reviewed by Holdsworth et al., 2019).

2.4.2. Biochemistry and structure

Human Scl is a 21573 Da, 213 amino acid (aa) glycoprotein initially identified as a member of the BMP antagonising Dan/Cerberus family (Brunkow et al., 2001; Kusu et al., 2003; Winkler et al., 2003; ten Dijke et al., 2008; Veverka et al., 2009; Krause et al., 2010). Arginine and lysine residues are highly abundant within the protein, resulting in a rather basic peptide with a calculated isoelectric point (pI) of approximately 9.5. A mature 190 aa protein is expressed in mammalian and insect expression systems and appears as a doublet on SDS-PAGE. This likely reflects variations in glycosylation, of which the functional significance is not fully understood (Krause et al., 2010; Holdsworth et al., 2012).

In solution, Scl exists as a highly flexible monomer that comprises flexible amino (N) and carboxy (C) terminal arms and a central cysteine knot motif surrounded by three loops (Figure 2.8) (Veverka et al., 2009; Weidauer et al., 2009). The rigid first (Loop 1) and third (Loop 3) loops stem from the top of the cysteine knot motif and are held in place by a disulphide bond at their tips, giving the protein a structured core. The second loop (Loop 2) is unstructured and highly flexible in solution and exists on the opposing side of the central cysteine knot. It

contains a region that binds to LRP5/6 and is critical for Scl function (Veverka et al., 2009; Weidauer et al., 2009; Holdsworth et al., 2012). Loops 1 and 3 form a hydrophobic patch (possibly a protein interaction site) on the concave protein face. One of the protein sides is covered with a linear stretch of positively charged residues in loops 2 and 3. This linear stretch of positively charged residues has been shown to interact with heparin to localise Scl to cell surfaces (Figure 2.8) (Veverka et al., 2009). In addition, various sulphated glycosaminoglycans (GAGs) within the bone extracellular matrix binds to this region, suggesting that Scl binding to these GAGs and the cell surface might play a role in local regulation of Scl function. GAGs that interfere with Scl LRP5/6 interaction also bind to this region and has been shown to restore Wnt signalling in a reporter cell line (Salbach-Hirsch et al., 2015; Holdsworth et al., 2019).
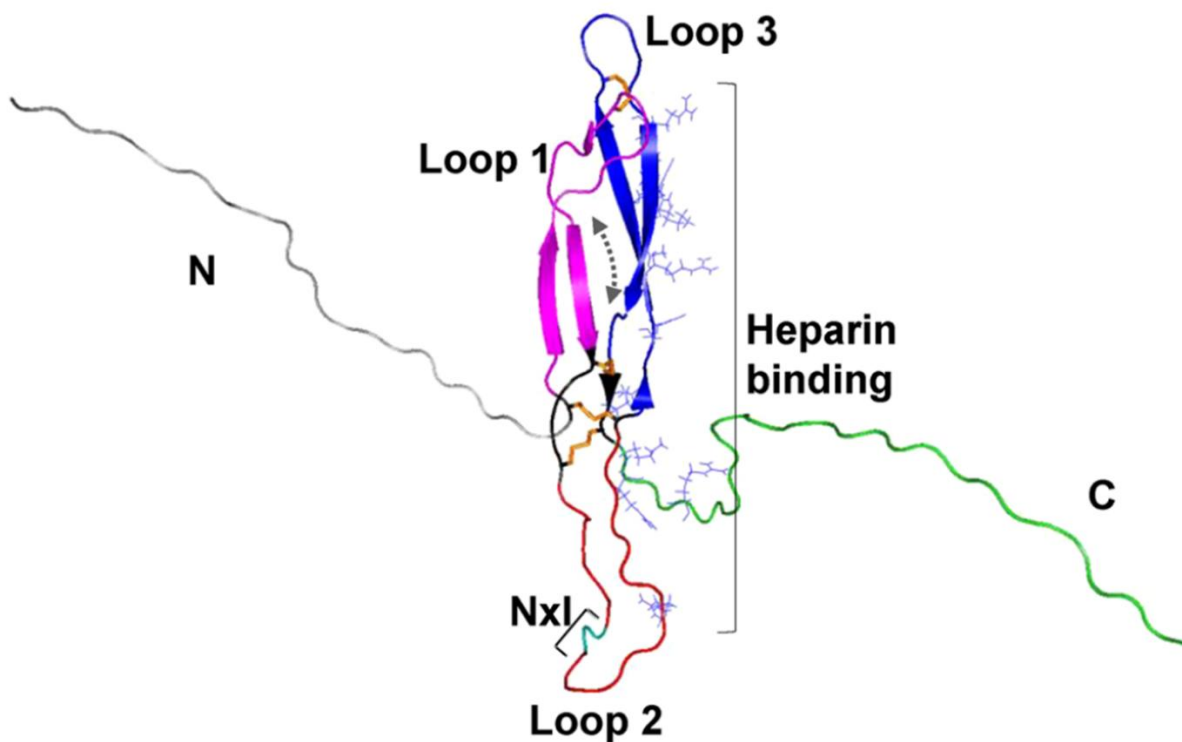
Figure 2.8: Ribbon illustration of the human sclerostin protein. The illustration shows the backbone topology of human Scl (Protein Data Bank accession number 2K8P): The N-terminal (grey) and C-terminal (green) arms of the protein are partially truncated for simplicity (aa 30–170 shown). The central cysteine knot (black) and its disulphide bonds (orange) are surrounded by three loops. The rigid loops 1 (magenta) and 3 (blue) are joined by a disulphide bond (orange) at their tips. In contrast, Loop 2 (red) is unstructured and highly flexible. The hydrophobic pocket (dotted grey curved arrow) is situated between loops 1 and 3. The NxI motif (teal) that interacts with LRP5/6 is located on Loop 2. Blue side chains indicate residues thought to be involved in heparin binding. Figure from Holdsworth et al., 2019.

The 'NxI' motif (asparagine (N) and isoleucine (I) residues separated by any other aa residue (x)) in Loop 2 is conserved and crucial for high-affinity interaction between Scl and LRP5/6 (Bourhis et al., 2011; Holdsworth et al., 2012). Sclerostin binds to the first (E1) and potentially the second (E2) of four β propellers that form part of the extracellular domain of the LRP5/6 Wnt co-receptors to inhibit canonical Wnt signalling (Li et al., 2005; Semënov et al., 2005; Bourhis et al., 2011; Holdsworth et al., 2012). In doing so, Scl inhibits Wnt binding to the E1 propeller and subsequent WNT1 class canonical signalling (Bourhis et al., 2010; Ettenberg et al., 2010). Sclerostin also binds to LRP4, a proposed Scl co-receptor (non-Wnt co-receptor). Mutations in the E3 propeller of LRP4 impairs binding with Scl and results in similar symptoms to that of sclerosteosis. These mutations are also associated with increased serum Scl levels, suggesting Scl is retained in the skeleton by the anchoring action of LRP4 (Leupin et al., 2011; Chang et al., 2014; Fijalkowski et al., 2016).

Sclerostin's action in sclerosteosis as an antagonist of the Wnt/β-catenin signalling pathway by binding to LRP4/5/6 is further supported by high bone mass phenotypes resulting from mutations in the LRP5 E1 region of LRP5/6 that impair Scl binding and its subsequent action as a Wnt inhibitor. Moreover, monoclonal anti-Scl antibodies inhibit Scl binding to LRP4/5/6 and induces osteoblast activity and bone formation, thereby increasing BMD and bone mass and improving bone architecture and strength. Anti-Scl antibodies have therefore been explored as a therapeutic strategy for low bone mass conditions such as osteoporosis (Wesenbeeck et al., 2003; Semenov and He, 2006; Little et al., 2017; Lovato and Lewiecki, 2017; McClung, 2017). One such antibody, Romosozumab (Evenity®), shows marked increases in bone formation and BMD and rapid and substantial reduction in fracture risk, and has recently been approved as a first-in-class antibody treatment for osteoporosis (Mullard, 2019).

2.4.3. Sclerostin as regulator of bone mass and strength

SOST knockout mice progressively showed rapid elevation of bone mineral density (BMD) in the lumbar spine and long bones, increased bone formation parameters in endocortical, trabecular, periosteal surfaces, and no significant observed changes in bone resorption biomarkers in serum and at osteoclast surface areas (Ke et al., 2012). These results supported

development of anti-sclerostin antibodies (as potential therapeutic agents for low bone mass conditions such as osteoporosis) that successfully induced increased bone formation, bone mass and bone strength, thereby providing more data that demonstrates Scl's function as a negative regulator of these bone parameters (reviewed by Holdsworth et al., 2019). Inversely, overexpression of Scl has shown insignificant changes in bone resorption and has been shown to reduce cortical bone thickness and trabecular bone volume (Kramer et al., 2010; Zhang et al., 2016). It also decreases bone strength by significantly reducing bone formation, thus raising the question of whether increasing Scl could be used as a treatment for sclerosteosis.

2.5. Sclerostin replacement as a potential treatment for sclerosteosis

As mentioned earlier (2.2), no treatment is available to prevent or reverse sclerosteosis. However, based on results from previous studies, where the over-expression of Scl has been shown to decrease the BMD in mouse models, it is possible that exogenous Scl could serve as a viable treatment, either early on in the disease as a means of prevention, or later as a bone formation control agent (Ke et al., 2012; Zhang et al., 2016; Kim et al., 2017). The manufacturing of therapeutic proteins is, however, extremely complex and has limitations, such as complex purification processes, low oral availability due to denaturing in the gut, and high production costs. Complex secondary and tertiary structures need to be maintained and post-translational modifications are usually required, necessitating production in living cells or organisms. Moreover, proteins usually have a short half-life, and large proteins are unable to efficiently penetrate tissues to reach targets due to their large size and immunogenicity (Lagassé et al., 2017; Murray et al., 2017; Haggag et al., 2018). Despite these drawbacks, there are ways to overcome or reduce the impact of some of these limitations.

Production

Proteins are often too complex to be manufactured by chemical processes alone and require living cells or organisms for production. Functional Scl has previously been produced in recombinant plasmid-expressing HEK293 mammalian cells, which maintained the necessary protein folding and post translational modifications that would occur during expression in a mammalian organism (Holdsworth et al., 2012). Such an approach could be replicated and

adapted to produce larger quantities of protein required for *in vivo* studies. Furthermore, additional nanofiltration and purification steps that require low ionic strength buffer, such as cation exchange chromatography, could be implemented to reduce possible endotoxin and viral contamination (Petsch, 2000; Korneyeva and Rosenthal, 2005).

Half-life

Of concern for protein replacement therapies is the short half-life of the product, which could render the protein ineffective due to lack of efficacy or need for frequent administration. Whilst the serum half-life of mouse Scl (~20 kDa) has not been reported, we speculated that, as they are small, the peptides would likely display a short plasma half-life (Werle and Bernkop-Schnürch, 2006; Veverka et al., 2009). From literature, a bioactive recombinant protein can be fused to the fragment crystallisable (Fc) domain of immunoglobulin G1 (IgG1) antibody to create a fusion protein with a potential increased half-life of up to 23 days (Lobo et al., 2004; Shimamoto et al., 2012; Wu and Sun, 2014; Rath et al., 2015). Additionally, the Fc fusion protein has a slower renal clearance due to its increased size, and facilitates *in vivo* protein stability by binding to the neonatal Fc receptor (FcRn) (Rath et al., 2015; Kontermann, 2016). Two Fc molecules can also spontaneously homodimerise to generate two peptides in each fusion protein, which could increase avidity for its target (Kontermann, 2011; Shimamoto et al., 2012; Wu and Sun, 2014). Eleven Fc-fusion proteins have currently been approved for therapeutic use, with more (26) in clinical trials (reviewed by Strohl, 2018).

Distribution

Considering that Scl is produced by osteocytes and effects its action in the skeleton, localisation of Scl to bone could improve the effectiveness of the fusion construct. Drugs could potentially be selectively delivered to bone by directing the drug to hydroxyapatite, an inorganic component of bone, as hydroxyapatite does not exist in soft tissues. Numerous non-collagenous, hydroxyapatite binding bone proteins have repeating acidic aa (aspartic (Asp) and glutamic (Glu) acid) sequences in their structures that act as potential hydroxyapatite-binding sites (Kasugai et al., 2010). Nishioka et al. demonstrated that the addition of an

aspartate sequence to the C-terminal of anchorless recombinant human tissue-nonspecific alkaline phosphatase (rhTNALP) enhanced its affinity for hydroxyapatite, extended retention times, and had little influence on other biochemical properties (Nishioka et al., 2006). These properties were replicated by Asfotase alfa (Enobia Pharma), marketed as STRENSIQ® by Alexion, a commercially available drug that demonstrates higher affinity for hydroxyapatite due to inclusion of a deca-Asp sequence (Millán et al., 2008; Whyte et al., 2012). It is thus possible that addition of such an aspartate sequence to Scl or a Scl-Fc fusion protein could enhance its distribution and efficacy.

Although expression of functional Scl is a complex process, multiple steps are available to circumvent production and protein limitations to produce a potential protein-based therapeutic for sclerosteosis.

2.6.   Conclusion

Sclerosteosis, a severe genetic disorder with no available treatment, is caused by mutations in the *SOST* gene, which result in a lack of Scl, a negative regulator of bone formation. This lack of Scl results in excessive bone formation, producing the typical sclerosteosis phenotype. This thesis explores the concept that administration of exogenous Scl constructs to sclerosteosis patients could antagonise the canonical Wnt signalling pathway, thereby reducing abnormal bone formation. The efficacy of such exogenous Scl constructs could be improved by extending protein half-life through fusion of Scl with Fc and improving distribution to bone by addition of poly-aspartate motifs, thus presenting a novel approach to treat this debilitating, sometimes fatal condition.

Chapter 3: Materials and methods

3.1. Plasmid design, cloning and protein production

3.1.1. Plasmid design and cloning

The aim of the plasmid design and cloning section was to design, clone and produce three recombinant expression plasmids that encode for wild type mouse Scl (mScl), mScl fused with human Fc (mScl hFc), and mScl hFc with an octa-aspartate motif (poly-aspartate, PD) attached at the hFc C-terminus (mScl hFc PD). All plasmids were prepared for expression in a mammalian expression system.

General cloning procedures

A proprietary pMH vector with modified CMV promotors (UCB Pharma, Slough, UK) (used for all recombinant constructs) and plasmids containing hFc, hFc poly D, mSOST, and mSOST WT fragments, obtained from DNA2.0 (Newark, NJ, USA), were used to construct the three expression plasmids via restriction digest and DNA ligation. All plasmids were resuspended in 10 mM Tris-HCl pH 8 buffer to give a final concentration of 0.5 µg/µL DNA2.0 plasmids and 1 µg/µL UCB vector.

3.1.1.1. Restriction enzyme digest

For general restriction digests, 20 µL reaction mixtures were prepared with 1 µg DNA and 1 or 2 units of each restriction enzyme in an appropriate enzyme buffer. Amounts and volumes of each component were increased and decreased proportionally if more DNA was required for ligation reactions. Restriction digest mixtures were incubated at 37 °C for 1 hour, except when stated otherwise. DNA loading dye was added to each restriction digest sample after incubation and loaded onto an agarose gel for gel electrophoresis.

3.1.1.2. Gel electrophoresis

For DNA fragment analysis by horizontal electrophoresis, appropriate size markers and restriction digest samples were loaded onto a 1% (w/v) agarose gel in 1x TAE buffer, which were run at 90 V/cm for typically 1 hour on a Bio-Rad Horizontal Electrophoresis System coupled to a Bio-Rad PowerPac™ Basic Power Supply (Bio-Rad, Hercules, CA, USA). Gels were stained with ethidium bromide (EtBr) (Thermo Fischer Scientific, Waltham, MA, USA) and DNA bands were visualised using UV transillumination at 254 nm, followed by excision for ligation reactions. Agarose gel electrophoresis was also used for restriction analysis (3.1.1.6).

3.1.1.3. DNA fragment preparation

Selected DNA fragments were excised and purified from agarose gels with two different DNA recovery kits: a QIAGEN QIAquick Gel Extraction Kit (Qiagen, Hilden, Germany) at UCB (UCB Pharma, Slough, UK) and a Zymoclean Gel DNA Recovery Kit (Zymo Research, Irvine, CA, USA) at the University of Pretoria, as per the respective manufacturers' instructions. All purified DNA was eluted with 10 µL distilled water (dH$_2$O).

3.1.1.4. DNA ligation

Ligation reaction mixtures (20 µL) were prepared with 1 µL vector DNA, 7 µL insert fragment, 1 µL T4 DNA ligase buffer (Thermo Fischer Scientific, Waltham, MA, USA), 1 µL PEG4000 (Sigma-Aldrich, St. Louis, MO, USA), 0.5 µL T4 DNA ligase (Invitrogen, Carlsbad, CA, USA) and made up to 20 µL with dH$_2$O. Volumes used were the same for all reactions, unless stated otherwise. Ligation reaction mixtures were incubated at 22 °C for 75 minutes, followed by heat inactivation at 65 °C for 10 minutes and transformation into chemically competent *E. coli* cells. Reactions without insert DNA were performed as controls to assess background noise of uncut vector and transformation efficiency.

3.1.1.5. Transformation of competent *E. coli* cells and plasmid preparation

At UCB, Oneshot TOP10 chemically competent cells (Thermo Fischer Scientific, Waltham, MA, USA) were transformed with ligation samples, in accordance with the manufacturer's instructions. However, to increase the probability of successful colonies, incubation samples were briefly centrifuged and 250 μL supernatant was discarded. Pellets were resuspended in the remaining 50 μL media and plated on pre-warmed agar (50 μg/mL kanamycin) plates. To assess transformation efficiency, non-transformed cells and cells transformed with control ligation reactions or vector only were plated. The following morning colonies were selected for mini prep and restriction analysis. Each selected colony was added to 5 mL Luria-Bertani broth (LB) with 50 μg/mL kanamycin and incubated overnight. Recombinant plasmid DNA from overnight cultures were purified via QIAGEN QIAprep Spin Miniprep Kit (Qiagen, Hilden, Germany), as per the manufacturer's instructions, for subsequent analysis by restriction enzyme digests or DNA sequencing.

At the University of Pretoria, DH5α chemically competent cells (Thermo Fischer Scientific, Waltham, MA, USA) were transformed with ligation reaction mixtures, as per provided instructions. Incubation samples were treated as described for Oneshot TOP10 cells and were plated on pre-warmed 50 μg/mL kanamycin agar plates. Overnight cultures were prepared, and recombinant plasmids were purified the following day using a GeneJET Miniprep Kit (Thermo Fischer Scientific, Waltham, MA, USA), as per kit instructions.

3.1.1.6. Analytical restriction enzyme digest

Analytical restriction enzyme digests were performed and visualised as described earlier (3.1.1.1 and 3.1.1.2). Restriction enzymes for analytical digests were selected for identification of successfully inserted fragments. Recombinant plasmid DNA samples that tested positive for DNA fragment insertion were selected for sequencing.

3.1.1.7. DNA sequencing

The three recombinant plasmid constructs were sequenced to confirm successful cloning. Reactions were prepared via BigDye™ Terminator v3.1 Cycle Sequencing Kit (Applied Biosystems, Foster City, CA, USA), as per the manufacturer's guidelines. Sequencing samples (7.5 µL) were prepared in microcentrifuge tubes (Anachem Ltd, Leicester, UK) and comprised of 0.5 µg DNA sample, 2 µL sequencing buffer, 0.3 µL Big Dye Terminator Reaction Ready sequencing pre-mix, 1 µL forward and reverse sequencing primers (5' GCAGTACTCGTTGCTGCCGC; 3' CACGGTGGGCATGTGTGAGT), made up to 7.5 µL with dH_2O. Reactions were cycled under the following conditions on a T100™ Thermal Cycler (Bio-Rad, Hercules, CA, USA) and submitted to the UCB in house sequencing technician:

96°C   30 seconds

96 °C   10 seconds

50 °C   5 seconds

60 °C   4 minutes

Repeat from step 2 x 35

4 °C   Constant

Results were analysed via sequence alignment in ContigExpress software (Vector NTI Advanced, Invitrogen, Carlsbad, CA, USA).

3.1.1.8. Large scale plasmid preparation

After sequence analysis, larger quantities of successfully cloned recombinant plasmid DNA were produced for use in a HEK293 mammalian expression system. Briefly, Oneshot TOP10 chemically competent cells were transformed with the selected plasmids, as per manufacturer's instructions. Starter cultures were prepared the following day by selecting single colonies and culturing them overnight in 2 mL LB (50 µg/mL kanamycin) at 37 °C and 230 rpm in a shaking incubator. Starter cultures were then added to 500 mL 2x YT medium (50 µg/mL kanamycin) and incubated at 37 °C for 24 hours. Recombinant plasmid DNA from overnight cultures was purified via QIAGEN Plasmid Plus Giga Kit (Qiagen, Hilden, Germany), using a vacuum pump, as per kit instructions. Purified plasmid DNA was eluted with 1 mL

Elution buffer and stored at -20 °C for use in protein expression. All DNA concentrations were measured using a NanoDrop™ 1000 spectrophotometer (Thermo Fischer Scientific, Waltham, MA, USA).

3.1.1.9. Plasmid preparation and transport

Larger quantities of mSOST hFc PD plasmid DNA were prepared at University of the Pretoria using a GeneJET Plasmid Maxiprep Kit (Thermo Fischer Scientific, Waltham, MA, USA), as per the manufacturer's instructions. The pMH mSOST hFc PD plasmid DNA was then precipitated for storage and transportation to UCB. Briefly, 1 mL cold isopropanol was added to eluted plasmid DNA. Sample was then incubated at -70 °C for 60 minutes and centrifuged at 16000 x g for 30 minutes at 4 °C. All supernatant was removed, and the plasmid pellet was washed with 800 µL 70% ethanol, followed by 10 minutes incubation at room temperature. After incubation, the sample was centrifuged at 16000 x g for 30 minutes at 4 °C, and supernatant was discarded. The DNA pellet was left to air dry and sealed and stored for transport.

3.1.2. Protein expression, extraction, purification, and analysis

The aim of this section was to express and purify the three recombinant mouse Scl constructs (mScl, mScl hFc and mScl hFc PD) using a human embryonic kidney (HEK) 293 mammalian expression system and standard chromatography approaches.

3.1.2.1. Transfection and expression

Recombinant plasmid constructs were transiently expressed in an Expi293™ Expression system (Thermo Fischer Scientific, Waltham, MA, USA), as per manufacturer's guidelines. For a 5 L transfection procedure (done for each recombinant plasmid construct), cell culture with a cell count of 3×10^6 cells was added to five 1 L containers. The volume in each container was adjusted to 850 mL with prewarmed Expi293™ media. To make up the transfection mixture, 5 mg DNA was added to 250 mL Opti-MEM® I and mixed by inversion. Additionally, 13.5 mL

Expifectamine™ 293 Reagent was added to 236.5 mL Opti-MEM® I and mixed by inversion. Both solutions were incubated and mixed as per kit instructions. After incubation, 100 mL transfection complex mixture was added to each 850 mL cell culture. Each new 950 mL culture was added to a 3 L flask with a vent cap and was incubated overnight at 37 °C, 75% humidity, 8% CO_2 and 120 rpm in a shaking incubator. The following day, 5 mL Enhancer 1 and 50 mL Enhancer 2 were added to each 950 mL Expi293™ culture, and incubation was continued for 72 hours.

3.1.2.2. Collecting and filtering supernatant

The 5 L transfected cell culture was divided between six 1000 mL polypropylene centrifuge bottles with cap and autovent plug assemblies (Beckman Coulter, Brea, CA, USA) that were washed and rinsed with 0.1 M NaOH and endotoxin free PBS respectively. Balanced flasks were then centrifuged for 1.5 hours at 4 °C and 12 000 x g. After centrifugation, supernatant was vacuum filtered (Stericup®-GP Quick Release Sterile Vacuum Filtration System, 500ml, 0.22 µm PES; Merck, Kenilworth, NJ, USA) and collected in a sterile 5 L container, which was stored at 4 °C until supernatant was loaded onto chromatography columns.

3.1.2.3. ÄKTA Pure and column preparation

An ÄKTA Pure chromatography system (GE Healthcare, Chicago, IL, USA) was used to load and elute samples onto and from chromatography columns. Before loading the supernatant, all ÄKTA Pure pumps and lines were primed and washed with 0.1 M NaOH. Pumps and lines were then primed and rinsed with endotoxin free 10 mM PBS to remove NaOH from the system. All chromatography columns were washed with 0.1 M NaOH and then equilibrated with their respective equilibration buffers (1 column volume NaOH followed by 3 column volumes equilibration buffer to ensure all NaOH is removed from columns).

3.1.2.4. Affinity chromatography

Filtered supernatant (5 L) containing hFc fusion protein (mScl hFc or mScl hFc PD) was loaded onto two HiTrap™ Protein A HP (5 mL) columns (GE Healthcare Life Sciences, Chicago, IL, USA) that were connected in series and equilibrated with PBS. The following day, protein was eluted by a linear or stepwise increase in 0.1 M citric acid pH 2, and peak fractions (≥20 mAU) were collected. Tris-HCl (1 M, pH 8.5) was added to peak samples to adjust pH to 7 and selected fractions were then analysed by sodium dodecyl-sulphate polyacrylamide gel electrophoresis (SDS-PAGE; 3.1.2.7). Protein-containing fractions were pooled and protein aggregate was removed by centrifugation. Samples were then stored at 4 °C for loading onto a HiLoad™ 26/600 Superdex™ 200 pg size exclusion chromatography (SEC) column (GE Healthcare Life Sciences, Chicago, IL, USA). Loading and elution steps were repeated with flow through collected during the first loading step to collect remaining protein from the supernatant.

3.1.2.5. Cation exchange chromatography

For wild type mScl, filtered supernatant was loaded onto a 6 mL RESOURCE S™ cation exchange chromatography (CEC) column (GE Healthcare Life Sciences, Chicago, IL, USA) equilibrated with Buffer A1 (50 mM MES, 100 mM NaCl, pH 6), whilst mScl hFc or mScl hFc PD pooled samples from the SEC step (2.1.2.6) were loaded onto a 1 mL RESOURCE S™ CEC column that was equilibrated with Buffer A2 (10 mM PBS, pH 7.4). All columns were washed with PBS after samples were loaded. Wild type mScl was then eluted by increasing Buffer B1 (50mM MES, 500 mM NaCl, pH 6) and decreasing Buffer A1 in a step wise manner, whilst mScl hFc and mScl hFc PD were eluted by linear gradient using Buffer A2 and B2 (10 mM PBS, 1 M NaCl, pH 7.4). Peak fractions (≥20 mAU) were collected in 96 well collection plates (mScl hFc and mScl hFc PD) or 8 mL collection tubes (mScl). Selected samples were then pooled for loading onto a SEC column (mScl) or tested for endotoxin and stored at -80°C (mScl hFc and mScl hFc PD).

3.1.2.6. Size exclusion chromatography

Sample containing mScl was loaded onto a HiLoad™ 26/600 Superdex™ 75 pg SEC column, whilst sample containing mScl hFc or mScl hFc PD were loaded onto a HiLoad™ 26/600 Superdex™ 200 pg column, followed by 1.2 column volume elution and collection of peak fractions (≥20 mAU) in 96 well collection plates. Selected fractions were analysed by SDS-PAGE and fractions containing protein were pooled for loading onto a RESOURCE S™ column (mScl hFc and mScl hFc PD) or tested for endotoxin and stored at -80 °C (mScl).

3.1.2.7. Purified protein analyses

SDS-PAGE

Samples were collected throughout the purification process for SDS-PAGE analysis. NuPAGE® LDS Sample Buffer (Thermo Fischer Scientific, Waltham, MA, USA) was added to each sample for non-reducing conditions and NuPAGE® Sample Reducing Agent was used for reducing conditions. Samples were prepared and loaded onto NuPAGE™ 4-12% Bis-Tris Protein Gels that were placed in a mini gel tank (Thermo Fischer Scientific, Waltham, MA, USA) filled with NuPAGE™ MES SDS Running Buffer. SeeBlue™ Plus2 Pre-stained Protein Standard (Thermo Fischer Scientific, Waltham, MA, USA) was used as a standard and gels were run according to manufacturer's guidelines. To visualise protein bands, gels were stained with InstantBlue™ Protein Stain (Expedeon, San Diego, CA, USA) and imaged with an ImageQuant LAS 4000 camera system (GE Healthcare Life Sciences, Chicago, IL, USA).

Analytical gel filtration

Samples (120 µL of 0.7 mg/mL sample) were loaded onto a Superdex® 200 10/30 GL column connected to an Agilent 1100 HPLC system (Agilent, Santa Clara, CA, USA), followed by elution with 10 mM PBS. Bio-Rad Gel Filtration Standard (Bio-Rad, Hercules, CA, USA) was used to calculate protein size.

Deglycosylation

N-linked oligosaccharides were removed from protein using peptide-N-glycosidase F (PNGase F) and supplied reagents, as described by the manufacturer's guidelines (New England Biolabs, Ipswich, MA, USA). Analysis was done by SDS-PAGE under reducing and non-reducing conditions, as described earlier.

N-terminal sequencing

Denaturing loading buffer was added to protein samples in a 1:3 ratio for SDS-PAGE analysis. After SDS-PAGE, protein was transferred to a polyvinylidene fluoride (PVDF) membrane with an Invitrogen™ iBlot™ Gel Transfer Stack and iBlot™ Dry Blot System (Thermo Fischer Scientific, Waltham, MA, USA), as per provided instructions. The PVDF membrane was then stained with Ponceau S solution (Merck KGaA, Darmstadt, Germany), rinsed with dH$_2$O and left to dry overnight. Briefly, bands of interest were excised from the PVDF membrane and individually applied to reaction cartridges on a Procise® Protein Sequencing System (Life Technologies, Carlsbad, CA, USA). Samples were subjected to 13 cycles of Edman Chemistry, including 2x blanks and 1x PTH-amino acid standard, and data was analysed using SequencePro™ Data Analysis Application (Applied Biosystems, Foster City, CA, USA). ImageJ (U. S. National Institutes of Health, Bethesda, Md, USA) was used to calculate the percentage truncated mScl hFc PD (based on SDS-PAGE band intensity) (Schneider et al., 2012).

3.1.2.8. Protein concentration

Protein concentration was measured using a NanoDrop™ 1000 spectrophotometer (Thermo Fischer Scientific, Waltham, MA, USA). NanoDrop™ software uses a default extinction coefficient value of 1, therefore, to determine proper protein concentrations, the correct protein extinction coefficient for each protein construct was calculated using ProtParam (Gasteiger et al., 2005). Concentration in mg/mL was then calculated as follows (adapted from Beer-Lambert Law): $c_{prot} = c_{A280} * (\frac{MW}{\varepsilon})$, where c$_{prot}$ = concentration in mg/L, c$_{A280}$ = absorbance at 280 nm or concentration calculated by NanoDrop™, MW = molecular weight

of protein (daltons), and ε = extinction coefficient ($M^{-1}.cm^{-1}$) (Table 3.1) (Grimsley and Pace, 2004).

Table 3.1: Extinction coefficients of recombinant mScl constructs.

Protein	Extinction coefficient ($M^{-1}.cm^{-1}$)
mScl hFc PD	61288
mScl hFc	61288
mScl	25690

3.1.2.9. Endotoxin measurement and removal

Sample endotoxin levels were measured with an Endosafe®-PTS™ system (Charles River, Wilmington, MA, USA) to ensure endotoxin levels were <2 EU/mg in all purified protein samples. Proteus NoEndo™ S spin columns (Generon, Slough, UK) were used to remove endotoxins from mScl samples with endotoxin levels above 2 EU/mg, as per the provided kit instructions. RESOURCE™ S CEC (3.1.2.5) was repeated to reduce endotoxin levels in mScl hFc and mScl hFc PD samples to <2EU/mg. Samples were then aliquoted and stored at -80 °C.

3.1.2.10. Protein storage

To protect protein against cryodamage, 10% endotoxin free glycerol was added to mScl, mScl hFc and mScl hFc PD samples. Samples were then aliquoted to 2 mL Greiner Cryo.s™ vials (Greiner Bio-One, Kremsmünster, Austria) and stored at -80 °C.

3.2. *In vitro* functionality and efficacy of recombinant sclerostin constructs

3.2.1. Isothermal titration calorimetry

The aim of the isothermal titration calorimetry (ITC) assays, a technique that measures heat exchange during a biomolecular binding event in solution directly, were to investigate binding

interactions between the recombinant mScl constructs and a label-free fragment of the Wnt co-receptor LRP6 containing the first and second β-propellers of the receptor extracellular domain (LRP6-E1E2; Holdsworth et al., 2012), and determine the KD for each construct (Doyle, 1997).

3.2.1.1. Buffer exchange

To prevent heat changes arising from buffer differences, all recombinant protein samples (mScl, mScl hFc and mScl hFc PD) were desalted using 2 mL Zeba™ Spin Desalting Columns 7K molecular weight cut-off (MWCO) (Thermo Fischer Scientific, Waltham, MA, USA). Columns were prepared as per the manufacturer's protocol. Briefly, protein samples (500 μL) were applied directly to column resin, followed by addition of 200 μL Dulbeco's phosphate buffered saline (DPBS) stacker. Columns were then centrifuged and 700 μL samples were collected.

3.2.1.2. ITC assay

A MicroCal PEAQ-ITC (Malvern Instruments Ltd, Malvern, UK) instrument was used for all ITC measurements. The system was cleaned and prepared as per test kit guidelines and on-screen instructions provided by MicroCal PEAQ-ITC Control Software (Malvern Instruments Ltd, Malvern, UK). LRP6-E1E2 (111 μM) (UCB, Slough, UK) was added to the syringe, whilst 20 μM desalted recombinant protein sample was added to the sample cell, as per on-screen instructions. Runs for each protein construct was performed in triplicate and parameters were set as follows before starting the assays: syringe concentration (LRP6-E1E2) = 111 μM; cell concentration (recombinant Scl constructs) = 20 μM; Temperature = 25 °C; Reference power (μcal/s) = 10; Feedback = High. To maximise number of experiments per day, due to limited time on the machine as well as to improve protein stability, injection parameters were set as: number of injections = 10 and volume (μL) = 4 (a 0.4 μL injection was done prior to experimental runs to minimise impact of equilibration artefacts). To reduce artefacts, the test cell was rinsed manually with DPBS after each run, before adding new protein sample. Both the reference cell and syringe were rinsed between runs for different recombinant protein constructs.

3.2.1.3. Analysis

ITC data was fitted to a single site binding model using the MicroCal PEAQ-ITC Analysis Software (Malvern Instruments Ltd, Malvern, UK). KD and binding stoichiometry were calculated from fitted data, whilst entropy changes (ΔS) and Gibbs free energy changes (ΔG) were derived from the thermodynamic relationships: ΔG = ΔH–TΔS (where T is absolute temperature in Kelvin) (Hammes and Hammes-Schiffer, 2015).

3.2.2. Microscale thermophoresis

Microscale thermophoresis (MST) assays are based on detection of a temperature-induced change in fluorescence of labelled protein as a function of the concentration of a non-fluorescent ligand (Jerabek-Willemsen et al., 2014). Therefore, the aim of the MST assays was to investigate binding reactions between the recombinant mScl constructs and fluorescently labelled LRP6-E1E2 (Holdsworth et al., 2012). A Monolith NT™ Protein Labelling Kit RED-NHS with a Monolith NT.115 instrument (NanoTemper Technologies, Munich, Germany) were used for the assays.

3.2.2.1. Labelling LRP6-E1E2 with NT647

Fluorescence labelling of purified LRP6-E1E2 (UCB, Slough, UK) was performed as per provided protocol for N-hydroxysuccinimide (NHS) coupling of NT647 dye (NanoTemper Technologies, Munich, Germany) to lysine residues of the receptor protein. Quality of the purified labelled LRP6-E1E2 (LRP6-NT647) was assessed by calculating degree of labelling (average number of NT647 dye molecules coupled with an LRP6-E1E2 molecule). Absorbance of purified fractions was measured at 280 nm and 647 nm. Concentration of LRP6-NT647 (A_{280}) and NT647 only (A_{647}) were then calculated using a modified Beer-Lambert Law equation: $c = \frac{A - CF}{\varepsilon l}$, where c is the protein concentration (M), A is the absorbance, ε is the molar extinction coefficient ($M^{-1}.cm^{-1}$), l is the pathlength (cm) and CF is the correction factor. Degree of labelling was then calculated by dividing NT647 concentration with LRP6-NT647 concentration.

3.2.2.2. Optimal LRP6-NT647 concentration

To determine the optimal LRP6-NT647 concentration for MST assays, a serial dilution (100, 50, 25 and 12.5 nM) of LRP6-NT647 was prepared. Premium capillaries (NanoTemper Technologies, Munich, Germany) filled with LRP6-NT647 dilution samples were loaded onto a Monolith NT.115 instrument and capillary scans (Cap Scan in the NanoTemper software suite) were performed to measure the signal strength of the labelled LRP6. Sample concentrations with a raw fluorescence count >200 (minimum signal required for optimal readings) were selected for MST assays.

3.2.2.3. Sample preparation

LRP6-NT647 (25 nM) samples were prepared, and a Cap Scan was performed to confirm that newly prepared samples provided the required signal strength. Recombinant Scl stock samples (human Scl, mScl, mScl hFc, and mScl hFc PD) were diluted to 500 nM with DPBS (pH 7.4) containing 0.05% Tween 20 and 50% (w/v) PEG8000, and a 12-point titration of the diluted Scl samples were prepared with fixed LRP6-NT647 (Table 3.2).

Table 3.2: Scl and LRP6-NT647 twelve-point titrations.

Microcentrifuge tube	1	2	3	4	5	6	7	8	9	10	11	12
Scl (nM)	250	125	62.5	31.25	15.63	7.81	3.91	1.95	0.977	0.49	0.25	0
LRP6-NT647 (nM)	12.5	12.5	12.5	12.5	12.5	12.5	12.5	12.5	12.5	12.5	12.5	12.5

3.2.2.4. MST assay

A 12-point dilution series was completed for each MST run, which was performed separately and in triplicate for each recombinant protein construct. Premium capillaries were filled with Scl/LRP6-NT647 samples and loaded onto an NT.115 instrument. Running parameters were set as follows using MO.Control software (NanoTemper Technologies, Munich, Germany): Temperature: 23.9 °C; 5s/30s/5s infrared (IR) laser off/on/off times; LED power = 100%; MST power = 40%; Fixed LRP6-NT647 concentration = 12.5 nM; Ligand concentration of each

capillary: as per Table 3.2. A Cap Scan was performed to confirm LRP6-NT647 signal was evenly distributed across capillaries and to monitor for any adsorption effects. The experimental run was started once linear, narrow, smooth sample peaks, similar in size and height, were observed for each capillary. Dose response curves, plotted as change in MST signal versus ligand concentration, for each Scl construct were fitted using the KD model (a 1:1 interaction model) of the MO. Affinity Analysis v2.2.6 software (NanoTemper Technologies, Munich, Germany). The dissociation constant (KD) was then derived from fitted data using the law of mass action (Kenakin, 2016).

3.2.3. Surface plasmon resonance

Surface plasmon resonance (SPR) measures change in the refractive index at a gold sensor chip coated with immobilised ligands. A change in this refractive index when analytes are passed over the receptor coated chip surface is observed as a response and is linearly related to the number of molecules bound (Jason-Moller et al., 2006). Therefore, the aim of the Biacore SPR assays was to provide additional evidence that the recombinant mScl constructs were functionally active and able to bind to LRP6. To achieve this, a competition assay was set up on a Biacore™ 3000 instrument (GE Healthcare Life Sciences, Chicago, IL, USA). Biacore™ experiments were conducted at 25 °C.

3.2.3.1. Sensor surface preparation

Flow cells on a CM5 gold carboxymethyl dextran coated sensor (GE Healthcare Life Sciences, Chicago, IL, USA) were activated by addition of a mixture, in water, of 0.1 M N-hydroxysuccinimide (NHS) and 0.5 M ethyl(dimethylaminopropyl)carbodiimide (EDC) (GE Healthcare Life Sciences, Chicago, IL, USA) to the sensor (60 μL injection at a 10 μL/min flow rate). Recombinant Scl constructs (20 μg/mL human Scl (hScl; UCB), mScl, mScl hFc and mScl hFc PD) in 10 mM sodium acetate pH 4 were added to selected flow cells, at 10 μL/min, using HBS-EP pH 7.4 (10 mM HEPES, 150 mM NaCl, 3 mM EDTA and 0.05% v/v surfactant P20; GE Healthcare Life Sciences, Chicago, IL, USA), to immobilise ~1600 RU (response unit) on the

sensor surface. A reference flow cell and remaining unreacted activated sites were blocked by addition of 1 M ethanolamine (50 μL injection at 10 μL/min).

3.2.3.2. Establishing LRP6-E1E2 concentration for Scl coated sensors in a competition assay

To show that Scl coated sensor surfaces were active and to establish how much LRP6-E1E2-Fc (UCB, Slough, UK) to use in the Scl-LRP6 competition assay, LRP6-E1E2-Fc dilutions (30, 10, 3, 1, 0.3 and 0.1 nM) in HBS-EP pH 7.4 containing 1 mg/mL CM-dextran (to inhibit non-specific interactions; Honeywell Fluka™, Charlotte, NC, USA) were passed over selected flow cells (30 μL injections at 10 μL/min) coated with the different Scl preparations, using HBS-EP H 7.4 (with 1 mg/mL CM-dextran) as the running buffer. The surface was regenerated following each run using two injections of 30 mM HCl (10 μL) at a flow rate of 10 μL/min. Following positive results, LRP6-E1E2-Fc (300, 100, 30, 10, 3 and 1 nM) dilutions in HBS-EP containing 1 mg/mL CM-dextran were passed over flow cells coated with hScl (UCB). A change in refractive index when LRP6-E1E2-Fc passes over the Scl coated chip surface was observed as a response signal that was quantified in resonance units. The response was plotted on SPR sensorgrams as a function of LRP6-E1E2-Fc concentration, and a dilution curve was used to determine the LRP6-E1E2-Fc concentration to use in the competition assay.

3.2.3.3. SPR competition assay

A range of dilutions (1000, 500, 250, 125, 62.5, 31.25, 15.63, 7.81 and 0 nM) of the Scl constructs (hScl, mScl, mScl hFc and mScl hFc PD) in HBS-EP pH 7.4, containing 1 mg/mL CM-dextran, were pre-incubated with 100 nM LRP6-E1E2-Fc for 30 minutes at room temperature. Duplicate hScl/LRP6-E1E2-Fc samples were prepared, one for the start and one for the end of the assay, to confirm that the sensor surface did not change during the assay. The Scl/LRP6-E1E2-Fc samples were passed over a reference and hScl coated flow cells using 30 μL injections and a flow rate of 10 μL/min. HBS-EP containing 1 mg/mL CM-dextran was used as the running buffer. Responses at each concentration were used to construct dilution curves with XLfit version 5.5.0.5 (IDBS, Guildford, UK). EC50 (the concentration of Scl needed to achieve 50% of the maximum response) for each recombinant Scl construct were derived

from the midpoint between the minimum and maximum response rate ($\frac{(Y_{max}-Y_{min})}{2} + Y_{min}$) on the fitted dilution curves. The cell surface was regenerated following each run using two injections of 30 mM HCl (10 µL) at a flow rate of 10 µL/min.

3.2.4. Mineralised nodule formation assay

The aim of the mineralised nodule formation assay was to investigate the effect of recombinant mScl constructs on *in vitro* bone formation. Three independent assays were completed for each recombinant mScl construct.

3.2.4.1. Cell revival from cryopreservation

MC3T3-E1 Subclone 14 (ATCC® CRL-2594™) mouse pre-osteoblasts (ATCC, Manassas, VA, USA) (passage number 22) were selected as an appropriate mineralisation model since they express LRP4/5/6 and have been shown to be sensitive to Scl (Li et al., 2009). Cells were prepared from frozen with pre-warmed complete growth medium (Minimum Essential Medium Alpha (Thermo Fischer Scientific, Waltham, MA, USA) containing 2 mM L-Glutamine, Ribonucleosides, Deoxyribonucleosides, 10% foetal bovine serum (FBS), and no ascorbic acid), as described by the product sheet provided with the cells. Resuspended cells were then added to pre-warmed complete growth medium in 175 cm² rectangular straight neck cell culture flasks with vented caps and incubated at 37 °C and 5% CO_2 until confluent (approximately 72 hours).

3.2.4.2. Cell sub-culturing

Once cells achieved ≥80% confluence, culture medium was discarded, and residual culture medium was removed by rinsing cells with sterile DPBS. Cells were detached using TrypLE™ Express (with EDTA; without phenol red; Thermo Fischer Scientific, Waltham, MA, USA) cell dissociation solution, as per provided instructions, and transferred to a 50 mL Falcon tube containing complete growth medium. The cell suspension was centrifuged, supernatant

discarded, and the cell pellet was resuspended in complete growth medium. To count the cells, 10 µL 0.4% Trypan Blue Stain (Thermo Fischer Scientific, Waltham, MA, USA) was added to 10 µL resuspended cells. The Trypan blue/cell solution was added to a Cellometer cell counting chamber and cells were counted using the Trypan Blue program on a Cellometer Auto 1000 (Nexcelcom Biosciences, Lawrence, MA, USA). The total number of cells required per well on a 24 well cell culture plate was 11438 (6020 cells/cm^2 x 1.9 cm^2). Thus, a total of 1.83×10^6 cells were required for 144 wells (6 x 24 well cell culture plates). Complete growth medium (500 µL) and 500 µL cell suspension was added to each well (1 mL total volume per well) and cells were maintained at 37 °C and 5% CO_2 for 48 hours.

3.2.4.3. Anti-Scl antibody Fab preparation

Fragment antigen binding (Fab) fragments of a Scl neutralising antibody (Scl-Ab1; UCB, Slough, UK) were used as an experimental control and were generated using a Pierce™ Fab Preparation Kit (Thermo Fischer Scientific, Waltham, MA, USA). PBS/1% BSA (w/v) and PBS 3% BSA were prepared fresh for each preparation and Fabs were prepared as described by the provided kit guidelines.

3.2.4.4. Cell treatment

After 48 hours, media was replaced with 500 µL osteogenic media (complete growth medium supplemented with 50 µg/mL ascorbate-2-phosphate and 10 mM β-glycerophosphate) and cells were treated with 50 nM recombinant mScl constructs (mScl hFc and mScl hFc PD concentrations were the molar equivalent of mScl concentration) (Table 3.3). Antibody controls were co-treated with 50 nM recombinant mScl and 230 nM Scl neutralising antibody (Scl-Ab1; Veverka et al., 2009) (UCB, Slough, UK), Scl-Ab1 Fab, or an irrelevant isotype control Ab. Vehicle controls were treated with DPBS (DPBS volume was equivalent to the highest volume of protein used for treatment), whilst medium controls were treated with complete growth media only (Table 3.3, Row 1). Cells were maintained at 37 °C and 5% CO_2, and treatment was repeated approximately every 48 hours, until ≥90% mineralisation was observed in osteogenic media control wells.

Table 3.3: MC3T3-E1 mineralised nodule formation assay 24-well plate layout and well contents.

	A	B	C	D	E	F
1	• Complete growth medium	• Complete growth medium	• Complete growth medium	• Complete growth medium	• Complete growth medium	• Complete growth medium
2	• Osteogenic media	• Osteogenic media	• Osteogenic media	• Osteogenic media • DPBS	• Osteogenic media • DPBS	• Osteogenic media • DPBS
3	• Osteogenic media • mScl construct	• Osteogenic media • mScl construct	• Osteogenic media • mScl construct	• Osteogenic media • mScl construct • Anti-Scl Ab	• Osteogenic media • mScl construct • Anti-Scl Ab	• Osteogenic media • mScl construct • Anti-Scl Ab
4	• Osteogenic media • mScl construct • Anti-Scl Fab	• Osteogenic media • mScl construct • Anti-Scl Fab	• Osteogenic media • mScl construct • Anti-Scl Fab	• Osteogenic media • mScl construct • Control Ab	• Osteogenic media • mScl construct • Control Ab	• Osteogenic media • mScl construct • Control Ab

3.2.4.5. Cell fixing

Cells were fixed in formalin once sufficient mineralisation occurred. Briefly, supernatant was discarded, and cells were washed twice with DPBS. Neutral buffered formalin (NBF) (200 μL 10%) was added to each well, followed by incubation at room temperature for 20 minutes. NBF was removed by rinsing wells with 200 μL DPBS, and plates were left to dry at room temperature. Dry plates were scanned using a Canon flatbed scanner (Canon, Ota City, Tokyo, Japan) with a black background.

3.2.4.6. Alizarin Red S staining

Fixed cells were stained with Alizarin Red S to detect mineralisation (Taylor et al., 2014). Freshly prepared 40 mM Alizarin Red S pH 4 was added to each well (500 μL/well), followed by incubation at room temperature for 10 minutes. After incubation, excess Alizarin Red S was discarded, and wells were washed with 70% ethanol until all unbound stain was removed. Plates were then placed face down on paper towel to air dry. Once dried, plates were scanned

using a Canon flatbed scanner (Canon, Ota City, Tokyo, Japan) with a white background and were stored in darkness at room temperature for cetylpyridinium chloride (CPC) staining.

3.2.4.7. Cetylpyridinium chloride staining

Cetylpyridinium chloride (CPC) extracts Alizarin Red S from the stained mineral and was used to quantify mineralisation (Shah et al., 2020). CPC (10% w/v) was freshly prepared and added to each well (500 µL/well), followed by 60 minutes incubation in darkness. Samples (100 µL) were then transferred from the 24 well plates to 96 well plates, and absorbance was measured at 570 nm with a Synergy™ 2 Multi-Mode Microplate Reader instrument using Gen5 2.09 software (BioTek, Winooski, VT, USA).

3.3. *In vivo* biological activity and efficacy of recombinant sclerostin constructs

3.3.1. Single dose pharmacokinetic and pharmacodynamic study

The aim of the *in vivo* single dose pharmacokinetic and pharmacodynamic study was to determine the circulating half-life of the recombinant mScl constructs and to assess any changes in serum procollagen type I N-terminal propeptide (P1NP, a bone formation marker) levels. Dose administration and serum sample collection were done by technicians at Charles River Laboratories Edinburgh Ltd (Tranent, Edinburgh, UK).

3.3.1.1. Animals

SOST$^{-/-}$ mice (*Mus musculus*) were sourced from Charles River Laboratories Edinburgh Ltd (Tranent, Edinburgh, UK) and were used as a pre-clinical model that mimics sclerosteosis, whilst C57/BL6 mice were used as wild type (WT) controls (Li et al., 2008). SOST$^{-/-}$ mice and WT littermates (8-10 week old) weighing approximately 20 g were housed at Charles River Laboratories Edinburgh Ltd (Tranent, Edinburgh, UK). WT control groups consisted of 12 female and 12 male mice (Table 3.4), whilst SOST$^{-/-}$ groups consisted of 12 females and three males (N_{total}=117). Female mice were housed in groups (three per cage) and males were kept

individually (one per cage) in UK Home Office-compliant solid bottom polycarbonate and stainless-steel caging. A 12-hour light/dark cycle and temperature of 21 °C was maintained, and mice were offered play tunnels, wooden chew sticks and nestlets for environmental enrichment. Tap water was available *ad libitum* and all animals were fed a laboratory diet of known formulation (details held at the Charles River test facility) throughout the study. Animals were allowed to acclimatise for five days and were observed to ensure that they were in good health and suitable for inclusion in the study. Animals were under the care of Charles River's clinical veterinary surgeons. Animal experiments were performed in accordance with South African (South African National Standard (SANS 10386-2008)) and UK (Animals (Scientific Procedures) Act 1986) guidelines, and were approved by the University of Pretoria Animal Ethics Committee and UCB Pharma Animal Welfare and Ethical Review Body.

3.3.1.2. Dose formulation and regimen for the pharmacokinetic and pharmacodynamic study

Protein samples (mScl, mScl hFc and mScl hFc PD) were removed from -80°C storage on the afternoon prior to dose administration and allowed to thaw overnight at 2-8°C. The following morning PBS was added to homogenous samples to dilute the samples to required dose concentrations (Table 3.4). A single dose formulation of mScl hFc (10 mg/kg), mScl hFc PD (10 mg/kg), or a molar equivalent of mScl (4.4 mg/kg), to adjust for molecular weight differences between proteins, was administered intravenously as a bolus injection via the tail vein over a 30 second period. The 10 mg/kg/wk dose was selected based on prior experience of the PK behaviour of Fc-fusion proteins.

Table 3.4: Animal and dosing information for the pharmacokinetic and pharmacodynamic study.

Group	Mouse strain	Route	No. of Animals		Protein compound	Dose Level (mg/kg)	Dose Concentration (mg/mL)	Dose Volume (mL/kg)
			Female	Male				
1	C57/BL6	IV	12	12	mScl	4.4	0.88	5
2	SOST$^{-/-}$	IV	12	3	mScl	4.4	0.88	5
3	C57/BL6	IV	12	12	mScl hFc	10	2	5
4	SOST$^{-/-}$	IV	12	3	mScl hFc	10	2	5
5	C57/BL6	IV	12	12	mScl hFc PD	10	2	5
6	SOST$^{-/-}$	IV	12	3	mScl hFc PD	10	2	5

IV: intravenous

3.3.1.3. Blood sample collection and processing

Predose blood samples were collected from all mice prior to dose administration (Table 3.5 and 3.6). Thereafter, serial blood samples were collected at allocated time points (5 minutes, 1, 2, 6 hours, 1, 2, 3, 4, 5, 6, 7, 8, 10 days; N=3) and terminal blood samples were collected at mouse takedown on Day 10. Predose and serial blood samples were collected via the saphenous vein, whilst terminal samples were collected from the orbital sinus. Blood samples were kept at room temperature for a minimum of 30 minutes and maximum of 60 minutes, followed by centrifugation at 4 °C and 1500 g for 10 minutes. The resulting serum was stored at -80 °C until shipment to UCB labs.

Table 3.5: Sampling schedule for WT mice in the pharmacokinetic and pharmacodynamic study.

Time (hours)	Animal 016F 028M	Animal 017F 029M	Animal 018F 030M	Animal 019F 031M	Animal 020F 032M	Animal 021F 033M	Animal 022F 034M	Animal 023F 035M	Animal 024F 036M	Animal 025F 037M	Animal 026F 038M	Animal 027F 039M
Predose	A	A	A	A	A	A	A	A	A	A	A	A
0.083	A	A	A									
1				B	B	B						
2							B	B	B			
6										B	B	B
24	B	B	B									
48				B	B	B						
72							B	B	B			
96										B	B	B
120	B	B	B									
144				C	C	C						
168							C	C	C			
192										C	C	C
240	C	C	C									

Blood sample volume collected: A) 60µL; B) 120µL; C) terminal sample. F: female; M: male; N=24: 12 females and 12 males.

Table 3.6: Sampling schedule for SOST$^{-/-}$ mice in the pharmacokinetic and pharmacodynamic study.

Time (hours)	Animal 001F	Animal 002F	Animal 003F	Animal 004F	Animal 005F	Animal 006F	Animal 007F	Animal 008F	Animal 009F	Animal 010F	Animal 011F	Animal 012F	Animal 013M	Animal 014M	Animal 015M
Predose	A	A	A	A	A	A	A	A	A	A	A	A	A	A	A
0.083	A	A	A												
1				B	B	B									
2							B	B	B						
6										B	B	B			
24	B	B	B										B	B	B
48				B	B	B									
72							B	B	B						
96										B	B	B	B	B	B
120	B	B	B												
144				C	C	C									
168							C	C	C				A	A	A
192										C	C	C			
240	C	C	C										C	C	C

Blood sample volume collected: A) 60µL; B) 120µL; C) terminal sample. F: female; M: male; N=15: 12 females and 3 males.

3.3.1.4. Circulating sclerostin concentrations measured by LC-MS/MS

The method for measuring circulating Scl levels consisted of three steps: peptide selection, trypsin digestion and liquid chromatography coupled to tandem mass spectrometry (LC-MS/MS) analysis.

Peptide selection

The amino acid (aa) sequences of the recombinant mScl constructs were used to create an *in silico* library of surrogate tryptic peptides using Skyline 20.1 software (MacCoss Lab, University of Washington Genome Sciences, Seattle, WA, USA; MacLean et al., 2010). From this library, surrogate peptide candidates were selected mainly based on their uniqueness to the protein of interest and eligibility criteria, such as no post-translational modification and peptide lengths between 6-16 aa (Kamiie et al., 2008). Selected peptides were verified against tryptically digested samples (see below) of the proteins of interest on the LC-MS/MS system and then further screened to select the best responders in terms of LC-MS/MS performance, such as good MS sensitivity (Signal/Noise >5) and good chromatographic separation. Best responding peptides were used to analyse the collected serum samples.

Tryptic digestion

Serum, myoglobin internal standard, LC-MS grade acetonitrile and 0.2 M Tris(2-carboxyethyl)-phosphine (TCEP) were transferred to deep well plates and heated at 70 °C for 30 minutes.

Once cooled to room temperature, 7 µL 0.1 M iodoacetamide (IAA) was added and samples were incubated in the dark for 30 minutes at 37 °C. After incubation, 500 µL 100 mM ammonium bi-carbonate buffer and 10 µL resuspended trypsin (in 50 mM acetic acid) was added to each sample to achieve a 1:78 enzyme to protein ratio. Samples were then incubated in a shaking incubator for a minimum of 4 hours at 37 °C.

Digested samples were desalted using Waters Oasis® Hydrophilic-Lipophilic-Balanced solid phase extraction sorbent (Waters Corporation, Milford, MA, USA). Briefly, samples were centrifuged at 10000 g for 15 minutes and loaded onto equilibrated cartridges. Cartridges were then washed with 1 mL 5% methanol + 0.5% formic acid (FA), followed by elution and collection of peptides using 1 mL methanol + 0.5% FA. Thereafter, 10% glycerol was added to eluted samples, which were dried in a vacuum concentrator until samples were completely dry. Dried samples were resuspended in 100 µL 5% methanol + 0.5% FA for use with the LC-MS/MS system.

LC MS/MS and pharmacokinetic analysis

Prepared samples were analysed using a Shimadzu UHPLC system (Shimadzu, Kyoto, Japan) coupled to a QTRAP® 6500 LC-MS/MS system (AB Sciex, Redwood City, CA, USA). Liquid chromatography was performed using a Phenomenex Luna® 3 µ C18 100 Å (150x2 mm) HPLC column (Phenomenex, Torrance, CA, USA). A linear gradient of 2-98% acetonitrile 0.1% FA were applied to elute peptides at a flow rate of 0.5 mL/min for 5 minutes. The mass spectrometer was set to run a multiple reaction monitoring experiment for detection of peptides in positive ionization mode. Instrument control and data processing was done using Analyst® 1.6.2 Software (AB Sciex, Redwood City, CA, USA). To determine pharmacokinetic parameters, data was fitted to non-compartmental models using Phoenix® WinNonlin® 8.1 software (Princeton, NJ, USA). Compartmental models were fitted with Berkeley Madonna 9.1.19 software (University of California, Berkeley, California, USA) to simulate a 42-day dosage study.

3.3.1.5. P1NP ELISA

Procollagen Type I N-terminal propeptide (P1NP) is a reference bone formation marker that increases during bone formation and decreases during bone resorption (Vasikaran et al., 2011). P1NP concentrations were therefore measured using P1NP ELISA kits (Immunodiagnostic Systems Holdings PLC, Tyne and Wear, UK). Prior to assaying experimental samples, the protocol was practised on untreated C57/BL6 mice serum samples to ensure that all samples can be transferred to 96-well ELISA plates within the recommended time limit, to minimise sample drift. Standards, controls and reagents were prepared as described by the included instructions and the provided assay procedure was followed precisely. Individual serum samples were added to two wells (N=2) and two independent ELISAs were performed. Absorbance was measured at 450 nm (reference 650 nm) and calibration curves were plotted in GraphPad Prism 8.4.1 (GraphPad Software, San Diego, CA, USA) to determine, through interpolation, the P1NP concentrations in controls and serum samples.

3.3.2. Pharmacology study

The pharmacology study aimed to determine the safety and effect of the recombinant mScl constructs on bone formation, bone density, and skeletal architecture of WT and SOST$^{-/-}$ mice over a six-week dosing period.

3.3.2.1. Animals

Female SOST$^{-/-}$ mice and wild type (WT) C57/BL6 littermates (7-10 week old; males were excluded to eliminate gender-related data discrepancies) weighing approximately 20 g were obtained from Charles River Laboratories Edinburgh Ltd (Tranent, Edinburgh, UK). Mice were allocated to eight groups (N=6 mice per group; group 5 had an additional mouse) based on a validated UCB testing protocol and to maintain the integrity of the collected data (Table 3.7). Animals were housed in cages with environmental enrichment (as prescribed in the Animal (Scientific Procedures) Act UK 1986) and a 12-hour light/dark cycle. Temperature was maintained at approximately 21 °C and mice had access to water and RM1 food pellets (Aston

Pharma, London, UK) *ad libitum*. Mice received a seven-day acclimatisation period and were observed to ensure that they were in good health and suitable for inclusion in the study. Animals were cared for by qualified UCB animal technicians with experience from similar mouse studies (qualifications included UK IAT Certification up to Level 4) and were weighed once weekly to monitor body weights. Animal experiments were performed in accordance with South African (South African National Standard (SANS 10386-2008)) and UK (Animals (Scientific Procedures) Act 1986) guidelines, and were approved by the University of Pretoria Animal Ethics Committee and UCB Pharma Animal Welfare and Ethical Review Body.

3.3.2.2. Dose formulation and regimen for the pharmacology study

Recombinant protein samples (mScl, mScl hFc and mScl hFc PD) and 0.3% rat serum albumin (RSA) were removed from -80 °C storage on the afternoon prior to dose administration and thawed overnight. PBS pH 7.4 and 0.3% RSA were added to homogenous samples the following morning to dilute samples to the required dose concentrations (Table 3.7). Mice were restrained by scruffing (grasping the skin at the nape) and 100 μL dose formulation (mScl construct; PBS pH 7.4; 0.1% RSA) was administered subcutaneously (SC) over a 30 second period. A 4.4 mg/kg mScl dose was administered six days a week for six weeks (Table 3.7 and 3.8). The seventh day was omitted to keep the number of needle pricks per animal ≤40, as specified by the project licence. mScl hFc and mScl hFc PD doses (10 mg/kg) were administered once a week for six weeks (Table 3.7 and 3.8). Since these were new protein constructs, a cautious administration strategy was used, whereby an initial mouse was dosed with mScl hFc PD and observed for adverse effects before dosing the remainder of the cohort. Animals treated with mScl hFc and mScl hFc PD were dosed with vehicle (0.1% RSA; PBS pH 7.4) five days a week for the duration of the study to keep administration consistent across the groups (Table 3.7 and 3.8). On day 31 and 39 (Table 3.8), Calcein (Sigma-Aldrich, St. Louis, MO, USA), a fluorescent chromophore that specifically binds to calcium, was administered intraperitoneally (100 μL at 20 mg/kg) to all mice for optional *ex vivo* bone histomorphometry (Ducy et al., 2000).

Table 3.7: Animal and dosing information for the pharmacology study.

Group	Mouse strain	No. of Animals	Route	Protein compound	Dose Level (mg/kg)	Dose Concentration (mg/mL)	Dose Volume (μL)
1	C57/BL6	6	SC	Vehicle	N/A	0	100
2	SOST$^{-/-}$	6	SC	Vehicle	N/A	0	100
3	C57/BL6	6	SC	mScl	4.4	1.1	100
4	SOST$^{-/-}$	6	SC	mScl	4.4	1.1	100
5	C57/BL6	7	SC	mScl hFc	10	2.5	100
6	SOST$^{-/-}$	6	SC	mScl hFc	10	2.5	100
7	C57/BL6	6	SC	mScl hFc PD	10	2.5	100
8	SOST$^{-/-}$	6	SC	mScl hFc PD	10	2.5	100

SC: subcutaneous; N/A: not applicable

Table 3.8: Dosing and sampling schedule for the pharmacology study.

66

3.3.2.3. Sample collection and processing

Blood samples

Animals were restrained using a standard restraining device and all blood samples, except terminal, were collected via tail bleed. All blood samples were collected by UCB animal technicians (UCB, Slough, UK). Predose (50 µL) blood samples were collected by from all mice (N=49) prior to dose administration (Table 3.8). Thereafter, serial blood samples were collected from selected mice at allocated time points (N=3) (Table 3.8). To collect terminal blood samples, mice were anaesthetised under terminal anaesthesia (gaseous isoflurane administered by inhalation) and maximum possible terminal blood samples were collected via cardiac puncture. After sample collection, animals were euthanised via cervical dislocation. Blood samples were centrifuged at 4 °C and 10000 g for 5 minutes and the resulting serum was aliquoted and stored at -80 °C.

Bone samples

Lumbar vertebrae (L2-5), femurs, tibiae, and skulls were collected from euthanised animals, cleaned of soft tissue and fixed in 10% neutral buffered formalin (NBF) (Table 3.9). After 48 hours, micro computed tomography (µCT) samples were removed from 10% NBF and washed and stored in PBS for the duration of the µCT scans. Samples selected for optional histology and immunohistochemistry assays were removed from 10% NBF after five days and decalcified with Osteosoft® (Merck, Kenilworth, NJ, USA). Animal carcasses and removed skin and soft tissue were incinerated.

Table 3.9: Bone sample collection and preparation.

Tissue	Tissue Prep after termination	Purpose	Fixation	Post-fix destination
L2 and L3	Soft tissue removed	Histology	10% NBF	Decalcification and histology
L4 and L5	Soft tissue removed	µCT	10% NBF	µCT and 70% ethanol
Left Femur	Skin and soft tissue removed	Histology	10% NBF	Decalcification and histology
Left Tibia	Skin and soft tissue removed	Histology	10% NBF	Decalcification and histology
Right Femur	Skin and soft tissue removed	µCT	10% NBF	µCT and 70% ethanol
Right Tibia	Skin and soft tissue removed	µCT	10% NBF	µCT and 70% ethanol
Skull	Skin removed	µCT	10% NBF	µCT and 70% ethanol

L2-5: lumbar vertebrae; µCT: micro computed tomography; NBF: neutral buffered saline

3.3.2.4. Bone densitometry

Whole body areal bone mineral density (aBMD) of anaesthetised mice were measured by dual X-ray absorptiometry (DXA). To immobilise animals and avoid distress, mice were anaesthetised with isoflurane and then placed in a Faxitron® UltraFocus DXA cabinet (Tucson, AZ, USA) for aBMD measurement on Day 0 (baseline), 21 and 42 (Table 3.8). In addition to aBMD measurement, regular X-ray analysis allowed for assessment of sub-clinical adverse bone events.

3.3.2.5. Pharmacokinetics and pharmacodynamics

LC-MS/MS was performed by Dr Apoorva Kotian as described in 3.3.1.4. Briefly, serum samples collected at 5, 30 minutes, 2, 8 hours, 1, 7, 42 days were prepared by tryptic digestion and serum Scl levels were measured by LC-MS/MS, using the peptides selected in 3.3.1.4. To determine pharmacokinetic parameters, compartmental models were fitted with Berkeley Madonna 9.1.19 software (University of California, Berkeley, California, USA).

P1NP ELISA was performed once as described in 3.3.1.5, using samples collected at predose, 1, 7 and 42 days.

3.3.2.6. Anti-drug antibody assay

The severity of immune responses against the administered mScl constructs were determined by electrochemiluminescence (ECL) anti-drug antibody (ADA) assays. Serum anti-Scl antibodies (Abs) bound to biotinylated mScl captured on streptavidin coated plates (Figure 3.1). SULFO TAG labelled mScl then bound to the captured anti-Scl Abs and light was emitted due to a reaction between SULFO TAG and 2x MSD reading buffer (Meso Scale Diagnostics, Rockville, MD, USA). Measured signal was proportional to the amount of bound anti-Scl Abs.

Biotinylation

mScl and mScl hFc PD were biotinylated with EZ-Link™ NHS-LC-LC-Biotin (Thermo Fischer Scientific, Waltham, MA, USA) as per manufacturer's instructions. Excess Biotin was removed using 2 mL Zeba™ Spin Desalting Columns 7K MWCO (Thermo Fischer Scientific, Waltham, MA, USA).

SULFO-TAG labelling

mScl and mScl hFc PD were labelled with MSD GOLD™ SULFO-TAG NHS-Ester (150 nmol) (Meso Scale Diagnostics, Rockville, MD, USA) as per provided instructions. Excess SULFO-TAG was removed using 2 mL Zeba™ Spin Desalting Columns 7K MWCO (Thermo Fischer Scientific, Waltham, MA, USA).
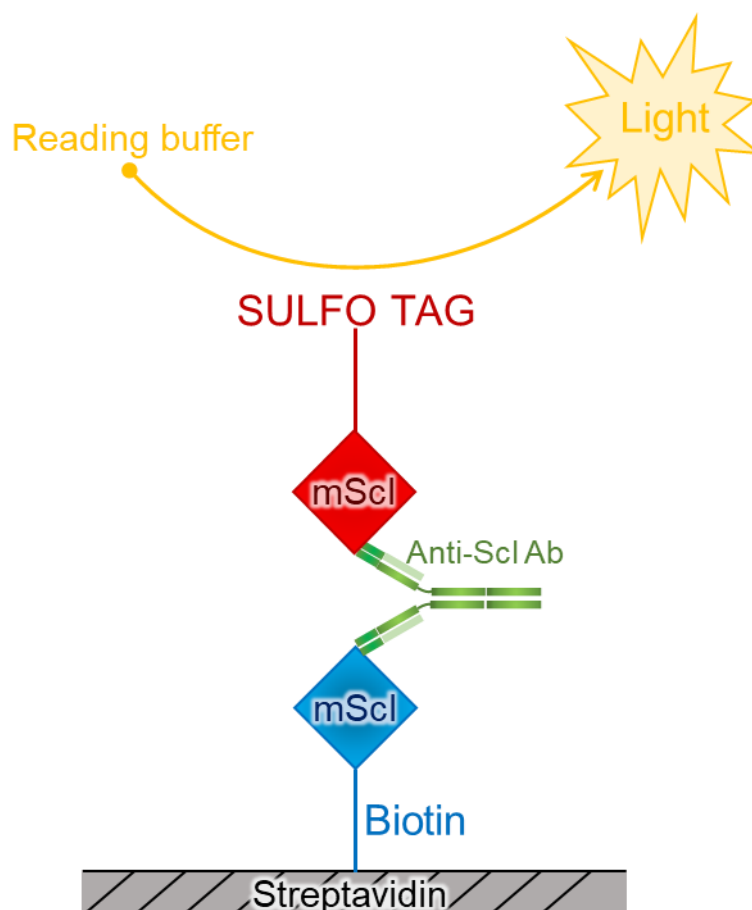
Figure 3.1: Electrochemiluminescence anti-drug antibody assay. Unbound anti-Scl Ab binds to biotinylated mScl immobilised on a streptavidin coated plate. Unbound SULFO TAG labelled mScl then binds to the captured anti-Scl Abs. MSD 2x Read buffer is added to the sample solution and the reaction with the SULFO TAG is measured at 450 nm (570 nm as reference). The measured signal is proportional to the amount of bound Anti-Scl Ab.

Assay test runs were performed prior to experimental assays to ensure large quantities of sample could be transferred efficiently and that 1 µg/mL biotinylated and SULFO TAG labelled mScl constructs provided sufficient signal.

Sclerostin neutralising antibody (3.2.4.4) standards (50 µL/sample; 2000, 667, 222, 74, 25, 8.2, 2.7 and 0 ng/mL) were prepared in PBS/1% BSA/10% WT serum. Biotinylated and SULFO TAG labelled mScl (50 µL/sample; 1 µg/mL) (for mScl treated mice) and mScl hFc PD (for mice treated with mScl hFc fusion proteins) were then added to the 50 µL standards, 50 µL experimental serum samples (1:10 dilution) and two controls (50 µL 500 ng and 20 ng anti-Scl Ab in PBS/1% BSA/10% WT serum). Sample solutions were incubated overnight at room temperature, in a shaking incubator. MSD GOLD 96-well Streptavidin SECTOR plates (Meso Scale Diagnostics,

Rockville, MD, USA) were washed (PBS/0.1% Tween wash buffer), blocked with 150 μL PBS/3% BSA blocking buffer and incubated overnight at 4 °C.

The following day, after washing the blocked plates with wash buffer, prepared samples (50 μL/well) were loaded onto 96-well plates. Plates were sealed and incubated, shaking at room temperature, followed by three washing steps. Two times MSD Read Buffer (Meso Scale Diagnostics, Rockville, MD, USA) was added (150 μL/well) and signal was read immediately at 450 nm (570 nm as reference) using an MSD SECTOR Imager 6000 system (Meso Scale Diagnostics, Rockville, MD, USA). A standard curve was generated by plotting MSD signal (logarithmic) against Anti-Scl Ab concentration (logarithmic) in Microsoft Excel (Microsoft, Redmond, WA, USA). Anti-Scl Ab serum concentrations were interpolated using GraphPad Prism 8.4.1 (GraphPad Software, San Diego, CA, USA) and results were corrected for 1:10 sample dilution.

Outliers were selected and ADA confirmation assays were performed. These assays were identical to assays described above, however, serum samples were saturated with 100 μg/mL mScl, mScl hFc or mScl hFc PD to confirm the presence of ADAs and to determine whether ADAs targeted the mScl or hFc regions of the recombinant mScl constructs.

3.3.2.7. Micro computed tomography

Micro computed tomography (μCT) analyses were performed to measure skeletal changes due to treatment with the recombinant mScl constructs. The right femurs and L5 lumbar vertebrae were cleaned of soft tissue, fixed in 10% neutral buffered formalin for 48 hours, then washed and stored in PBS for the duration of the μCT scans. Prior to scanning, samples were removed from storage pots, wrapped in PBS-soaked tissue for stabilisation, and placed in radiolucent custom containers.

After blinding sample details, whole femurs and vertebrae were placed in a 16-position high throughput sample carousel for automated scanning and were scanned using a Skyscan 1272 X-ray micro computed tomography instrument (Bruker, Kontich, Belgium), MA, USA). X-ray projection images, taken with a 0.6° rotation step over 180° sample rotation, were acquired using

the Skyscan acquisition software version 1.1.17. The X-ray tube was operated at 50 kV source voltage, 200 µA current, 1100 ms exposure time using a 0.5 mm aluminium filter to reduce X-ray diffraction of high-density sample, and a 6 µm voxel size (adapted from Javaheri et al., 2016; Shah et al., 2010). Vertebrae and femurs were reconstructed using Skyscan NRecon version 1.7.4.6 (reconstruction engine: GPUReconServer) with the following settings: Smoothing: 1; Ring artefacts correction: 4; Beam hardening correction: 20% for vertebrae and 30% for femurs. Subsequently, reconstructed data sets were viewed and reoriented in SkyScan DataViewer version 1.5.6. Vertebrae were orientated and straightened with the spinous process projecting upwards, and femurs were rotated and straightened using a straight 90° vertical reference line, ensuring that the femoral head was positioned proximally. Morphometric regions of interest (ROIs) for cortical and trabecular bone were automatically segmented using custom task-list algorithms (developed by Phil Salmon, Bruker MicroCT) in CTAn version 1.19.3.1 software (Bruker, Kontich, Belgium). In addition, prior to measuring bone mineral density (BMD), hydroxyapatite phantoms (dense and non-dense) were scanned and used to calibrate BMD. Representative images were generated using Skyscan NRecon version 1.7.4.6.

Femur analysis

Trabecular and cortical bone compartments were analysed in the distal metaphysis and diaphysis, respectively. A reference point for analysis of distal femur metaphyseal trabecular bone and diaphyseal cortical bone was selected where the trabecular 'bridge' that connects the two primary spongiosa bone 'islands' appeared (where the distal growth plate ends). Five hundred (3 mm) slices from a proximal offset of 150 slices (0.9 mm) from the reference point were selected as ROI to capture the metaphyseal region for trabecular analysis, with cortical shell excluded (Figure 3.2). An offset of 430 slices from the reference point was selected for the femoral cortical bone within the diaphysis, with an analysis region of 250 slices (1.5 mm) selected (Figure 3.2). Three-dimensional algorithms were used to calculate trabecular bone parameters: volumetric bone mineral density (vBMD), bone volume as a percentage of the total volume scanned (BV/TV), trabecular thickness (Tb.Th), trabecular space (Tb.Sp), trabecular number (Tb.N), trabecular bone pattern factor (Tb.Pf), structural model index (SMI) and degree of anisotropy (DA). Cortical bone parameters were calculated with two-dimensional algorithms: BV/TV, tissue area (T.Ar), bone area (B.Ar), medullary area (Ma.Ar), tissue perimeter (T.Pm), bone

perimeter (B.Pm), bone cross-sectional thickness (Cs.Th), mean polar moment of inertia (MMI(polar)) and mean eccentricity.

Vertebra analysis

The distal and proximal growth plates were used as reference marks and trabecular bone of the vertebral body within this region was analysed (Figure 3.2). For analysis, an upper threshold value of 255 and a lower threshold value of 83 was used to delineate each pixel as "bone" or "non-bone" when automatically segmenting ROIs with custom task-list algorithms in CTAn version 1.19.3.1 software (Bruker, Kontich, Belgium). Three-dimensional and two-dimensional morphometric traits were then calculated for trabecular and cortical bone respectively (see Femur analysis above).

Coefficients of variation

To examine variations between bone scans, the coefficients of variation (CVs) were determined with six independent, full femoral scans (including repositioning, reconstruction and analysis) performed on the same bone sample, to account for operator and automated algorithm bias, and determine reproducibility of the analysis. Only trabecular bone analysis was chosen, due to the greater margin of error involved in segmenting the ROIs, since the cortical shell shape changes markedly throughout the analysed region. CVs of each parameter were determined as the ratio between the standard deviation and mean, and were as follows for the relevant parameters: BV/TV: 2.53%; Tb.Th: 1.72%; Tb.N: 3.2%; cortical B.Ar: 0.15% and cortical thickness: 0.46%.
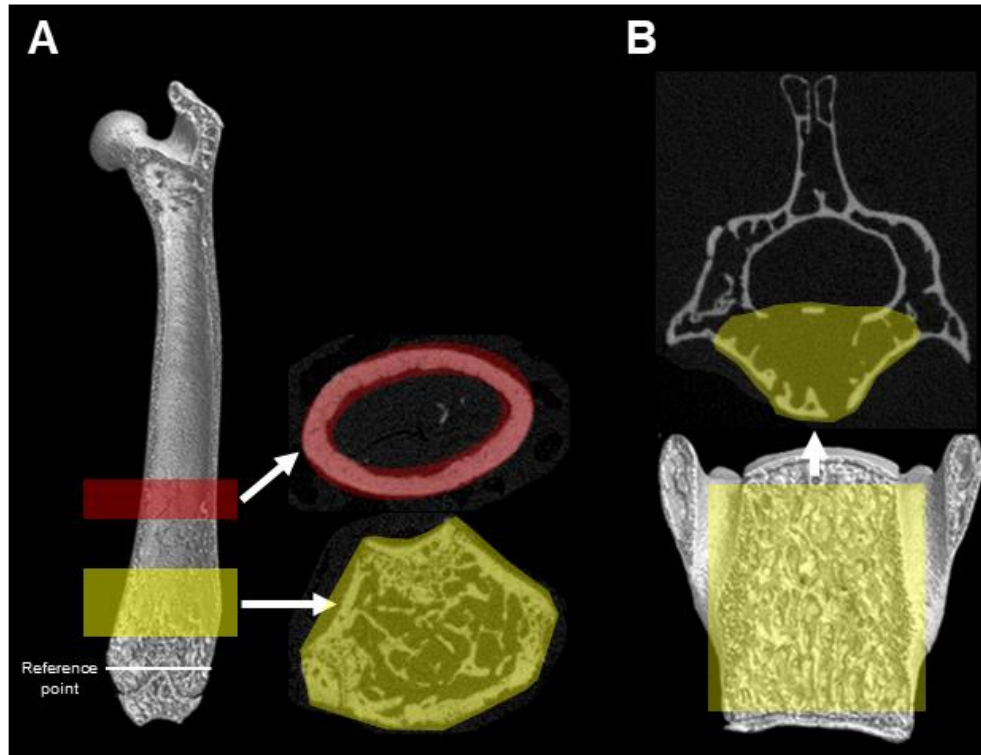
Figure 3.2: Femoral and vertebral regions of interest. Trabecular microarchitecture was assessed by µCT in wild type and SOST^{-/-} mice aged ~3 months. A) A reference point was selected where the distal femoral growth plate ends. An offset of 150 slices from the reference point and 500 slices were selected (yellow) as ROI for femoral trabecular analysis. An offset of 430 slices from the references point and a region of 250 slices (red region) was selected for analysis of femoral cortical bone. B) The vertebral body region (top yellow region) between the distal and proximal growth plates (bottom yellow region) was selected as the region of interest for vertebral trabecular analysis.

3.4. Statistical analysis

Results were presented as mean±SD. Data comparison was performed with GraphPad Prism 8.4.1 (GraphPad Software) using two-way ANOVA for the bone nodule formation assays, and unpaired t-tests or ordinary one-way ANOVA for trabecular and cortical bone parameters. A p-value of <0.05 was considered significant.

Chapter 4: Results

4.1.   Plasmid design, cloning, and protein production

4.1.1. Plasmid design and cloning

4.1.1.1.   pMH mSOST WT

The pMH mSOST WT recombinant plasmid for mScl expression was cloned in a single step at the UCB labs in Slough, UK. The mSOST WT fragment (648 bp) contained a Kozak sequence (to enhance translation) adjacent to a 5' *Hind*III site, followed by an initiation codon and mSOST sequence, and ending in a stop codon before a 3' *Eco*RI site (Figure 4.1). The UCB pMH vector (approximately 5.2 kb) contained a modified human cytomegalovirus (CMV) promoter and enhancer for transient expression of inserted gene sequences and a kanamycin resistance gene for antibiotic selection. Restriction digest with *Eco*RI and *Hind*III in 10x NEBuffer™ 3.1 (New England Biolabs, Ipswich, MA, USA) removed a stuffer region (702 bp) and linearised the pMH vector (now 4534 bp), and excised the mSOST WT fragment from the DNA2.0 (Newark, NJ, USA) plasmid (Figure 4.1). The linearised vector and excised fragment were extracted from agarose gel and ligated to yield a 5182 bp pMH mSOST WT vector (Figure 4.1). OneShot Top10 competent cells were then transformed with the ligation mixture and colonies were selected the following day for miniprep plasmid preparation. Prepared DNA was analysed via restriction digest, using *Hind*III High-Fidelity (HF®) and *Eco*RI HF® restriction enzymes in CutSmart® Buffer (New England Biolabs, Ipswich, MA, USA). Bands of approximately 648 bp and 4534 bp confirmed successful insertion of an mSOST WT fragment to form a pMH mSOST WT recombinant plasmid (Figure 4.4 and 4.5).
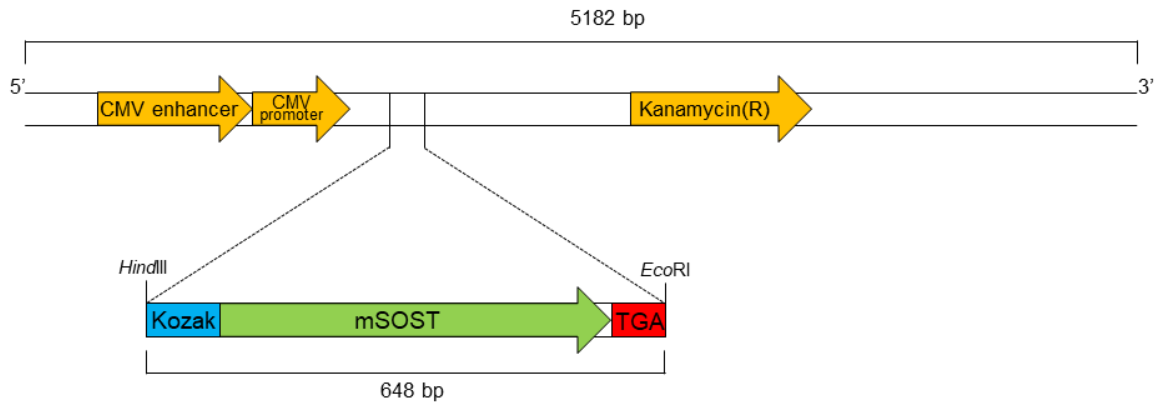
Figure 4.1: pMH mSOST WT construction. To construct a pMH mSOST WT expression vector (5884 bp), a 648 bp mSOST WT fragment, consisting of a Kozak sequence, followed by mSOST and ending with a stop codon (TGA), was inserted into a 5236 bp pMH vector (containing a CMV promoter and enhancer for transient gene expression and a kanamycin resistance gene for antibiotic selection) using *Hind*III and *Eco*RI restriction digest (a 702 bp stuffer region was removed from the vector in this process; not shown).

4.1.1.2. pMH mSOST hFc

A pMH mSOST hFc recombinant plasmid, developed for mScl hFc expression, was also cloned at the UCB labs in Slough, UK. Cloning was done in two steps: a pMH hFc vector was constructed first, followed by insertion of an mSOST fragment into the new pMH hFc plasmid.

pMH hFc construction

The hFc fragment (705 bp) was designed with a 5' *Xho*I restriction site, followed by the hFc sequence and a stop codon, and ended with a 3' *Eco*RI restriction site. Restriction digest was performed with *Eco*RI and *Xho*I in 10x NEBuffer™ 3.1 to remove the stuffer region and linearise the pMH vector (UCB, Slough, UK), and to excise the hFc fragment from the DNA2.0 plasmid (Figure 4.2). The hFc fragment (705 bp) was extracted from agarose gel and ligated with the linearised vector (4534 bp). Following ligation, OneShot Top 10 cells were transformed with ligation mixture. The following day, five colonies were selected and prepared via miniprep for restriction analysis. Prepared DNA was digested with *Eco*RI and *Xho*I, and an approximately 705 bp band was observed for successfully cloned pMH hFc plasmids (5239 bp).

pMH mSOST hFc construction

An mSOST fragment (645 bp) was designed with a 5' *Hind*III restriction site, followed by a Kozak sequence and the mSOST sequence, and ending with a 3' *Eco*RI restriction site (Figure 4.2). No stop codon was included to ensure that translation continued in frame through the hFc sequence. Restriction digest with *Hind*III and *Eco*RI in NEBuffer3.1 linearised the pMH hFc vector and excised the mSOST fragment from the DNA2.0 plasmid. The mSOST fragment was then ligated into the pMH hFc vector to yield pMH mSOST hFc (5884 bp) (Figure 4.2). Competent OneShot Top 10 cells were transformed with the ligation mix and the following day colonies were selected for restriction analysis. DNA was purified via miniprep and digested with *Hind*III HF® and *Eco*RI HF® restriction enzymes in CutSmart® Buffer for restriction analysis. Bands of approximately 1350 bp and 4534 bp were observed, confirming successful insertion of mSOST into pMH hFc to yield a pMH mSOST hFc recombinant plasmid (Figure 4.4 and 4.5).
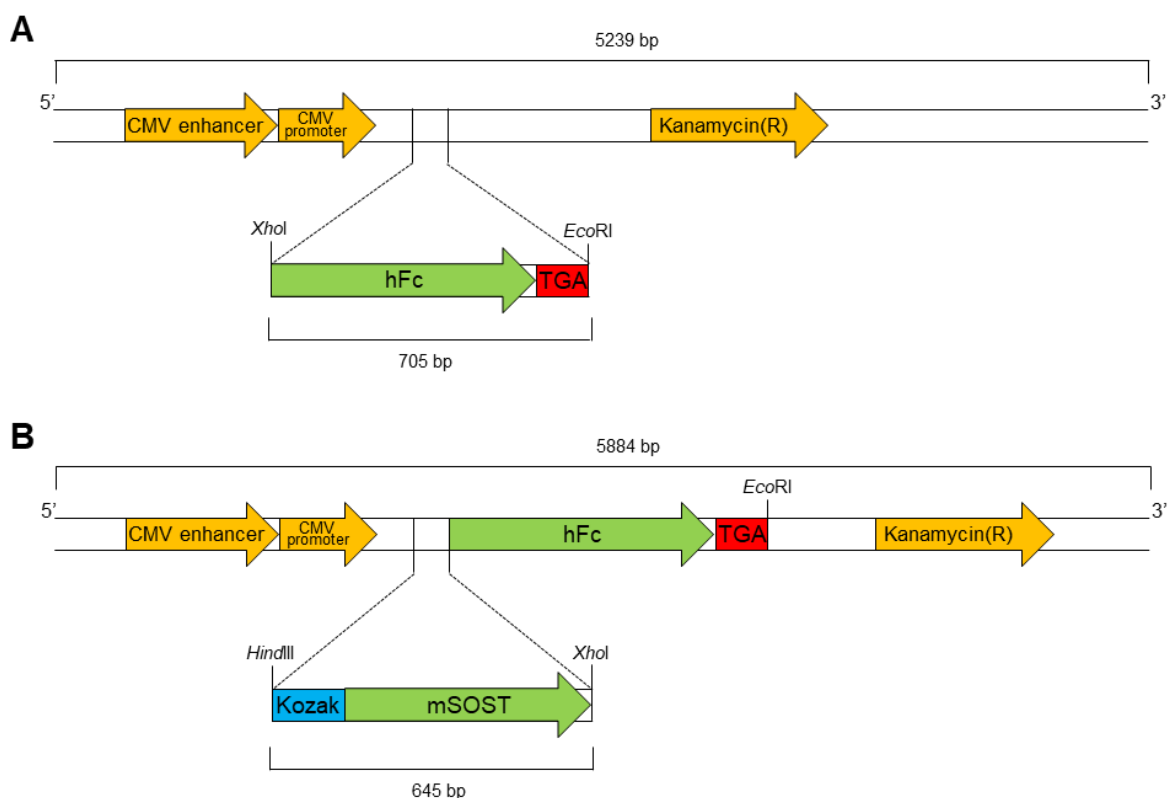
Figure 4.2: pMH mSOST hFc construction. To construct a pMH mSOST hFc expression vector (5884 bp): A) a 705 bp hFc sequence with a stop codon (TGA) was inserted into a 5236 bp pMH vector (containing a CMV promoter and enhancer for transient gene expression and a kanamycin resistance gene for antibiotic selection) that was linearised by *Xho*I and *Eco*RI restriction digest (a 702 bp stuffer region was removed from the vector in this process; not shown). B) A 645 bp mSOST WT sequence, consisting of a Kozak sequence and mSOST, was inserted into the new 5239 bp pMH hFc vector using *Hind*III and *Xho*I restriction digest.

4.1.1.3. pMH mSOST hFc PD

A pMH mSOST hFc PD recombinant plasmid, developed to express mScl hFc PD, was cloned at the Department of Microbiology and Plant Pathology labs, University of Pretoria, South Africa. Cloning was done in two steps: a pMH hFc PD vector was constructed first, followed by insertion of an mSOST fragment into the new pMH hFc PD plasmid (Figure 4.3).

pMH hFc PD construction

The hFc PD fragment (729 bp) was designed with a 5' *Xho*I restriction site, followed by the hFc PD sequence, a stop codon, and a 3' *Eco*RI restriction site. FastDigest Green Buffer and FastDigest *Xho*I and *Eco*RI restriction enzymes (Thermo Fischer Scientific, Waltham, MA, USA) were used to linearise the UCB vector by removing the 705 bp stuffer region, and to excise the hFc PD fragment from the DNA2.0 plasmid. The FastDigest reaction mixtures were incubated at 37 °C for 15 minutes and loaded straight onto an agarose gel. The linearised pMH and excised hFc PD fragment were ligated, followed by transformation of competent DH5α *E. coli* cells with the ligation mixture. The following day, colonies were selected for miniprep and restriction analysis. DNA digested with *Eco*RI and *Xho*I showed an approximately 729 bp band, confirming successful cloning of hFc PD into the vector to yield the new 5263 bp pMH hFc PD recombinant plasmid (Figure 4.3).

pMH mSOST hFc PD construction

*Hind*III and *Eco*RI restriction digest was performed to linearise the pMH hFc PD vector and excise the mSOST fragment (identical to the fragment described in 4.1.1.2) from the DNA2.0 plasmid. The mSOST fragment (645 bp) was then ligated into the linear pMH hFc PD vector to yield a 5908 bp pMH mSOST hFc PD plasmid (Figure 4.3). DH5α *E. coli* cells were transformed with the ligation mixture and colonies were selected for miniprep and restriction analysis the following day. The purified DNA was digested with *Hind*III HF® and *Eco*RI HF® restriction enzymes in CutSmart® Buffer, and bands of approximately 1374 bp and 4534 bp were observed for successfully cloned pMH mSOST hFc PD recombinant plasmids (Figure 4.4 and 4.5).

4.1.2. Sequencing

All three recombinant plasmids were prepared with QIAprep Spin Miniprep Kits and submitted for sequencing. ContigExpress (Invitrogen Vector NTI Advanced 11.5.5 software package; Thermo Fischer Scientific, Waltham, MA, USA) was used to align sequencing results with reference sequences (Figure 4.6). No errors were found, confirming that all three mSOST constructs were successfully cloned into the vectors.
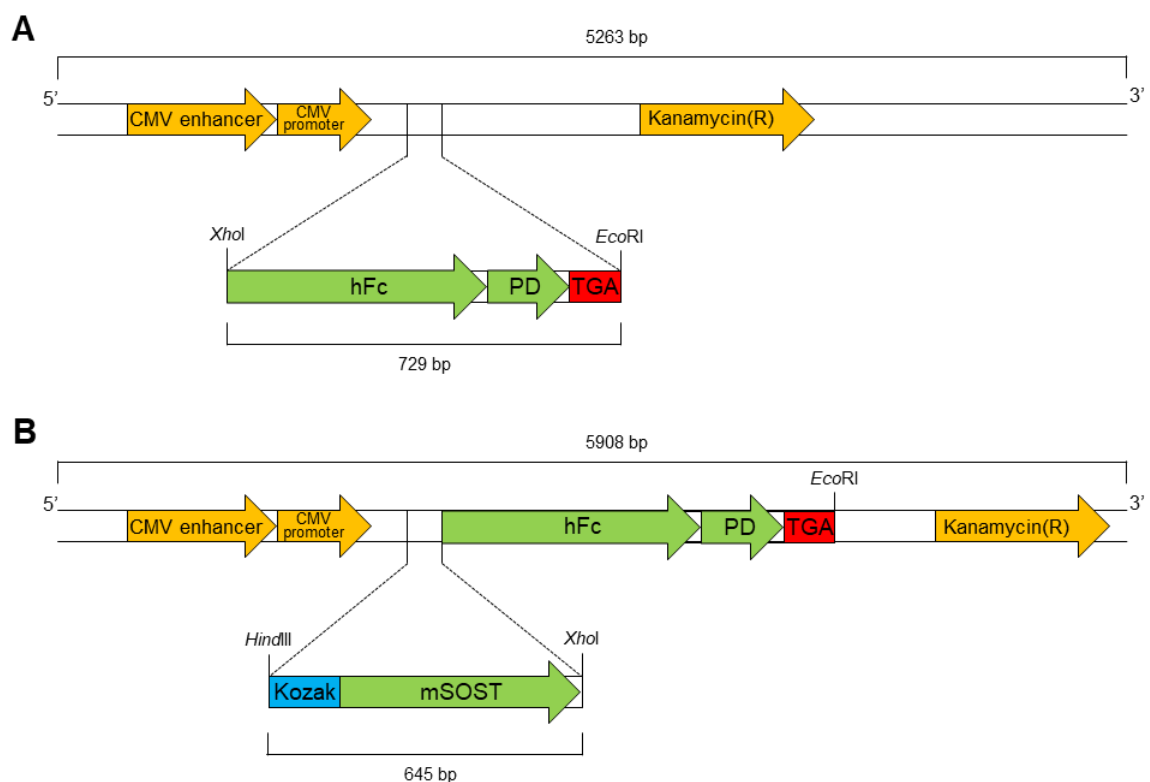
Figure 4.3: pMH mSOST hFc PD construction. To construct a pMH mSOST hFc PD expression vector (5908 bp): A) a 729 bp fragment consisting of an hFc sequence, an octa-aspartate sequence (PD), and a stop codon (TGA) was inserted into a 5236 bp pMH vector (containing a CMV promoter and enhancer for transient gene expression and a kanamycin resistance gene for antibiotic selection) that was linearised by *Xho*I and *Eco*RI restriction digest (a 702 bp stuffer region was removed from the vector in this process; not shown). B) A 645 bp mSOST WT fragment, consisting of a Kozak and mSOST sequence, was inserted into the new 5263 bp pMH hFc PD vector using *Hind*III and *Xho*I restriction digest.
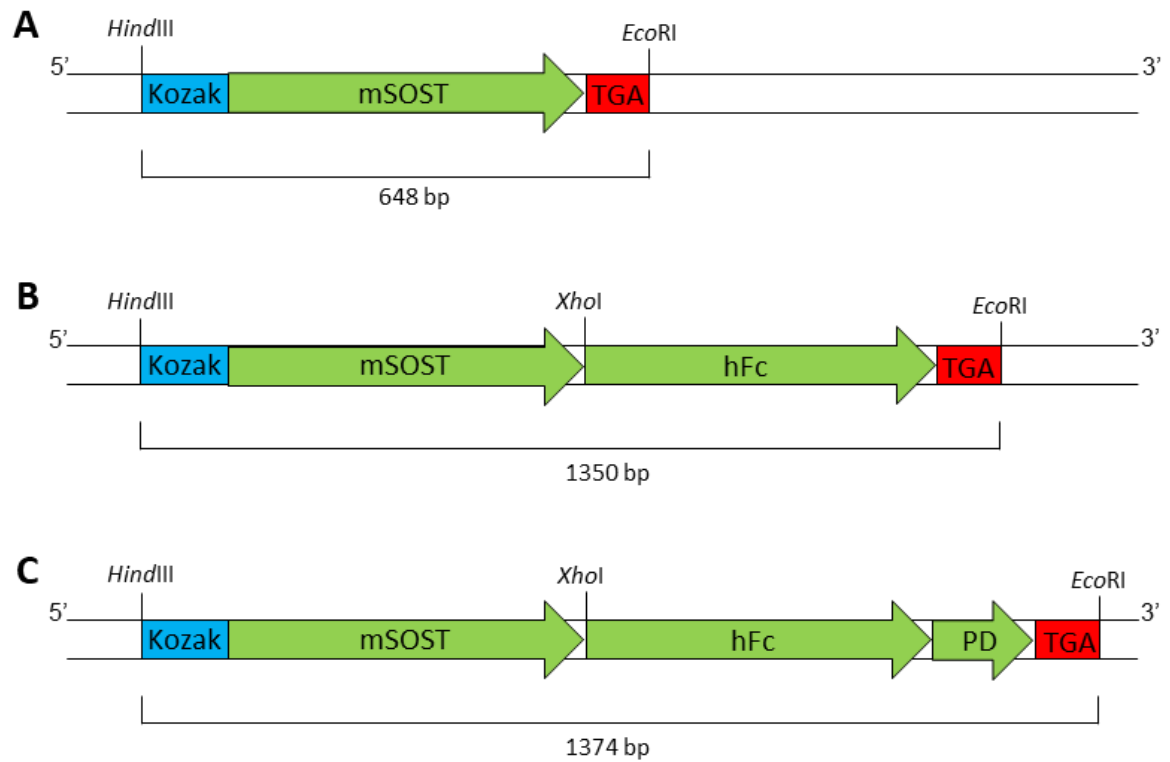
Figure 4.4: Schematic diagram of the three mSOST vector inserts. A) The 654 bp mSOST WT sequence consists of a Kozak sequence, followed by mSOST, and ending with a stop codon (TGA). B) mSOST hFc (1350 bp) is made up of a Kozak sequence, mSOST, hFc, and a stop codon at the 3' end. C) The 1374 bp mSOST hFc PD insert consists of a Kozak and mSOST sequence, followed by hFc, an octa-aspartate sequence and a stop codon (TGA).
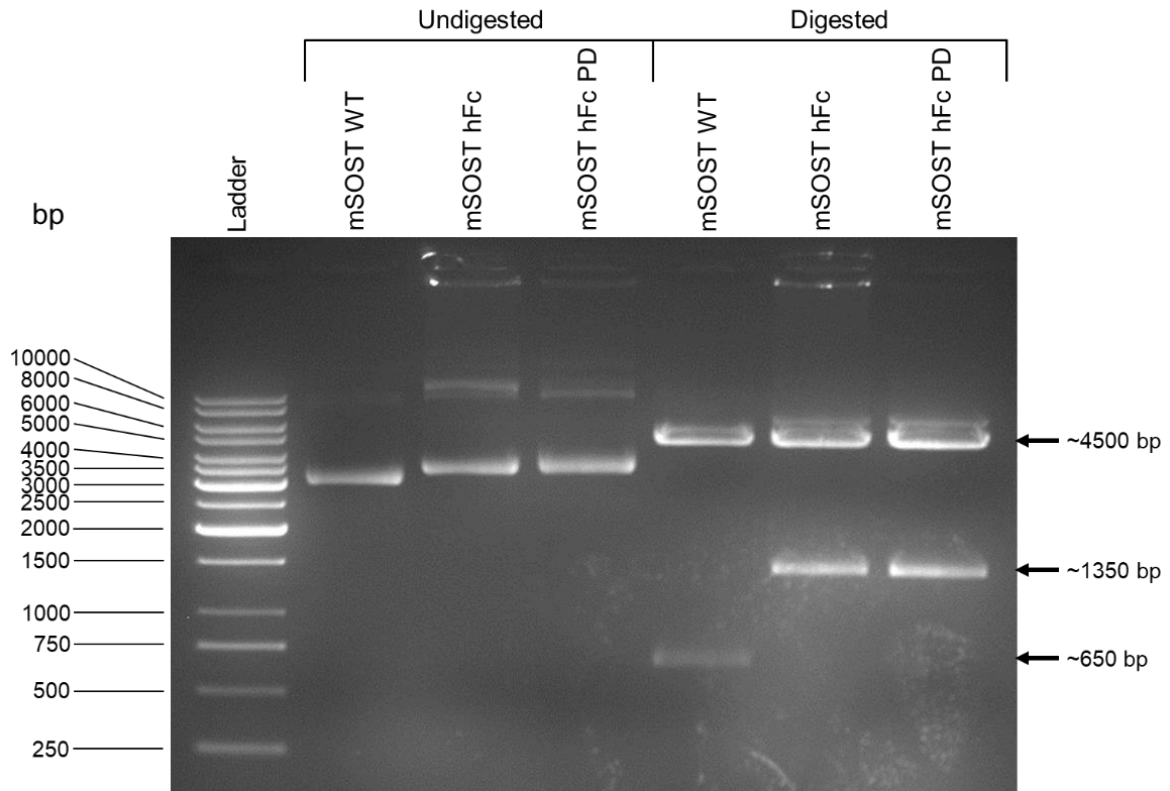
Figure 4.5: Restriction analysis of pMH mSOST WT, pMH mSOST hFc and pMH mSOST hFc PD. Undigested DNA samples were used as controls. Plasmids were digested with *Hind*III HF® and *Eco*RI HF® restriction enzymes in CutSmart® Buffer. Digestion with these enzymes removed the inserted mSOST, mSOST hFc and mSOST hFc PD fragments from the respective plasmids. An ~650 bp band was observed for pMH mSOST WT (bottom arrow), whilst ~1350 bp bands were observed for pMH mSOST hFc and pMH mSOST hFc PD (middle arrow), indicating successful insertion into the pMH vector. All three constructs showed an ~4500 bp band (top arrow) for the linearised vector (same for all constructs once inserts removed). Samples were run on a 1% agarose gel and a GeneRuler 1kb DNA ladder was used.

Figure 4.6 Sequence alignment of cloned constructs. The complete A) mSOST, B) mSOST hFc and C) mSOST hFc PD inserts were sequenced. Forward and reverse sequences (lower and middle arrows) were aligned with their respective reference sequences (top arrows). The bottom bar indicates the sequence lengths and shows where the forward and reverse sequences overlap (dark sections in the middle). Sequences were aligned with ContigExpress (Invitrogen Vector NTI Advanced 11.5.5 software package).

4.1.3. Protein expression and purification

Recombinant wild type mouse sclerostin (mScl) and two novel recombinant mScl fusion proteins were produced for this study. To increase protein half-life, mScl was fused with a monomeric Fc region of a human immunoglobulin G (IgG) antibody (hFc) positioned at the mScl C-terminus (mScl hFc). In a third construct, an octa-aspartate motif (PD) was included downstream of the hFc in an attempt to improve the protein's ability to localise to bone (mScl hFc PD).

4.1.3.1. Chromatography

mScl hFc PD

SDS-PAGE analysis showed mScl hFc PD (~96.7 kDa) was present (~98 kDa and ~55 kDa bands under non-reducing and reducing conditions respectively) (Figure 4.7) in the filtered supernatant of 5 L HEK293 mammalian expression culture. As a first step, mScl hFc PD was purified by hFc-

tag affinity to Protein A. To elute the protein after loading it onto Protein A columns, elution buffer (0.1 M citric acid) was increased linearly from 0-100% and a single peak (>2500 mAU) was observed approximately 35 mL after elution started (at 35% 0.1 M citric acid) (Figure 4.8). Peak fractions were slightly turbid, however, addition of 1 mL 1 M Tris-HCl pH 8.5 to each fraction adjusted sample pH to 7, thereby decreasing sample turbidity. Fractions were pooled and centrifuged to remove protein aggregate, resulting in a clear sample. Multiple bands were visible on SDS-PAGE gels, however, three bands: two (~98 kDa and ~80 kDa) under non-reducing conditions and one (~55 kDa) under reducing conditions, were distinct (Figure 4.7). This was as expected, as the hFc component of the constructs is expected to form disulphide-linked dimers under non-reducing conditions (~98 kDa) and become or remain monomers under reducing conditions (~55 kDa). Remaining protein was extracted from the first 5 L flow through by a single repetition of the loading and elution steps. Samples from both runs were pooled (22 mL total volume) for size exclusion chromatography (SEC).

The 22 mL affinity chromatography sample was loaded onto a HiLoad™ 26/600 Superdex™ 200 pg column. A single peak (1900 mAU) was observed after 110 mL elution (Figure 4.9) and peak fractions were pooled (48 mL total volume). SDS-PAGE showed two distinct (~98 kDa and ~80 kDa) and one minor (~55 kDa) band under non-reducing conditions, whilst one major (~55 kDa) and two minor (~38 kDa and ~30 kDa) bands were visible under reducing conditions (Figure 4.7).

The SEC sample was loaded onto a 1 mL RESOURCE™ S cation exchange chromatography (CEC) column (equilibrated with Buffer A2: 10 mM PBS, pH 7.4) and eluted by increasing Buffer B2 (10 mM PBS, 1 M NaCl, pH 7.4) linearly from 50% to 100%. A single, narrow peak (>2500 mAU) was observed at 65% Buffer B2 (0.65 M NaCl, 10 mM PBS, pH 7.4), after approximately 17 mL elution (Figure 4.10). Peak fractions were pooled (5.25 mL total sample volume) and removal of remaining impurities was confirmed by SDS-PAGE. Distinct bands, identical to those seen in the SEC purification step, were observed (Figure 4.7).

mScl hFc

Filtered HEK293 supernatant (5 L) containing mScl hFc (94.8 kDa) (confirmed by an ~50 kDa band under reducing conditions) (Figure 4.11) was loaded onto Protein A columns. A lack of ~98kDa and ~55kDa bands in the flow through, under non-reducing and reducing conditions respectively,

showed that mScl hFc successfully bound to the Protein A column (Figure 4.11). To elute protein, the concentration of 0.1 M citric acid was increased to 50% and a single tall and wide peak (>2500 mAU) was observed at approximately 30 mL after elution started (Figure 4.12). An additional 1 mL 1 M Tris-HCl pH 8.5 was added to each fraction to adjust sample pH to 7, resulting in clear eluted samples that were pooled. Multiple protein bands were observed when analysing the pooled samples by SDS-PAGE (Figure 4.11). However, distinct ~98kDa and ~50kDa bands, under non-reducing and reducing conditions respectively, indicated the presence of mScl hFc in samples. As with mScl hFc PD purification, loading and elution steps were repeated with 5 L flow through collected during the first run. Although SDS-PAGE indicated little to no mScl hFc in the flow through, elution results from the second run were similar to the first. Fractions from both runs were pooled together.

Pooled affinity chromatography samples were loaded onto a HiLoad™ 26/600 Superdex™ 200 pg column in two separate steps and fractions were collected from three distinct elution peaks (Figure 4.13). Peaks were analysed by SDS-PAGE and the following distinct protein bands were observed under non-reducing conditions: Peak 1: ~98 kDa; Peak 2: ~98 kDa and ~80 kDa (similar to mScl hFc PD SEC results); Peak 3: ~90 kDa (Figure 4.14). An ~50 kDa band was observed for all three peaks under reducing conditions, with additional ~38 kDa and ~30 kDa bands visible for Peak 2. Peak 3 eluted late and likely consisted of impurities. Analytical gel filtration (Superdex® 200 10/30 GL column) of Peak 1 and 2 (Figure 4.15) showed that Peak 1 possibly consisted of mScl hFc hexamers or protein aggregate (~630 kDa), whilst Peak 2 consisted of dimeric mScl hFc (~95 kDa). Peak 2 had the same SDS-PAGE profile as purified mScl hFc PD and was therefore selected and stored for purification by CEC.

SEC samples were loaded onto a 1 mL RESOURCE™ S column equilibrated with Buffer A2. During elution, Buffer B2 (10 mM PBS, 1 M NaCl, pH 7.4) was increased linearly from 50% to 100% and a narrow >2500 mAU peak was observed at 60% Buffer B2 (0.6 M NaCl, 10 mM PBS, pH 7.4), 48 mL after elution started (Figure 4.16). Peak fractions were pooled (4 mL total sample) and analysed by SDS-PAGE. Two distinct ~98kDa and ~80kDa bands were observed under non-reducing conditions, whilst a single ~50kDa and two ~38kDa and ~30kDa bands were visible under reducing conditions. As expected, monomeric mScl hFc was slightly smaller than mScl hFc PD monomers (~55 kDa). Impurities remaining from the SEC step were successfully removed with CEC (Figure 4.11).

mScl WT

Some impurities were removed from HEK293 cell culture supernatant by vacuum filtration (0.22 µm PES) (Figure 4.17). Filtered supernatant contained wild type mScl, as indicated by a light, fuzzy ~35kDa band, and was loaded onto a 6 mL RESOURCE™ S CEC column equilibrated with Buffer A1 (50 mM MES, 100 mM NaCl, pH 6). Absence of an ~35 kDa protein band in SDS-PAGE analysis of the Resource™ S flow through showed that the protein successfully bound to the Resource™ S column (Figure 4.17). Protein was eluted with Buffer B1 (50mM MES, 500 mM NaCl, pH 6) and a single peak (>2500 mAU) was observed after 25 mL elution, when Buffer B1 was increased from 20% to 90% (Figure 4.18). Peak fractions were pooled (9 mL total volume) and analysed by SDS-PAGE. Pooled sample was very concentrated and multiple bands were observed, however, an ~35kDa band indicated the presence of mScl in the sample (Figure 4.17).

The 9 mL CEC sample was loaded onto a HiLoad Superdex 75 pg prepacked column. A single, narrow, tall peak (~2200 mAU) was observed after 50 mL elution (Figure 4.19) and all peak fractions were pooled (20 mL total sample). SEC removed impurities and protein aggregate, and mScl appeared as a single, large and fuzzy ~35 kDa band under both reducing and non-reducing conditions (Figure 4.17).
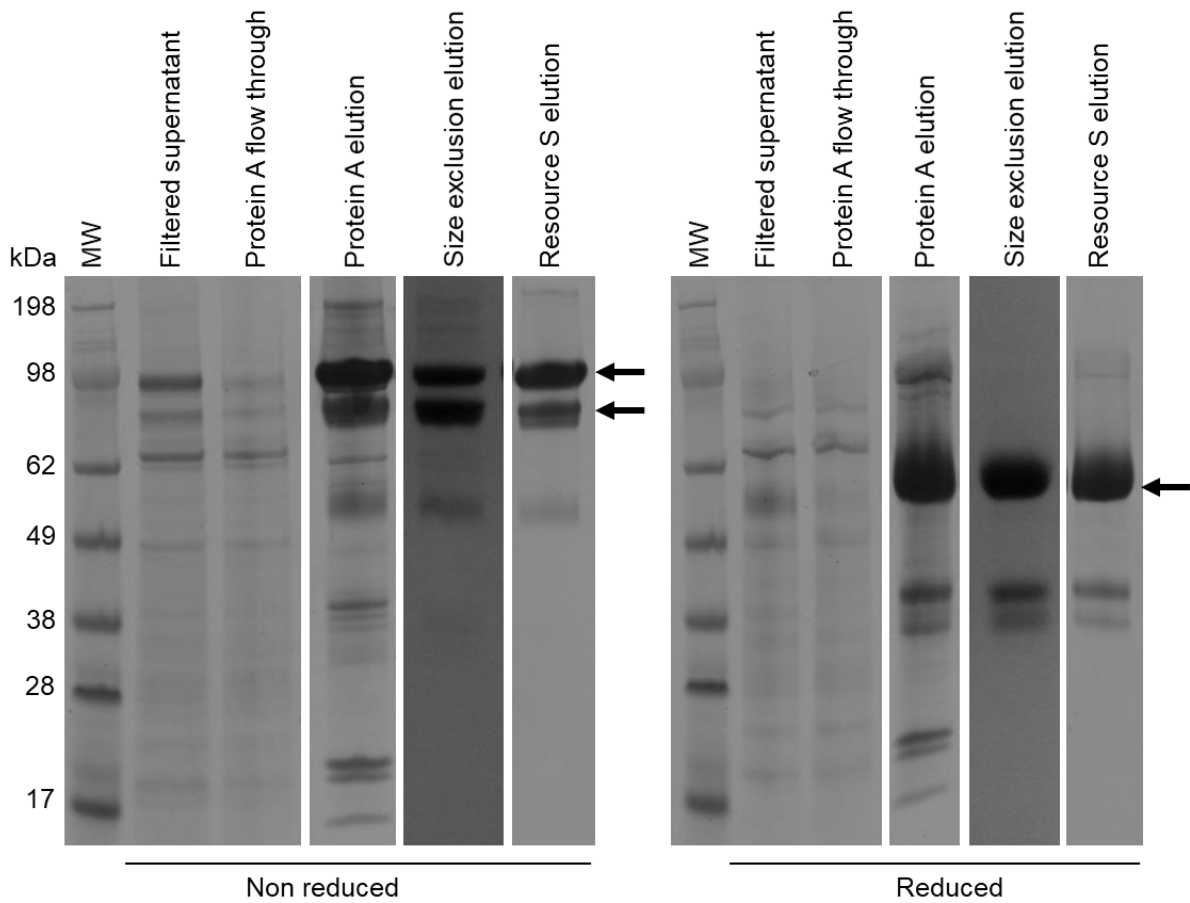
Figure 4.7: SDS-PAGE of the mScl hFc PD purification process. mScl hFc PD was present in filtered HEK293 supernatant (an ~98 kDa protein band under non-reducing conditions and an ~55 kDa band under reducing conditions). Approximately 98 kDa and ~80 kDa bands under non-reducing conditions and a ~55 kDa band under reducing conditions (black arrows) indicated the presence of mScl hFc PD in protein A affinity, size exclusion (SEC), and Resource™ S cation exchange (CEC) chromatography fractions. Impurities remained after Protein A affinity chromatography and were removed by SEC and CEC. Samples were analysed on NuPAGE™ 4-12% Bis-Tris Protein Gels.
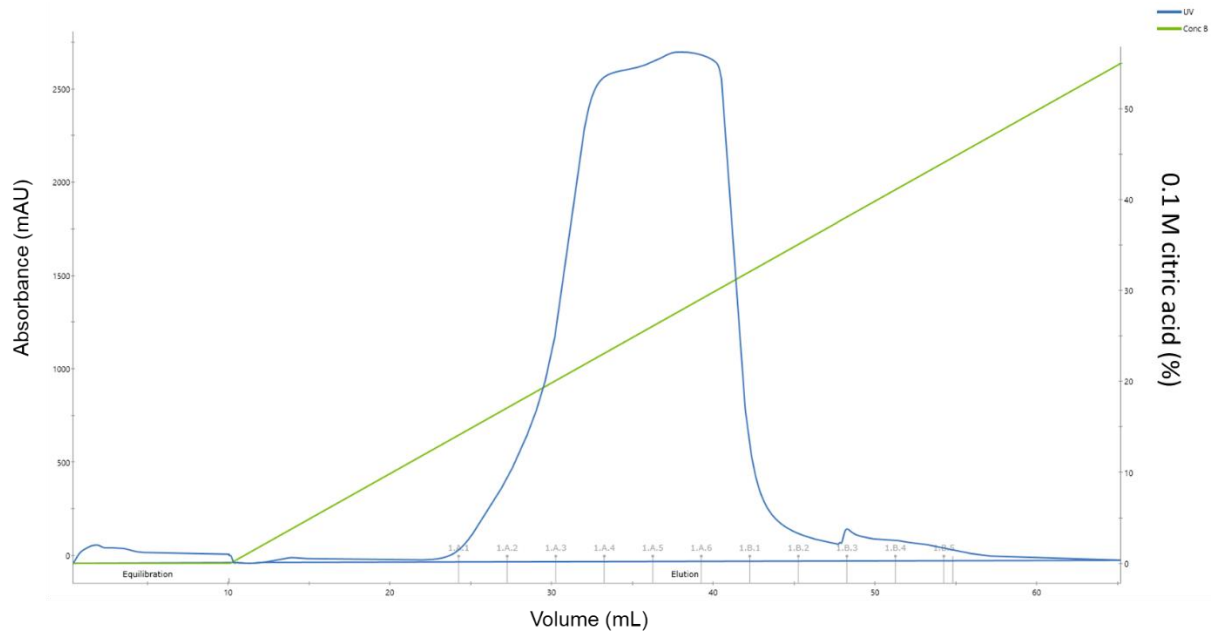
Figure 4.8: mScl hFc PD Protein A affinity chromatography elution profile. A representative chromatogram of mScl hFc PD purification by Protein A affinity chromatography. Citric acid (0.1 M) concentration was increased linearly (green line) to elute mScl hFc PD from a Protein A affinity chromatography column. A single >2500 mAU peak appeared after 30 mL elution, at ~35% 0.1 M citric acid. Absorbance measured at 280 nm.

Figure 4.9: mScl hFc PD size exclusion chromatography elution profile. A representative chromatogram of mScl hFc PD purification by SEC (HiLoad™ 26/600 Superdex™ 200 pg column). A single peak (~1900mAU) containing mScl hFc PD appeared approximately 110 mL after elution started. Absorbance measured at 280 nm.
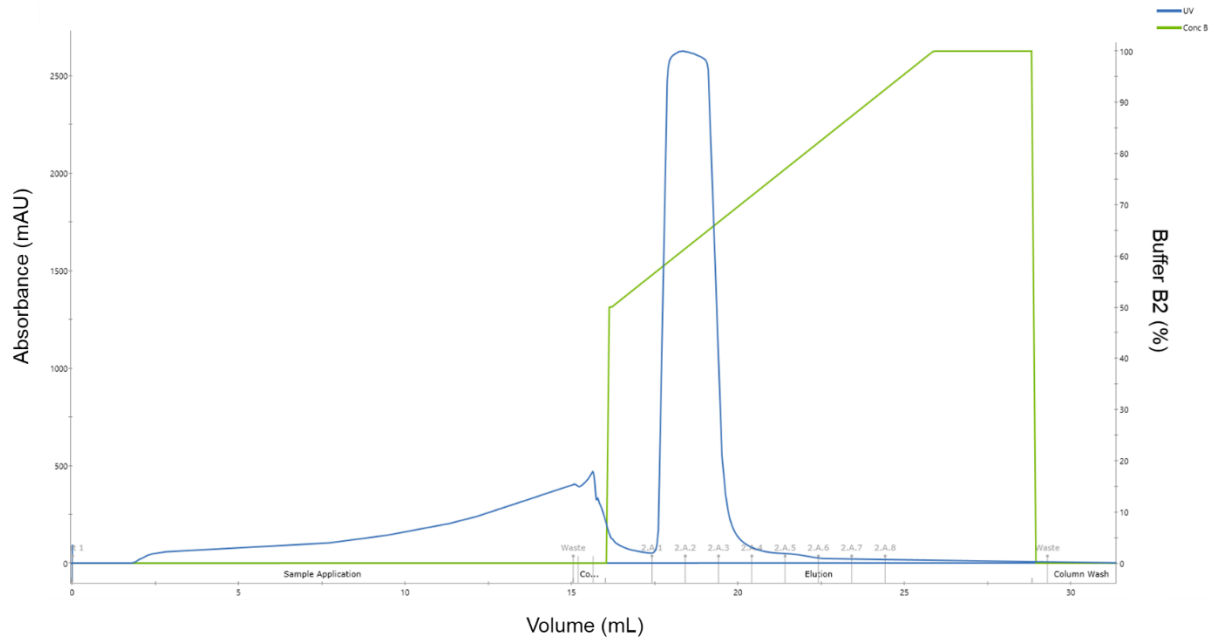
Figure 4.10: mScl hFc PD cation exchange chromatography elution profile. A representative chromatogram of mScl hFc PD purification by CEC. Buffer B2 (10 mM PBS, 1 M NaCl, pH 7.4) was increased linearly from 50% to 100% (green line) after approximately 15 mL elution to elute protein from a 1 mL Resource™ S CEC column. A single peak (>2500 mAU) appeared after approximately 17 mL elution, at ~55% Buffer B2 (0.55M NaCl, 10 mM PBS, pH 7.4). Absorbance measured at 280 nm.
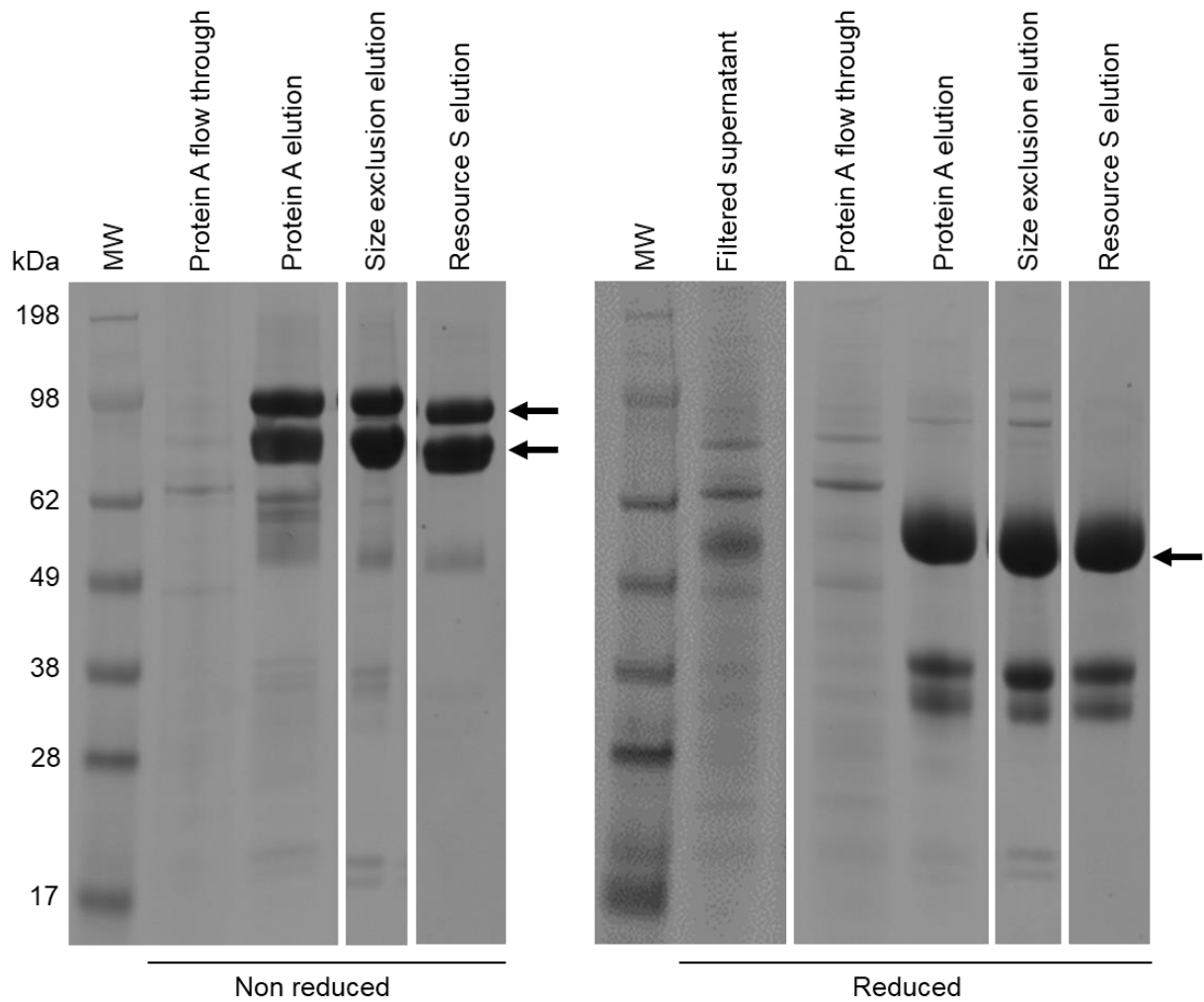
Figure 4.11: SDS-PAGE of the mScl hFc purification process. mScl hFc was present in filtered HEK293 supernatant (indicated by ~50 kDa protein band under reducing conditions). No mScl hFc was present in the Protein A flow through. Approximately 98 kDa and ~80 kDa bands (left arrows) under non-reducing conditions and an ~50 kDa band under reducing conditions (right arrow) indicated that mScl hFc was present in protein A affinity, SEC, and CEC fractions. Remaining impurities after Protein A affinity chromatography were removed by SEC and CEC. Samples were analysed on NuPAGE™ 4-12% Bis-Tris Protein Gels.
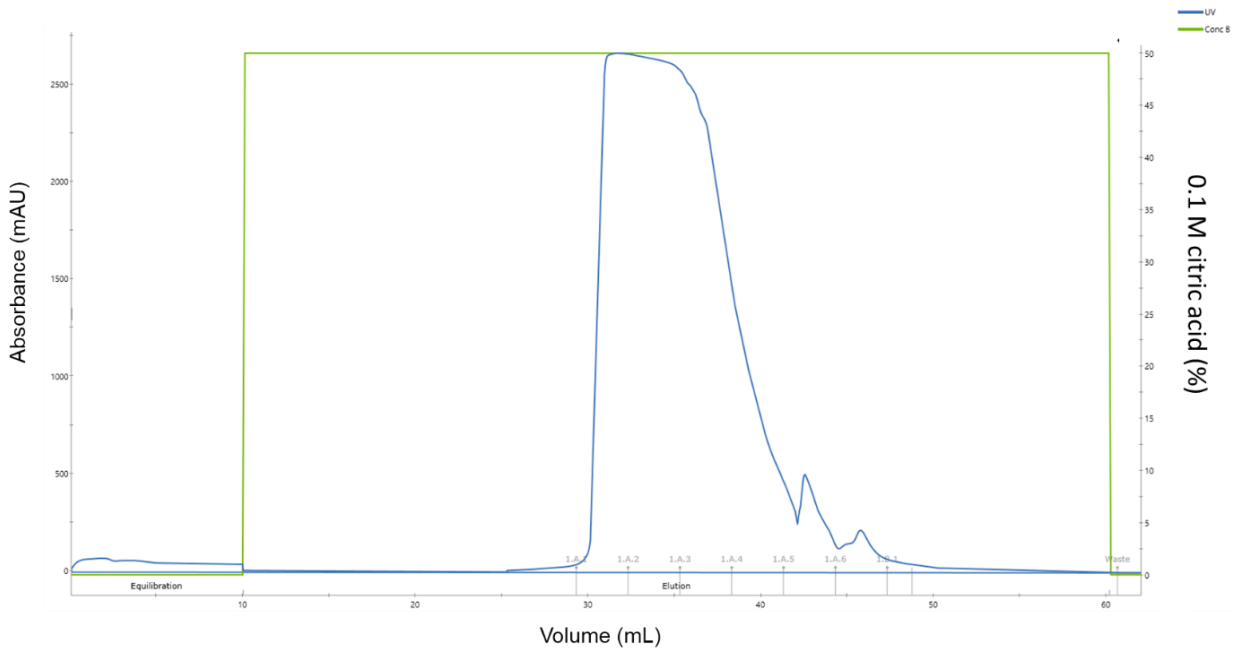
Figure 4.12: mScl hFc Protein A affinity chromatography elution profile. A representative chromatogram of mScl hFc purification by Protein A affinity chromatography. Citric acid (0.1 M) was increased to 50% (green line) to elute protein from a Protein A affinity chromatography column. A single >2500 mAU peak was observed after 30 mL elution, at 50% 0.1 M citric acid. Absorbance measured at 280 nm.
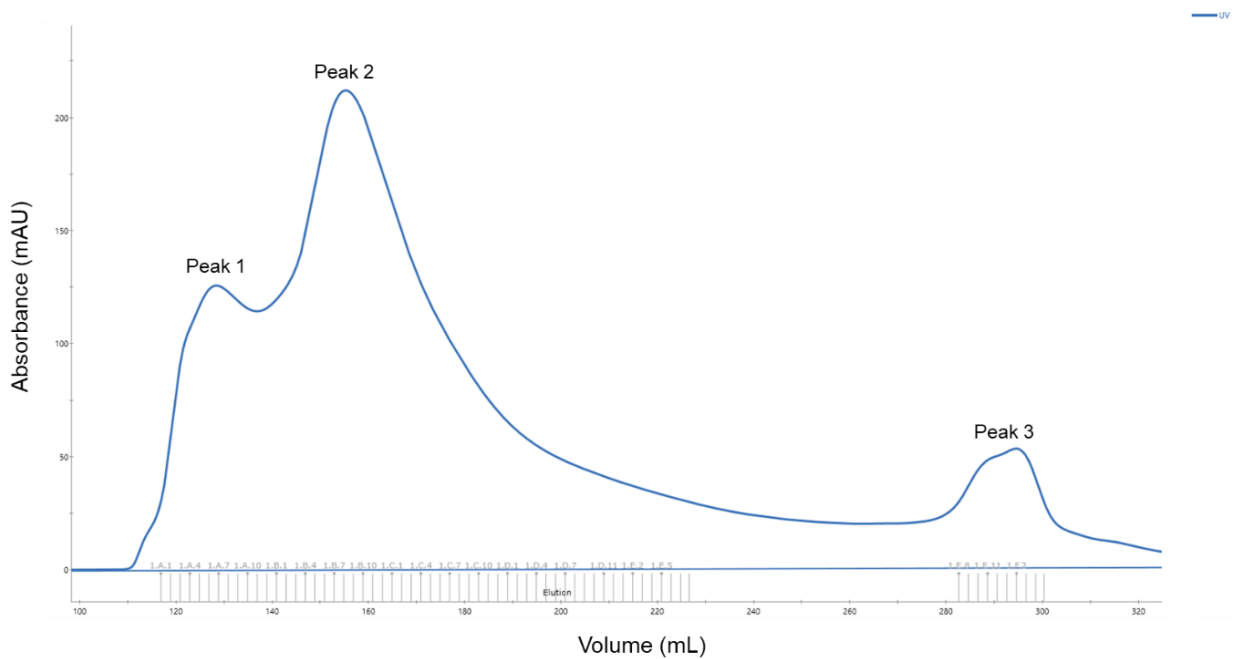
Figure 4.13: mScl hFc size exclusion chromatography elution profile. A representative chromatogram of mScl hFc purification by SEC (HiLoad™ 26/600 Superdex™ 200 pg column). Three peaks were observed when eluting protein from a HiLoad Superdex 200 pg column. Peak 1 (170 mAU), 2 (380 mAU) and 3 (40 mAU) appeared after 120 mL, 140 mL, and 260 mL elution, respectively. Absorbance measured at 280 nm.
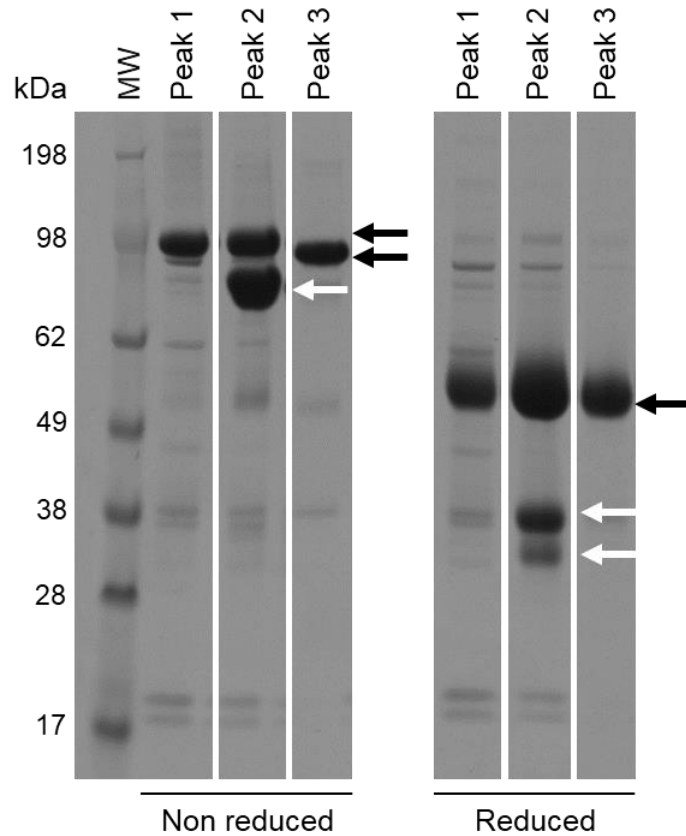
Figure 4.14: SDS-PAGE of mScl hFc size exclusion chromatography. Refer to peaks in Figure 4.13. Distinct bands were visible for all peaks under non-reducing conditions: Peak 1: ~98 kDa (top left black arrow); Peak 2: ~98 kDa and ~80 kDa (left white arrow); Peak 3: ~70 kDa (lower left black arrow). An ~50 kDa band is visible for all peaks under reducing conditions (right black arrow). Peak 2 also have two additional distinct bands: ~38 kDa and ~30 kDa (right white arrows), consistent with purified mScl hFc PD. Samples were analysed on NuPAGE™ 4-12% Bis-Tris Protein Gels.
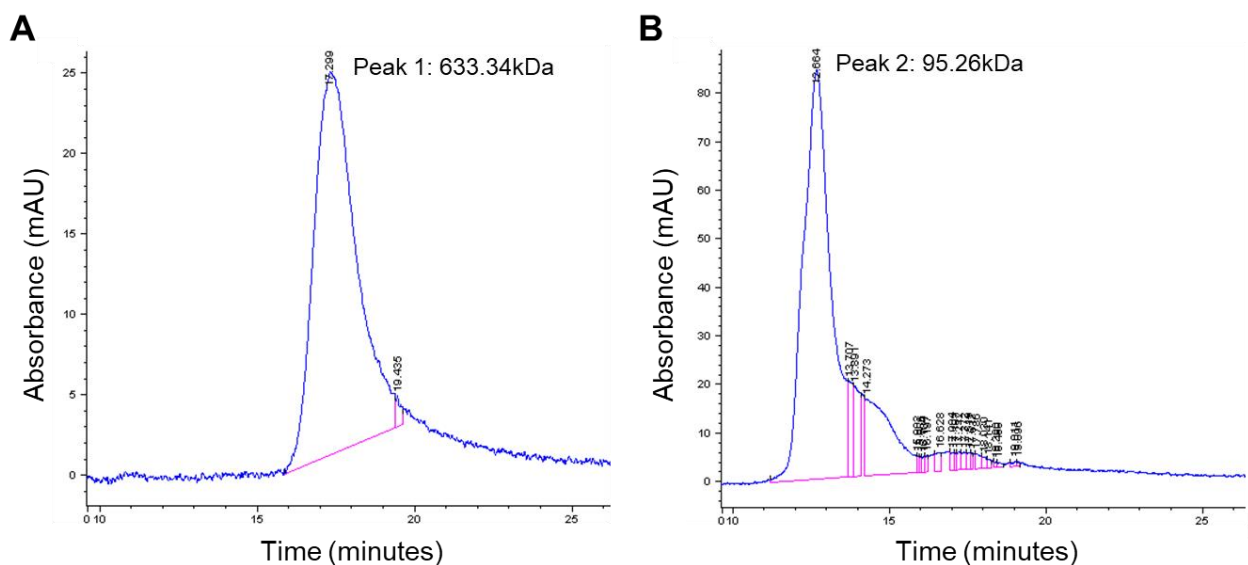
Figure 4.15: Analytical gel filtration of Peak 1 and 2 of mScl hFc size exclusion chromatography profile. A) Peak 1: 633.34 kDa. B) Peak 2: 95.26 kDa. Samples were analysed with a Superdex® 200 10/30 GL column and a Bio-Rad Gel Filtration standard was used to calculate peak sizes. Absorbance measured at 280 nm.
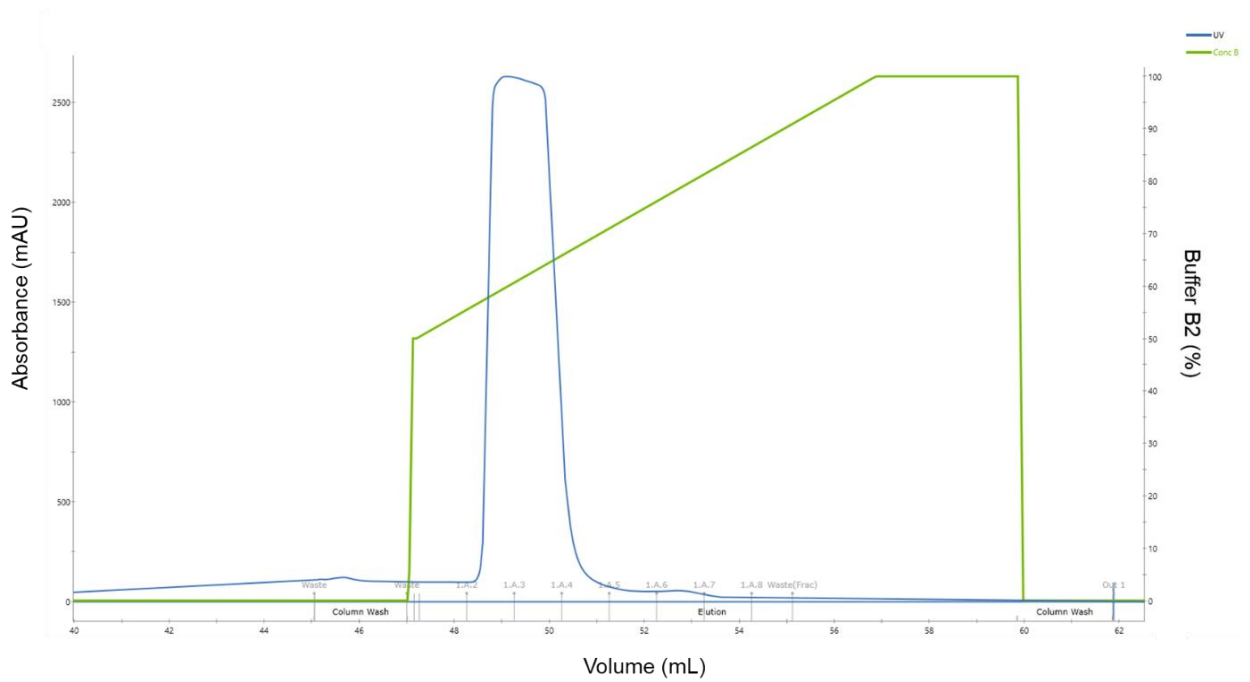
Figure 4.16: mScl hFc cation exchange chromatography elution profile. A representative chromatogram of mScl hFc purification by CEC. Buffer B2 (10 mM PBS, 1 M NaCl, pH 7.4) was increased linearly from 50% to 100% (green line) after approximately 47 mL elution to elute protein from a 1 mL Resource™ S column. A single peak (>2500 mAU) appeared after approximately 48.5 mL elution, at ~55% Buffer B2 (0.55M NaCl, 10 mM PBS, pH 7.4). Absorbance measured at 280 nm.
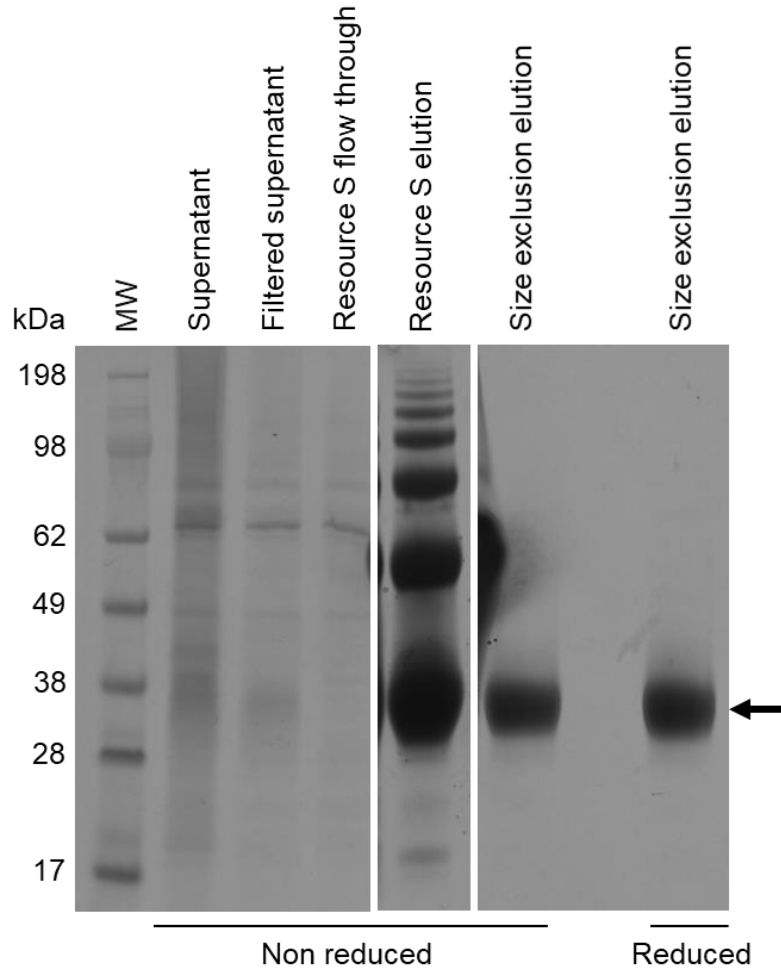
Figure 4.17: SDS-PAGE of the mScl purification process. Filtration removed some impurities from HEK293 culture supernatant. Wild type mScl appeared as an ~35 kDa band (black arrow) throughout purification process, under both non reducing and reducing conditions. No mScl was present in CEC (6 mL Resource™ S column) flow through. Resource™ S fractions were highly concentrated, and impurities were removed by SEC. Samples were analysed on NuPAGE™ 4-12% Bis-Tris Protein Gels.
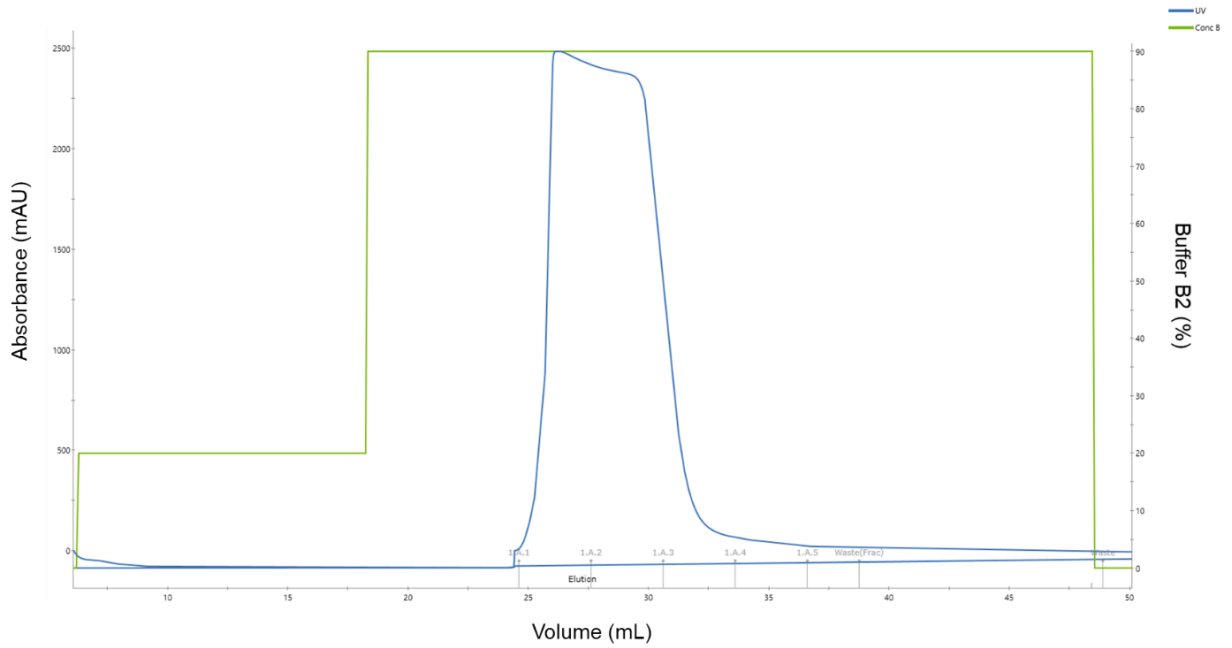
Figure 4.18: mScl cation exchange chromatography elution profile. A representative chromatogram of mScl purification by CEC. Buffer B1 (50mM MES, 500 mM NaCl, pH 6) was increased from 20% to 90% (green line) after approximately 18 mL to elute protein from a 6mL Resource™ S column. A single peak (>2500 mAU) was observed after approximately 25mL elution, at 90% Buffer B1. Absorbance measured at 280 nm.

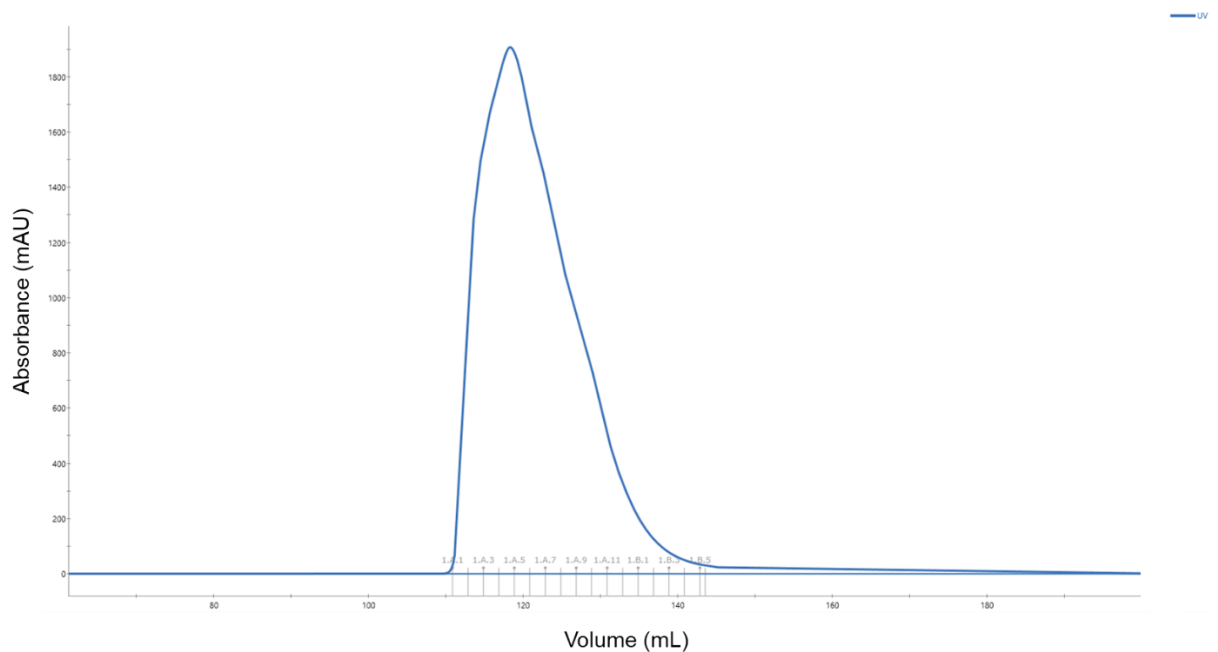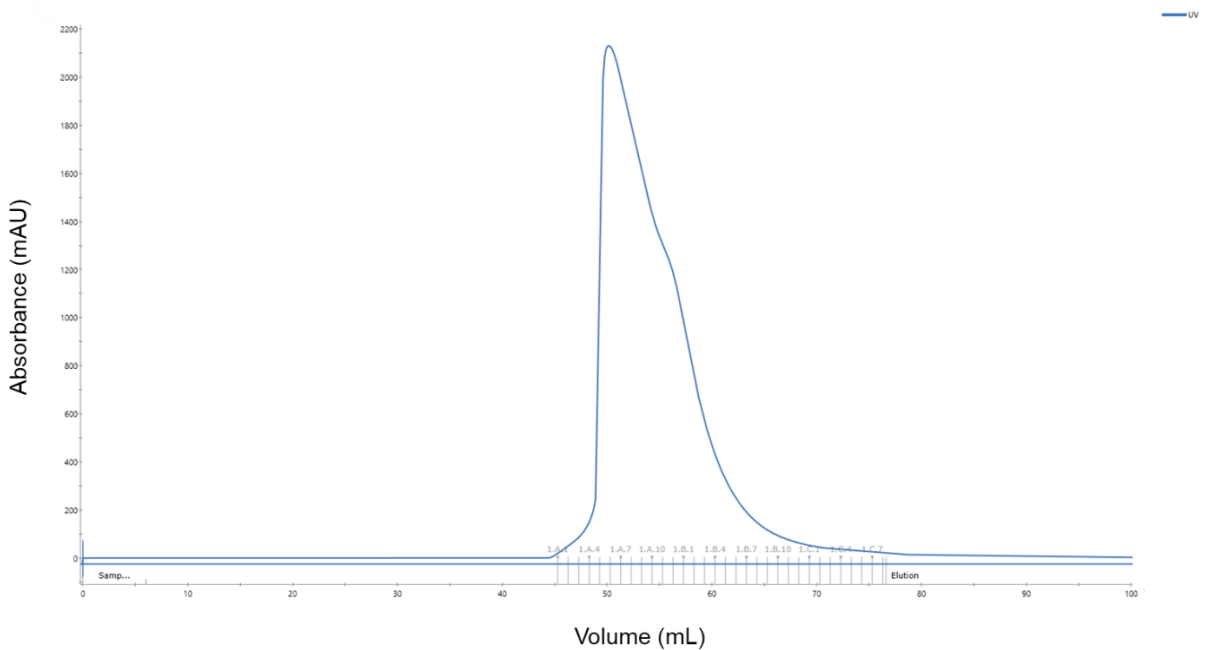**Figure 4.19: mScl size exclusion chromatography elution profile.** A representative chromatogram of mScl purification by SEC (HiLoad™ 26/600 Superdex™ 75 pg column). A single peak (~2200 mAU) appeared ~45 mL after elution was initiated. Absorbance measured at 280 nm.

4.1.3.2. Protein analysis

Recombinant mScl hFc PD (used as a representative for the dimeric Fc-fusion proteins) was analysed by deglycosylation and N-terminal sequencing to investigate the heterogenous nature of the purified fusion-protein samples.

PNGase F was used to deglycosylate 6.5 μg mScl hFc PD. Under reducing conditions, bands consisting of mScl hFc PD treated with PNGase F decreased in size, from ~55 kDa (non-PNGase F treated sample) to ~50 kDa (Figure 4.20), suggesting that glycosylation affected protein size. Identical bands (~35 kDa and ~50 kDa) were observed for protein treated with PNGase F under both reducing and non-reducing conditions.

For N-terminal sequencing, mScl hFc PD samples were transferred from SDS-PAGE to a PVDF membrane. An ~35 kDa band was excised from the dried PVDF membrane and N-terminal sequencing showed that a small proportion (~20%) of the mScl hFc PD protein (Table 4.1) was truncated at a site (AKANQAELEN) 176 amino acids downstream from the mScl N-terminus, towards the end of the mScl C-terminal flexible region fused to hFc, resulting in truncation of the majority of the mScl sequence from the captured mScl hFc PD material.

Figure 4.20: Deglycosylation of mScl hFc PD. Under reducing conditions mScl hFc PD treated with PNGase F decreased from ~55 kDa (non-PNGase F treated sample) to ~50 kDa (black arrows). Identical bands (~35 kDa and ~50 kDa) were observed for protein treated with PNGase F under both reducing and non-reducing conditions. Samples were analysed on a NuPAGE™ 4-12% Bis-Tris Protein Gel.

Table 4.1: mScl hFc PD amino acid sequence.

<u>qgwqafrndatevipglgeypeppppennqtmnraenggrpphhpydakdvseyscrelhytrfltdgp</u>
<u>crsakpvtelvcsgqcgparllpnaigrvkwwrpngpdfrcipdryraqrvqllcpggaaprsrkvrl</u>
<u>vasckckrltrfhnqselkdfgpetarpqkgrkprpgarg</u>**|AKANQAELEN**ayleepksadkthtcpp
cpapellggpsvflfppkpkdtlmisrtpevtcvvvdvshedpevkfnwyvdgvevhnaktkpreeqy
nstyrvvsvltvlhqdwlngkeykckvsnkalpapiektiskakgqprepqvytlppsrdeltknqvs
ltclvkgfypsdiavewesngqpennykttppvldsdgsfflyskltvdksrwqqgnvfscsvmheal
hnhytqkslslspgkdddddddd

Underlined: mScl sequence; Red line: cleavage point; Bold and capitals: dominant N-terminus.

4.1.3.3. Protein concentration and quality control

mScl hFc PD

A total of 107.7 mg mScl hFc PD was produced from 5 L HEK293 culture. The Nanodrop measured protein concentration (26 mg/mL) was corrected to 20.5 mg/mL using the correct extinction coefficient for mScl hFc PD (61288 $M^{-1}cm^{-1}$). Sample concentration was diluted to 4 mg/mL with PBS and 10% endotoxin free glycerol, and a final endotoxin test result was 1.025 EU/mg, below the 2 EU/mg maximum limit considered suitable for *in vitro* and *in vivo* studies.

mScl hFc

A total of 71.8 mg mScl hFc was collected from 5 L HEK293 culture. Protein concentration was 18 mg/mL (corrected using mScl hFc extinction coefficient: 61288 $M^{-1}cm^{-1}$), with an initial endotoxin level of 2.58 EU/mg, above the maximum limit of 2 EU/mg. CEC was repeated to remove excess endotoxin, with minimal to no protein loss. Protein sample was diluted to 4 mg/mL with PBS and 10% endotoxin free Glycerol and the final endotoxin level was 1.15 EU/mg, below the 2 EU/mg maximum limit.

mScl

A total of 98.8mg mScl was collected from 5 L HEK293 culture, with a concentration of 4.94 mg/mL (calculated using mScl extinction coefficient: 25690$M^{-1}cm^{-1}$). The initial endotoxin level for the collected sample was 5.75 EU/mg, above the 2 EU/mg maximum limit. Purification with a Proteus NoEndo™ S spin column reduced the endotoxin level from 5.26 EU/mg to 4.3 EU/mg, with an ~10% loss of protein (4.94 mg/mL to 4.4 mg/mL mScl). The endotoxin clean-up step was repeated with a new column and the final endotoxin result was 1.7 4EU/mg, with a final protein concentration of 4.2 mg/mL.

4.2.   *In vitro* functionality and efficacy of recombinant sclerostin constructs

Sclerostin normally exists as a monomer, therefore it was important to confirm that the dimeric hFc constructs did not impair the mScl activity *in vitro*. The recombinant mScl constructs' ability

to bind a fragment of the Wnt co-receptor LRP6 containing the first and second β-propellers of the receptor extracellular domain (LRP6-E1E2; Holdsworth et al., 2012) were thus tested *in vitro* to confirm the functional activity of the recombinant mScl proteins.

4.2.1. Isothermal titration calorimetry

Isothermal titration calorimetry (ITC) was performed to assess the binding interactions between label-free LRP6-E1E2 and the recombinant mScl protein, and to determine the dissociation constants (KD) of the recombinant constructs.

4.2.1.1. Buffer exchange

Protein loss was observed for all samples when performing buffer exchange and stock concentrations were reduced from 4.9, 4, 4.24 and 10.6 mg/mL to 3.76, 2.06, 2.8 and 7.9 mg/mL for mScl, mScl hFc, mScl hFc PD and LRP6-E1E2 respectively. Remaining recombinant mScl construct concentrations were however sufficient to set up 20 µM recombinant protein assay samples (above the minimum sample concentration of 10 µM that will typically produce a confidently measurable heat change for a 1:1 interaction), and LRP6-E1E2 concentration was kept constant at 111 µM.

4.2.1.2. ITC assays

mScl hFc PD

Raw ITC data showed that all experimental runs were successful and fitted data indicated that mScl hFc PD interacted dose dependently with LRP6-E1E2 (Figure 4.21). The average KD was 746±163 nM and average stoichiometry was 0.85 (Table 4.2), suggesting moderate interaction with LRP6-E1E2 and an approximately 1:1 (Scl:LRP6) binding ratio. All reactions proceeded exothermically.

mScl hFc

No anomalies were observed in the raw ITC data and fitted data demonstrated that dose dependent interaction occurred between mScl hFc and LRP6-E1E2 (Figure 4.21). The KD and average stoichiometry was 117±15 nM and 0.57 respectively (Table 4.2), suggesting strong interaction and a 1:2 (Scl:LRP6) binding ratio. All reactions were exothermic.

mScl

Raw ITC data indicated that all experimental runs were successful. However, a possible air bubble occurred during the third run and a single data point was excluded from the results (Figure 4.21). Data fitted to a single site binding model demonstrated dose dependent interaction between mScl and LRP6-E1E2, with an average KD of 147±75 nM (Table 4.2), indicating moderate to strong binding to the Wnt co-receptor (Figure 4.21). The average binding stoichiometry was 0.76 (a binding ratio of 1:1.5 (Scl:LRP6)) and the enthalpy of the reactions were negative, indicating that interactions proceeded exothermically.
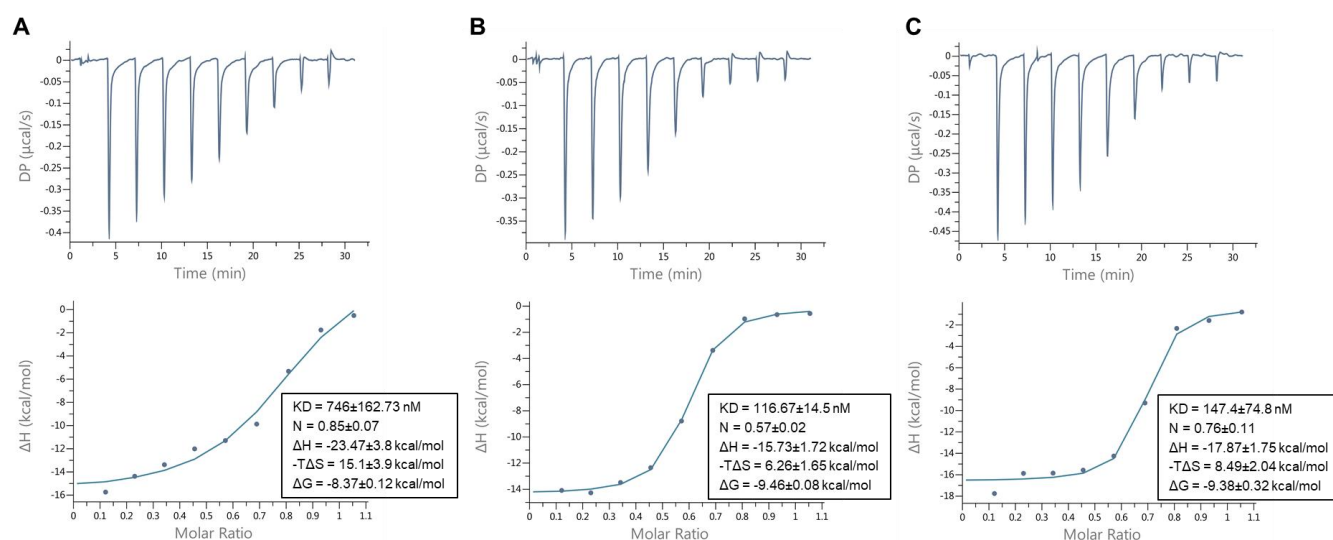
Figure 4.21: Recombinant mScl constructs binding to LRP6-E1E2 (ITC). A, B and C) Raw calorimetric data and representative experimental titration curves of mScl hFc PD (A), mScl hFc (B), and mScl (C) binding to LRP6-E1E2 are shown in the upper and lower panels, respectively. Average binding affinities and thermodynamic parameters for three replicates are shown next to the binding isotherms. KD: dissociation constant; N: stoichiometry; ΔH: change in enthalpy; −TΔS: temperature delta entropy; ΔG: change in Gibb's free energy.

Table 4.2: Recombinant mScl constructs binding to LRP6-E1E2 (ITC).

Protein	Run	mScl (µM)	LRP6-E1E2 (µM)	N (binding sites)	KD (nM)	ΔH (kcal/mol)	ΔG (kcal/mol)	-TΔS (kcal/mol)
mScl	1	20	111	0.79	139±63.5	-17.9±1.7	-9.36	8.56
mScl	2	20	111	0.64	77.2±41.4	-16.1±0.94	-9.70	6.42
mScl	3	20	111	0.85	226±147	-19.6±3.94	-9.07	10.50
mScl hFc	1	20	111	0.58	102±43.3	-17.6±0.89	-9.54	8.06
mScl hFc	2	20	111	0.55	131±19.7	-14.2±0.27	-9.39	4.83
mScl hFc	3	20	111	0.59	117±31.8	-15.4±0.52	-9.46	5.90
mScl hFc PD	1	20	111	0.86	931±457	-27.3±6.82	-8.23	19.10
mScl hFc PD	2	20	111	0.78	682±416	-19.7±4.39	-8.41	11.30
mScl hFc PD	3	20	111	0.91	625±377	-23.4±8.98	-8.46	14.90

N: stoichiometry; KD: dissociation constant; ΔH: change in enthalpy; ΔG: change in Gibb's free energy. −TΔS: temperature delta entropy.

4.2.2. Microscale thermophoresis

Microscale thermophoresis (MST) assays were performed to investigate the binding reactions between the recombinant mScl constructs and fluorescently labelled LRP6-E1E2 (LRP6-NT647).

4.2.2.1. Labelling LRP6-E1E2 with NT647

After labelling LRP6-E1E2 with NT647 fluorescent dye, unreacted NT647 dye was removed from the LRP6-NT647 sample using the provided purification column. The initial clear flow through contained DPBS only and was discarded, whereas the following 150 µL fraction had a blue colour, indicating presence of labelled protein. Measured absorbance of the blue fraction was A_{280} = 1.2 and A_{647} = 0.95, and the concentrations of LRP6-NT647 (A_{280}) and NT647 (A_{647}) were 6.7×10^{-6} M and 3.8×10^{-6} M respectively. The degree of labelling (DOL) was 0.57, within the acceptable range (between 0.5 and 1) recommended by the manufacturer guidelines.

4.2.2.2. Optimal LRP6-NT647 concentration

The raw fluorescence count for the 100, 50 and 25 nM serial LRP6-NT647 dilutions were above acceptable levels (>1500), whilst the ~300 fluorescence count for the 12.5 nM sample fell within the optimal range of 200 and 1500 signal counts stipulated by the manufacturer guidelines. Fixed 12.5 nM LRP6-NT647 concentrations were therefore maintained throughout the MST experiments to ensure that observed changes in fluorescence were not due to differences in LRP6-NT647 concentrations. Additionally, a symmetrical fluorescence peak indicated that no adsorption occurred between the 12.5 nM LRP6-NT647 sample and the capillary wall.

4.2.2.3. Sclerostin interaction with LRP6-NT647

Human Scl

An ~350 fluorescence signal count and symmetrical peaks were observed during a capillary check prior to the experimental assay, indicating no adsorption to the capillary walls (Figure 4.22). All capillary points (excluding two outliers) fell within a 10% range of the average initial fluorescence, demonstrating comparable capillary LRP6-NT647 concentrations. No protein aggregation was observed on MST traces and a single outlier trace, which correlated with a point that fell outside the 10% fluorescence range, was excluded from the data (Figure 4.22). A dose response curve was fitted to a one-site binding model using data from 1.5 seconds MST on-time, and the reported KD was <6nM (Table 4.3), indicating strong interaction between hScl and LRP6-E1E2. The signal to noise ratio of the MST run was 8.9, above the minimum recommended ratio of five (Nanotemper MO.Control software manual v03_2018-03-14).

mScl hFc PD

A capillary check done prior to the MST assay showed an ~300 fluorescence signal count for the 12 capillaries and symmetrical peaks indicated no adsorption to capillary walls (Figure 4.23). However, five out of 36 capillary points fell outside the 10% average initial intensity range. No protein aggregation occurred, as indicated by the smooth MST traces, and a single outlier MST trace was removed. Five seconds MST on-time data were used to fit a dose response curve and

the reported KD was <6nM (Table 4.3), indicating strong interaction between mScl hFc PD and LRP6-E1E2. The signal to noise ratio (6.9) was above the lower recommended limit.

mScl hFc

Symmetrical peaks observed after an initial capillary check showed no adsorption to capillary walls and the fluorescence signal count for the 12 capillaries were ~300, with 2 out of 36 capillary points falling outside the 10% average initial intensity range (Figure 4.24). For the experimental run, smooth MST traces indicated that no protein aggregate was present and showed a ligand concentration-dependent shift in magnitude (Figure 4.24). A dose response curve was fitted from five seconds MST on-time data and the calculated KD was <6nM (Table 4.3), demonstrating strong interaction between mScl hFc and LRP6-E1E2. The signal to noise ratio of 8.9 was above the recommended lowest limit.

mScl

A capillary check prior to the MST assay showed a fluorescence signal count of ~300, confirming similar LRP6-NT647 concentrations in the 12 capillaries, and only a single capillary point (out of 36) fell outside the 10% average initial intensity range (Figure 4.25). Symmetrical capillary shapes confirmed no adsorption to the capillary walls. Smooth experimental MST traces showed no protein aggregation and a single outlier trace that correlated with the single point outside the 10% signal range was removed from the data set (Figure 4.25). Binding constants were derived from a dose response curve fitted to five seconds MST on-time data and calculated KD was 30 nM (Table 4.3), indicating strong interaction between mScl and LRP6-E1E2. The signal to noise ratio (10.9) was above the recommended minimum ratio.

Table 4.3: Microscale thermophoresis parameters and results.

Ligand	Target	KD (nM)	KD Confidence (nM)	Response Amplitude	Target Conc. (nM)	Signal to Noise	Std. Error of Regression	Reduced χ^2	n
hScl	LRP6-NT647	2	2	6.9	12.5	8.9	0.9	1.3	4
mScl hFc PD	LRP6-NT647	0.54	1.23	19.8	12.5	6.9	3.2	4.3	3
mScl hFc	LRP6-NT647	2	2	25.3	12.5	8.9	3.1	2.9	3
mScl	LRP6-NT647	30	16	12.8	12.5	10.9	1.3	29.9	3

KD: dissociation constant; n: number of separate MST runs performed.
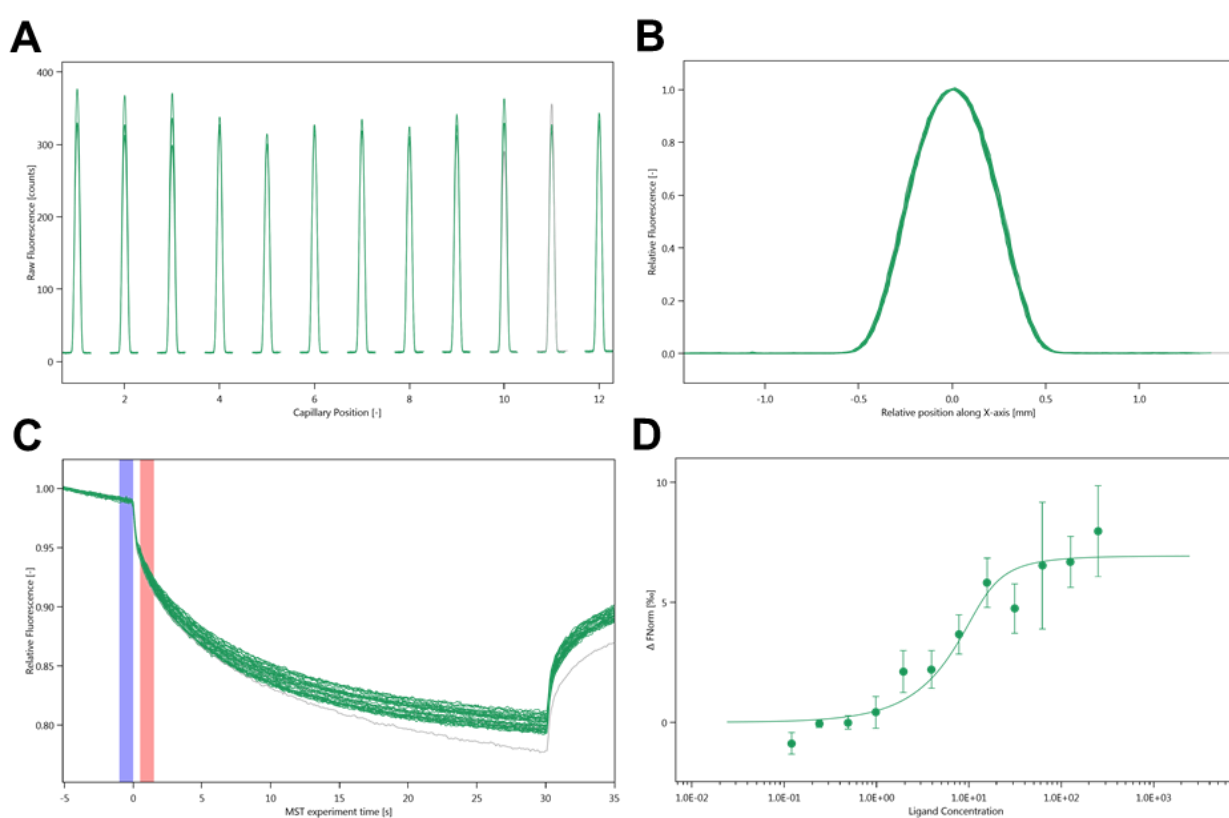
Figure 4.22: Interaction between hScl and fluorescently labelled LRP6-E1E2 (MST). A) Capillary Scan. B) LRP6-NT647 adsorption test. C) MST traces (12 capillaries) and D) dose-response curve. A single MST trace (grey trace) was excluded from the data (C). Gradual change in thermophoresis is plotted as ΔFnorm (F1/F0, where F1 and F0 correspond to average fluorescence values between red and blue areas) versus ligand concentration to yield a dose response curve that was fitted to a one-site binding model. Mean±SD of four independent experiments shown in (D). Experiments were carried out at 40% MST and 100% red LED excitation power.
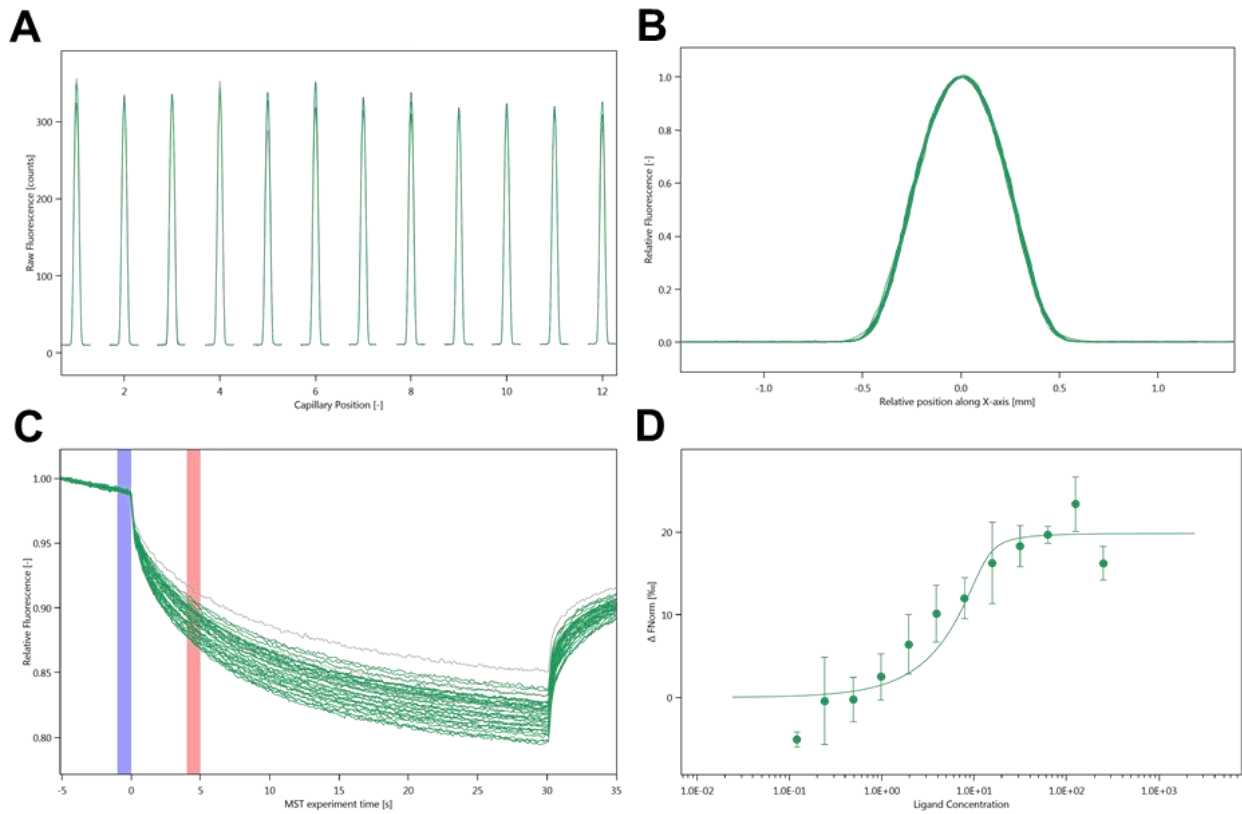
Figure 4.23: Interaction between mScl hFc PD and fluorescently labelled LRP6-E1E2 (MST). A) Capillary Scan. B) LRP6-NT647 adsorption test. C) MST traces (12 capillaries) and D) dose-response curve. A single MST trace (grey trace) was excluded from the data (C). Gradual change in thermophoresis is plotted as ΔFnorm (F1/F0, where F1 and F0 correspond to average fluorescence values between red and blue areas) versus ligand concentration to yield a dose response curve that was fitted to a one-site binding model. Mean±SD of three independent experiments shown in (D). Experiments were carried out at 40% MST and 100% red LED excitation power.
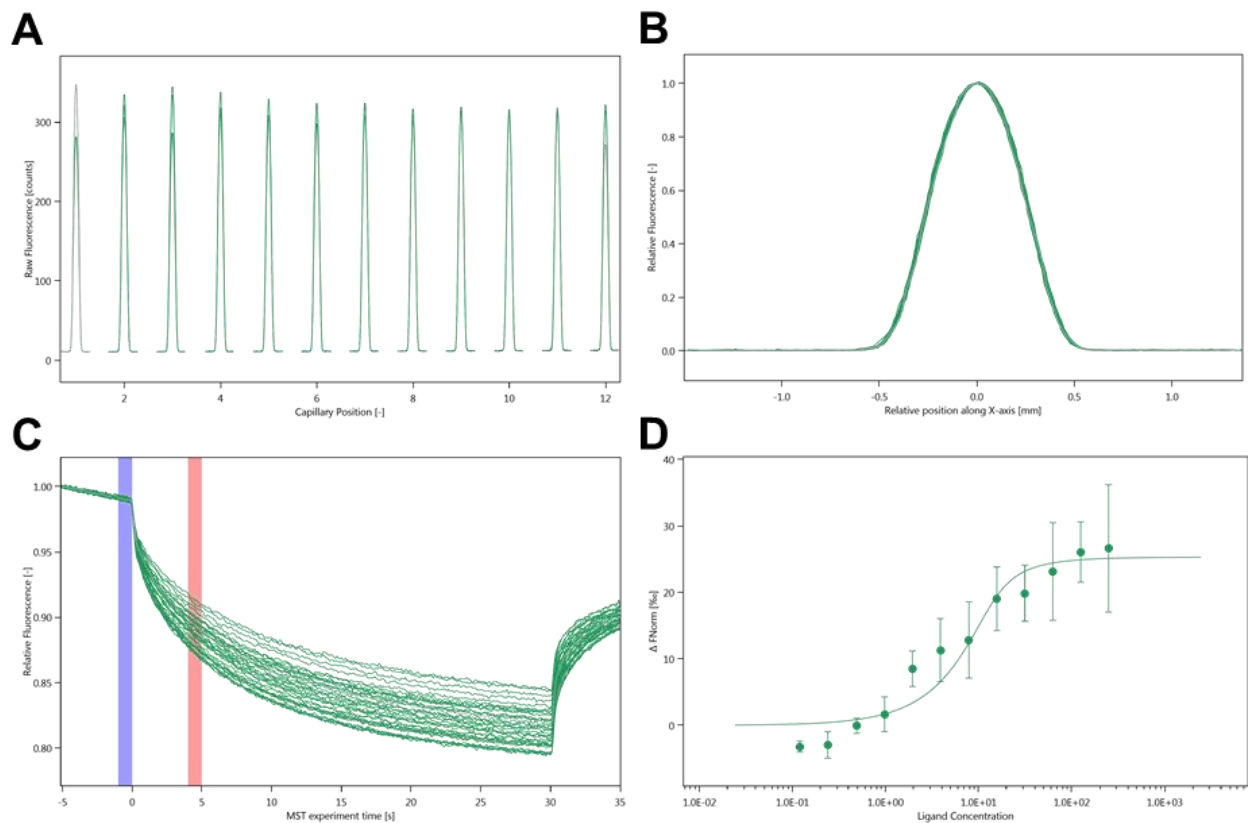
Figure 4.24: Interaction between mScl hFc and fluorescently labelled LRP6-E1E2 (MST). A) Capillary Scan. B) LRP6-NT647 adsorption test. C) MST traces (12 capillaries) and D) dose-response curve. Gradual change in thermophoresis is plotted as ΔFnorm (F1/F0, where F1 and F0 correspond to average fluorescence values between red and blue areas) versus ligand concentration to yield a dose response curve that was fitted to a one-site binding model. Mean±SD of three independent experiments shown in (D). Experiments were carried out at 40% MST and 100% red LED excitation power.
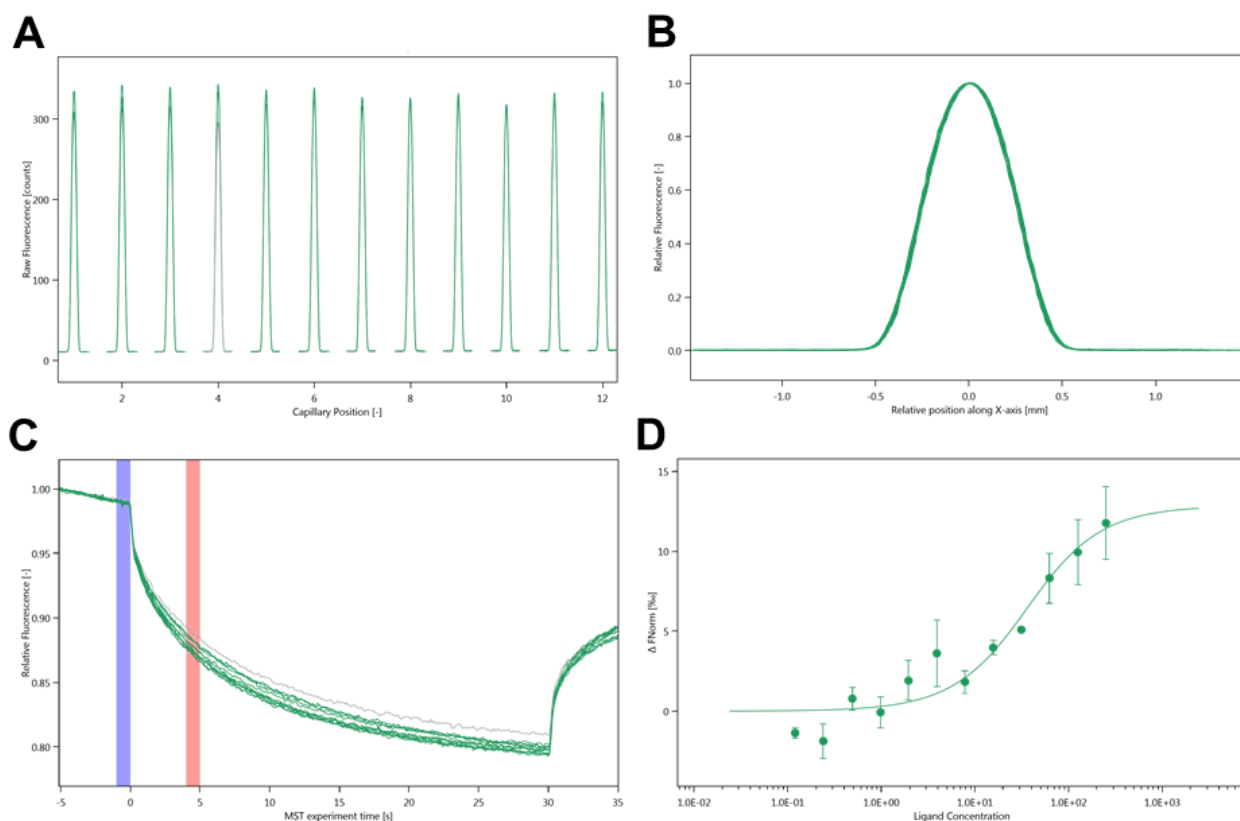
Figure 4.25: Interaction between mScl and fluorescently labelled LRP6-E1E2 (MST). A) Capillary Scan. B) LRP6-NT647 adsorption test. C) MST traces (12 capillaries) and D) dose-response curve. A single MST trace (grey trace) was excluded from the data (C). Gradual change in thermophoresis is plotted as ΔFnorm (F1/F0, where F1 and F0 correspond to average fluorescence values between red and blue areas) versus ligand concentration to yield a dose response curve that was fitted to a one-site binding model. Mean±SD of three independent experiments shown in (D). Experiments were carried out at 40% MST and 100% red LED excitation power.

4.2.3. Surface plasmon resonance

Surface plasmon resonance (SPR) competition assays were performed to provide additional evidence that the recombinant mScl constructs were functional and able to bind to LRP6.

4.2.3.1. Coating of SPR sensor surface

SPR sensor surface (carboxy methyl dextran coated) was coated with four different Scl preparations (Table 4.4), using standard ethyl(dimethylaminopropyl)-carbodiimide (EDC) and N-hydroxysuccinimide (NHS) chemistry for activation of the carboxy groups. The Scl preparations were added to the activated sensor in 10 mM sodium acetate pH 4 and unreacted groups were

blocked by addition of ethanolamine. Reference surfaces were prepared similarly, but without addition of 10 mM sodium acetate pH 4 Scl preparations.

Table 4.4: Amount of Scl bound to CM5 sensor surface.

Protein	Amount added to CM5 sensor (RU)
mScl	2164
hScl	3731
hScl (UCB)	1624

RU: resonance unit

4.2.3.2. Establishing Scl and LRP6-E1E2-Fc concentrations to be used

SPR sensorgrams of LRP6-E1E2-Fc passed over the Scl coated flow cells on the sensor surface, using HBS-EP pH 7.4 containing 1 mg/mL carboxymethyl-dextran (CM-dextran) as running buffer, showed that binding occurred with only one of the Scl preparations (hScl (UCB)) (Figure 4.26). Therefore, hScl (UCB) was used to coat the sensor for use in the competition assay. An aliquot of 100 nM LRP6-E1E2-Fc, determined from a dilution curve constructed with hScl (UCB) (Figure 4.27), was selected for use in the competition assay, as it gave a reasonable response (100 resonance units (RU), a measure of ligand concentration) and did not saturate the flow cell surfaces.
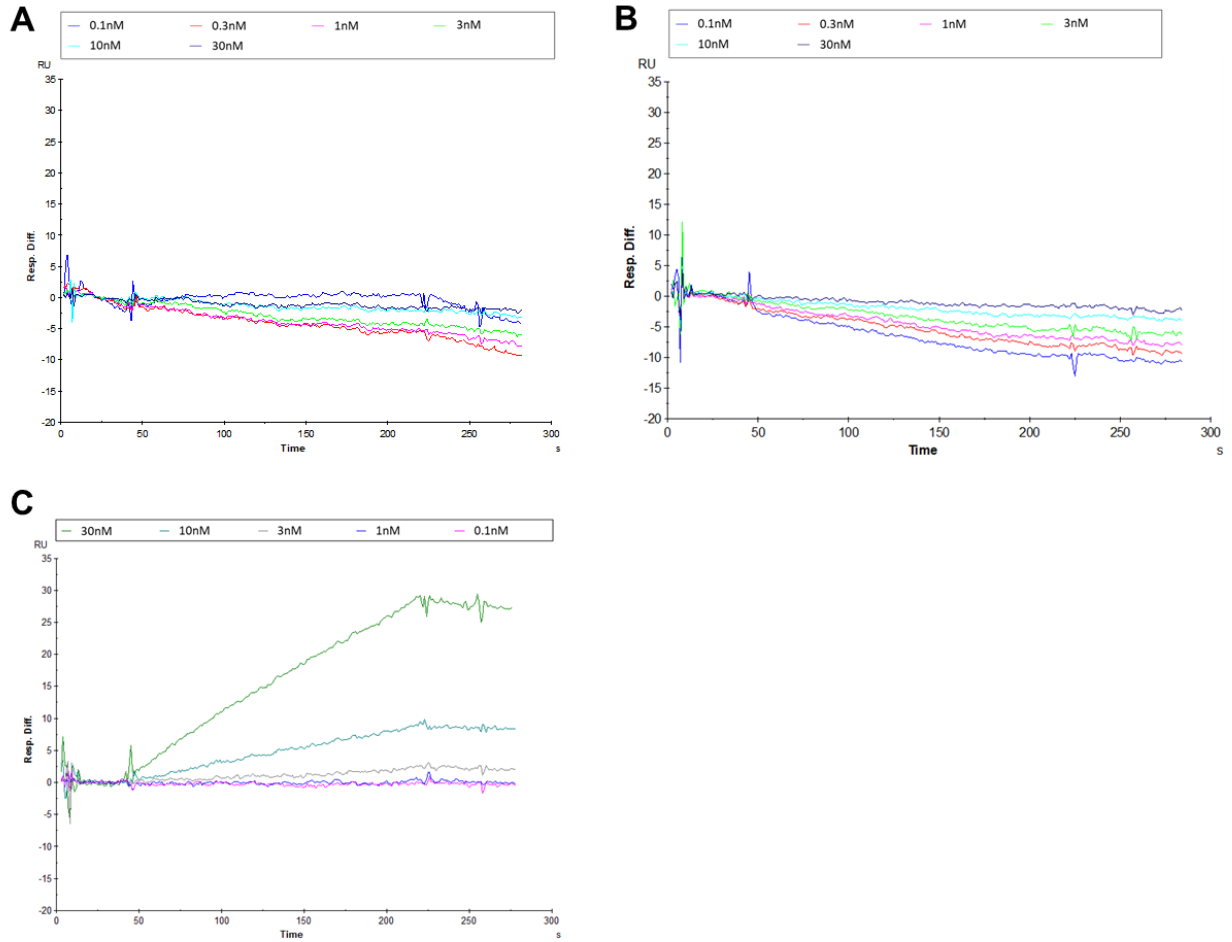
Figure 4.26: SPR sensorgrams of LRP6-E1E2-Fc interaction with test Scl preparations. Sensor surfaces were coated with A) mScl, B) hScl and C) hScl (UCB). LRP6-E1E2-Fc dilutions used were 30, 10, 3, 1, 0.3 and 0.1 nM. Running buffer was HBS-EP pH 7.4 containing 1 mg/mL CM-dextran.
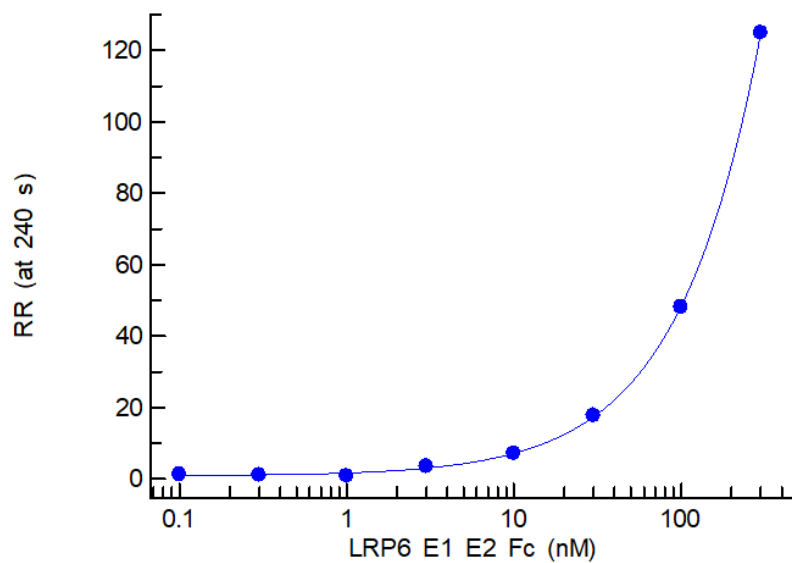
Figure 4.27: LRP6-E1E2-Fc SPR dilution curve. A dilution curve showing relative response rate at 240 s vs LRP6-E1E2-Fc concentration. LRP6-E1E2-Fc (300, 100, 30, 10, 3, 1, 0.3 and 0.1 nM) was passed over a sensor coated with hScl (UCB) (1624 RU). Running buffer was HBS-EP pH 7.4 containing 1 mg/mL CM-dextran.

4.2.3.3. SPR competition assay

A mixture of 100 nM LRP6-E1E2-Fc and Scl (hScl (UCB), mScl, mScl hFc or mScl hFc PD), at concentrations of 1000, 500, 250, 125, 62.5, 31.25, 15.63, 7.81 and 0 nM, were pre-incubated prior to injection onto the sensor. SPR sensorgrams showed association of unbound LRP6-E1E2-Fc with hScl (UCB) coated on the sensor surface (Figure 4.28). Weak transient associations of the recombinant Scl constructs, with the hScl (UCB) coated surface sensor, were observed at higher concentrations. The response at 260 seconds, a position with a stable signal and close to the maximum, was used to construct dilution curves for each recombinant Scl construct (Figure 4.29). The dilution curves showed that increasing the amount of Scl construct resulted in decreased LRP6-E1E2-Fc bound to the coated sensor, signifying interaction between the Scl constructs and LRP6-E1E2-Fc. The EC50 value for each Scl construct, determined from the midpoints of the dilution curves as the concentration of Scl halfway between the baseline and maximum response rate (Figure 4.29), was ~30 nM (Table 4.5), demonstrating that the constructs bound well to LRP6-E1E2-Fc. Little to no changes occurred on the sensor surface between SPR runs, as indicated by the small difference between the first and second hScl (UCB) SPR runs (Figure 4.29; Table 4.5).
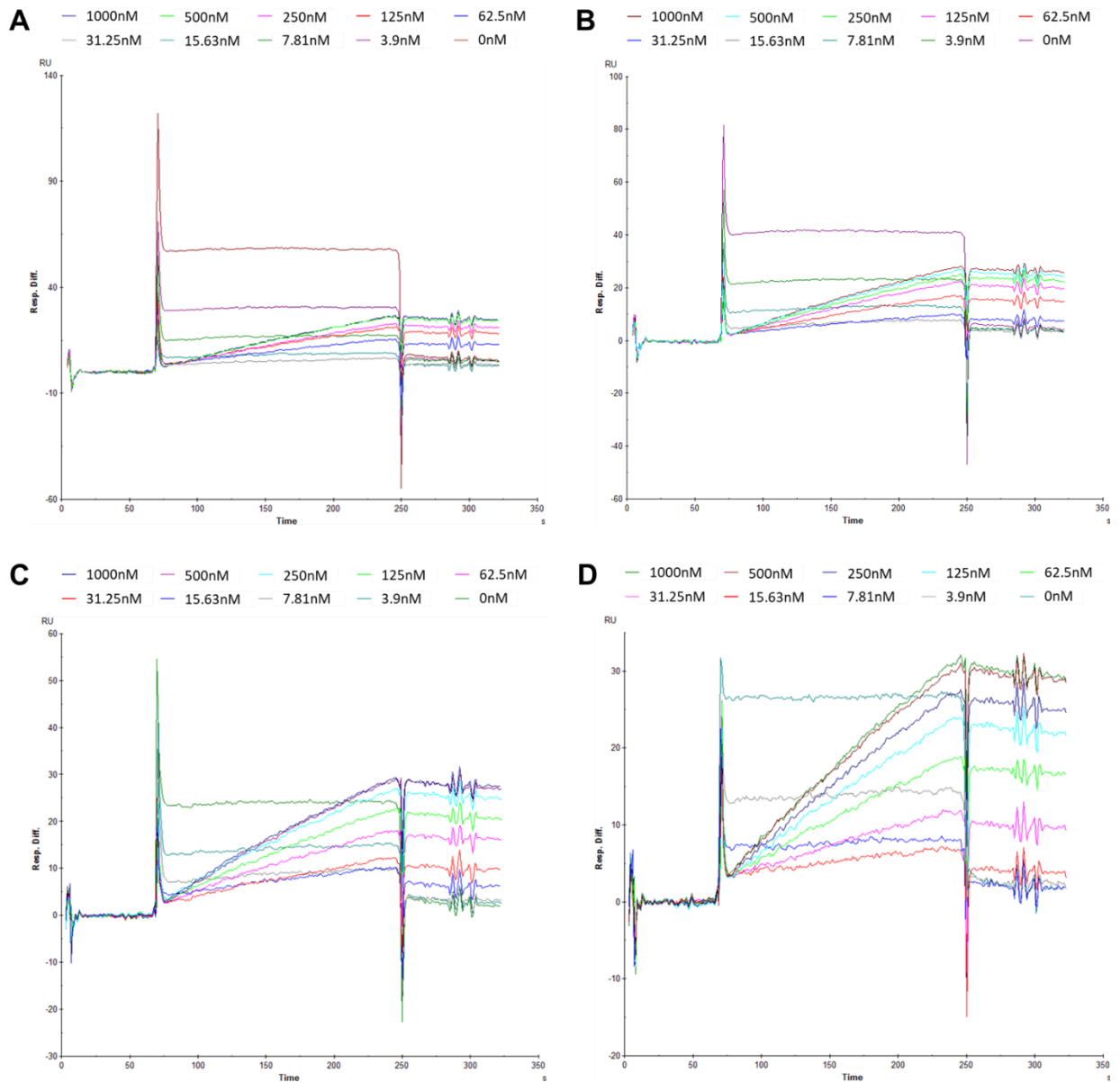
Figure 4.28: SPR sensorgrams of LRP6-E1E2-Fc with recombinant Scl constructs. Samples consisting of fixed 100 nM LRP6-E1E2-Fc and a range of A) mScl hFc PD, B) mScl hFc, C) mScl and D) hScl (UCB) dilutions (1000, 500, 250, 125, 62.5, 31.25, 15.63, 7.81 and 0 nM) were injected onto flow cells coated with hScl Pool 3. Running buffer was HBS-EP pH7.4 containing 1 mg/mL CM-dextran.
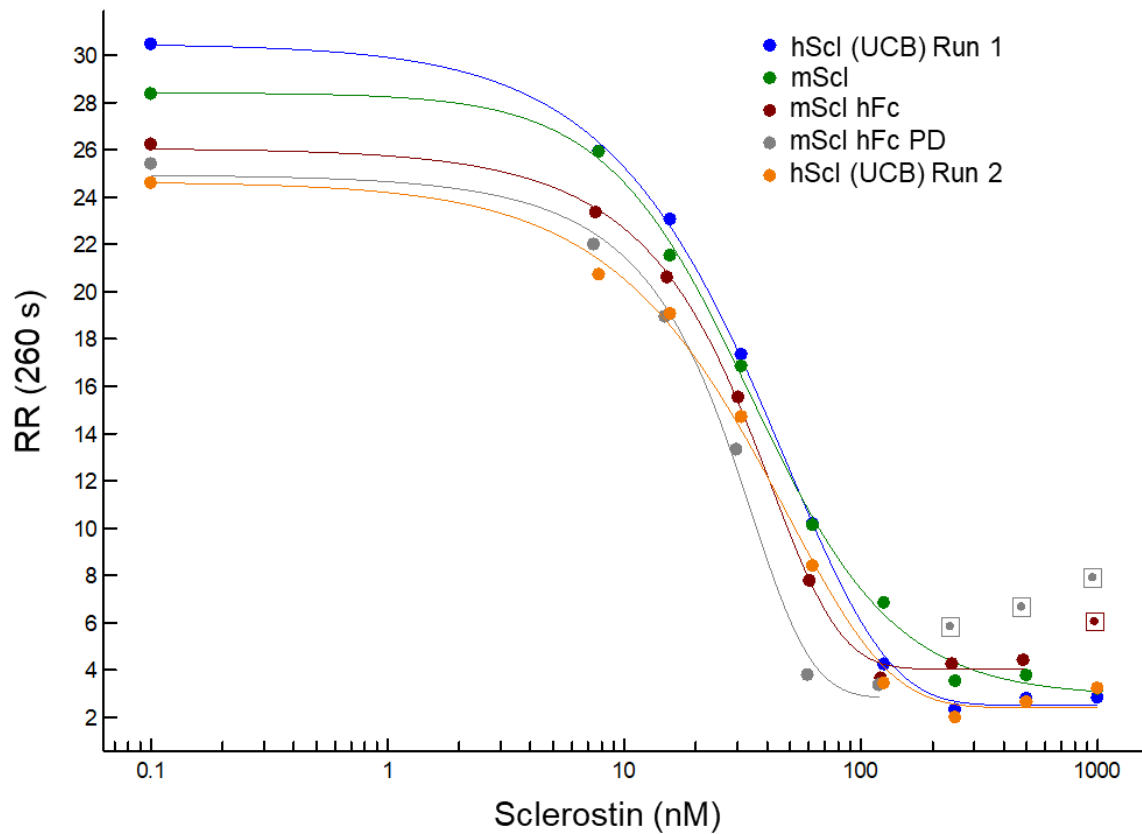
Figure 4.29: Combined SPR dilution curves of hScl (UCB), mScl, mScl hFc and mScl hFc PD. Recombinant Scl interaction with LRP6-E1E2-Fc. Relative response (RR) at 260 s was plotted against the concentration of recombinant Scl in solution. Points with squares were marked as outliers.

Table 4.5: EC50 of recombinant Scl constructs.

Protein	EC50 (nM)
mScl hFc PD	26.7
mScl hFc	31.1
mScl	33.9
hScl (UCB) Run 1	33.5
hScl (UCB) Run 2	33.9

4.2.4. Mineralised nodule formation assay

Sclerostin is a potent negative regulator of bone formation, therefore recombinant mScl protein's ability to inhibit this process was tested in three independent *in vitro* mineralised

nodule formation assays. MC3T3-E1 cells express LRP4/5/6 and have been shown to be sensitive to Scl, and were selected as an appropriate model for mineralisation (Wang et al., 1999, p. 3; Li et al., 2009).

4.2.4.1. Cell treatment and media change

For initial assays, 250 µL of 500 µL/well media were removed and replaced with 250 µL new sample solution every 2-3 days. Confluent MC3T3-E1 cells treated with osteogenic (OM) media (complete growth medium supplemented with 50 µg/mL ascorbate-2-phosphate and 10 mM β-glycerophosphate) differentiated into osteoblast-like cells and started to form mineralised nodules after approximately 11 days. Mineralisation was complete after approximately 14 days and covered ≤50% of the OM treated control wells. Cells were then fixed, as extended incubation time did not result in increased mineralisation. To improve mineralisation efficiency, all culture medium in subsequent assays was discarded and replaced with 500 µL new sample solution, resulting in a well-mineralised extracellular matrix that covered ≥90% of the plate surface after approximately nine days, consistent with previously reported results (Li et al., 2009).

4.2.4.2. Alizarin Red S staining

Mineralisation was visualised by Alizarin Red S staining (Figure 4.30). Considerable inhibition of mineralisation was observed in cells treated with 50 nM of the recombinant mScl proteins (Figure 4.30). This inhibition was reversed when co-treating cells with 230 nM Scl neutralising Ab (Anti-Scl Ab) or Fab and 50 nM recombinant mScl constructs. In contrast, little to no mineralisation was observed when co-treating cells with 50 nM recombinant mScl constructs and 230 nM of an irrelevant isotype control Ab (Control Ab) (Figure 4.30). Control wells treated with complete growth media (CT) showed no mineralisation, whilst complete mineralisation occurred when treating cells with OM, demonstrating the requirement of ascorbate-2-phosphate and β-glycerophosphate for cell differentiation and subsequent mineralised extra cellular matrix formation. Mineralisation of PBS controls was comparable to the OM treated control cells.

4.2.4.3. Cetylpyridinium chloride staining

Mineralisation was quantified following Alizarin Red S solubilisation with cetylpyridinium chloride (CPC) and corroborated the qualitative results (Figure 4.30 and 4.31). The three recombinant mScl proteins (50 nM) inhibited mineralisation substantially ($p < 0.0001$). Co-treatment with 230 nM Anti-Scl Ab confirmed that inhibition was due to functional inhibition by mScl since mineralisation was restored in the presence of Anti-Scl Ab ($p < 0.0001$) but was unaffected by the Control Ab ($p < 0.0001$) (Figure 4.31).
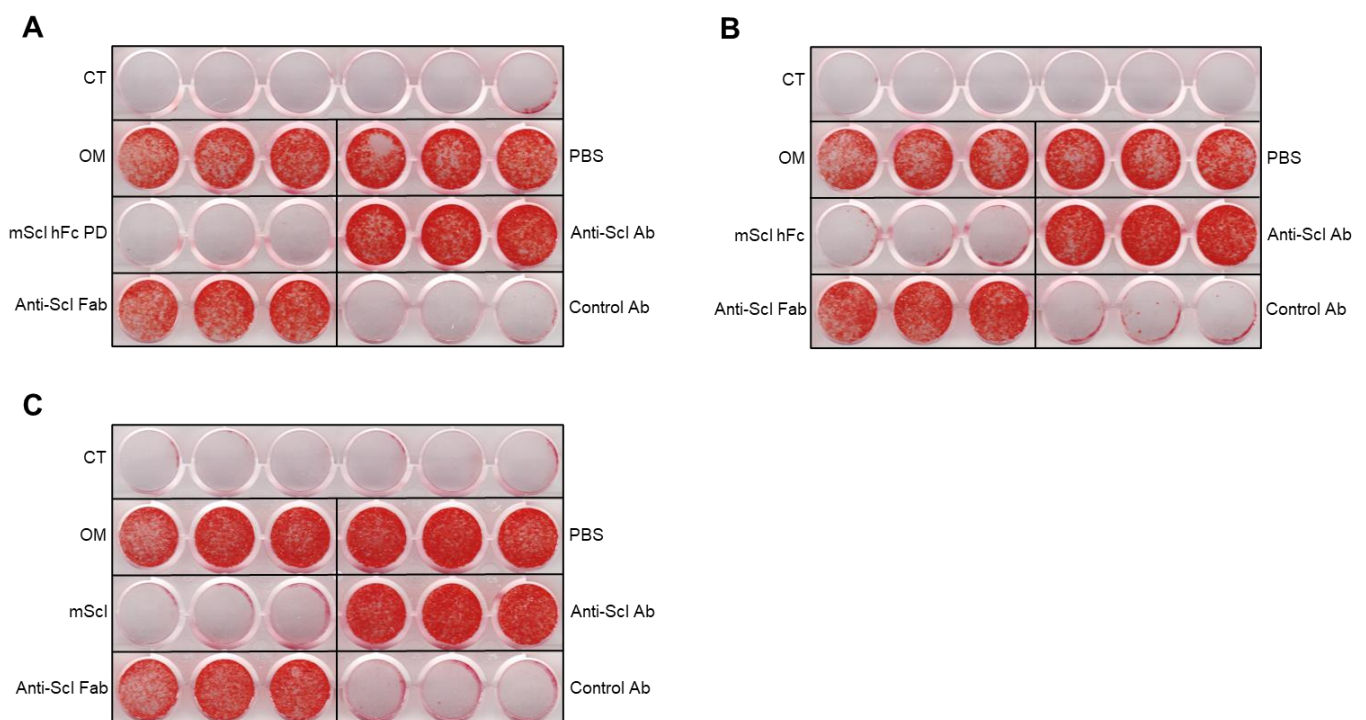
Figure 4.30: Recombinant mScl proteins inhibit osteoblast mineralisation *in vitro* (Alizarin Red S). MC3T3-E1 cells were cultured for nine days and mineral was stained with Alizarin Red S. A, B, C) Cells treated with mScl hFc PD (A), mScl hFc (B) and mScl (C). CT: complete growth media control; OM: osteogenic media control; PBS: osteogenic media with PBS vehicle control; mScl/mScl hFc/mScl hFc PD: osteogenic media with 50 nM recombinant mScl as indicated; Anti-Scl Ab or Fab: osteogenic media with 230 nM Anti-Scl Ab or Fab and 50 nM of indicated recombinant mScl; Control Ab: osteogenic media with 230 nM irrelevant isotype Control Ab and 50nM of indicated recombinant mScl. All conditions were set up in triplicate, except for CT (6 wells).
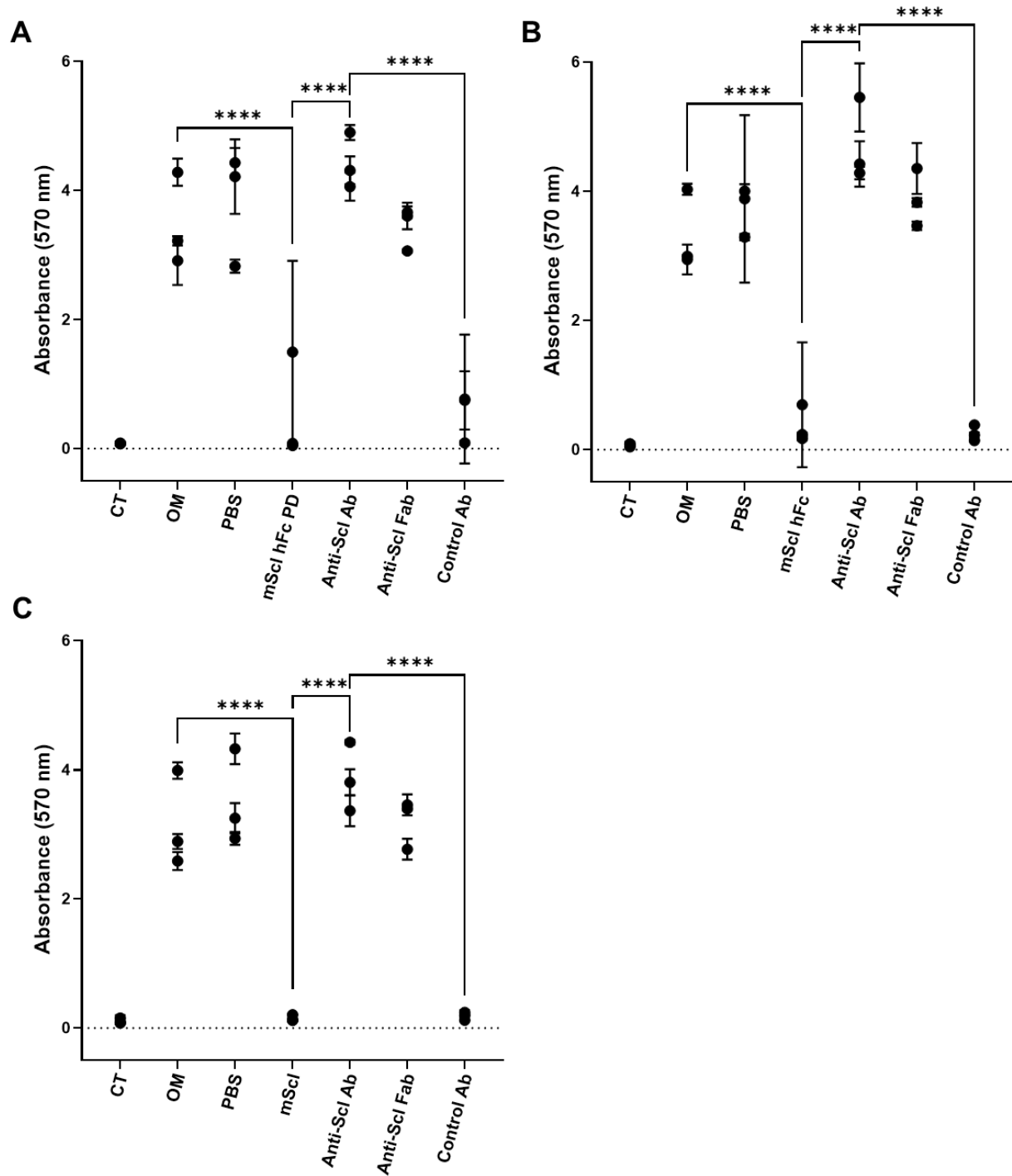
Figure 4.31: Recombinant mScl proteins inhibit osteoblast mineralisation *in vitro* (CPC). Alizarin Red S-stained mineral (Figure 4.30) was solubilised using CPC for quantitative analysis of mineralisation. Absorbance (570 nm) data from three independent experiments was plotted for the three recombinant mScl constructs: A) mScl hFc PD, B) mScl hFc and C) mScl. Mean±SD of triplicates (except CT, for which N=6) from three independent experiments shown. Two-way ANOVA was used for statistical analysis. **** p<0.0001.

4.3. *In vivo* biological activity and efficacy of recombinant sclerostin constructs

4.3.1 Single dose pharmacokinetic and pharmacodynamic study

The *in vivo* single dose pharmacokinetic and pharmacodynamic study was completed to determine the circulating half-life of the recombinant mScl constructs and assess any changes in serum P1NP levels.

4.3.1.1. Animals and blood sample collection

The pharmacokinetic (PK) properties of the recombinant mScl constructs were assessed in 7-10 week old C57/BL6 (wild type) and SOST$^{-/-}$ mice following a single intravenous (IV) administration of mScl hFc PD (10 mg/kg), mScl hFc (10 mg/kg), or a molar equivalent of mScl (4.4 mg/kg). All dose administrations were performed without incident. However, a male wild type (WT) mouse (28M) (Table 3.5) treated with mScl hFc PD suffered a convulsion and cardiac arrest five minutes post dose and died. This animal was replaced with a spare male mouse (028MR). At approximately 2.25 hours post dose, two additional WT males (034M and 037M) treated with mScl hFc PD were hunched, showed reduced activity, had erect fur and were cold to the touch. After 30 minutes the clinical signs for 34M and 37M had not improved and both animals were prostrate, lying on their sides with shallow breathing. Mouse 034M was deceased approximately three hours post dose, and no blood sample was collected. Mouse 37M was sacrificed at approximately 3.5 hours post dose due to clinical signs and a partial sample was collected. A male SOST$^{-/-}$ mouse (13M) (Table 3.6) and a WT male (039M) treated with mScl hFc PD were both hunched and cold to the touch and showed reduced activity at approximately 2.5 and 5.75 hours post dose, respectively. However, after 6.5 hours both animals showed no abnormalities. No abnormalities were detected in any of the other animals treated with mScl hFc PD. Additionally, no clinical signs were observed, and no unscheduled deaths occurred when dosing mice with wild type mScl or mScl hFc.

4.3.1.2. Pharmacokinetics of recombinant mScl proteins

Blood samples were collected at various intervals post-dose for LC-MS/MS quantification of the recombinant protein in serum. LC-MS/MS data for male and female groups were comparable, therefore pharmacokinetic analyses were based on genotype data only. Six samples were analysed at each time-point (N=6), except predose (N=24 in WT mice and N=15 in SOST$^{-/-}$ mice). No Scl was detected in predose samples, suggesting that Scl concentrations before dosing were below the limit of sensitivity of the LC-MS/MS assay. Wild type mScl had a very short half-life and was undetectable after five minutes post dose, whereas hFc fusion proteins were detectable at later time points (Figure 4.32; Table 4.6). Non-compartmental analyses (NCA) were therefore completed for mScl hFc and mScl hFc PD data only (Table 4.6). Recombinant mScl hFc had an extended half-life estimated at 1.5 and 1.8 days in WT and SOST$^{-/-}$ mice, respectively. Some abnormal distribution occurred at the beginning for mice treated with mScl hFc PD, however, this stabilised over time and serum half-life was estimated to be approximately 4 days in WT mice (Figure 4.32; Table 4.6). SOST$^{-/-}$ mice treated with mScl hFc PD had a flat profile (Figure 4.32), preventing accurate assessment of half-life and other pharmacokinetic parameters. The steady-state volume of distribution (V$_{ss}$) for WT and SOST$^{-/-}$ mice treated with mScl hFc was 1109.82 and 1390.67 mL/kg respectively and 483.19 mL/kg for WT mice treated with mScl hFc PD (Table 4.6). This was approximately 6.3x (mScl hFc) and 2.5x (mScl hFc PD) lower than the expected distribution (<200 mL/kg bodyweight) (Øie and Tozer, 1979; Smith et al., 2015). The maximum concentration (C$_{max}$) was also lower than expected (250 µg/mL expected for a 10 mg/kg dose): 11.98 and 9.8 µg/mL for WT and SOST$^{-/-}$ mice treated with mScl hFc (~23x lower) and 20.87 and 21.87 µg/mL for WT and SOST$^{-/-}$ mice treated with mScl hFc PD (~12x lower).

Compartmental pharmacokinetic analysis of IV administered mScl hFc fitted two-compartment kinetics, where the drug concentration decreases bi-exponentially as the sum of distribution and elimination of the construct (Figure 4.32). Data from this fitted model (mScl hFc PD data was excluded due to weak half-life estimation) was used to simulate a 42-day prediction model for a repeat dose pharmacology study with weekly subcutaneous (SC) dosing of 10 mg/kg hFc fusion proteins (Figure 4.32). In this model IV administration was switched to subcutaneous (SC), bioavailability was assumed to be 0.5 (50%) and absorption rate was assumed as 0.1/hour, giving a T$_{max}$ of ±1 day. The simulated peak and trough mScl hFc concentrations over 42 days were 2.8-3.2 µg/mL and 0.4-0.5 µg/mL respectively, indicating that the total serum concentration of mScl

hFc would increase slightly after each dose (every seven days) (Figure 4.32). The trough levels exceeded previously reported serum sclerostin levels (<100 pg/mL), therefore a weekly, SC administered 10 mg/kg mScl hFc or mScl hFc PD dose were considered suitable for use in the 42-day repeat dose pharmacology study (Jastrzebski et al., 2013; Shahnazari et al., 2012a; Tu et al., 2012).

Table 4.6: Pharmacokinetic summary of mScl, mScl hFc and mScl hFc PD.

Mouse strain	Treatment	Dose (mg/kg)	Route	Half-life	C_{max} (µg/mL)	AUC (hour*µg/mL)	Clearance (mL/day/kg)	V_{ss} (mL/kg)
WT	mScl	4.4	IV	≤5 mins	ND	ND	ND	ND
SOST^{-/-}	mScl	4.4	IV	≤5 mins	ND	ND	ND	ND
WT	mScl hFc	10	IV	1.5 days	12.0	273.8	529.8	1109.8
SOST^{-/-}	mScl hFc	10	IV	1.8 days	9.8	236.1	566.1	1390.7
WT	mScl hFc PD	10	IV	4 days	20.9	829.8	80.4	483.2
SOST^{-/-}	mScl hFc PD	10	IV	ND	21.9	577.1	ND	ND

Half-life was not well estimated for mScl hFc PD in SOST^{-/-} mice. IV: intravenous; C_{max}: maximum concentration; AUC: area under curve; V_{ss}: steady-state volume of distribution; ND: not determined.
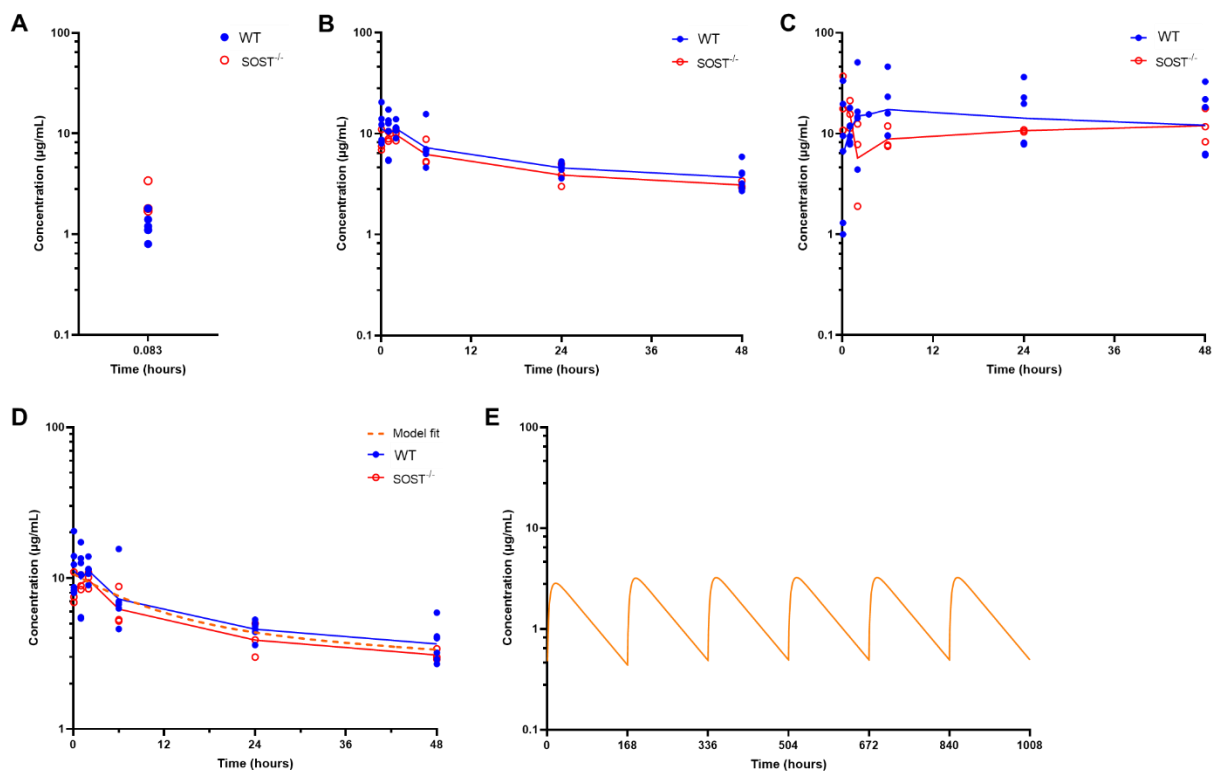
Figure 4.32: Single dose study pharmacokinetic profiles and models. A, B, and C) Pharmacokinetic (PK) profiles of mice (WT and SOST^{-/-}) treated with IV administered mScl (A), mScl hFc (B) and mScl hFc PD (C) respectively. D) Compartmental pharmacokinetic fitted model (orange dotted line) of IV administered mScl hFc. E) Prediction model of weekly SC administered 10 mg/mL mScl hFc dosage over 42 days, with 0.5 bioavailability and 0.1/hour absorption.

4.3.1.3. Effect of recombinant mScl on serum P1NP concentration

P1NP (a bone formation marker measured by ELISA) levels were expected to decrease if the recombinant mScl proteins inhibited bone formation (Vasikaran et al., 2011). All P1NP ELISAs were repeated once (Assay 1 and 2 in Figure 4.33), with serum samples from three mice per time point (individual serum samples were analysed in duplicate, thus N=6 per timepoint in a single assay). Almost all ELISAs fell within the acceptable range of the high and low concentration quality controls (3.3-6.6 and 30.3-56.4 ng/mL respectively), except for a single ELISA with samples from SOST^{-/-} mice treated with mScl hFc PD. In this case the high concentration control (68 ng/mL) fell outside the expected range and the data set was excluded from further analysis. Mice treated with native mScl and all predose samples were also excluded, as no change in P1NP concentrations were expected from mScl due to its short half-life, and predose sample volumes were insufficient for repeated ELISAs. No significant difference was observed in mean P1NP concentrations (N=12 per time point) of WT and SOST^{-/-} mice treated with mScl hFc or mScl hFc

PD (Figure 4.33). P1NP concentrations were near constant in WT mice treated with mScl hFc and no significant difference was seen between the beginning and end of the study. Variation in data points was possibly due to differences in two readings from the same serum sample and variation in the three mice assayed at specific timepoints. SOST$^{-/-}$ mice treated with mScl hFc showed two spikes, one at 72 and another at 168 hours, with only the 168-hour spike being significant (Figure 4.33). However, the P1NP levels in both cases decreased again after 24 hours and no significant difference in concentrations were observed between start and end of study. P1NP concentrations were stable in WT mice treated with mScl hFc PD and no significant differences were observed between 24 hours and 240 hours post dose. ELISA data from the first assay of SOST$^{-/-}$ mice treated with mScl hFc PD was discarded due to invalid controls (Figure 4.33). Results from the second ELISA showed some variation, but no difference between start and end of study was observed. Comparison between WT and SOST$^{-/-}$ treated mice demonstrated little to no difference between genotypes and overall results indicated that treatment with the recombinant mScl constructs resulted in no change in P1NP concentrations.
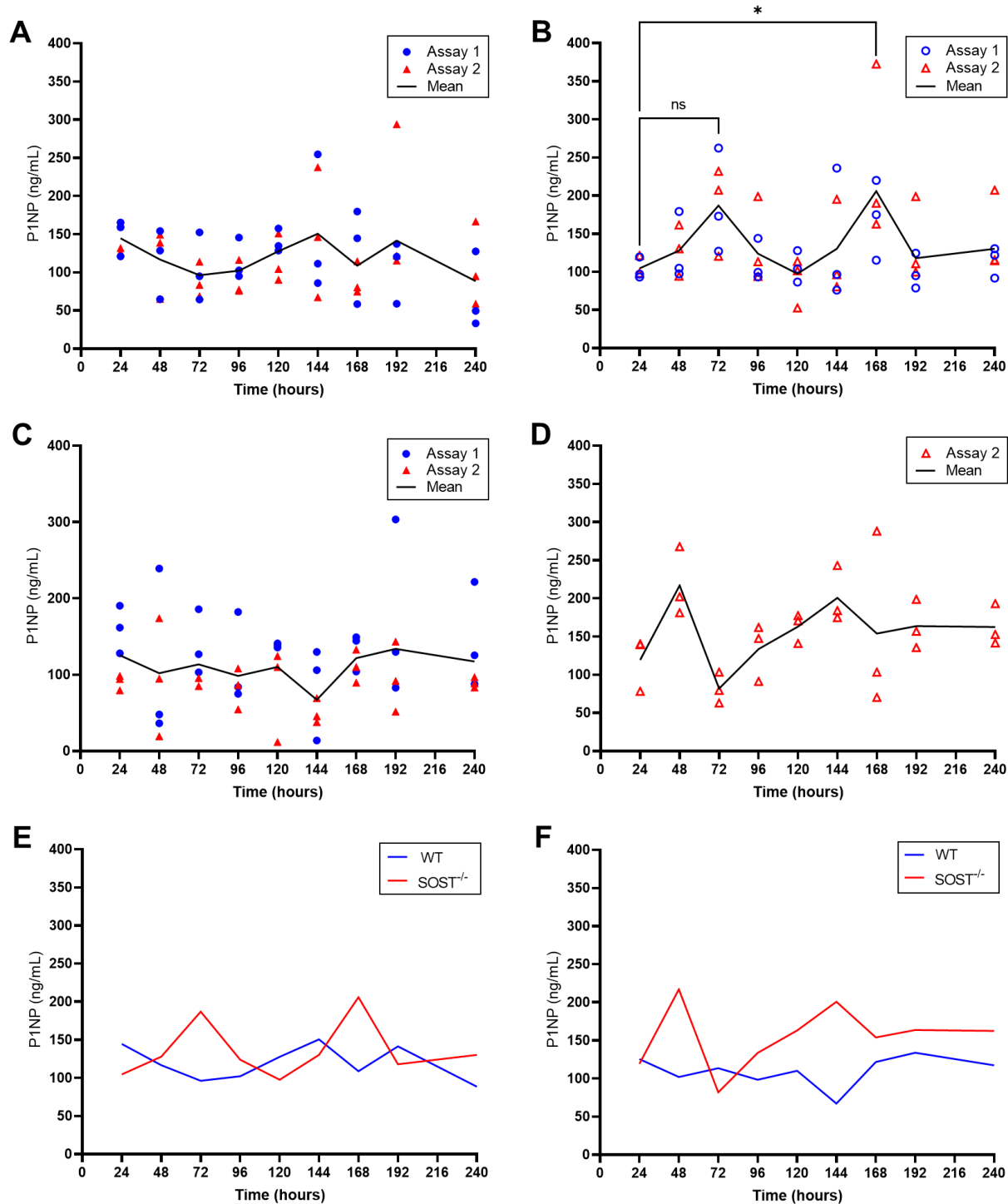
Figure 4.33: WT and SOST$^{-/-}$ P1NP levels in the single dose pharmacokinetic study. A and B) P1NP concentrations of WT (A) and SOST$^{-/-}$ (B) mice treated with mScl hFc. C and D) P1NP concentrations of WT (C) and SOST$^{-/-}$ (D) mice treated with mScl hFc PD. For each assay, P1NP concentration of three independent mice was measured at each time point (N=3) (blue dots and red triangles). Black line depicts mean of all data points (N=6) at each time point (except for (D), where N=3). E and F) Mean comparison of WT (blue line) and SOST$^{-/-}$ (red line) mice treated with mScl hFc (E) and mScl hFc PD (F). Ordinary one-way ANOVA was performed for statistical analysis: ns=non-significant; $p<0.05$.

4.3.2. Pharmacology study

4.3.2.1. Body weight and whole body bone mineral density

All dose administrations (4.4 mg/kg mScl dose administered six days a week and 10 mg/kg mScl hFc and mScl hFc PD doses administered once a week for six weeks) were performed without incident and no adverse effects were observed in any of the treated mice. Body weights of 7-10 week old female WT and SOST$^{-/-}$ mice were comparable for both genotypes throughout the 6-week study (Figure 4.34). Weights ranged from 18-23 g and as expected for growing mice, increased gradually over the experimental period. Whole body areal bone mineral density (aBMD), vertebral BMD, and femoral BMD, measured by dual-energy X-ray absorptiometry (DXA), was higher in SOST$^{-/-}$ mice than WT mice throughout the study (aBMD: 80±9 g/cm^2 (WT) vs 100±10 g/cm^2 (SOST$^{-/-}$), p<0.0001; vertebral BMD: 81±17 g/cm^2 vs 107±22 g/cm^2, p<0.0001; femoral BMD: 76±12 g/cm^2 vs 97±1710 g/cm^2, p<0.0001) (Figure 4.35), consistent with the previously reported phenotype (Li et al., 2008). None of these parameters were however affected by the recombinant mScl proteins (compared with Vehicle treated controls) (Figure 4.35).
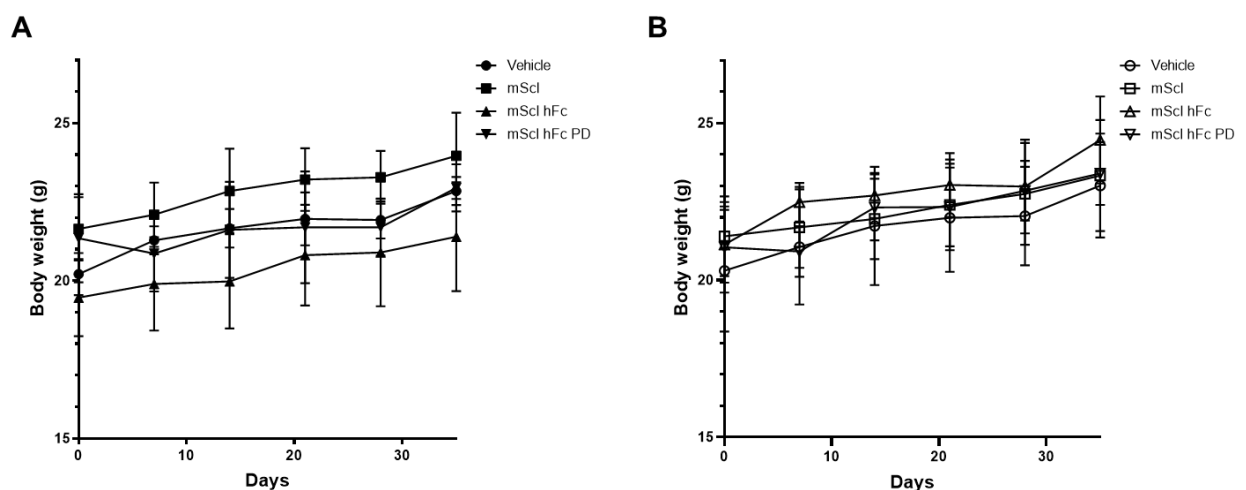
Figure 4.34: Body weights of WT and SOST$^{-/-}$ mice groups. A and B) Body weights of 7-10 week old female WT (A) and SOST$^{-/-}$ (B) mice treated with vehicle, mScl, mScl hFc and mScl hFc PD.
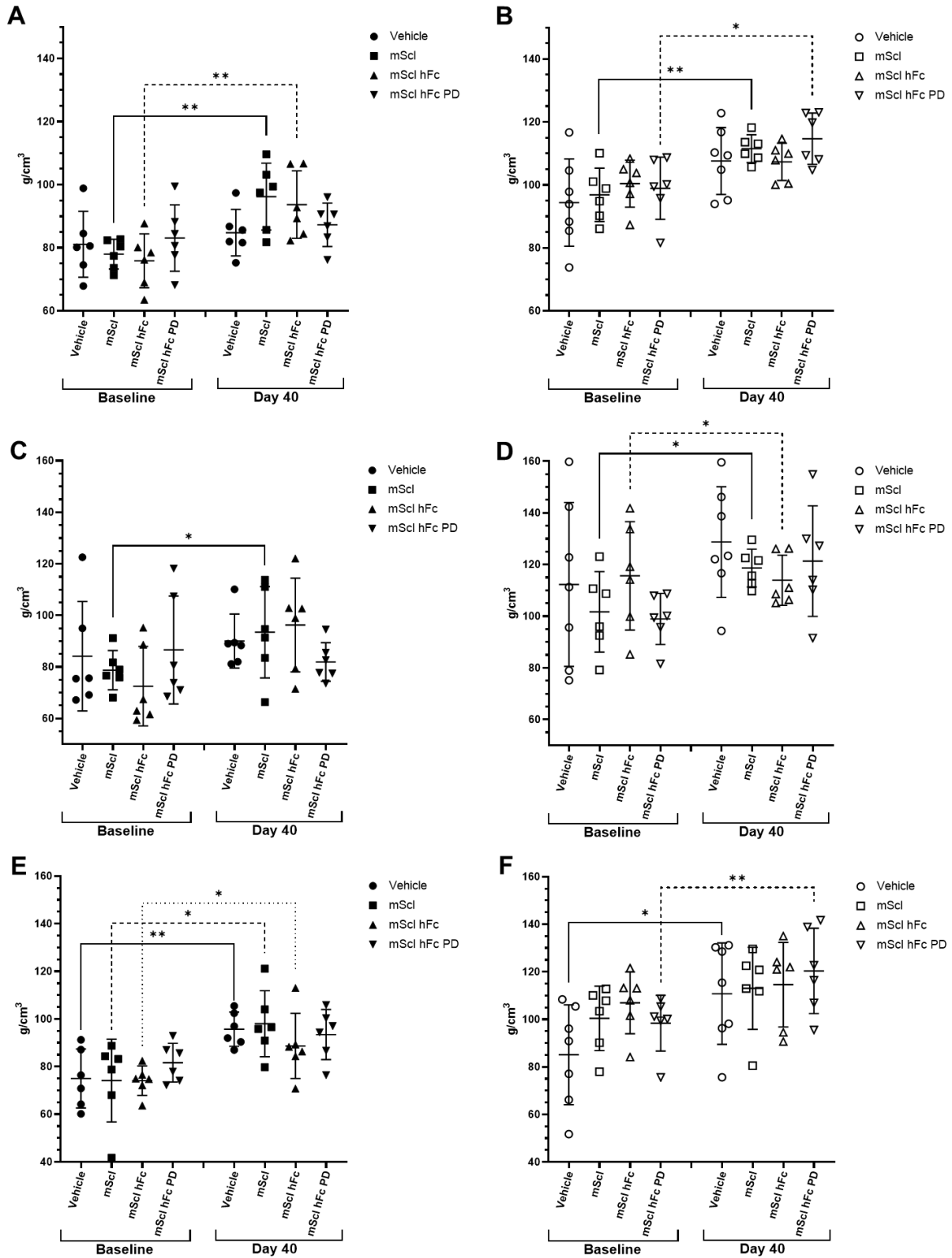
Figure 4.35: Whole body areal, vertebral, and femoral BMD of WT and SOST^{-/-} mice groups. A and B) Whole body areal BMD of WT (A) and SOST[-/-](B) mice measured by DXA at Baseline and at Day 40, which was just prior to the end of the study. C and D) Vertebral BMD of WT (C) and SOST[-/-](D) mice. E and F) Femoral BMD of WT (E) and SOST[-/-](F) mice. Mean±SD from each group shown (N=6 mice/group except for SOST^{-/-} vehicle N=7). Unpaired t-test was performed for statistical analysis of baseline vs Day 40 comparison: ns=non-significant; *p<0.05; **p<0.01.

4.3.2.2. Pharmacokinetics and pharmacodynamics of recombinant mScl

Pharmacokinetics

Fitted LC-MS/MS results were consistent with one compartment kinetics and compartmental analysis showed an estimated half-life of 1.6 days and 2.6 days for mScl hFc and mScl hFc PD respectively. Volume of distribution (V_{ss}) was 497 mL/kg for mScl hFc and 188 mL/kg for mScl hFc PD and, allowing for loss due to SC route of administration, was consistent with the distribution seen in the single dose PK study. Serum mScl hFc concentration was lower than mScl hFc PD throughout the study. WT and SOST$^{-/-}$ serum mScl hFc (μg/mL) were however comparable and stayed constant after each dose, whilst serum mScl hFc PD differed slightly between WT and SOST$^{-/-}$ mice, and increased with each dose (difference between Day 0 and Day 42 serum mScl hFc PD concentrations was approximately 7 μg/mL) (Figure 4.36). Exposure was better than predicted, with comparable trough values, but higher peak values for fitted mScl hFc compared to the simulated 42-day prediction model from the single dose PK study. This difference is likely due to the switch from IV to SC administration, extrapolated single dose study modelling data, and parameters used for the 42-day simulation (a more conservative 50% bioavailability was used for the prediction algorithm).
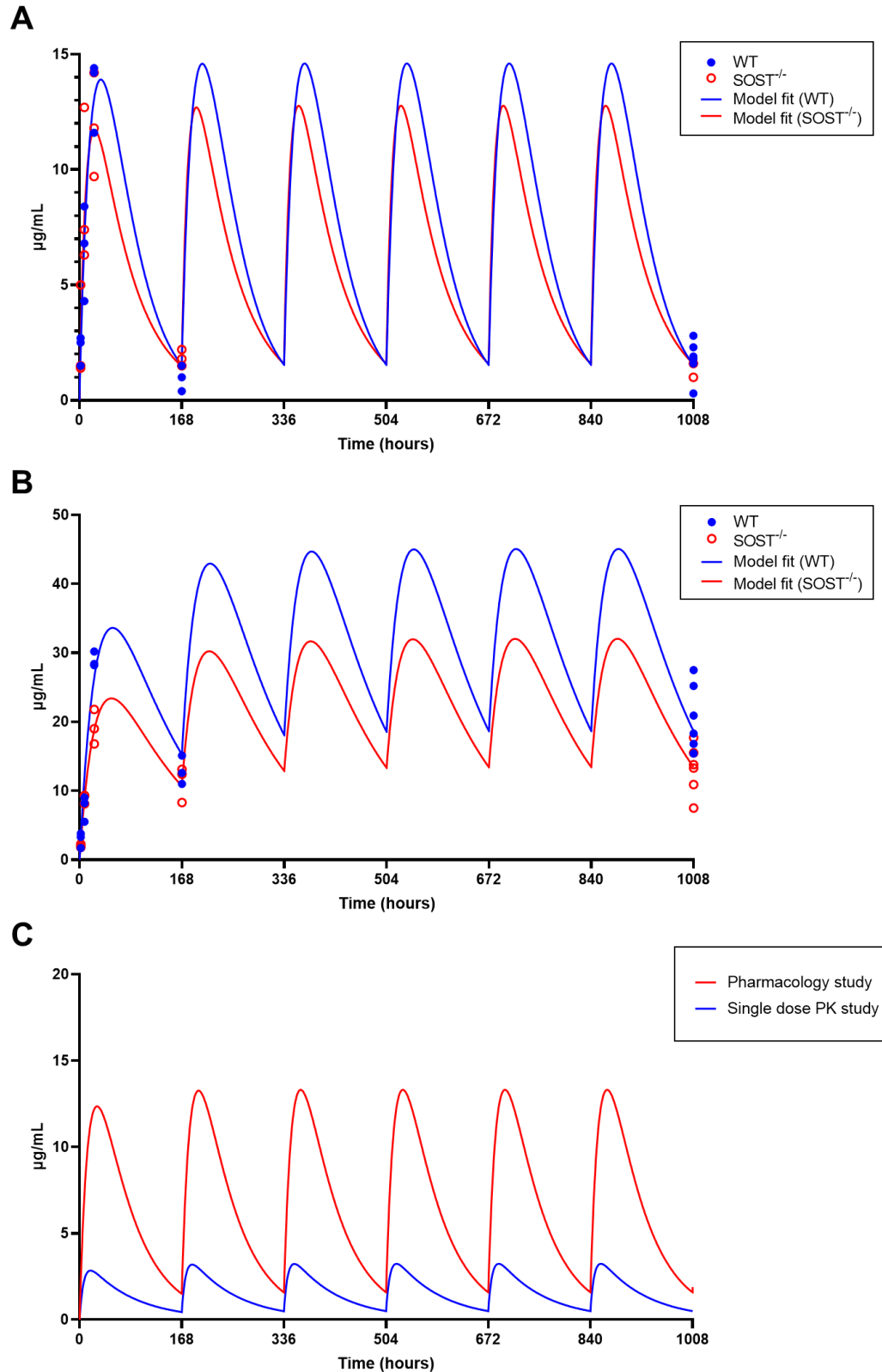
Figure 4.36: Multidose pharmacology study pharmacokinetic profiles and models. A and B) mScl hFc (A) and mScl hFc PD (B) fitted models. Models were fitted for mScl hFc and mScl hFC PD data from WT (blue lines) and SOST^{-/-} (red lines) mice, using data from predose (0 hours), Day 7 (168 hours) and Day 42 (1008 hours) time points. C) Comparison of pharmacology study mScl hFc fitted model (red line) and the mScl hFc simulated 42-day prediction model from the single dose PK study (blue line).

Effect on P1NP concentration

P1NP ELISA kit accuracy was determined using kit standards and controls (low and high control ranges were 3.6-6.6 ng/mL and 30.3-56.4 ng/mL respectively). A single ELISA plate, containing Vehicle and mScl samples from WT mice, fell outside the high concentration control (71.12 ng/mL) and were excluded from analysis. ELISAs showed that treatment with recombinant mScl did not reduce serum P1NP (Figure 4.37). However, a small, but significant reduction in P1NP concentration was observed at the 24-hour point in SOST^{-/-} mice treated with wild type mScl ($p<0.05$). The final P1NP concentration was however similar to the Vehicle control, indicating no effective change in P1NP levels from start to end of study (Figure 4.37).
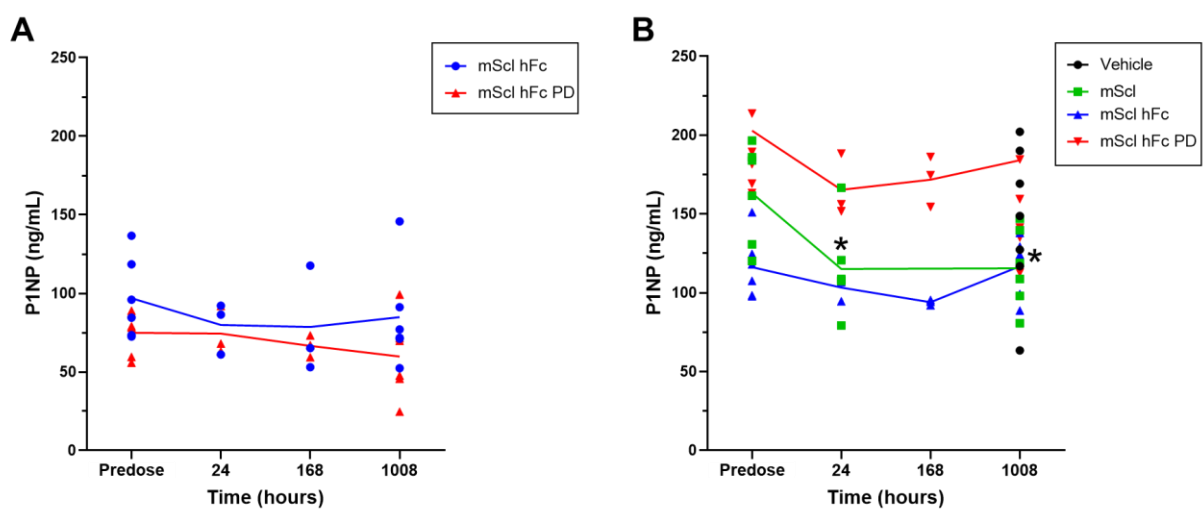
Figure 4.37: WT and SOST^{-/-} P1NP levels in the multidose pharmacology study. A) P1NP concentrations of WT mice treated with mScl hFc (blue line) and mScl hFc PD (red line). B) P1NP concentrations of SOST^{-/-} mice treated with Vehicle, mScl (green line), mScl hFc (blue line) and mScl hFc PD (red line). N=6 at each time point, except SOST^{-/-} Vehicle N=7. Vehicle data was collected at Day 42 only. Unpaired t-test was performed for statistical analysis of mScl (Predose vs 24 hour), and mScl vs Vehicle (Day 42) comparison (*$p<0.05$).

4.3.2.3. Anti-drug antibody assays

Anti-drug antibody (ADA) assays were performed with biotinylated and SULFO TAG labelled native mScl (for samples from mScl treated mice) and mScl hFc PD (for samples from mScl hFc or mScl hFc PD treated mice). Outlier ADA concentrations were seen in WT mice treated with mScl hFc (2/6 mice) and mScl hFc PD (1/6 mice), and SOST^{-/-} mice treated with mScl (2/6 mice), mScl hFc (2/6 mice) and mScl hFc PD (1/6 mice) (4.38). Outliers were selected for additional ADA confirmation assays, where selected samples were saturated with 100 µg/mL mScl or mScl hFc to suppress ADA signal. Lack of ADA signal in mScl saturated samples suggest that selected WT and SOST^{-/-} samples contained ADAs against the recombinant mScl constructs. For some mScl hFc treated mice, ADA signal was observed when oversaturating samples with

mScl, whilst no ADA signal was seen for samples oversaturated with mScl hFc, suggesting that ADAs target the hFc region of the mScl hFc construct. ADAs appeared to target both the mScl and hFc PD regions of mScl hFc PD in WT and SOST$^{-/-}$ samples. These ADA confirmation assays show that all selected outlier samples contained ADAs, confirming that approximately one to two out of six mice developed ADAs against the recombinant Scl constructs. It is however unclear how much an effect these ADAs would have on drug efficacy.
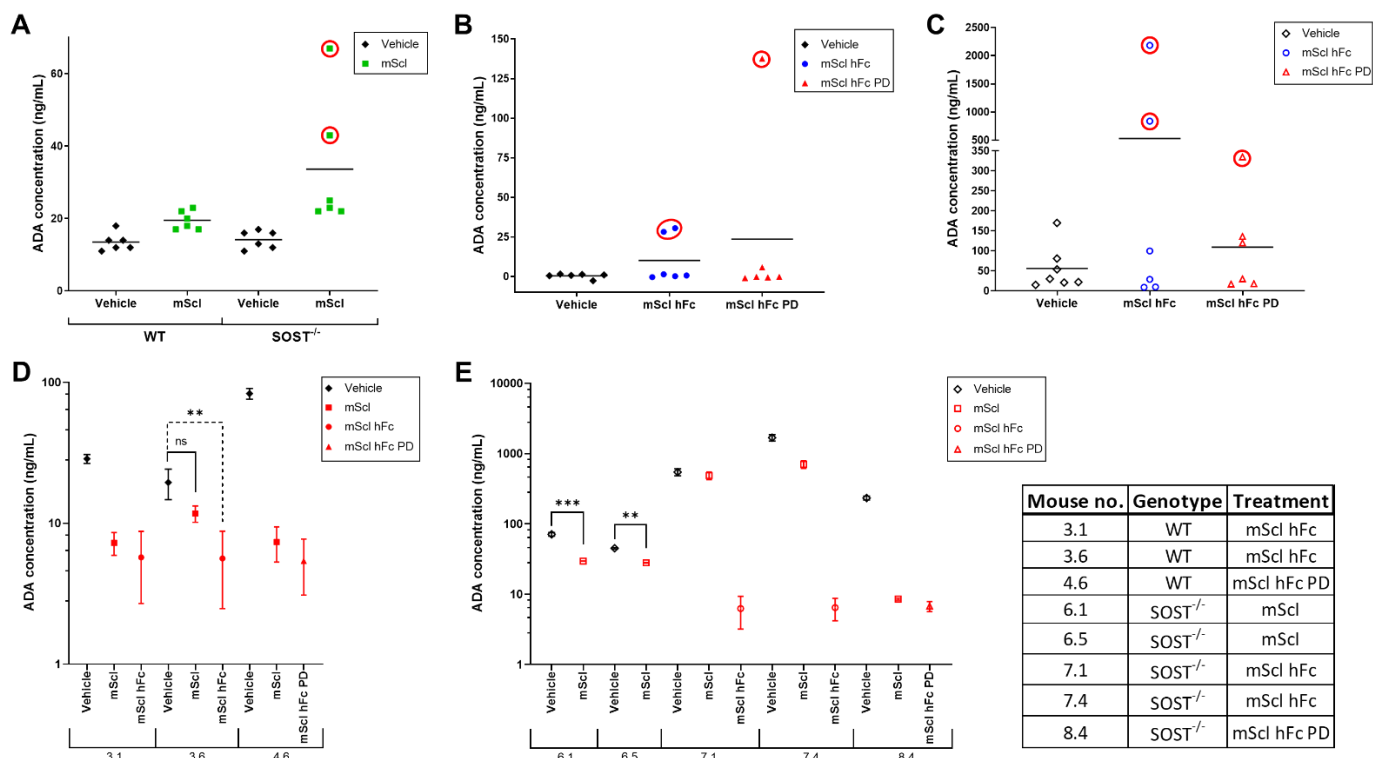
Figure 4.38: Anti-drug antibodies against recombinant mScl in WT and SOST$^{-/-}$ mice. A) Anti-drug antibody (ADA) assay (biotinylated and SULFO TAG labelled mScl added to samples) of WT and SOST$^{-/-}$ mice treated with wild type mScl. B) and C) ADA assay of WT (B) and SOST$^{-/-}$ (C) mice treated with mScl hFc or mScl hFc PD (biotinylated and SULFO TAG labelled mScl hFc PD added to samples). Potential ADA responses are indicated with a red circle around the data point(s). D) and E) Potential ADA samples were tested in confirmation ADA assays: WT (D) and SOST$^{-/-}$ (E) mice treated with the recombinant mScl constructs (used biotinylated and SULFO TAG labelled mScl and mScl hFc PD). Samples were saturated as follows: group 6 with mScl; group 3 and 7 with mScl hFc and mScl; group 4 and 8 with mScl and mScl hFc PD. Table to right of E) indicates genotype and treatment of selected samples with potential ADA responses. Unpaired t-test was performed for statistical analysis of vehicle vs mScl or mScl hFc/PD comparison: ns=non-significant; **p<0.01; ***p<0.001.

4.3.2.4. Microcomputed CT

The effect of the recombinant mScl proteins on skeletal phenotype of WT and SOST$^{-/-}$ mice was analysed by microcomputed tomography (µCT) scanning and 2D and 3D bone

histomorphometry, following the 42-day treatment period. Consistent with the genotype effect observed by DXA, there was a clear difference in trabecular and cortical parameters of WT compared with vehicle treated SOST$^{-/-}$ mice (Table 4.7, 4.8 and 4.9), demonstrating the suitability of SOST$^{-/-}$ as a sclerosteosis model. However, WT and SOST$^{-/-}$ mice had similar connected trabecular lattices and plate- and rod-like architecture in vertebral trabecular bone, as indicated by the vertebral trabecular pattern factors (Tb.Pf) and structure model indexes (SMI). In addition, the medullary area (M.Ar) was the only femoral cortical parameter that showed no difference between the two genotypes, suggesting similar sized medullary cavities in WT and SOST$^{-/-}$ diaphyses.

Administration of mSc hFc PD resulted in a modest but statistically significant effect on trabecular bone parameters of SOST$^{-/-}$ mice (Figure 4.39 and 4.40; Table 4.7 and 4.8). Volumetric BMD (vBMD), bone volume fraction (BV/TV) and trabecular number (Tb.N) in lumbar vertebrae of SOST$^{-/-}$ mice treated with mScl hFc PD were approximately 20%, 15% and 19% lower compared with the vehicle control group, whilst trabecular separation (Tb.S) was 27% higher (Figure 4.39, Table 4.7). Lack of changes in Tb.Pf, SMI and DA however indicated that treatment with recombinant proteins did not affect the connected trabecular lattices, plate- and rod-like architecture, and relative stiffness of vertebral trabecular bone in different directions, as measured by μCT. In femoral trabecular bone, a modest but statistically significant 37% increase in trabecular separation (p<0.05) and a non-significant trend towards reduced BV/TV (27%), vBMD (21%), and Tb.N (25%) was observed (Figure 4.40, Table 4.8). No significant effects on vertebral and femoral trabecular bone were observed in SOST$^{-/-}$ mice treated with mScl or mScl hFc. In contrast to vertebrae, femoral cortical indices appeared to be unchanged following treatment across all three proteins tested (Figure 4.41, Table 4.9), and no significant effects were seen in trabecular or cortical bone of any of the WT treated groups.

Representative μCT images of the L5 vertebral body and right femur from vehicle, mScl, mScl hFc and mScl hFc PD treated WT and SOST$^{-/-}$ mice (approximately 3 months of age) were selected for visual comparison (Figure 4.42 and 4.43). Compared to WT, vertebral and femoral trabecular and cortical bone volume appeared to be higher in SOST$^{-/-}$ mice. There also seemed to be a decrease in vertebral trabecular bone and an increase in intravertebral foramina in both WT and SOST$^{-/-}$ mice treated with mScl hFc and mScl hFc PD, compared to vehicle controls (Figure 4.42), whilst no apparent changes were visible in femoral trabecular and cortical bone.

Table 4.7: Trabecular bone histomorphometry of vertebral body between growth plates of L5 lumbar vertebrae.

	WT								SOST^{-/-}							
	Vehicle		mScl		mScl hFc		mScl hFc PD		Vehicle		mScl		mScl hFc		mScl hFc PD	
	Mean	SD	Mean	SD	Mean	SD	Mean	SD	Mean	SD	Mean	SD	Mean	SD	Mean	SD
vBMD (g/cm³)	0.27	0.06	0.32	0.14	0.23	0.11	0.26	0.03	0.64	0.05	0.63	0.07	0.61	0.07	0.51	0.14*
BV/TV (%)	16.21	1.85	17.49	5.66	14.97	3.78	16.14	1.12	29.40	1.83	29.03	2.39	28.47	2.61	24.91	4.92*
Tb.Th (mm)	0.05	0.00	0.05	0.00	0.05	0.00	0.05	0.00	0.06	0.00	0.06	0.00	0.06	0.00	0.06	0.00
Tb.Sp (mm)	0.21	0.02	0.22	0.02	0.25	0.04	0.22	0.01	0.15	0.01	0.15	0.01	0.16	0.03	0.19	0.04*
Tb.N (mm⁻¹)	3.52	0.20	3.24	0.46	3.10	0.68	3.43	0.19	4.75	0.25	4.61	0.35	4.59	0.39	3.85	0.80**
Tb.Pf (mm⁻¹)	18.19	3.64	17.26	4.19	17.15	4.01	15.85	1.79	16.53	2.20	15.90	1.73	17.09	4.19	17.34	2.18
SMI	1.37	0.16	1.36	0.22	1.37	0.24	1.26	0.11	1.52	0.12	1.51	0.13	1.55	0.25	1.66	0.21
DA	0.46	0.03	0.49	0.04	0.46	0.03	0.49	0.03	0.24	0.06	0.27	0.05	0.21	0.04	0.27	0.07

Data are expressed as the mean±SD of N=6 mice/group (except SOST^{-/-} vehicle group: N=7). Ordinary one-way ANOVA was performed for statistical analysis: *$p<0.05$; **$p<0.01$ compared with SOST^{-/-} vehicle group. The region of interest was the vertebral body of the L5 lumbar vertebrae. vBMD: volumetric bone mineral density; BV/TV: bone volume fraction; Tb.Th: trabecular thickness; Tb.Sp: trabecular space; Tb.N: trabecular number; Tb.Pf: trabecular pattern factors; SMI: structure model indexes; DA: degree of anisotropy.

Table 4.8: Trabecular bone histomorphometry of bone close to the femoral distal growth plate.

	WT								SOST^{-/-}							
	Vehicle		mScl		mScl hFc		mScl hFc PD		Vehicle		mScl		mScl hFc		mScl hFc PD	
	Mean	SD	Mean	SD	Mean	SD	Mean	SD	Mean	SD	Mean	SD	Mean	SD	Mean	SD
vBMD (g/cm³)	0.15	0.01	0.14	0.04	0.14	0.03	0.15	0.01	0.35	0.04	0.32	0.05	0.35	0.06	0.27	0.10
BV/TV (%)	8.66	0.71	8.41	2.81	7.66	2.52	8.78	0.63	23.96	3.51	22.20	3.66	23.67	4.80	17.61	7.79
Tb.Th (mm)	0.05	0.00	0.06	0.01	0.06	0.00	0.05	0.00	0.09	0.00	0.09	0.00	0.09	0.01	0.09	0.01
Tb.Sp (mm)	0.28	0.01	0.31	0.06	0.37	0.12	0.29	0.03	0.21	0.01	0.23	0.02	0.22	0.03	0.28	0.09*
Tb.N (mm⁻¹)	1.62	0.11	1.50	0.46	1.31	0.44	1.66	0.14	2.62	0.34	2.44	0.30	2.63	0.50	1.95	0.78
Tb.Pf (mm⁻¹)	29.14	2.63	29.07	5.74	26.05	3.49	25.88	2.30	13.58	2.48	13.47	2.16	13.30	2.65	16.76	5.22
SMI	2.25	0.13	2.30	0.23	2.21	0.19	2.07	0.12	1.85	0.27	1.82	0.17	1.82	0.37	2.09	0.42
DA	0.38	0.03	0.34	0.03	0.36	0.06	0.39	0.03	0.49	0.03	0.47	0.02	0.45	0.04	0.46	0.04

Data are expressed as the mean±SD of N=6 mice/group (except WT mScl hFc PD group: N=5; SOST^{-/-} vehicle group: N=7). Ordinary one-way ANOVA was performed for statistical analysis: *$p<0.05$ compared with SOST^{-/-} vehicle group. The distal metaphyseal region of interest of the right femur was analysed. vBMD: volumetric bone mineral density; BV/TV: bone volume fraction; Tb.Th: trabecular thickness; Tb.Sp: trabecular space; Tb.N: trabecular number; Tb.Pf: trabecular pattern factors; SMI: structure model indexes; DA: degree of anisotropy.

Table 4.9: Cortical bone histomorphometry near the femoral midshaft.

	WT								SOST^{-/-}							
	Vehicle		mScl		mScl hFc		mScl hFc PD		Vehicle		mScl		mScl hFc		mScl hFc PD	
	Mean	SD	Mean	SD	Mean	SD	Mean	SD	Mean	SD	Mean	SD	Mean	SD	Mean	SD
vBMD (g/cm³)	1.06	0.07	1.01	0.04	1.02	0.05	1.01	0.05	1.41	0.06	1.38	0.07	1.43	0.12	1.37	0.12
BV/TV (%)	44.73	2.41	42.80	1.42	43.23	1.84	42.88	1.66	56.95	2.26	55.90	2.64	57.72	4.22	55.51	4.22
T.Ar (mm²)	1.84	0.09	1.89	0.12	1.73	0.11	1.91	0.07	2.59	0.18	2.57	0.15	2.48	0.16	2.56	0.11
B.Ar (mm²)	0.82	0.05	0.81	0.06	0.75	0.07	0.82	0.05	1.47	0.12	1.44	0.14	1.44	0.19	1.42	0.14
Ma.Ar (mm²)	1.02	0.08	1.08	0.06	0.98	0.05	1.09	0.05	1.11	0.10	1.13	0.05	1.05	0.06	1.14	0.10
T.Pm (mm)	5.29	0.15	5.34	0.20	5.11	0.15	5.40	0.13	6.34	0.28	6.29	0.19	6.20	0.28	6.25	0.15
B.Pm (mm)	9.39	0.32	9.49	0.37	9.09	0.22	9.63	0.26	11.54	0.61	11.51	0.78	11.30	0.58	11.25	0.56
Es.Pm (mm)	4.10	0.19	4.16	0.17	3.98	0.09	4.22	0.14	5.21	0.36	5.22	0.61	5.11	0.34	5.00	0.45
Cs.Th (mm)	0.17	0.01	0.17	0.01	0.16	0.01	0.17	0.01	0.25	0.02	0.25	0.01	0.26	0.02	0.25	0.01
MMI(polar) (mm⁴)	0.40	0.04	0.41	0.06	0.35	0.05	0.43	0.04	0.95	0.15	0.92	0.13	0.88	0.17	0.89	0.10
Eccentricity	0.75	0.01	0.74	0.02	0.75	0.01	0.76	0.02	0.78	0.01	0.77	0.02	0.78	0.03	0.76	0.02

Data are expressed as the mean±SD of N=6 mice/group (except WT mScl hFc PD group: N=5; SOST^{-/-} vehicle group: N=7). The diaphyseal region of interest of the right femur was analysed. vBMD: volumetric bone mineral density; BV/TV: bone volume fraction; T.Ar: tissue area; B.Ar: bone area; Ma.Ar: medullary area; T.Pm: tissue perimeter; B.Pm: bone perimeter; Es.Pm: eccentric perimeter; Cs.Th: cross section thickness; MMI(polar): polar moment of inertia.
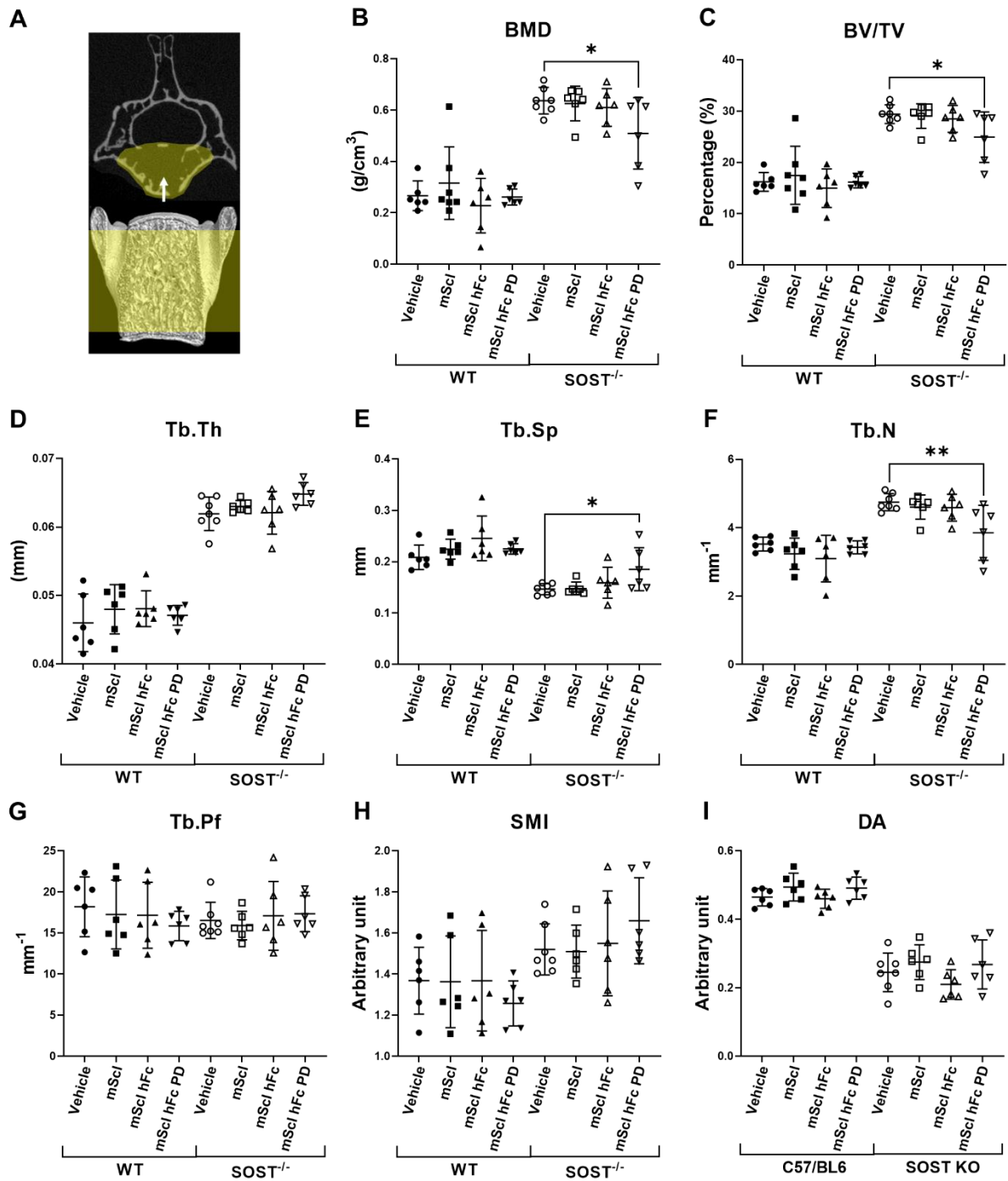
Figure 4.39: Vertebral trabecular bone parameters of WT and SOST^{-/-} mice treated with Vehicle, mScl, mScl hFc and mScl hFc PD. Trabecular microarchitecture was assessed by μCT in WT and SOST^{-/-} mice aged ~3 months. A) Vertebral body region (top yellow region) between the distal and proximal growth plates (bottom yellow region) was selected as the region of interest for vertebral trabecular analysis. B, C, D, E, F, G, H and I) vBMD (B), BV/TV (C), Tb.Sp (D), Tb.N (E), Tb.N (F), Tb.Pf (G), SMI (H) and DA (I). Bars represent mean±SD of N=6 mice/group (except SOST^{-/-} mice vehicle group: N=7). Ordinary one-way ANOVA was performed for statistical analysis: *p<0.05; **p<0.01.
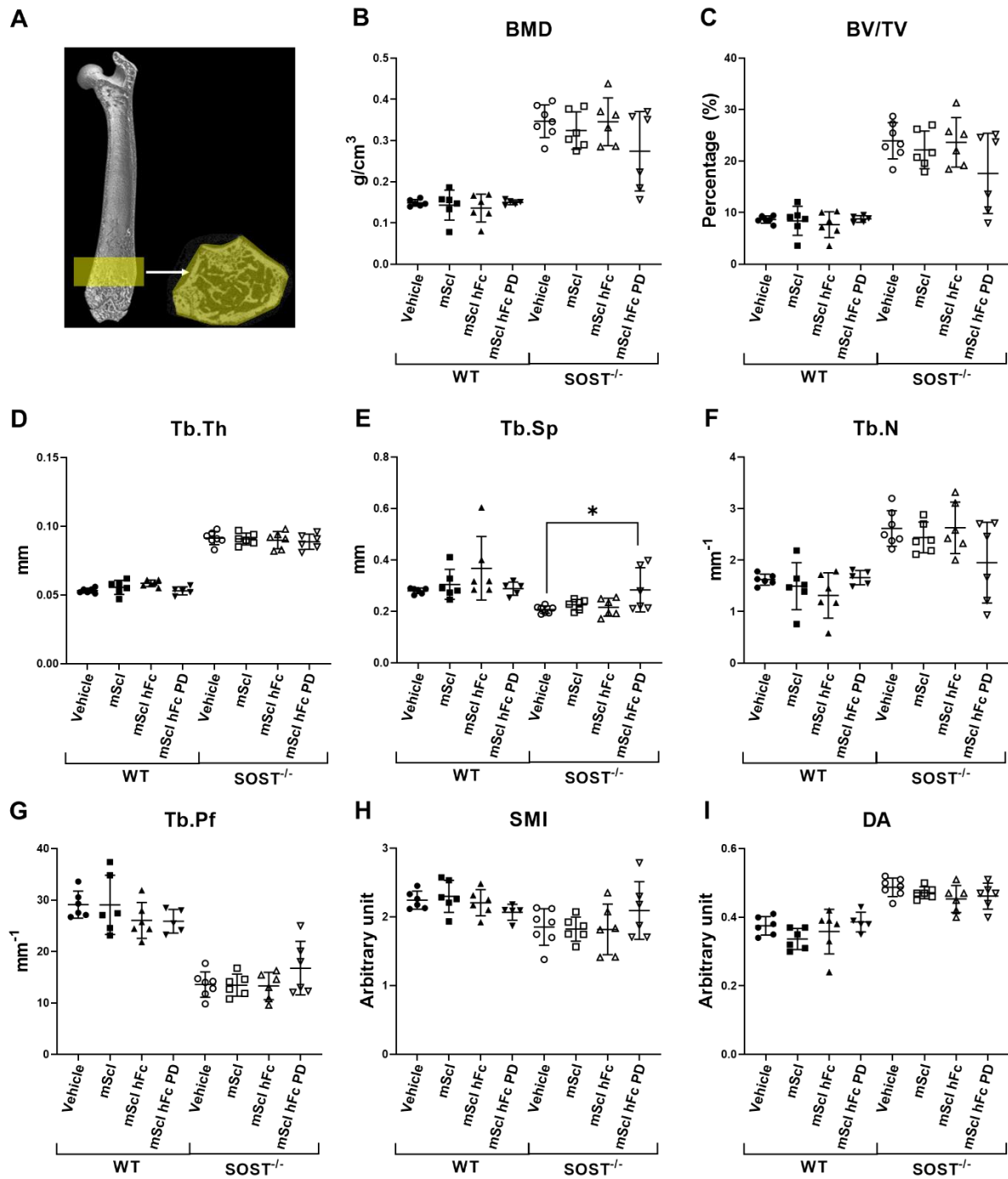
Figure 4.40: Femoral trabecular bone parameters of WT and SOST$^{-/-}$ mice treated with Vehicle, mScl, mScl hFc and mScl hFc PD. Trabecular microarchitecture was assessed by μCT in WT and SOST$^{-/-}$ mice aged ~3 months. A) Region of interest for femoral trabecular (yellow) bone analysis. B, C, D, E, F, G, H and I) vBMD (B), BV/TV (C), Tb.Sp (D), Tb.Sp (E), Tb.N (F), Tb.Pf (G), SMI (H) and DA (I). Bars represent mean±SD of N=6 mice/group (except WT mScl hFc PD group: N=5; SOST$^{-/-}$ vehicle group: N=7). Ordinary one-way ANOVA was performed for statistical analysis: *$p<0.05$.
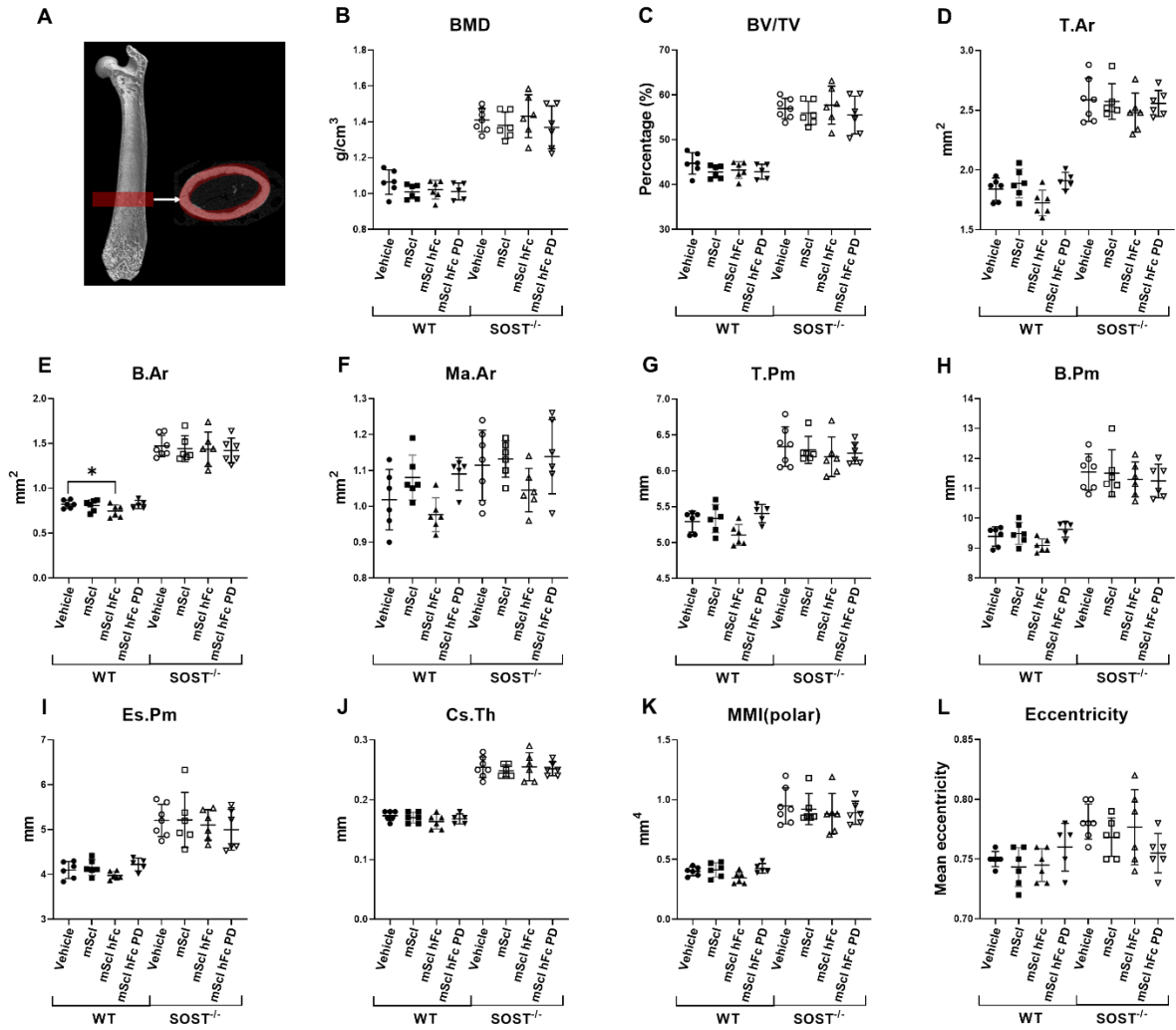
Figure 4.41: Femoral trabecular bone parameters of WT and SOST^{-/-} mice treated with Vehicle, mScl, mScl hFc and mScl hFc PD. Trabecular microarchitecture was assessed by μCT in WT and SOST^{-/-} mice aged ~3 months. A) Region of interest for femoral cortical (red) bone analysis. B, C, D, E, F, G, H, I, J, K and L) vBMD (B), BV/TV (C), Tb.Sp (D), B.Ar (E), M.Ar (F), T.Pm (G), B.Pm (H), Es.Pm (I), Cs.Th (J), polar MMI (K) and Eccentricity (L). Bars represent mean±SD of N=6 mice/group (except WT mScl hFc PD group: N=5; SOST^{-/-} vehicle group: N=7).
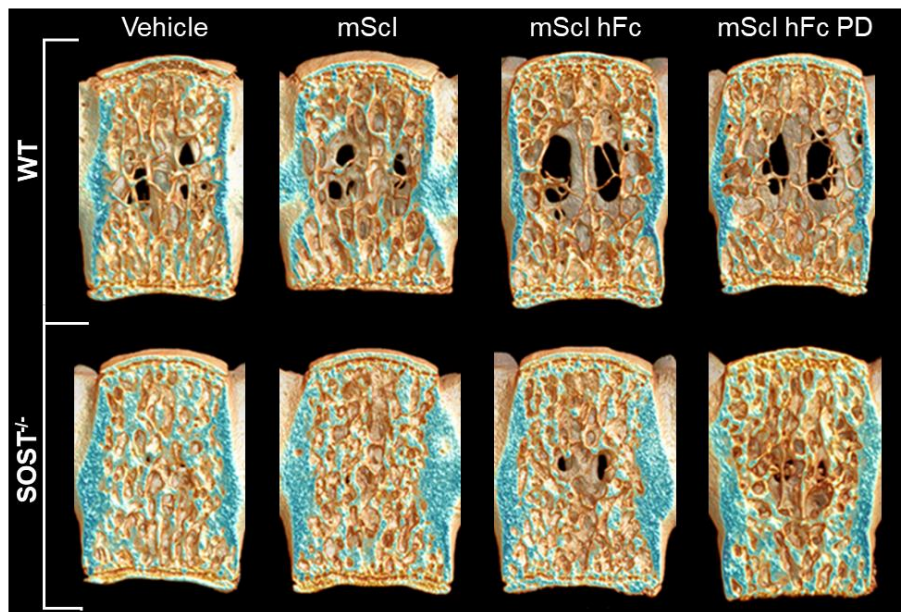
Figure 4.42: Representative frontal plane µCT images of fifth lumbar vertebral body in WT and SOST$^{-/-}$ mice treated with Vehicle, mScl, mScl hFc and mScl hFc PD. Trabecular microarchitecture was imaged by µCT in WT and SOST$^{-/-}$ mice aged ~3 months. Vertebral body is viewed from the front (white arrow in Figure 4.39A). Blue indicates bone density and are for illustration purposes only.

Figure 4.43: Representative sagittal plane µCT images of the right femurs of WT and SOST$^{-/-}$ mice treated with Vehicle, mScl, mScl hFc and mScl hFc PD. Trabecular microarchitecture was imaged by µCT in WT and SOST$^{-/-}$ mice aged ~3 months. Blue indicates bone density and are for illustration purposes only.

133

Chapter 5: Discussion

Sclerosteosis is a rare, severe autosomal recessive sclerosing skeletal dysplasia caused by loss of function mutations in the *SOST* or *LRP4* genes (Balemans et al., 2001; Fijalkowski et al., 2016; van Lierop et al., 2017). These mutations result in lack of functional sclerostin (Scl), a protein that is important for maintaining bone homeostasis, or impaired interaction between Scl and LRP4, a Scl co-receptor that plays a role in retaining and facilitating local Scl action (Fijalkowski et al., 2016; Holdsworth et al., 2019). It has been shown that Scl plays a key role in controlling bone formation in bone modelling and remodelling by antagonising the canonical Wnt signalling pathway through high-affinity binding to the extracellular domains of LRP4 Scl co-receptor and LRP5/6 Wnt co-receptors (Balemans et al., 2001; Poole et al., 2005; Semenov and He, 2006; van Lierop et al., 2011). The protein is expressed primarily by osteocytes, and lack thereof results in skeletal conditions such as sclerosteosis (Balemans et al., 2001; Brunkow et al., 2001). Sclerosteosis has no available treatment and is currently managed through difficult and protracted surgical decompression of entrapped cranial nerves and elevated intracranial pressure caused by excessive bone formation. Surgery is, however, only palliative, as bone soon regrows post-surgery and may cause recurrence of symptoms, necessitating repeated surgical intervention. Finding a less invasive treatment for the condition, either earlier on in its pathogenesis or to later manage the condition in adults, is thus sorely needed.

For this study we therefore hypothesised that replacing Scl with an exogenously produced equivalent protein could potentially reduce excessive bone formation in a SOST$^{-/-}$ mouse model of sclerosteosis by inhibiting the Wnt-signalling pathway. A protein-based approach was selected, as protein drugs bind avidly to their targets, making them highly specific (Joseph et al., 2017; Murray et al., 2017). Their specificity reduces drug toxicity, and drug related side-effects are mostly associated with exaggerated pharmacological effects. In contrast, small molecules cause off-target toxicity due to broad distribution to other tissues (Reynolds et al., 2013). Protein replacement therapies have previously been used to treat anaemia and haemophilia A or B by administrating recombinant erythropoietin and factors VIII or IX, respectively (Eschbach et al., 1987; Aledort et al., 2014; Peters and Harris, 2018). Exogenously supplied enzymes, purified from human or animal tissue or produced by recombinant techniques, have also been used to treat lysosomal storage disorders (Reynolds et al., 2013; Beck, 2018). Successful protein and enzyme

replacement in rare diseases that are linked to loss of functional proteins provide some degree of confidence that such an approach could be effective for sclerosteosis (Sun et al., 2017; Tambuyzer et al., 2020). For this study, wild type Scl and two novel recombinant Scl constructs were developed for evaluation and comparison.

5.1.   Protein design, cloning and expression

As a first step in developing effective treatment, the protein needed to be synthesised *in vitro*. For this, three recombinant constructs were cloned into expression plasmids using multiple steps of restriction enzyme digest and DNA ligation. Wild type mouse Scl (**mScl**), the first of the three distinct constructs, was used as a control throughout the project and was expected to have a short half-life due to its small size. The second construct (**mScl hFc**) consisted of a fusion between wild type mouse Scl and human Fc (hFc), a method used in multiple studies, including U.S. Food and Drug Administration (FDA) and European Medicines Agency (EMA) approved drugs, to improve protein half-life (Strohl, 2015; Kontermann, 2016; Sheffield et al., 2018; AlQahtani et al., 2019). The Fc region of immunoglobulin type 1 (IgG1), a type of antibody, binds to the neonatal Fc receptor (FcRn), which is part of a natural pathway that rescues and recycles IgG1 back into circulation, thereby increasing its plasma half-life (Sockolosky et al., 2014; Rath et al., 2015; Kontermann, 2016). The half-life is further increased by the greater molecular weight of a fusion protein (Rath et al., 2015). Thus, attaching hFc to the C-terminal flexible arm region of wild type mScl would in theory increase the half-life of the protein and decrease the dosage frequency for *in vivo* studies. While the danger of changing the protein structure could potentially result in a loss of biological function, we considered this to be of low possibility as the ability of Scl to bind to Wnt co-receptors LRP5/6 is mediated by a flexible loop region (loop 2) within the central core of the protein and does not involve the N- and C-terminal flexible arm regions (Holdsworth et al., 2012; Kim et al., 2020). Moreover, it has previously been shown that mouse Fc and hFc binds to mouse Fcγ receptors (FcγR) *ex vivo* with similar binding strength, suggesting fusion with hFc would not affect Fc effectiveness in a mouse model (Dekkers et al., 2017). The third fusion protein (**mScl hFc PD**) comprised of wild type mouse Scl fused with hFc and a poly-aspartate motif (PD) attached at the hFc C-terminus. Kasugai et al. demonstrated that a repeating sequence of acidic amino acids, such as aspartic acid and glutamic acid, binds to hydroxyapatite, an

inorganic component of bone, and was effective as a carrier for drug delivery to bone (Kasugai et al., 2010). Other studies have also shown that addition of a poly-aspartate motif to a protein resulted in safe, more efficient delivery to bone, longer retention times, and had little influence on other biochemical properties (Nishioka et al., 2006; Whyte et al., 2012). The aim of the PD motif was thus to localise the recombinant mScl hFc fusion construct to the bone area to further enhance effectivity. On completion of cloning, both restriction analysis and DNA sequencing confirmed that the hFc and hFc PD fragments were successfully attached to the wild type mScl sequences and all recombinant plasmid constructs (pMH mSOST WT, pMH mSOST hFc and pMH mSOST hFc PD) were cloned correctly.

Large quantities (~100 mg each) of the three recombinant protein constructs (mScl, mScl hFc and mScl hFc PD) were successfully expressed in 5 L Expi293™ cultures, signifying a viable approach for future protein production for *in vitro* and *in vivo* studies. After expression, native mScl was first purified by cation exchange chromatography (CEC), as the net positive surface charge of the protein allowed it to attach to the negatively charged ion exchange resin. This was followed by size exclusion chromatography (SEC), and yielded approximately 100 mg mScl per 5L HEK293 culture, comparable to quantities obtained by Veverka et al. (Veverka et al., 2009). Protein A affinity chromatography was the first step in mScl hFc and mScl hFc PD purification, as hFc was previously shown to have a high affinity for Protein A (Carter, 2011; Czajkowsky et al., 2012). While the method was adequate for protein purification, in some cases high protein concentrations obtained from Protein A affinity chromatography resulted in protein aggregation and sample turbidity. To overcome this, adjusting the sample pH to 7 with Tris-HCl pH 8.5 stabilised the protein and cleared the turbidity. Remaining protein aggregates had to be removed by centrifugation and any remaining impurities were then removed by SEC and CEC, yielding approximately 100 mg mScl hFc and mScl hFc PD per 5L HEK293 culture.

Subsequent endotoxin screening of all protein yields showed that endotoxin levels in some samples were above acceptable levels (mScl: 5.75 EU/mg; mScl hFc: 2.58 EU/mg) for use in *in vivo* studies (≤2 EU/mg being the required limit), necessitating additional endotoxin removal steps. Approximately 10% mScl was lost during endotoxin removal using Proteus NoEndo™ S spin columns, conforming with typical >90% recovery. However, attempting to remove endotoxin from mScl hFc samples with the same columns resulted in ~50% loss of protein, possibly due to protein aggregate blocking the column or some protein adhering to the column due to the sticky

nature of Scl (Boschert et al., 2016). As an alternative, an additional CEC step was implemented at the end of the mScl hFc and mScl hFc PD purification process, with no resultant protein loss. In this step the positively charged recombinant proteins (high pI) bound to the negatively charged column, whilst endotoxin (low pI) washed away with low ionic strength buffer (Petsch, 2000). Endotoxin removal by these methods was safe and efficient, with approximately 70% and 55% (mScl and mScl hFc respectively) reduction in endotoxin levels and little to no loss in protein. A sufficiently sterile work environment could also negate the need for further endotoxin removal, as seen with mScl hFc PD production. However, this was not entirely possible in the development laboratory in which this study was undertaken.

Different SDS-PAGE bands were observed for the respective purified recombinant Scl proteins, denoting samples that consist of heterogenous Scl conformations (Figure 5.1). Sclerostin contains two conserved, possible N-linked glycosylation sites, suggesting that differences in band sizes could be a result of glycosylation. Subsequent deglycosyslation of mScl hFc PD with PNGase F under reducing conditions suggested that discrepancies in protein size were indeed partially a result of glycosylation (Figure 4.20). Multiple protein bands were also observed in previous research, where human Scl was expressed in mammalian expression systems, possibly reflecting differences in the extent of glycosylation (Krause et al., 2010; Holdsworth et al., 2012). Glycosylation can vary on the same protein and thus likely contributed to the post translational heterogeneity that resulted in fuzzy bands observed for wild type mScl (Rudd and Dwek, 1997). Furthermore, truncation occurred 176 amino acids downstream from the N-terminal end of mScl hFc and mScl hFc PD, towards the end of the mScl C-terminal flexible region fused to hFc, thereby removing the majority of the mScl sequence in ~20% of the hFc-fusion samples and resulting in various possible protein conformations (Figure 5.1) (Veverka et al., 2009). Since the high flexibility of the hinge region between hFc and mScl and the relatively low dissociation energy of the disulphide bonds that form the Fc dimer could lead to further modifications and cleavages, it is possible that some captured dimers consisted of dimeric hFc and a single mScl, whilst some constructs comprised of monomeric mScl hFc PD or dimeric hFc without mScl (Figure 5.1) (Moritz and Stracke, 2017; Suzuki et al., 2018). Smaller protein bands could have consisted of hFc monomers, a different protein breakdown product, or even monomeric mScl (Figure 5.1). This heterogeneity could also be a result of proteolysis, which has been shown to be an issue in mammalian cell cultures and can range from complete hydrolysis of the protein to minor

truncation of the protein without impairing its biological function (Robert et al., 2009; Rogers and Overall, 2013; Lee et al., 2015; Chakrabarti et al., 2019). The functional significance of these post-translational modifications is however uncertain, as protein produced by *E. coli* expression systems showed similarly effective Scl function in Wnt reporter assays as Scl produced in mammalian systems (Veverka et al., 2009). Functional assays of the two recombinant fusion proteins suggested that truncation and glycosylation did not affect protein function considerably. However, further analysis of the different conformations could provide a clearer understanding of why truncation and glycosylation occur and whether some of these post-translational modifications are significant.
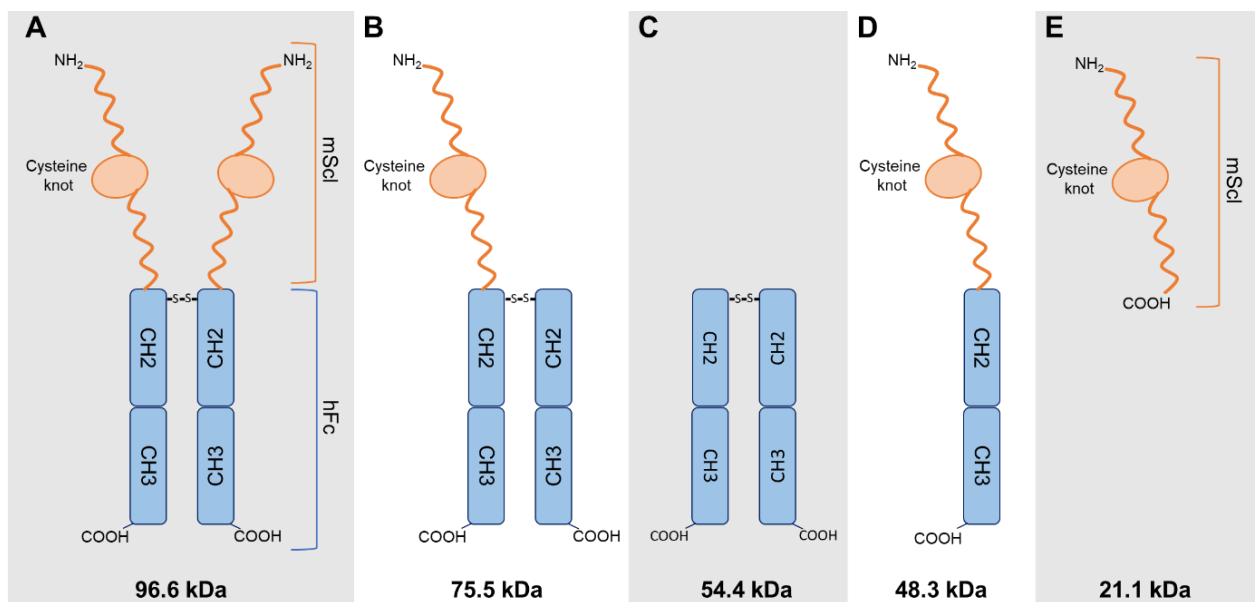
Figure 5.1: Possible conformations of heterogenous mScl hFc. mScl hFc could comprise of: A) dimeric hFc with two mScl, B) dimeric hFc with a single mScl, C) dimeric hFc without mScl, D) monomeric hFc with mScl and E) native mScl. Molecular weights are shown in kDa.

5.2. *In vitro* functionality and efficacy of recombinant sclerostin constructs

It was important to confirm that the formation of a dimeric molecule did not impair mScl activity *in vitro*, since Scl normally exists as a monomer. Sclerostin exerts its function through binding to LRP4/5/6 receptors, thus, the ability of the recombinant mScl protein to bind a fragment of the Wnt co-receptor LRP6 containing the first and second β-propellers of the receptor extracellular domain (LRP6-E1E2) (Holdsworth et al., 2012) were tested *in vitro*, using microscale

thermophoresis, isothermal titration calorimetry and a surface plasmon resonance competition assay. Binding to LRP6 gives confidence that the recombinant mScl proteins also interacted with LRP5, as Scl interacts with both via the same NxI motif (He et al., 2004; Holdsworth et al., 2012). Although Scl also binds to LRP4 to inhibit bone formation, this study focussed on the effect of the recombinant mScl proteins on the canonical Wnt signalling pathway. Investigation of the interaction between LRP4 and the recombinant proteins was therefore excluded for possible future studies. Lastly, with Scl being a potent negative regulator of bone formation, an *in vitro* bone nodule formation assay was used to test the ability of the recombinant mScl proteins to inhibit this process.

5.2.1. Microscale thermophoresis

The microscale thermophoresis (MST) assays investigated the binding reactions between the recombinant mScl constructs (mScl, mScl hFc and mScl hFc poly D) and fluorescently labelled LRP6-E1E2, based on temperature-induced changes in fluorescence of labelled LRP6 as a function of the concentration of non-fluorescent recombinant Scl constructs (Jerabek-Willemsen et al., 2014). These assays required low amounts of ligand and showed that the three recombinant mScl constructs interacted strongly with LRP6-E1E2. Calculated KD (equilibrium dissociation constant) values ≤6nM (less than half of the fixed 12.5nM LRP6-NT647 concentration) could however not be reported as absolute values, due to experimental constraints that result from ligand depletion. Once KD decreases past the labelled LRP6 concentration, the midpoint of the dose response curve converges to 0.5*[LRP6-NT647], making it impossible to determine the true KD (Wienken et al., 2010; Esteban Fernández de Ávila et al., 2013). The KD values for hScl, mScl hFc and mScl hFc PD (2nM, 2nM, and 0.54nM respectively) were therefore reported as <6nM, demonstrating strong interaction between the recombinant constructs and LRP6. These results were similar to the ~5nM KD previously reported for interaction between hScl and LRP6 (Holdsworth et al., 2012; Boschert et al., 2013). However, those previous studies used SPR instead of MST to determine KD. KD values reported here might thus not be completely comparable to the previously reported hScl KDs. Moreover, as reported in other studies, the fluorescent dye used to label LRP6-E1E2 may have altered protein properties or promoted aggregation, thereby affecting the interaction between labelled LRP6-E1E2 and the mScl

constructs unpredictably (Scheuermann et al., 2016). Although such interference could be assessed by a competition assay, the aim of undertaking the MST assays was not to quantify KD, but rather to demonstrate that interaction occurred as predicted.

5.2.2. Isothermal titration calorimetry

Isothermal titration calorimetry (ITC) was used as an orthogonal technique to generate additional data on protein affinity. The technique measures the heat exchange during a biomolecular binding event in solution directly and is highly sensitive and non-destructive (native proteins are used) of the tested ligands and receptors, making it a powerful tool and the leading technique used for measuring well-defined classical energetic parameters and the affinity constants of biochemical interactions (Doyle, 1997; Ma et al., 2018). Dissociation constants (KDs) in the nanomolar range were reported by multiple dose dependent ITC assays, indicating moderate to strong interaction between the recombinant mScl constructs and label-free LRP6-E1E2. The KD values (~147nM, ~116nM and ~746nM for mScl, mScl hFc and mScl hFc PD respectively) were similar to the recently reported KD for wild type Scl (170 nM) (Kim et al., 2020). It was however much higher than other previously reported values for wild type human Scl (~5nM), suggesting that mouse Scl might bind to human LRP6 with lower affinity (Holdsworth et al., 2012; Boschert et al., 2013). A BLAST alignment of wild type mouse Scl (Uniprot: Q99P68) and human Scl (Uniprot: Q9BQB4) showed overall structure homology, but indicated some differences in protein sequences, including an amino acid difference close to the NXI motif, the functional region of Scl that interacts with LRP6, which could affect mScl interaction with human LRP6 and may account for the shift in KD (Holdsworth et al., 2012; Sayers et al., 2019). It is also possible that the inactive truncated fractions (consisting of hFc without mScl) in the hFc-fusion protein samples affected protein affinity, and the higher sample concentration required for ITC could have promoted protein aggregation, thereby affecting KD values. Furthermore, different methods often give differing absolute values, thus some differences might be a result of different techniques used to determine KD: Boschert et al. used autoradiography, Kim et al. used MST, whilst Holdsworth et al. used SPR (Biacore) (Holdsworth et al., 2012; Boschert et al., 2013; Kim et al., 2020).

Binding of the dimeric recombinant mScl hFc fusions to LRP6-E1E2 was expected to occur in a 1:2 ratio (one mScl molecule binding to two LRP6-E1E2 molecules). Stoichiometries of 0.6 and

0.9 were obtained for mScl hFc and mScl hFc PD respectively, indicating that mScl hFc bound at the expected ratio. The reasons underlying the deviation from the expected binding ratio for mScl hFc PD is unclear, but it may reflect the level of active protein in the samples (hFc-fusion protein samples contained truncated products that may have been less active). Although unlikely, it is also possible that inaccurate sample concentrations in the sample cell or syringe of the ITC system could account for the unexpected binding stoichiometries, as concentration errors do not yield noticeably flawed titration profiles, but can nonetheless propagate to the fitted thermodynamic results (Kantonen et al., 2017).

5.2.3. Surface plasmon resonance

The Biacore™ surface plasmon resonance (SPR) competition assays provided additional evidence that the recombinant mScl constructs were functionally active and able to bind to the LRP6 Wnt co-receptor. Sclerostin is a 'sticky' protein that tends to bind non-specifically to the Biacore™ sensor surface, which can complicate the measurement of the association/dissociation rates of interactions when Scl is flowed across the chip to measure binding to a previously captured protein (Boschert et al., 2016). It was therefore decided to coat the sensor surface with Scl and pass a solution of LRP6-E1E2 and the selected mScl construct over the top. This approach also removed the necessity to coat a new sensor surface for each recombinant mScl construct, which would have made comparison more difficult. Additionally, in these competition assays the binding event was in solution and as a result were not influenced by the sensor surface (capturing a recombinant mScl protein on the sensor might have blocked its binding sites). EC50 values of the mScl constructs demonstrated that the recombinant constructs bound well to LRP6-E1E2. These assays were however not performed in triplicate and as a result the amount of possible variation in the measurements was not clear. The Biacore™ 3000 data were therefore only used as an additional indicator of interaction between the recombinant mScl proteins and LRP6.

5.2.4. Mineralised nodule formation assay

The mineralised nodule formation assays were done to show functional efficacy of the recombinant proteins and investigated the effect of the recombinant mScl constructs on

osteoblast mineralisation. MC3T3-E1 Subclone 14 mouse pre-osteoblasts (ATCC, Manassas, VA, USA) were selected for the mineralisation nodule assay as they express LRP4/5/6 and alkaline phosphatase, exhibit high level of osteoblast differentiation, produce an extensive collagenous extracellular matrix and deposits mineral after being cultured in 50 µg/mL ascorbate-2-phosphate and 10 mM β-glycerophosphate (Fratzl-Zelman et al., 1998; Li et al., 2009). Additionally, differentiated osteoblasts do not produce sclerostin (mainly produced by osteocytes), which provided the added benefit of minimal interference with the recombinant mScl constructs (Poole et al., 2005). The aim of this study was not to do a detailed mechanistic study of a novel class of protein, therefore a cell line, such as primary osteoblasts from rat neonates (needs to be isolated and are more difficult to culture than MC3T3-E1 cells), that deposits recognisable and quantifiable woven bone structures rather than just mineral was not required (Orriss et al., 2012; Taylor et al., 2014; Liu et al., 2019). However, although MC3T3-E1 mineralisation assays were sufficient for initial studies, independent evaluation of the effects of the mScl constructs on the mineralisation and organic matrix components of bone formation in rat neonate-derived primary osteoblast cultures would be of interest. The MC3T3-E1 cells, which are easier to culture and have demonstrated mineralisation and robust osteogenic gene and protein expression comparable to primary cells, were however a convenient, initial bioactivity screen to show a similar response to the well-studied and -understood wild type Scl protein (Franceschi et al., 1994; Fratzl-Zelman et al., 1998; Li et al., 2009). Moreover, use of MC3T3-E1 cells instead of primary cells for the purpose of our project were in line with the three Rs (replacement, reduction, and refinement) of animal use in science (Russell and Burch, 1959; Tannenbaum and Bennett, 2015). When treated with osteogenic media (growth media supplemented with ascorbic acid and β-glycerophosphate) only, cells differentiated into mature osteoblasts and deposited mineral that covered the well surface after approximately 9 days, consistent with previously reported results (Wang et al., 1999). As expected, wild type mScl and the mScl fusion proteins inhibited mineralisation substantially, consistent with previous reports for rat and human Scl (Li et al., 2009; Veverka et al., 2009). The inhibition of mineralisation by mScl hFc and mScl hFc PD indicated that mScl with C-terminal hFc retained its binding and biological activity, even when dimerised via that hFc. Consistent with previous reports, substantial inhibition of mineralisation was blunted by co-treatment with ~5x molar excess of sclerostin-neutralising antibody (anti-Scl Ab), confirming that inhibition was due to functional inhibition by mScl, since mineralisation was restored in its presence, but was unaffected by an

irrelevant isotype control Ab (Li et al., 2009). Moreover, the antigen-binding fragment (Fab) of the anti-Scl Ab inhibited mScl as effectively as the full anti-Scl Ab, demonstrating that inhibition of mineralisation was not due to possible aggregation of anti-Scl Ab and the dimeric mScl constructs. Direct interaction between LRP4 and the recombinant mScl constructs was not confirmed, however, since the expected Scl effect was demonstrated in the MC3T3-E1 mineralisation assay, the hFc fusion proteins appear able to bind related Scl receptors. These results, together with data from the three biophysical techniques, demonstrated that the recombinant mScl proteins bound to the necessary receptors (LRP4/5/6, although LRP4 interaction was not confirmed by binding assays), and were functional and effective *in vitro*. It was therefore decided to continue studying the recombinant mScl constructs in a SOST knockout (SOST$^{-/-}$) mouse model.

5.3. *In vivo* functionality and efficacy of recombinant sclerostin constructs

Although it has been reported that Scl also have effects on non-skeletal tissue, this study focussed on the effect of exogenous Scl on the skeleton as a potential approach to manage excessive bone formation in a mouse model of sclerosteosis (Moester et al., 2010; Zhu et al., 2011; Guañabens et al., 2016; Fulzele et al., 2017). Lack of obvious effects on non-skeletal tissue in sclerosteosis patients further suggests that, at least in humans, Scl would not have widespread pleiotropic effects (Brunkow et al., 2001). Thus, following confirmation of *in vitro* activity, the effect of the recombinant mScl proteins on the skeleton was investigated in SOST$^{-/-}$ mice that display increased bone mass throughout the skeleton in early life. This phenotype is driven by increased bone formation and rapid increase in BMD as mice grow, and lack of ectopic bone further copies the sclerosteosis phenotype, making SOST$^{-/-}$ mice an appropriate model in which to test the concept of sclerostin replacement as a strategy to mitigate the excessive bone formation of sclerosteosis (Li et al., 2008; Kramer et al., 2010; Ke et al., 2012; Schwarze et al., 2019). Two *in vivo* studies were completed for this project. In the first study, recombinant mScl constructs were administered in a single intravenously (IV) dose. Samples were then collected over a 10-day period to determine the pharmacokinetic and pharmacodynamic parameters of the different constructs. During the second study, multiple doses were administered subcutaneously over a 6-week period, and although pharmacokinetic and pharmacodynamic

data were collected, the primary aim of this study was to assess safety and efficacy of the different recombinant constructs.

5.3.1. Animal treatment

During early stages of the single dose pharmacokinetic and pharmacodynamic study, immediately after administration of recombinant mScl constructs, adverse effects and fatalities were observed in mice treated with mScl hFc PD. All affected animals were male, primarily C57/BL6 (wild type), with a single SOST$^{-/-}$ case. It was curious that not all animals reacted the same in given groups and although fatalities were observed, some animals did recover. Pathology reports from Charles River Laboratories were inconclusive. Mouse Scl hFc PD is a novel construct, but is highly similar to mScl hFc, which caused no adverse events. The only difference between the two constructs is the inclusion of an eight-aspartate residue motif at the C-terminus of mScl hFc PD, which was expected to mediate localisation of the protein to bone. It is unlikely that addition of such an acidic motif would result in the observed adverse events, as several bone non-collagenous proteins have repeating sequences of acidic amino acids, such as aspartate and glutamic acid, in their structures (Kasugai et al., 2010). Moreover, this approach has been used in the approved drug Asfotase Alfa, which utilised 10 aspartate residues at the C-terminus of hFc included in the fusion protein, suggesting that addition of the eight aspartate residues should be safe (Whyte et al., 2012). The inconsistent adverse effects remain unexplained, especially considering that no adverse events were observed in mice treated during the multidose pharmacology study. While it is possible that a contaminant may have been responsible for the evident signs, endotoxin levels of all samples from both studies were confirmed to be below the maximum level allowed by the project licence.

5.3.2. Pharmacokinetics of recombinant mScl proteins

To assess the pharmacokinetic (PK) properties of the recombinant mScl proteins, a single dose of mScl hFc (10 mg/kg), mScl hFc PD (10 mg/kg), or a molar equivalent of mScl (4.4 mg/kg), to adjust for molecular weight differences between proteins, was administered intravenously (IV) to 7-10 week old wild type (WT) and SOST knock out (SOST$^{-/-}$) mice. Concentrations of

recombinant mScl protein in blood samples collected at various intervals post-dose were quantified by LC-MS/MS, and PK profiles generated from these concentrations were broadly similar in WT and SOST$^{-/-}$ mice. Wild type mScl had a very short half-life and was undetectable after 5 minutes post dose. As expected, the half-life of the hFc fusion proteins were much longer, estimated at 1.5-1.8 days for mScl hFc and 4 days for mScl hFc PD. These extended half-lives were consistent with multiple Fc fusion drugs (e.g. eftrenonacog-α: 2.3 days; Aflibercept: 4.6 days), demonstrating that the mScl hFc fusion proteins could have potential as a treatment with lower dose frequencies (reviewed by Kontermann, 2016). The simulated 42-day prediction model based on the single dose study PK showed that mScl serum levels (0.5-3 µg/mL) would remain well above previously reported Scl serum concentration (<100 pg/mL) at 10 mg/kg mScl hFc and mScl hFc PD, and 4.4 mg/kg mScl, therefore dosage concentrations remained unchanged for the pharmacology study (Shahnazari et al., 2012a; Tu et al., 2012; Jastrzebski et al., 2013). The PK profiles for the multi-dose pharmacology study were comparable to the single dose study and showed a half-life of approximately 1.6 and 2.6 days for mScl hFc and mScl hFc PD respectively.

The steady-state volume of distribution (V_{ss}) for the recombinant mScl constructs were expected to be low (<200 mL/kg bodyweight, approximately the same as the amount of body-water in a mouse), as the hydrophilic nature and large size (~100 kDa) of the protein constructs should preclude significant cellular uptake and distribution (Øie and Tozer, 1979; Smith et al., 2015). The V_{ss} for the two hFc fusion constructs were however approximately 10x higher than expected. Immediately after protein administration, initial volume of distribution should approximate the serum volume of the mouse, which is approximately 40 mL/kg bodyweight. A dose of 10 mg/kg mScl hFc and mScl hFc PD was administered, therefore the expected maximum concentration (C_{max}) for the hFc fusion proteins were $\frac{10mg/kg}{40mL/kg} = 250$ µg/mL. The C_{max} for the hFc fusion proteins was however >10x lower than expected (approximately 10 µg/mL mScl hFc and 20 µg/mL mScl hFc PD), perhaps due to potential issues with dosing, where administered samples possibly contained less protein than expected (protein stock concentrations used to make up the administered solutions were correct), construct stability in the formulation, or impact of glycosylation on the Scl-hFc clearance profiles (Li and d'Anjou, 2009). Rapid elimination by the liver for biliary excretion, and subsequent decrease in V_{ss} is also a possibility (Kok-Yong and Lawrence, 2015; Almazroo et al., 2017). Lastly, Scl is a sticky protein, therefore it was also possible that the mScl constructs were sticking to the administration needle, or at the IV

administration point and then slowly dissipated in serum over time (Boschert et al., 2016). To reduce or eliminate possible sticking to the needle, rat serum albumin (RSA) was added to the solutions that were administered subcutaneously (SC) during the multi-dose pharmacology study (Towbin et al., 1979). Upon administration, RSA would act as a blocking agent by attaching to potential non-specific binding sites on the needle surface when the drug solution pass through, thereby leaving little to no room for mScl to attach, allowing recombinant mScl to pass through without sticking to the needle (Steinitz, 2000; Xiao and Isaacs, 2012). Compartmental analysis of the multi-dose study data showed volume of distribution of 497 mL/kg and 188 mL/kg for mScl hFc and mScl hFc PD respectively, which, allowing for loss due to SC route of administration, were consistent with pharmacokinetic results from the single dose study. Exposure was therefore reflective of what was seen before, suggesting that the sticky nature of Scl as well as the administration routes (IV and SC) were likely not the cause of the unexpected pharmacokinetic results in both studies.

Recombinant mScl constructs administered intravenously during the single dose study fitted a two-compartment model, where the drug concentration decreased bi-exponentially. In contrast, fitted data from the multi-dose study showed one compartment kinetics when two compartment kinetics were expected for the mScl constructs and a SC route of administration. It is likely that the slow absorption from SC administration hid the first distributional phase due to insufficient information (low number of samples were collected, and the concentration of the absorption phase and the rest of the data were at trough (pre-dose) levels) (Bonate, 2011; Ahmed, 2015). Distribution of the multi dose study mScl hFc data was comparable to the simulated 42-days dosage study: exposure samples obtained at trough levels (predose and just before another dose or end of study) were similar to the predicted exposure, demonstrating that the pharmacology study was well-performed. Considering the potential for error and the uncertainty of the effect of the SC route, these predictions allowed us to run the study with some confidence of achieving a given exposure and a standard with which to compare the ultimately observed exposure, so that the success of repeat dosing in the pharmacology study could be assessed. More accurate estimates of pharmacokinetic parameters, such as protein half-life, V_{ss} and C_{max}, would be derived from measuring whole profiles, but the available data from the single dose pharmacokinetic study gave good indications for planning of the multi-dose pharmacology study. The similarity between the trough data collected on Day 42 of the pharmacology study and the

predicted data suggests that significant interference from anti-drug antibodies (ADA) was unlikely (see 5.3.4). In contrast, peak exposure samples were much higher than the predicted peaks, likely due to bioavailability (possibly ~90%) being higher than the more conservative 50% bioavailability used in the prediction algorithm. This would suggest that bioavailability after administering drugs via IV and SC routes were similar, which, together with similarities between IV and SC PK profiles, further supports the SC administration route as a viable means of administration.

5.3.3. Pharmacodynamics

A decrease in the bone formation marker P1NP would be indicative of a reduction in bone formation, as demonstrated by a previous study and suggested by the difference between P1NP concentrations in WT and SOST$^{-/-}$ mice in this study (Vasikaran et al., 2011). A reduction in P1NP was therefore expected for effective recombinant mScl constructs, but P1NP concentrations in both the single dose pharmacodynamic study and the multidose pharmacology study were not affected by dosing with mScl hFc and mScl hFc PD. However, although this lack of change in P1NP would be consistent with the little or no changes observed in bone parameters, it is possible that the strategic time points at which samples were collected missed the windows in which P1NP levels were altered.

5.3.4. Anti-drug antibodies

Mice rarely developed anti-drug antibodies (ADAs) against the recombinant mScl constructs. As expected, no ADAs were observed in WT mice treated with wild type mScl, as these mice would produce their own mScl, which would be familiar to the mouse immune system (Beier et al., 2017). Curiously, ADAs targeted both hFc and mScl in WT mice treated with mScl hFc and mScl hFc PD when only ADAs against hFc were expected, as only hFc would have been foreign to the host (Krishna and Nadler, 2016). In contrast, ADAs targeted native mScl as well as fused mScl and/or hFc in SOST$^{-/-}$ mice, as both mScl and hFc/hFc PD were foreign to the mouse immune system (Li et al., 2008). ADAs were however only rarely observed in treated animals and would likely not affect the efficacy of the recombinant mScl proteins in mice. The unlikelihood of

significant interference by ADAs is further supported by the similarities between predicted and actual exposure data in the dosage study. In addition, there was no difference in bone parameters in mice either with or without ADAs. These results may however not translate well to humans (Leenaars et al., 2019; Brubaker and Lauffenburger, 2020). Human patients will likely receive repeated treatment over many months/years, during which ADAs against the recombinant mScl protein might continue to increase, thereby reducing drug effectivity or rendering the drug ineffective as a therapeutic agent to some patients.

5.3.5. Bone parameters

The effect of Scl administration on the skeleton of SOST$^{-/-}$ mice was measured and, as expected, whole body areal BMD of the growing mice, determined by dual X-ray absorptiometry (DXA) from isoflurane anaesthetised mice, increased throughout the study. Although a clear difference in bone mass was observed when comparing WT mice with SOST$^{-/-}$ mice, no difference in bone mass was observed between WT groups compared to other WT groups, and SOST$^{-/-}$ groups compared to other SOST$^{-/-}$ groups, likely due to DXA being unable to pick up small changes in bone mass over the six-week study period (Somerville et al., 2004; Li et al., 2008). Thus, microcomputed tomography (μCT) analysis was more applicable to the pharmacology study.

Although the skull is the most relevant to sclerosteosis, generalised bone overgrowth is observed in both sclerosteosis patients and SOST$^{-/-}$ mice. Assessment of lumbar and femoral trabecular and cortical bone by μCT are standard procedures, so these bones were examined first to understand the extent of any effect following treatment. As with DXA, a clear difference was observed between the bone mass of the two genotypes. A small, but significant decrease in vBMD, BV/TV, Tb.N, and an increase in Tb.Sp were observed in the vertebral trabecular bone of SOST$^{-/-}$ mice treated with mScl hFc PD. Notably, these changes did not correlate with a typical decrease one would expect in Tb.Th, as an increase in Tb.Sp is a direct result of a decrease in Tb.Th (Li et al., 2008). In contrast to changes observed in femoral trabecular bone, there was no clear effect on whole body aBMD or femoral cortical bone parameters following administration of any of the three recombinant mScl proteins. In addition, no significant changes in cortical or trabecular bone in response to treatment with any of the mScl proteins were observed in WT control mice. It is possible that the WT mice self-regulated their own Scl production to

compensate for the exogenous Scl. However, transgenic mice that over express Scl have low bone mass (reduced trabecular parameters), suggesting that exogenous Scl, whether given as a drug or through over expression, should indeed affect bone homeostasis in WT mice (Kramer et al., 2010; Zhang et al., 2016; Delgado-Calle et al., 2017).

Limited change in bone parameters could be the result of ADAs (see 5.3.4) or a too short treatment period. However, a typical bone remodelling cycle takes approximately 2-3 weeks, depending on mouse strain (Weinstein et al., 1998). The six-week study should thus have allowed for approximately 2-3 bone remodelling cycles, which should have been sufficient to see changes in the trabecular parameters, providing a degree of certainty that the study design was sound and likely not the reason for lack in protein efficacy. Sclerosteosis usually stabilises when patients reach skeletal maturity in the third decade of life (van Lierop et al., 2017). It is thus possible that the 7-10 week old mice were too old and a greater response might have been seen if treatment was started at an earlier age. Most likely, levels of recombinant mScl might have been too low to achieve sufficient efficacy and the recombinant proteins were not efficiently delivered to bone. A bigger response could possibly have been elicited if the dosage was increased significantly (e.g. 10x) to improve distribution, but the maximum injection volume and protein solubility (the recombinant mScl proteins tend to aggregate at higher concentrations) may have limited this approach. It is possible that the bone-targeting aspartate moiety of mScl hFc PD was beneficial in delivering the protein to the target tissue, since effects were seen in SOST$^{-/-}$ mice administered with this recombinant construct. The current study did however not explore whether the protein localised to bone tissue, or whether Wnt signalling was reduced in the bones of these mice.

Upon closer inspection of the µCT data it became apparent that the changes in bone parameter data observed in the SOST$^{-/-}$ mice treated with mScl hFc PD were primarily dictated by two outlier mice that showed a greater response. The difference in bone structure between one of these responding mice and an average mouse from the same group can clearly be seen in µCT images (Figure 5.2). Whilst it is possible that the responding mice received larger doses, a highly variable response between animals would have been expected, as a single dose formulation, from which each 100 µL dose was removed for administration, was prepared. Moreover, mice were not dosed in the same sequence at each dosing time point, making it unlikely that there were continuous dosing differences between the outlying mice and the rest of the group. It is also possible that there were slight variations in age and physiology between the SOST$^{-/-}$ mice

provided by Charles River. Answers to these questions would be of interest, but would likely require repetition of the study.
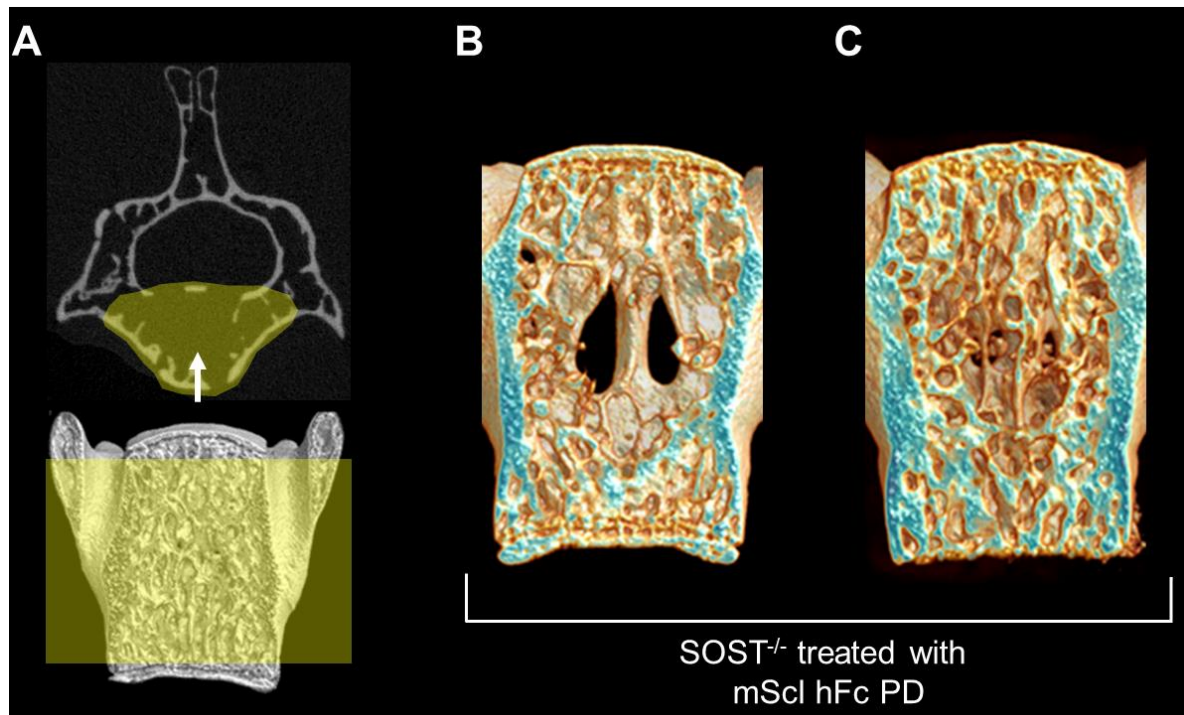
Figure 5.2: Vertebral trabecular bone phenotype of SOST^{-/-} mice treated with mScl hFc PD. Trabecular microarchitecture was assessed by µCT in SOST^{-/-} mice aged ~3 months. A) Vertebral body region (top yellow region) between the distal and proximal growth plates (bottom yellow region) was selected as the region of interest for vertebral trabecular analysis. B and C) Representative frontal plane µCT images of the fifth lumbar vertebral body in SOST^{-/-} mice that highlights the extent of the differences between mice treated with mScl hFc PD.

5.4. Future work

Future work would focus on finding a treatment for sclerosteosis by either revisiting the exogenous Scl route or exploring new approaches. To answer the questions raised by our multidose pharmacology study, the study would have to be repeated with additional doses, time-points and potentially a larger number of mice. Positive results from such a repeated study would justify further improving the existing Scl constructs or designing new or improved Scl constructs. A bone-targeting, mScl fusion protein-expressing adeno-associated virus would be an interesting proof of concept for a means to express the mScl proteins within the skeleton (Lee et al., 2019; Yang et al., 2019). Furthermore, there is evidence that Scl regulates non-skeletal tissue/organs in animal models and humans, and whilst the current study focussed on the skeletal effects of

the recombinant mScl proteins, further investigation of effects on other organs would be of interest (Moester et al., 2010). In addition to LRP6-Scl interactions, direct interaction between LRP4 and Scl should also be examined in future studies. Sclerostin gene therapy, or other strategies to inhibit Wnt signalling in bone, such as small molecules, could also be explored as alternatives to Scl replacement therapy, but might be a lengthy process (Funck-Brentano et al., 2018; Madan et al., 2018). Although this project focussed on the mutant *SOST* variant of sclerosteosis, future investigations could include the sclerosteosis variant that results from mutated LRP4 (Fijalkowski et al., 2016).

Chapter 6: Conclusion

This pilot study found that the recombinant mScl constructs (mScl, mScl hFc and mScl hFc PD) interacted with the LRP6 Wnt co-receptor and substantially supressed matrix mineralisation by osteoblast-like cells *in vitro.* Furthermore, administration of recombinant mScl hFc PD protein partially corrected the high bone mass phenotype of the SOST$^{-/-}$ mouse, suggesting that bone-targeting of Scl engineered to improve serum half-life and localise mScl to bone was able to negatively regulate bone formation in the SOST$^{-/-}$ mouse model of sclerosteosis.

The limited efficacy observed in this study may be due to one or a combination of the following possibilities: Firstly, the treatment period may have been too short. However, the six-week study should have allowed for approximately 2-3 bone remodelling cycles, which should have been sufficient to see changes in bone parameters (Weinstein et al., 1998). Secondly, although unlikely, protein immunogenicity could have reduced efficacy through production of ADAs. Thirdly, it is possible that the 7-10 week old mice were too old. Sclerosteosis usually stabilises when patients reach skeletal maturity in the third decade of life, thus, a greater response might have been seen if treatment was started at an earlier age (van Lierop et al., 2017). Lastly, and most likely, levels of recombinant mScl may have been too low to achieve sufficient efficacy, or systemic administration was not able to efficiently deliver the recombinant proteins to the target tissue. Significantly increasing the dosage (e.g. 10x) to improve distribution might have elicited a bigger response, but protein solubility and maximum injection volume could limit this approach. Inclusion of the bone targeting moiety in mScl hFc PD may have been beneficial, however, the current study did not explore whether the protein localised to bone tissue, or whether Wnt signalling was reduced in the bones of mice treated with mScl hFc PD.

The modest efficacy observed in this study indicates that Scl replacement may not be an optimal strategy to mitigate excessive bone formation in sclerosteosis. Alternative approaches such as novel and improved Scl constructs, *SOST* gene therapy, or other strategies to inhibit Wnt signalling in bone could be investigated. Continued research is certainly warranted for this debilitating, sometimes fatal condition, that is currently reliant on difficult and protracted surgical measures. Effective treatments would dramatically improve the quality of life of these patients and their families.

References

Ahmed, T.A., 2015. Pharmacokinetics of Drugs Following IV Bolus, IV Infusion, and Oral Administration. Basic Pharmacokinet. Concepts Some Clin. Appl. https://doi.org/10.5772/61573

Akiyama, H., Chaboissier, M.-C., Martin, J.F., Schedl, A., de Crombrugghe, B., 2002. The transcription factor Sox9 has essential roles in successive steps of the chondrocyte differentiation pathway and is required for expression of Sox5 and Sox6. Genes Dev. 16, 2813–2828. https://doi.org/10.1101/gad.1017802

Aledort, L., Ljung, R., Mann, K., Pipe, S., 2014. Factor VIII therapy for hemophilia A: current and future issues. Expert Rev. Hematol. 7, 373–385. https://doi.org/10.1586/17474086.2014.899896

Allen, M.R., Burr, D.B., 2014. Bone Modeling and Remodeling, in: Basic and Applied Bone Biology. Elsevier, pp. 75–90. https://doi.org/10.1016/B978-0-12-416015-6.00004-6

Almazroo, O.A., Miah, M.K., Venkataramanan, R., 2017. Drug Metabolism in the Liver. Clin. Liver Dis. 21, 1–20. https://doi.org/10.1016/j.cld.2016.08.001

AlQahtani, A.D., O'Connor, D., Domling, A., Goda, S.K., 2019. Strategies for the production of long-acting therapeutics and efficient drug delivery for cancer treatment. Biomed. Pharmacother. 113, 108750. https://doi.org/10.1016/j.biopha.2019.108750

Andersen, T.L., Sondergaard, T.E., Skorzynska, K.E., Dagnaes-Hansen, F., Plesner, T.L., Hauge, E.M., Plesner, T., Delaisse, J.-M., 2009. A Physical Mechanism for Coupling Bone Resorption and Formation in Adult Human Bone. Am. J. Pathol. 174, 239–247. https://doi.org/10.2353/ajpath.2009.080627

Angers, S., Moon, R.T., 2009. Proximal events in Wnt signal transduction. Nat Rev Mol Cell Biol 10, 468–477.

Asagiri, M., Takayanagi, H., 2007. The molecular understanding of osteoclast differentiation. Bone 40, 251–264. https://doi.org/10.1016/j.bone.2006.09.023

Atkins, G.J., Rowe, P.S., Lim, H.P., Welldon, K.J., Ormsby, R., Wijenayaka, A.R., Zelenchuk, L., Evdokiou, A., Findlay, D.M., 2011. Sclerostin is a locally acting regulator of late-osteoblast/preosteocyte differentiation and regulates mineralization through a MEPE-ASARM-dependent mechanism. J. Bone Miner. Res. 26, 1425–1436. https://doi.org/10.1002/jbmr.345

Bakker, A.D., Klein-Nulend, J., 2010. Mechanisms of Osteocyte Mechanotransduction. Clin. Rev. Bone Miner. Metab. 8, 163–169. https://doi.org/10.1007/s12018-010-9079-x

Balemans, W., Ebeling, M., Patel, N., Van Hul, E., Olson, P., Dioszegi, M., Lacza, C., Wuyts, W., Van Den Ende, J., Willems, P., Paes-Alves, A.F., Hill, S., Bueno, M., Ramos, F.J., Tacconi, P., Dikkers, F.G., Stratakis, C., Lindpaintner, K., Vickery, B., Foernzler, D., Van Hul, W., 2001. Increased bone density in sclerosteosis is due to the deficiency of a novel secreted protein (SOST). Hum. Mol. Genet. 10, 537–544. https://doi.org/10.1093/hmg/10.5.537

Balemans, W., Patel, N., Ebeling, M., Van Hul, E., Wuyts, W., Lacza, C., Dioszegi, M., Dikkers, F.G., Hildering, P., Willems, P.J., Verheij, J.B.G.M., Lindpaintner, K., Vickery, B., Foernzler, D., Van Hul, W., 2002. Identification of a 52 kb deletion downstream of the SOST gene in patients with van Buchem disease. J. Med. Genet. 39, 91–97. https://doi.org/10.1136/jmg.39.2.91

Balemans, W, Patel, N., Ebeling, M., Van Hul, E., Wuyts, W., Lacza, C., Dioszegi, M., Dikkers, F.G., Hildering, P., Willems, P.J., Verheij, J.B.G.M., Lindpaintner, K., Vickery, B., Foernzler, D., Van Hul, W., 2002. Identification of a 52 kb deletion downstream of the SOST gene in patients with van Buchem disease. J. Med. Genet. 39, 91–97.

Balemans, W., Van Den Ende, J., Freire Paes-Alves, A., Dikkers, F.G., Willems, P.J., Vanhoenacker, F., de Almeida-Melo, N., Alves, C.F., Stratakis, C.A., Hill, S.C., Van Hul, W., 1999. Localization of the Gene for Sclerosteosis to the van Buchem Disease–Gene Region on Chromosome 17q12–q21. Am. J. Hum. Genet. 64, 1661–1669. https://doi.org/10.1086/302416

Baron, R., Kneissel, M., 2013. WNT signaling in bone homeostasis and disease: from human mutations to treatments. Nat. Med. 19, 179–192. https://doi.org/10.1038/nm.3074

Beck, M., 2018. Treatment strategies for lysosomal storage disorders. Dev. Med. Child Neurol. 60, 13–18. https://doi.org/10.1111/dmcn.13600

Beier, E.E., Sheu, T.-J., Resseguie, E.A., Takahata, M., Awad, H.A., Cory-Slechta, D.A., Puzas, J.E., 2017. Sclerostin activity plays a key role in the negative effect of glucocorticoid signaling on osteoblast function in mice. Bone Res. 5, 1–14. https://doi.org/10.1038/boneres.2017.13

Beighton, P., 1988. Sclerosteosis. J. Med. Genet. 25, 200–203.

Beighton, P., Barnard, A., Hamersma, H., Wouden, A. van der, 1984. The syndromic status of sclerosteosis and van Buchem disease. Clin Genet 25, 175–181. https://doi.org/10.1111/j.1399-0004.1984.tb00481.x

Beighton, P., Davidson, J., Durr, L., Hamersma, H., 1977. Sclerosteosis — An autosomal recessive disorder. Clin Genet 11, 1–7. https://doi.org/10.1111/j.1399-0004.1977.tb01269.x

Beighton, P., Durr, L., Hamersma, H., 1976. The Clinical Features of SclerosteosisA Review of the Manifestations in Twenty-Five Affected Individuals. Ann. Intern. Med. 84, 393–397. https://doi.org/10.7326/0003-4819-84-4-393

Beighton, P., Hamersma, H., 1979. Sclerosteosis in South Africa. South Afr. Med. J. Suid-Afr. Tydskr. Vir Geneeskd. 55, 783–788.

Berendsen, A.D., Olsen, B.R., 2015. Bone development. Bone 80, 14–18. https://doi.org/10.1016/j.bone.2015.04.035

Bezooijen, R.L. van, Bronckers, A.L., Gortzak, R.A., Hogendoorn, P.C.W., Wee-Pals, L. van der, Balemans, W., Oostenbroek, H.J., Hul, W.V., Hamersma, H., Dikkers, F.G., Hamdy, N.A.T., Papapoulos, S.E., Löwik, C.W.G.M., 2009. Sclerostin in Mineralized Matrices and van Buchem Disease: J. Dent. Res. https://doi.org/10.1177/0022034509338340

Bezooijen, R.L. van, DeRuiter, M.C., Vilain, N., Monteiro, R.M., Visser, A., Wee-Pals, L. van der, Munsteren, C.J. van, Hogendoorn, P.C.W., Aguet, M., Mummery, C.L., Papapoulos, S.E., Dijke, P.T., Löwik, C.W.G.M., 2007. SOST expression is restricted to the great arteries during embryonic and neonatal cardiovascular development. Dev. Dyn. 236, 606–612. https://doi.org/10.1002/dvdy.21054

Bilezikian, J.P. (Ed.), 2019. Primer on the metabolic bone diseases and disorders of mineral metabolism, Ninth edition / editor-in-Chief, John P. Bilezikian, MD, PhD (hon) ; senior associate editors, Roger Bouillon, MD, PhD, FRCP, Tom Clemens, PhD, Juliet Compston, MD, FRCP, FRCPath, FMedSci ; associate editors, Doug Bauer, MD [and nine others]. ed. Wiley-Blackwell, Hoboken, NJ.

Bonate, P.L., 2011. Pharmacokinetic-Pharmacodynamic Modeling and Simulation, 2nd ed. Springer US. https://doi.org/10.1007/978-1-4419-9485-1

Bonewald, L.F., 2006. Mechanosensation and Transduction in Osteocytes. BoneKEy Osteovision 3, 7–15. https://doi.org/10.1138/20060233

Boschert, V., Frisch, C., Back, J.W., van Pee, K., Weidauer, S.E., Muth, E.-M., Schmieder, P., Beerbaum, M., Knappik, A., Timmerman, P., Mueller, T.D., 2016. The sclerostin-neutralizing antibody AbD09097 recognizes an epitope adjacent to sclerostin's binding site for the Wnt co-receptor LRP6. Open Biol. 6. https://doi.org/10.1098/rsob.160120

Boschert, V., van Dinther, M., Weidauer, S., van Pee, K., Muth, E.-M., ten Dijke, P., Mueller, T.D., 2013. Mutational Analysis of Sclerostin Shows Importance of the Flexible Loop and the Cystine-Knot for Wnt-Signaling Inhibition. PLoS ONE 8. https://doi.org/10.1371/journal.pone.0081710

Bouaziz, W., Funck-Brentano, T., Lin, H., Marty, C., Ea, H.-K., Hay, E., Cohen-Solal, M., 2015. Loss of sclerostin promotes osteoarthritis in mice via β-catenin-dependent and -independent Wnt pathways. Arthritis Res. Ther. 17, 24. https://doi.org/10.1186/s13075-015-0540-6

Bou-Gharios, G., de Crombrugghe, B., 2008. Chapter 15 - Type I Collagen Structure, Synthesis, and Regulation, in: Bilezikian, J.P., Raisz, L.G., Martin, T.J. (Eds.), Principles of Bone Biology (Third Edition). Academic Press, San Diego, pp. 285–318. https://doi.org/10.1016/B978-0-12-373884-4.00034-3

Bourhis, E., Tam, C., Franke, Y., Bazan, J.F., Ernst, J., Hwang, J., Costa, M., Cochran, A.G., Hannoush, R.N., 2010. Reconstitution of a Frizzled8·Wnt3a·LRP6 Signaling Complex Reveals Multiple Wnt and

Dkk1 Binding Sites on LRP6. J. Biol. Chem. 285, 9172–9179. https://doi.org/10.1074/jbc.M109.092130

Bourhis, E., Wang, W., Tam, C., Hwang, J., Zhang, Y., Spittler, D., Huang, O.W., Gong, Y., Estevez, A., Zilberleyb, I., Rouge, L., Chiu, C., Wu, Y., Costa, M., Hannoush, R.N., Franke, Y., Cochran, A.G., 2011. Wnt Antagonists Bind through a Short Peptide to the First β-Propeller Domain of LRP5/6. Structure 19, 1433–1442. https://doi.org/10.1016/j.str.2011.07.005

Boyce, B.F., Xing, L., 2008. Functions of RANKL/RANK/OPG in bone modeling and remodeling. Arch. Biochem. Biophys. 473, 139–146. https://doi.org/10.1016/j.abb.2008.03.018

Boyce, B.F., Yao, Z., Xing, L., 2009. Osteoclasts have Multiple Roles in Bone in Addition to Bone Resorption. Crit. Rev. Eukaryot. Gene Expr. 19, 171–180.

Boyce, R.W., Brown, D., Felx, M., Mellal, N., Locher, K., Pyrah, I., Ominsky, M.S., Taylor, S., 2018. Decreased osteoprogenitor proliferation precedes attenuation of cancellous bone formation in ovariectomized rats treated with sclerostin antibody. Bone Rep. 8, 90–94. https://doi.org/10.1016/j.bonr.2018.03.001

Boyle, W.J., Simonet, W.S., Lacey, D.L., 2003. Osteoclast differentiation and activation. Nature 423, 337–342. https://doi.org/10.1038/nature01658

Bozal, C.B., Sánchez, L.M., Ubios, A.M., 2012. The lacuno-canalicular system (LCS) and osteocyte network of alveolar bone by confocal laser scanning microscopy (CLSM). Acta Odontol. Latinoam. AOL 25, 123–131.

Brandao-Burch, A., Utting, J.C., Orriss, I.R., Arnett, T.R., 2005. Acidosis inhibits bone formation by osteoblasts in vitro by preventing mineralization. Calcif. Tissue Int. 77, 167–174. https://doi.org/10.1007/s00223-004-0285-8

Brodsky, B., Persikov, A.V., 2005. Molecular structure of the collagen triple helix. Adv. Protein Chem. 70, 301–339. https://doi.org/10.1016/S0065-3233(05)70009-7

Brubaker, D.K., Lauffenburger, D.A., 2020. Translating preclinical models to humans. Science 367, 742–743. https://doi.org/10.1126/science.aay8086

Brunkow, M.E., Gardner, J.C., Van Ness, J., Paeper, B.W., Kovacevich, B.R., Proll, S., Skonier, J.E., Zhao, L., Sabo, P.J., Fu, Y.-H., Alisch, R.S., Gillett, L., Colbert, T., Tacconi, P., Galas, D., Hamersma, H., Beighton, P., Mulligan, J.T., 2001. Bone Dysplasia Sclerosteosis Results from Loss of the SOST Gene Product, a Novel Cystine Knot–Containing Protein. Am. J. Hum. Genet. 68, 577–589.

Bueno, M., Olivan, G., Jimenez, A., Garagorri, J.M., Sarria, A., Bueno, A.L., Bueno Jr., M., Ramos, F.J., 1994. Sclerosteosis in a Spanish male: first report in a person of Mediterranean origin. J Med Genet 31, 976–977.

Burr, D.B., 2002. Targeted and nontargeted remodeling. Bone 30, 2–4. https://doi.org/10.1016/s8756-3282(01)00619-6

Capulli, M., Paone, R., Rucci, N., 2014. Osteoblast and osteocyte: games without frontiers. Arch. Biochem. Biophys. 561, 3–12. https://doi.org/10.1016/j.abb.2014.05.003

Carter, P.J., 2011. Introduction to current and future protein therapeutics: a protein engineering perspective. Exp. Cell Res. 317, 1261–1269. https://doi.org/10.1016/j.yexcr.2011.02.013

Chabadel, A., Bañon-Rodríguez, I., Cluet, D., Rudkin, B.B., Wehrle-Haller, B., Genot, E., Jurdic, P., Anton, I.M., Saltel, F., 2007. CD44 and β3 Integrin Organize Two Functionally Distinct Actin-based Domains in Osteoclasts. Mol. Biol. Cell 18, 4899–4910. https://doi.org/10.1091/mbc.E07-04-0378

Chakrabarti, A.M., Henser-Brownhill, T., Monserrat, J., Poetsch, A.R., Luscombe, N.M., Scaffidi, P., 2019. Target-Specific Precision of CRISPR-Mediated Genome Editing. Mol. Cell 73, 699-713.e6. https://doi.org/10.1016/j.molcel.2018.11.031

Chambers, T.J., Fuller, K., 1985. Bone cells predispose bone surfaces to resorption by exposure of mineral to osteoclastic contact. J. Cell Sci. 76, 155–165.

Chan, B.Y., Fuller, E.S., Russell, A.K., Smith, S.M., Smith, M.M., Jackson, M.T., Cake, M.A., Read, R.A., Bateman, J.F., Sambrook, P.N., Little, C.B., 2011. Increased chondrocyte sclerostin may protect against cartilage degradation in osteoarthritis. Osteoarthritis Cartilage 19, 874–885. https://doi.org/10.1016/j.joca.2011.04.014

Chandra, A., Lin, T., Young, T., Tong, W., Ma, X., Tseng, W.-J., Kramer, I., Kneissel, M., Levine, M.A., Zhang, Y., Cengel, K., Liu, X.S., Qin, L., 2017. Suppression of Sclerostin Alleviates Radiation-Induced Bone Loss by Protecting Bone-Forming Cells and Their Progenitors Through Distinct Mechanisms. J. Bone Miner. Res. 32, 360–372. https://doi.org/10.1002/jbmr.2996

Chang, M.-K., Kramer, I., Huber, T., Kinzel, B., Guth-Gundel, S., Leupin, O., Kneissel, M., 2014. Disruption of Lrp4 function by genetic deletion or pharmacological blockade increases bone mass and serum sclerostin levels. Proc. Natl. Acad. Sci. 111, E5187–E5195. https://doi.org/10.1073/pnas.1413828111

Charles, J.F., Aliprantis, A.O., 2014. Osteoclasts: more than "bone eaters." Trends Mol. Med. 20, 449–459. https://doi.org/10.1016/j.molmed.2014.06.001

Charles, J.F., Siris, E.S., Roodman, G.D., 2018. Paget Disease of Bone, in: Primer on the Metabolic Bone Diseases and Disorders of Mineral Metabolism. John Wiley & Sons, Ltd, pp. 713–720. https://doi.org/10.1002/9781119266594.ch92

Chouinard, L., Felx, M., Mellal, N., Varela, A., Mann, P., Jolette, J., Samadfam, R., Smith, S.Y., Locher, K., Buntich, S., Ominsky, M.S., Pyrah, I., Boyce, R.W., 2016. Carcinogenicity risk assessment of romosozumab: A review of scientific weight-of-evidence and findings in a rat lifetime pharmacology study. Regul. Toxicol. Pharmacol. 81, 212–222. https://doi.org/10.1016/j.yrtph.2016.08.010

Chow, J., Tobias, J.H., Colston, K.W., Chambers, T.J., 1992. Estrogen maintains trabecular bone volume in rats not only by suppression of bone resorption but also by stimulation of bone formation. J. Clin. Invest. 89, 74–78. https://doi.org/10.1172/JCI115588

Christakos, S., Dhawan, P., Verstuyf, A., Verlinden, L., Carmeliet, G., 2016. Vitamin D: Metabolism, Molecular Mechanism of Action, and Pleiotropic Effects. Physiol. Rev. 96, 365–408. https://doi.org/10.1152/physrev.00014.2015

Civitelli, R., 2008. Cell-Cell Communication in the Osteoblast/Osteocyte Lineage. Arch. Biochem. Biophys. 473, 188–192. https://doi.org/10.1016/j.abb.2008.04.005

Clarke, B., 2008. Normal Bone Anatomy and Physiology. Clin. J. Am. Soc. Nephrol. CJASN 3, S131–S139. https://doi.org/10.2215/CJN.04151206

Collette, N.M., Yee, C.S., Hum, N.R., Murugesh, D.K., Christiansen, B.A., Xie, L., Economides, A.N., Manilay, J.O., Robling, A.G., Loots, G.G., 2016. Sostdc1 deficiency accelerates fracture healing by promoting the expansion of periosteal mesenchymal stem cells. Bone 88, 20–30. https://doi.org/10.1016/j.bone.2016.04.005

Consensus development conference: diagnosis, prophylaxis, and treatment of osteoporosis, 1993. . Am. J. Med. 94, 646–650. https://doi.org/10.1016/0002-9343(93)90218-e

Cooper, C., Ferrari, S.L., 2017. IOF Compendium of Osteoporosis.

Costa, A.G., Cusano, N.E., Silva, B.C., Cremers, S., Bilezikian, J.P., 2011. Cathepsin K: its skeletal actions and role as a therapeutic target in osteoporosis. Nat. Rev. Rheumatol. 7, 447–456. https://doi.org/10.1038/nrrheum.2011.77

Crockett, J. C., Mellis, D.J., Scott, D.I., Helfrich, M.H., 2011. New knowledge on critical osteoclast formation and activation pathways from study of rare genetic diseases of osteoclasts: focus on the RANK/RANKL axis. Osteoporos. Int. J. Establ. Result Coop. Eur. Found. Osteoporos. Natl. Osteoporos. Found. USA 22, 1–20. https://doi.org/10.1007/s00198-010-1272-8

Crockett, Julie C., Rogers, M.J., Coxon, F.P., Hocking, L.J., Helfrich, M.H., 2011. Bone remodelling at a glance. J. Cell Sci. 124, 991–998. https://doi.org/10.1242/jcs.063032

Czajkowsky, D.M., Hu, J., Shao, Z., Pleass, R.J., 2012. Fc-fusion proteins: new developments and future perspectives. EMBO Mol. Med. 4, 1015–1028. https://doi.org/10.1002/emmm.201201379

Dallas, S.L., Prideaux, M., Bonewald, L.F., 2013. The Osteocyte: An Endocrine Cell … and More. Endocr. Rev. 34, 658–690. https://doi.org/10.1210/er.2012-1026

Day, T.F., Guo, X., Garrett-Beal, L., Yang, Y., 2005. Wnt/beta-catenin signaling in mesenchymal progenitors controls osteoblast and chondrocyte differentiation during vertebrate skeletogenesis. Dev. Cell 8, 739–750. https://doi.org/10.1016/j.devcel.2005.03.016

Dekkers, G., Bentlage, A.E.H., Stegmann, T.C., Howie, H.L., Lissenberg-Thunnissen, S., Zimring, J., Rispens, T., Vidarsson, G., 2017. Affinity of human IgG subclasses to mouse Fc gamma receptors. mAbs 9, 767–773. https://doi.org/10.1080/19420862.2017.1323159

Delgado-Calle, J., Sato, A.Y., Bellido, T., 2017. Role and mechanism of action of sclerostin in bone. Bone, Sclerostin: From Bench to Bedside 96, 29–37. https://doi.org/10.1016/j.bone.2016.10.007

Demay, M.B., Sabbagh, Y., Carpenter, T.O., 2007. Calcium and vitamin D: what is known about the effects on growing bone. Pediatrics 119 Suppl 2, S141-144. https://doi.org/10.1542/peds.2006-2023F

Dempster, D.W., Lindsay, R., 1993. Pathogenesis of osteoporosis. Lancet Lond. Engl. 341, 797–801. https://doi.org/10.1016/0140-6736(93)90570-7

Doyle, M.L., 1997. Characterization of binding interactions by isothermal titration calorimetry. Curr. Opin. Biotechnol. 8, 31–35. https://doi.org/10.1016/S0958-1669(97)80154-1

Drake, M.T., Khosla, S., 2018. Sex Steroids and the Pathogenesis of Osteoporosis, in: Primer on the Metabolic Bone Diseases and Disorders of Mineral Metabolism. John Wiley & Sons, Ltd, pp. 412–418. https://doi.org/10.1002/9781119266594.ch52

du Plessis, J.J., 1993. Sclerosteosis: neurosurgical experience with 14 cases. J. Neurosurg. 78, 388–392. https://doi.org/10.3171/jns.1993.78.3.0388

Duchamp de Lageneste, O., Julien, A., Abou-Khalil, R., Frangi, G., Carvalho, C., Cagnard, N., Cordier, C., Conway, S.J., Colnot, C., 2018. Periosteum contains skeletal stem cells with high bone regenerative potential controlled by Periostin. Nat. Commun. 9, 1–15. https://doi.org/10.1038/s41467-018-03124-z

Ducy, P., Schinke, T., Karsenty, G., 2000. The osteoblast: a sophisticated fibroblast under central surveillance. Science 289, 1501–1504. https://doi.org/10.1126/science.289.5484.1501

Dwek, J.R., 2010. The periosteum: what is it, where is it, and what mimics it in its absence? Skeletal Radiol. 39, 319–323. https://doi.org/10.1007/s00256-009-0849-9

Eghbali-Fatourechi, G., Khosla, S., Sanyal, A., Boyle, W.J., Lacey, D.L., Riggs, B.L., 2003. Role of RANK ligand in mediating increased bone resorption in early postmenopausal women. J. Clin. Invest. 111, 1221–1230. https://doi.org/10.1172/JCI17215

Engelbert, R.H., Uiterwaal, C.S., van der Hulst, A., Witjes, B., Helders, P.J., Pruijs, H.E., 2003. Scoliosis in children with osteogenesis imperfecta: influence of severity of disease and age of reaching motor milestones. Eur. Spine J. 12, 130–134. https://doi.org/10.1007/s00586-002-0491-x

Eschbach, J.W., Egrie, J.C., Downing, M.R., Browne, J.K., Adamson, J.W., 1987. Correction of the anemia of end-stage renal disease with recombinant human erythropoietin. Results of a combined phase I and II clinical trial. N. Engl. J. Med. 316, 73–78. https://doi.org/10.1056/NEJM198701083160203

Esteban Fernández de Ávila, B., Watkins, H.M., Pingarrón, J.M., Plaxco, K.W., Palleschi, G., Ricci, F., 2013. Determinants of the Detection Limit and Specificity of Surface-Based Biosensors. Anal. Chem. 85, 6593–6597. https://doi.org/10.1021/ac4012123

Ettenberg, S.A., Charlat, O., Daley, M.P., Liu, S., Vincent, K.J., Stuart, D.D., Schuller, A.G., Yuan, J., Ospina, B., Green, J., Yu, Q., Walsh, R., Li, S., Schmitz, R., Heine, H., Bilic, S., Ostrom, L., Mosher, R., Hartlepp, K.F., Zhu, Z., Fawell, S., Yao, Y.-M., Stover, D., Finan, P.M., Porter, J.A., Sellers, W.R., Klagge, I.M., Cong, F., 2010. Inhibition of tumorigenesis driven by different Wnt proteins requires blockade of distinct ligand-binding regions by LRP6 antibodies. Proc. Natl. Acad. Sci. 107, 15473–15478. https://doi.org/10.1073/pnas.1007428107

Everts, V., Delaissé, J.M., Korper, W., Jansen, D.C., Tigchelaar-Gutter, W., Saftig, P., Beertsen, W., 2002. The bone lining cell: its role in cleaning Howship's lacunae and initiating bone formation. J. Bone Miner. Res. Off. J. Am. Soc. Bone Miner. Res. 17, 77–90. https://doi.org/10.1359/jbmr.2002.17.1.77

Falahati-Nini, A., Riggs, B.L., Atkinson, E.J., O'Fallon, W.M., Eastell, R., Khosla, S., 2000. Relative contributions of testosterone and estrogen in regulating bone resorption and formation in normal elderly men. J. Clin. Invest. 106, 1553–1560.

Farr, J.N., Roforth, M.M., Fujita, K., Nicks, K.M., Cunningham, J.M., Atkinson, E.J., Therneau, T.M., McCready, L.K., Peterson, J.M., Drake, M.T., Monroe, D.G., Khosla, S., 2015. Effects of Age and

Estrogen on Skeletal Gene Expression in Humans as Assessed by RNA Sequencing. PloS One 10, e0138347. https://doi.org/10.1371/journal.pone.0138347

Feng, J.Q., Huang, H., Lu, Y., Ye, L., Xie, Y., Tsutsui, T.W., Kunieda, T., Castranio, T., Scott, G., Bonewald, L.B., Mishina, Y., 2003. The Dentin matrix protein 1 (Dmp1) is specifically expressed in mineralized, but not soft, tissues during development. J. Dent. Res. 82, 776–780. https://doi.org/10.1177/154405910308201003

Feng, X., McDonald, J.M., 2011. Disorders of Bone Remodeling. Annu. Rev. Pathol. 6, 121–145. https://doi.org/10.1146/annurev-pathol-011110-130203

Fijalkowski, I., Geets, E., Steenackers, E., Hoof, V.V., Ramos, F.J., Mortier, G., Fortuna, A.M., Hul, W.V., Boudin, E., 2016. A Novel Domain-Specific Mutation in a Sclerosteosis Patient Suggests a Role of LRP4 as an Anchor for Sclerostin in Human Bone. J. Bone Miner. Res. 31, 874–881. https://doi.org/10.1002/jbmr.2782

Finkelstein, J.S., Lee, H., Leder, B.Z., Burnett-Bowie, S.-A.M., Goldstein, D.W., Hahn, C.W., Hirsch, S.C., Linker, A., Perros, N., Servais, A.B., Taylor, A.P., Webb, M.L., Youngner, J.M., Yu, E.W., 2016. Gonadal steroid-dependent effects on bone turnover and bone mineral density in men. J. Clin. Invest. 126, 1114–1125. https://doi.org/10.1172/JCI84137

Florencio-Silva, R., Sasso, G.R. da S., Sasso-Cerri, E., Simões, M.J., Cerri, P.S., 2015. Biology of Bone Tissue: Structure, Function, and Factors That Influence Bone Cells. BioMed Res. Int. 2015. https://doi.org/10.1155/2015/421746

Fosmoe, R.J., Holm, R.S., Hildreth, R.C., 1968. Van Buchem's disease (hyperostosis corticalis generalisata familiaris). A case report. Radiology 90, 771–774. https://doi.org/10.1148/90.4.771

Franceschi, R.T., Iyer, B.S., Cui, Y., 1994. Effects of ascorbic acid on collagen matrix formation and osteoblast differentiation in murine MC3T3-E1 cells. J. Bone Miner. Res. Off. J. Am. Soc. Bone Miner. Res. 9, 843–854. https://doi.org/10.1002/jbmr.5650090610

Francis, R.M., Selby, P.L., 1997. Osteomalacia. Baillières Clin. Endocrinol. Metab., Metabolic Bone Disease 11, 145–163. https://doi.org/10.1016/S0950-351X(97)80569-1

Fratzl-Zelman, N., Fratzl, P., Hörandner, H., Grabner, B., Varga, F., Ellinger, A., Klaushofer, K., 1998. Matrix mineralization in MC3T3-E1 cell cultures initiated by beta-glycerophosphate pulse. Bone 23, 511–520.

Frost, H.M., 1994. Wolff's Law and bone's structural adaptations to mechanical usage: an overview for clinicians. Angle Orthod. 64, 175–188. https://doi.org/10.1043/0003-3219(1994)064<0175:WLABSA>2.0.CO;2

Fuchs, R.K., Thompson, W.R., Warden, S.J., 2019. Bone biology, in: Bone Repair Biomaterials. Elsevier, pp. 15–52. https://doi.org/10.1016/B978-0-08-102451-5.00002-0

Fulzele, K., Lai, F., Dedic, C., Saini, V., Uda, Y., Shi, C., Tuck, P., Aronson, J.L., Liu, X., Spatz, J.M., Wein, M.N., Pajevic, P.D., 2017. Osteocyte-Secreted Wnt Signaling Inhibitor Sclerostin Contributes to Beige Adipogenesis in Peripheral Fat Depots. J. Bone Miner. Res. 32, 373–384. https://doi.org/10.1002/jbmr.3001

Funck-Brentano, T., Nilsson, K.H., Brommage, R., Henning, P., Lerner, U.H., Koskela, A., Tuukkanen, J., Cohen-Solal, M., Movérare-Skrtic, S., Ohlsson, C., 2018. Porcupine inhibitors impair trabecular and cortical bone mass and strength in mice. J. Endocrinol. 238, 13–23. https://doi.org/10.1530/JOE-18-0153

Gardner, J.C., van Bezooijen, R.L., Mervis, B., Hamdy, N.A.T., Löwik, C.W.G.M., Hamersma, H., Beighton, P., Papapoulos, S.E., 2005. Bone Mineral Density in Sclerosteosis; Affected Individuals and Gene Carriers. J. Clin. Endocrinol. Metab. 90, 6392–6395. https://doi.org/10.1210/jc.2005-1235

Gasser, J.A., Kneissel, M., 2017. Bone Physiology and Biology, in: Smith, S.Y., Varela, A., Samadfam, R. (Eds.), Bone Toxicology, Molecular and Integrative Toxicology. Springer International Publishing, Cham, pp. 27–94. https://doi.org/10.1007/978-3-319-56192-9_2

Gehron Robey, P., 2008. Chapter 17 - Noncollagenous Bone Matrix Proteins, in: Bilezikian, J.P., Raisz, L.G., Martin, T.J. (Eds.), Principles of Bone Biology (Third Edition). Academic Press, San Diego, pp. 335–349. https://doi.org/10.1016/B978-0-12-373884-4.00036-7

Gherardi, G., Lo Cascio, V., Bonucci, E., 1980. Fine structure of nuclei and cytoplasm of osteoclasts in Paget's disease of bone. Histopathology 4, 63–74. https://doi.org/10.1111/j.1365-2559.1980.tb02898.x

Gifre, L., Peris, P., Monegal, A., Martinez de Osaba, M.J., Alvarez, L., Guañabens, N., 2011. Osteomalacia revisited. Clin. Rheumatol. 30, 639–645. https://doi.org/10.1007/s10067-010-1587-z

Glass, D.A., Bialek, P., Ahn, J.D., Starbuck, M., Patel, M.S., Clevers, H., Taketo, M.M., Long, F., McMahon, A.P., Lang, R.A., Karsenty, G., 2005. Canonical Wnt signaling in differentiated osteoblasts controls osteoclast differentiation. Dev. Cell 8, 751–764. https://doi.org/10.1016/j.devcel.2005.02.017

Goldring, S.R., 2015. The osteocyte: key player in regulating bone turnover. RMD Open 1. https://doi.org/10.1136/rmdopen-2015-000049

Golds, G., Houdek, D., Arnason, T., 2017. Male Hypogonadism and Osteoporosis: The Effects, Clinical Consequences, and Treatment of Testosterone Deficiency in Bone Health. Int. J. Endocrinol. 2017. https://doi.org/10.1155/2017/4602129

Golub, E.E., 2009. Role of Matrix Vesicles in Biomineralization. Biochim. Biophys. Acta 1790, 1592–1598. https://doi.org/10.1016/j.bbagen.2009.09.006

Greenbaum, A., Chan, K.Y., Dobreva, T., Brown, D., Balani, D.H., Boyce, R., Kronenberg, H.M., McBride, H.J., Gradinaru, V., 2017. Bone CLARITY: Clearing, imaging, and computational analysis of osteoprogenitors within intact bone marrow. Sci. Transl. Med. 9. https://doi.org/10.1126/scitranslmed.aah6518

Grimsley, G.R., Pace, C.N., 2004. Spectrophotometric determination of protein concentration. Curr. Protoc. Protein Sci. Chapter 3, Unit 3.1. https://doi.org/10.1002/0471140864.ps0301s33

Guañabens, N., Ruiz-Gaspà, S., Gifre, L., Miquel, R., Peris, P., Monegal, A., Dubrueil, M., Arias, A., Parés, A., 2016. Sclerostin Expression in Bile Ducts of Patients With Chronic Cholestasis May Influence the Bone Disease in Primary Biliary Cirrhosis. J. Bone Miner. Res. Off. J. Am. Soc. Bone Miner. Res. 31, 1725–1733. https://doi.org/10.1002/jbmr.2845

Gurevitch, O., Slavin, S., Feldman, A.G., 2007. Conversion of red bone marrow into yellow - Cause and mechanisms. Med. Hypotheses 69, 531–536. https://doi.org/10.1016/j.mehy.2007.01.052

Haapasalo, H., Kontulainen, S., Sievänen, H., Kannus, P., Järvinen, M., Vuori, I., 2000. Exercise-induced bone gain is due to enlargement in bone size without a change in volumetric bone density: a peripheral quantitative computed tomography study of the upper arms of male tennis players. Bone 27, 351–357. https://doi.org/10.1016/s8756-3282(00)00331-8

Haggag, Y.A., Donia, A.A., Osman, M.A., El-Gizawy, S.A., 2018. Peptides as Drug Candidates: Limitations and Recent Development Perspectives. Biomed. J. Sci. Tech. Res. 8. https://doi.org/10.26717/BJSTR.2018.08.001694

Hall, B.K., Miyake, T., 1992. The membranous skeleton: the role of cell condensations in vertebrate skeletogenesis. Anat. Embryol. (Berl.) 186, 107–124. https://doi.org/10.1007/BF00174948

Hamersma, H., Gardner, J., Beighton, P., 2003. The natural history of sclerosteosis. Clin Genet 63, 192–197.

Hamersma, H., Hofmeyr, L., 2007. Too much bone: the middle ear in sclerosing bone dysplasias. Adv Otorhinolaryngol 65, 61–67. https://doi.org/10.1159/000098673

Hammes, G.D., Hammes-Schiffer, S., 2015. Entropy and Gibbs Energy, in: Physical Chemistry for the Biological Sciences. John Wiley & Sons, Ltd, pp. 23–42. https://doi.org/10.1002/9781118859148.ch2

Han, Y., You, X., Xing, W., Zhang, Z., Zou, W., 2018. Paracrine and endocrine actions of bone—the functions of secretory proteins from osteoblasts, osteocytes, and osteoclasts. Bone Res. 6, 1–11. https://doi.org/10.1038/s41413-018-0019-6

Hartmann, C., 2007. Skeletal development--Wnts are in control. Mol. Cells 24, 177–184.

Hasegawa, T., Yamamoto, T., Tsuchiya, E., Hongo, H., Tsuboi, K., Kudo, A., Abe, M., Yoshida, T., Nagai, T., Khadiza, N., Yokoyama, A., Oda, K., Ozawa, H., de Freitas, P.H.L., Li, M., Amizuka, N., 2017. Ultrastructural and biochemical aspects of matrix vesicle-mediated mineralization. Jpn. Dent. Sci. Rev. 53, 34–45. https://doi.org/10.1016/j.jdsr.2016.09.002

Hattner, R., Epker, B.N., Frost, H.M., 1965. Suggested sequential mode of control of changes in cell behaviour in adult bone remodelling. Nature 206, 489–490. https://doi.org/10.1038/206489a0

He, W.-T., Chen, C., Pan, C., Zhang, M.-X., Yu, X.-F., Wang, D.-W., Hu, S.-H., 2016. Sclerosteosis caused by a novel nonsense mutation of SOST in a consanguineous family. Clin. Genet. 89, 205–209. https://doi.org/10.1111/cge.12655

He, X., Semenov, M., Tamai, K., Zeng, X., 2004. LDL receptor-related proteins 5 and 6 in Wnt/β-catenin signaling: Arrows point the way. Development 131, 1663–1677. https://doi.org/10.1242/dev.01117

Henriksen, K., Sørensen, M.G., Nielsen, R.H., Gram, J., Schaller, S., Dziegiel, M.H., Everts, V., Bollerslev, J., Karsdal, M.A., 2006. Degradation of the Organic Phase of Bone by Osteoclasts: A Secondary Role for Lysosomal Acidification. J. Bone Miner. Res. 21, 58–66. https://doi.org/10.1359/JBMR.050905

Higinbotham, N.L., Alexander, S.F., 1941. Osteopetrosis: Four cases in one family. Am. J. Surg. 53, 444–454. http://dx.doi.org/10.1016/S0002-9610(41)90660-8

Hill, T.P., Später, D., Taketo, M.M., Birchmeier, W., Hartmann, C., 2005. Canonical Wnt/beta-catenin signaling prevents osteoblasts from differentiating into chondrocytes. Dev. Cell 8, 727–738. https://doi.org/10.1016/j.devcel.2005.02.013

Hodsman, A.B., Steer, B.M., 1993. Early histomorphometric changes in response to parathyroid hormone therapy in osteoporosis: evidence for de novo bone formation on quiescent cancellous surfaces. Bone 14, 523–527. https://doi.org/10.1016/8756-3282(93)90190-l

Hofbauer, L.C., Khosla, S., Dunstan, C.R., Lacey, D.L., Spelsberg, T.C., Riggs, B.L., 1999. Estrogen stimulates gene expression and protein production of osteoprotegerin in human osteoblastic cells. Endocrinology 140, 4367–4370. https://doi.org/10.1210/endo.140.9.7131

Holdsworth, G., Greenslade, K., Jose, J., Stencel, Z., Kirby, H., Moore, A., Ke, H.Z., Robinson, M.K., 2018. Dampening of the bone formation response following repeat dosing with sclerostin antibody in mice is associated with up-regulation of Wnt antagonists. Bone 107, 93–103. https://doi.org/10.1016/j.bone.2017.11.003

Holdsworth, G., Roberts, S.J., Ke, H.Z., 2019. Novel actions of sclerostin on bone. J. Mol. Endocrinol. 62, R167–R185. https://doi.org/10.1530/JME-18-0176

Holdsworth, G., Slocombe, P., Doyle, C., Sweeney, B., Veverka, V., Le Riche, K., Franklin, R.J., Compson, J., Brookings, D., Turner, J., Kennedy, J., Garlish, R., Shi, J., Newnham, L., McMillan, D., Muzylak, M., Carr, M.D., Henry, A.J., Ceska, T., Robinson, M.K., 2012. Characterization of the Interaction of Sclerostin with the Low Density Lipoprotein Receptor-related Protein (LRP) Family of Wnt Co-receptors. J. Biol. Chem. 287, 26464–26477. https://doi.org/10.1074/jbc.M112.350108

Houschyar, K.S., Tapking, C., Borrelli, M.R., Popp, D., Duscher, D., Maan, Z.N., Chelliah, M.P., Li, J., Harati, K., Wallner, C., Rein, S., Pförringer, D., Reumuth, G., Grieb, G., Mouraret, S., Dadras, M., Wagner, J.M., Cha, J.Y., Siemers, F., Lehnhardt, M., Behr, B., 2019. Wnt Pathway in Bone Repair and Regeneration – What Do We Know So Far. Front. Cell Dev. Biol. 6. https://doi.org/10.3389/fcell.2018.00170

Hu, H., Hilton, M.J., Tu, X., Yu, K., Ornitz, D.M., Long, F., 2005. Sequential roles of Hedgehog and Wnt signaling in osteoblast development. Dev. Camb. Engl. 132, 49–60. https://doi.org/10.1242/dev.01564

Hughes, D.E., Dai, A., Tiffee, J.C., Li, H.H., Mundy, G.R., Boyce, B.F., 1996. Estrogen promotes apoptosis of murine osteoclasts mediated by TGF–β. Nat. Med. 2, 1132–1136. https://doi.org/10.1038/nm1096-1132

Ichida, F., Nishimura, R., Hata, K., Matsubara, T., Ikeda, F., Hisada, K., Yatani, H., Cao, X., Komori, T., Yamaguchi, A., Yoneda, T., 2004. Reciprocal roles of MSX2 in regulation of osteoblast and adipocyte differentiation. J. Biol. Chem. 279, 34015–34022. https://doi.org/10.1074/jbc.M403621200

Islam, A., Glomski, C., Henderson, E.S., 1990. Bone lining (endosteal) cells and hematopoiesis: a light microscopic study of normal and pathologic human bone marrow in plastic-embedded sections. Anat. Rec. 227, 300–306. https://doi.org/10.1002/ar.1092270304

Itin, P.H., Keseru, B., Hauser, V., 2001. Syndactyly/brachyphalangy and nail dysplasias as marker lesions for sclerosteosis. Dermatology 202, 259–260. https://doi.org/51649

Ito, Y., Fitzsimmons, J.S., Sanyal, A., Mello, M.A., Mukherjee, N., O'Driscoll, S.W., 2001. Localization of chondrocyte precursors in periosteum. Osteoarthritis Cartilage 9, 215–223. https://doi.org/10.1053/joca.2000.0378

Jason-Moller, L., Murphy, M., Bruno, J., 2006. Overview of Biacore systems and their applications. Curr. Protoc. Protein Sci. Chapter 19, Unit 19.13. https://doi.org/10.1002/0471140864.ps1913s45

Jastrzebski, S., Kalinowski, J., Stolina, M., Mirza, F., Torreggiani, E., Kalajzic, I., Won, H.Y., Lee, S.-K., Lorenzo, J., 2013. Changes In Bone Sclerostin Levels In Mice After Ovariectomy Vary Independently Of Changes In Serum Sclerostin Levels. J. Bone Miner. Res. 28, 618–626. https://doi.org/10.1002/jbmr.1773

Javaheri, B., Hopkinson, M., Poulet, B., Pollard, A.S., Shefelbine, S.J., Chang, Y.-M., Francis-West, P., Bou-Gharios, G., Pitsillides, A.A., 2016. Deficiency and Also Transgenic Overexpression of Timp-3 Both Lead to Compromised Bone Mass and Architecture In Vivo. PLoS ONE 11. https://doi.org/10.1371/journal.pone.0159657

Jerabek-Willemsen, M., André, T., Wanner, R., Roth, H.M., Duhr, S., Baaske, P., Breitsprecher, D., 2014. MicroScale Thermophoresis: Interaction analysis and beyond. J. Mol. Struct., Fluorescence studies of biomolecular association processes. 1077, 101–113. https://doi.org/10.1016/j.molstruc.2014.03.009

Jilka, R.L., Bellido, T., Almeida, M., Plotkin, L.I., O'Brien, C.A., Weinstein, R.S., Manolagas, S.C., 2008. Chapter 13 - Apoptosis of Bone Cells, in: Bilezikian, J.P., Raisz, L.G., Martin, T.J. (Eds.), Principles of Bone Biology (Third Edition). Academic Press, San Diego, pp. 237–261. https://doi.org/10.1016/B978-0-12-373884-4.00032-X

Jimi, E., Nakamura, I., Amano, H., Taguchi, Y., Tsurukai, T., Tamura, M., Takahashi, N., Suda, T., 1996. Osteoclast function is activated by osteoblastic cells through a mechanism involving cell-to-cell contact. Endocrinology 137, 2187–2190. https://doi.org/10.1210/endo.137.5.8612568

Johnston, C.C., Lavy, N., Lord, T., Vellios, F., Merritt, A.D., Deiss, W.P., 1968. Osteopetrosis. A clinical, genetic, metabolic, and morphologic study of the dominantly inherited, benign form. Medicine (Baltimore) 47, 149–167.

Joseph, M., Trinh, H.M., Mitra, A.K., 2017. Chapter 7 - Peptide and Protein-Based Therapeutic Agents∗, in: Mitra, A.K., Cholkar, K., Mandal, A. (Eds.), Emerging Nanotechnologies for Diagnostics, Drug Delivery and Medical Devices, Micro and Nano Technologies. Elsevier, Boston, pp. 145–167. https://doi.org/10.1016/B978-0-323-42978-8.00007-3

Kamiie, J., Ohtsuki, S., Iwase, R., Ohmine, K., Katsukura, Y., Yanai, K., Sekine, Y., Uchida, Y., Ito, S., Terasaki, T., 2008. Quantitative Atlas of Membrane Transporter Proteins: Development and Application of a Highly Sensitive Simultaneous LC/MS/MS Method Combined with Novel In-silico Peptide Selection Criteria. Pharm. Res. 25, 1469–1483. https://doi.org/10.1007/s11095-008-9532-4

Kantonen, S.A., Henriksen, N.M., Gilson, M.K., 2017. Evaluation and Minimization of Uncertainty in ITC Binding Measurements. Biochim. Biophys. Acta 1861, 485–498. https://doi.org/10.1016/j.bbagen.2016.09.002

Karaplis, A.C., 2008. Chapter 3 - Embryonic Development of Bone and Regulation of Intramembranous and Endochondral Bone Formation, in: Bilezikian, J.P., Raisz, L.G., Martin, T.J. (Eds.), Principles of Bone Biology (Third Edition). Academic Press, San Diego, pp. 53–84. https://doi.org/10.1016/B978-0-12-373884-4.00025-2

Kasugai, S., Fujisawa, R., Waki, Y., Miyamoto, K.-I., Ohya, K., 2010. Selective Drug Delivery System to Bone: Small Peptide (Asp)6 Conjugation. J. Bone Miner. Res. 15, 936–943. https://doi.org/10.1359/jbmr.2000.15.5.936

Kawane, T., Qin, X., Jiang, Q., Miyazaki, T., Komori, H., Yoshida, C.A., Matsuura-Kawata, V.K. dos S., Sakane, C., Matsuo, Y., Nagai, K., Maeno, T., Date, Y., Nishimura, R., Komori, T., 2018. Runx2 is required for the proliferation of osteoblast progenitors and induces proliferation by regulating Fgfr2 and Fgfr3. Sci. Rep. 8, 1–17. https://doi.org/10.1038/s41598-018-31853-0

Ke, H.Z., Richards, W.G., Li, X., Ominsky, M.S., 2012. Sclerostin and Dickkopf-1 as Therapeutic Targets in Bone Diseases. Endocr. Rev. 33, 747–783. https://doi.org/10.1210/er.2011-1060

Kelley, C.H., Lawlah, J.W., 1946. Albers-Schonberg disease; a family survey. Radiology 47, 507–513. https://doi.org/10.1148/47.5.507

Kenakin, T., 2016. The mass action equation in pharmacology. Br. J. Clin. Pharmacol. 81, 41–51. https://doi.org/10.1111/bcp.12810

Kenkre, J., Bassett, J., 2018. The bone remodelling cycle. Ann. Clin. Biochem. 55, 308–327. https://doi.org/10.1177/0004563218759371

Kennedy, O.D., Herman, B.C., Laudier, D.M., Majeska, R.J., Sun, H.B., Schaffler, M.B., 2012. Activation of resorption in fatigue-loaded bone involves both apoptosis and active pro-osteoclastogenic signaling by distinct osteocyte populations. Bone 50, 1115–1122. https://doi.org/10.1016/j.bone.2012.01.025

Khani, F., Thaler, R., Paradise, C.R., Deyle, D.R., Kruijthof-de Julio, M., Galindo, M., Gordon, J.A., Stein, G.S., Dudakovic, A., van Wijnen, A.J., 2017. Histone H4 Methyltransferase Suv420h2 Maintains Fidelity of Osteoblast Differentiation. J. Cell. Biochem. 118, 1262–1272. https://doi.org/10.1002/jcb.25787

Kiberstis, P., Smith, O., Norman, C., 2000. Bone Health in The Balance. Science 289, 1497–1497. https://doi.org/10.1126/science.289.5484.1497

Kim, C.A., Honjo, R., Bertola, D., Albano, L., Oliveira, L., Jales, S., Siqueira, J., Castilho, A., Balemans, W., Piters, E., Jennes, K., Van Hul, W., 2008. A Known SOST Gene Mutation Causes Sclerosteosis in a Familial and an Isolated Case from Brazilian Origin. Genet. Test. 12, 475–479. https://doi.org/10.1089/gte.2008.0036

Kim, H.-J., Zhao, H., Kitaura, H., Bhattacharyya, S., Brewer, J.A., Muglia, L.J., Patrick Ross, F., Teitelbaum, S.L., 2007. Glucocorticoids and the osteoclast. Ann. N. Y. Acad. Sci. 1116, 335–339. https://doi.org/10.1196/annals.1402.057

Kim, Jinuk, Han, W., Park, T., Kim, E.J., Bang, I., Lee, H.S., Jeong, Y., Roh, K., Kim, Jeesoo, Kim, J.-S., Kang, C., Seok, C., Han, J.-K., Choi, H.-J., 2020. Sclerostin inhibits Wnt signaling through tandem interaction with two LRP6 ectodomains. Nat. Commun. 11, 5357. https://doi.org/10.1038/s41467-020-19155-4

Kim, S.P., Frey, J.L., Li, Z., Kushwaha, P., Zoch, M.L., Tomlinson, R.E., Da, H., Aja, S., Noh, H.L., Kim, J.K., Hussain, M.A., Thorek, D.L.J., Wolfgang, M.J., Riddle, R.C., 2017. Sclerostin influences body composition by regulating catabolic and anabolic metabolism in adipocytes. Proc. Natl. Acad. Sci. 114, E11238–E11247. https://doi.org/10.1073/pnas.1707876115

Kim, S.W., Lu, Y., Williams, E.A., Lai, F., Lee, J.Y., Enishi, T., Balani, D.H., Ominsky, M.S., Ke, H.Z., Kronenberg, H.M., Wein, M.N., 2017. Sclerostin Antibody Administration Converts Bone Lining Cells Into Active Osteoblasts. J. Bone Miner. Res. 32, 892–901. https://doi.org/10.1002/jbmr.3038

Koga, T., Matsui, Y., Asagiri, M., Kodama, T., de Crombrugghe, B., Nakashima, K., Takayanagi, H., 2005. NFAT and Osterix cooperatively regulate bone formation. Nat. Med. 11, 880–885. https://doi.org/10.1038/nm1270

Kogawa, M., Khalid, K.A., Wijenayaka, A.R., Ormsby, R.T., Evdokiou, A., Anderson, P.H., Findlay, D.M., Atkins, G.J., 2017. Recombinant sclerostin antagonizes effects of ex vivo mechanical loading in trabecular bone and increases osteocyte lacunar size. Am. J. Physiol.-Cell Physiol. 314, C53–C61. https://doi.org/10.1152/ajpcell.00175.2017

Kok-Yong, S., Lawrence, L., 2015. Drug Distribution and Drug Elimination. Basic Pharmacokinet. Concepts Some Clin. Appl. https://doi.org/10.5772/59929

Komori, T., 2019. Regulation of Proliferation, Differentiation and Functions of Osteoblasts by Runx2. Int. J. Mol. Sci. 20. https://doi.org/10.3390/ijms20071694

Kontermann, R.E., 2016. Half-life extended biotherapeutics. Expert Opin. Biol. Ther. 16, 903–915. https://doi.org/10.1517/14712598.2016.1165661

Kontermann, R.E., 2011. Strategies for extended serum half-life of protein therapeutics. Curr. Opin. Biotechnol. 22, 868–876. https://doi.org/10.1016/j.copbio.2011.06.012

Kontulainen, S., Sievänen, H., Kannus, P., Pasanen, M., Vuori, I., 2003. Effect of long-term impact-loading on mass, size, and estimated strength of humerus and radius of female racquet-sports players: a peripheral quantitative computed tomography study between young and old starters and controls. J. Bone Miner. Res. 18, 352–359. https://doi.org/10.1359/jbmr.2003.18.2.352

Korneyeva, M., Rosenthal, S., 2005. Virus Removal by Nanofiltration, in: Smales, C.M., James, D.C. (Eds.), Therapeutic Proteins: Methods and Protocols, Methods in Molecular Biology™. Humana Press, Totowa, NJ, pp. 221–231. https://doi.org/10.1385/1-59259-922-2:221

Kosher, R.A., Kulyk, W.M., Gay, S.W., 1986. Collagen gene expression during limb cartilage differentiation. J. Cell Biol. 102, 1151–1156. https://doi.org/10.1083/jcb.102.4.1151

Kovero, O., Pynnönen, S., Kuurila-Svahn, K., Kaitila, I., Waltimo-Sirén, J., 2006. Skull base abnormalities in osteogenesis imperfecta: a cephalometric evaluation of 54 patients and 108 control volunteers. J. Neurosurg. 105, 361–370. https://doi.org/10.3171/jns.2006.105.3.361

Kramer, I., Loots, G.G., Studer, A., Keller, H., Kneissel, M., 2010. Parathyroid Hormone (PTH)–Induced Bone Gain Is Blunted in SOST Overexpressing and Deficient Mice. J. Bone Miner. Res. 25, 178–189. https://doi.org/10.1359/jbmr.090730

Krause, C., Korchynskyi, O., de Rooij, K., Weidauer, S.E., de Gorter, D.J.J., van Bezooijen, R.L., Hatsell, S., Economides, A.N., Mueller, T.D., Löwik, C.W.G.M., ten Dijke, P., 2010. Distinct Modes of Inhibition by Sclerostin on Bone Morphogenetic Protein and Wnt Signaling Pathways. J. Biol. Chem. 285, 41614–41626. https://doi.org/10.1074/jbc.M110.153890

Krishna, M., Nadler, S.G., 2016. Immunogenicity to Biotherapeutics – The Role of Anti-drug Immune Complexes. Front. Immunol. 7. https://doi.org/10.3389/fimmu.2016.00021

Krishna Smriti Murali, Seto Sai-Wang, Jose Roby J., Li Jiaze, Morton Susan K., Biros Erik, Wang Yutang, Nsengiyumva Vianne, Lindeman Jan H.N., Loots Gabriela G., Rush Catherine M., Craig Jeffrey M., Golledge Jonathan, 2017. Wnt Signaling Pathway Inhibitor Sclerostin Inhibits Angiotensin II–Induced Aortic Aneurysm and Atherosclerosis. Arterioscler. Thromb. Vasc. Biol. 37, 553–566. https://doi.org/10.1161/ATVBAHA.116.308723

Kusu, N., Laurikkala, J., Imanishi, M., Usui, H., Konishi, M., Miyake, A., Thesleff, I., Itoh, N., 2003. Sclerostin Is a Novel Secreted Osteoclast-derived Bone Morphogenetic Protein Antagonist with Unique Ligand Specificity. J. Biol. Chem. 278, 24113–24117.

Kuurila, K., Kentala, E., Karjalainen, S., Pynnönen, S., Kovero, O., Kaitila, I., Grénman, R., Waltimo, J., 2003. Vestibular dysfunction in adult patients with osteogenesis imperfecta. Am. J. Med. Genet. A. 120A, 350–358. https://doi.org/10.1002/ajmg.a.20088

Lagassé, H.A.D., Alexaki, A., Simhadri, V.L., Katagiri, N.H., Jankowski, W., Sauna, Z.E., Kimchi-Sarfaty, C., 2017. Recent advances in (therapeutic protein) drug development. F1000Research 6. https://doi.org/10.12688/f1000research.9970.1

Langdahl, B., Ferrari, S., Dempster, D.W., 2016. Bone modeling and remodeling: potential as therapeutic targets for the treatment of osteoporosis. Ther. Adv. Musculoskelet. Dis. 8, 225–235. https://doi.org/10.1177/1759720X16670154

Lee, H.S., Qi, Y., Im, W., 2015. Effects of N -glycosylation on protein conformation and dynamics: Protein Data Bank analysis and molecular dynamics simulation study. Sci. Rep. 5, 1–7. https://doi.org/10.1038/srep08926

Lee, L.R., Peacock, L., Lisowski, L., Little, D.G., Munns, C.F., Schindeler, A., 2019. Targeting Adeno-Associated Virus Vectors for Local Delivery to Fractures and Systemic Delivery to the Skeleton. Mol. Ther. Methods Clin. Dev. 15, 101–111. https://doi.org/10.1016/j.omtm.2019.08.010

Leenaars, C.H.C., Kouwenaar, C., Stafleu, F.R., Bleich, A., Ritskes-Hoitinga, M., De Vries, R.B.M., Meijboom, F.L.B., 2019. Animal to human translation: a systematic scoping review of reported concordance rates. J. Transl. Med. 17, 223. https://doi.org/10.1186/s12967-019-1976-2

Lerner, U.H., Ohlsson, C., 2015. The WNT system: background and its role in bone. J. Intern. Med. 277, 630–649. https://doi.org/10.1111/joim.12368

Leupin, O., Piters, E., Halleux, C., Hu, S., Kramer, I., Morvan, F., Bouwmeester, T., Schirle, M., Bueno-Lozano, M., Fuentes, F.J.R., Itin, P.H., Boudin, E., Freitas, F. de, Jennes, K., Brannetti, B., Charara, N., Ebersbach, H., Geisse, S., Lu, C.X., Bauer, A., Hul, W.V., Kneissel, M., 2011. Bone Overgrowth-associated Mutations in the LRP4 Gene Impair Sclerostin Facilitator Function. J. Biol. Chem. 286, 19489–19500. https://doi.org/10.1074/jbc.M110.190330

Li, H., d'Anjou, M., 2009. Pharmacological significance of glycosylation in therapeutic proteins. Curr. Opin. Biotechnol. 20, 678–684. https://doi.org/10.1016/j.copbio.2009.10.009

Li, X., Ominsky, M.S., Niu, Q.-T., Sun, N., Daugherty, B., D'Agostin, D., Kurahara, C., Gao, Y., Cao, J., Gong, J., Asuncion, F., Barrero, M., Warmington, K., Dwyer, D., Stolina, M., Morony, S., Sarosi, I., Kostenuik, P.J., Lacey, D.L., Simonet, W.S., Ke, H.Z., Paszty, C., 2008. Targeted Deletion of the Sclerostin Gene in Mice Results in Increased Bone Formation and Bone Strength. J. Bone Miner. Res. 23, 860–869. https://doi.org/10.1359/jbmr.080216

Li, X., Ominsky, M.S., Warmington, K.S., Morony, S., Gong, J., Cao, J., Gao, Y., Shalhoub, V., Tipton, B., Haldankar, R., Chen, Q., Winters, A., Boone, T., Geng, Z., Niu, Q.-T., Ke, H.Z., Kostenuik, P.J., Simonet, W.S., Lacey, D.L., Paszty, C., 2009. Sclerostin antibody treatment increases bone formation, bone mass, and bone strength in a rat model of postmenopausal osteoporosis. J. Bone Miner. Res. Off. J. Am. Soc. Bone Miner. Res. 24, 578–588. https://doi.org/10.1359/jbmr.081206

Li, X., Zhang, Y., Kang, H., Liu, W., Liu, P., Zhang, J., Harris, S.E., Wu, D., 2005. Sclerostin Binds to LRP5/6 and Antagonizes Canonical Wnt Signaling. J. Biol. Chem. 280, 19883–19887. https://doi.org/10.1074/jbc.M413274200

Lin, C., Jiang, X., Dai, Z., Guo, X., Weng, T., Wang, J., Li, Y., Feng, G., Gao, X., He, L., 2009. Sclerostin Mediates Bone Response to Mechanical Unloading Through Antagonizing Wnt/β-Catenin Signaling. J. Bone Miner. Res. 24, 1651–1661. https://doi.org/10.1359/jbmr.090411

Lindsay, R., Cosman, F., Zhou, H., Bostrom, M.P., Shen, V.W., Cruz, J.D., Nieves, J.W., Dempster, D.W., 2006. A novel tetracycline labeling schedule for longitudinal evaluation of the short-term effects of anabolic therapy with a single iliac crest bone biopsy: early actions of teriparatide. J. Bone Miner. Res. Off. J. Am. Soc. Bone Miner. Res. 21, 366–373. https://doi.org/10.1359/JBMR.051109

Lips, P., Schoor, N.M. van, Bravenboer, N., 2013. Vitamin D-Related Disorders, in: Primer on the Metabolic Bone Diseases and Disorders of Mineral Metabolism. John Wiley & Sons, Ltd, pp. 613–623. https://doi.org/10.1002/9781118453926.ch75

Little, D.G., Peacock, L., Mikulec, K., Kneissel, M., Kramer, I., Cheng, T.L., Schindeler, A., Munns, C., 2017. Combination sclerostin antibody and zoledronic acid treatment outperforms either treatment alone in a mouse model of osteogenesis imperfecta. Bone 101, 96–103. https://doi.org/10.1016/j.bone.2017.04.016

Liu, B., Lu, Y., Wang, Y., Ge, L., Zhai, N., Han, J., 2019. A protocol for isolation and identification and comparative characterization of primary osteoblasts from mouse and rat calvaria. Cell Tissue Bank. 20, 173–182. https://doi.org/10.1007/s10561-019-09751-0

Lobo, E.D., Hansen, R.J., Balthasar, J.P., 2004. Antibody pharmacokinetics and pharmacodynamics. J. Pharm. Sci. 93, 2645–2668. https://doi.org/10.1002/jps.20178

Loots, G.G., Kneissel, M., Keller, H., Baptist, M., Chang, J., Collette, N.M., Ovcharenko, D., Plajzer-Frick, I., Rubin, E.M., 2005. Genomic deletion of a long-range bone enhancer misregulates sclerostin in Van Buchem disease. Genome Res. 15, 928–935. https://doi.org/10.1101/gr.3437105

Loría-Cortés, R., Quesada-Calvo, E., Cordero-Chaverri, C., 1977. Osteopetrosis in children: a report of 26 cases. J. Pediatr. 91, 43–47. https://doi.org/10.1016/s0022-3476(77)80441-1

Lovato, C., Lewiecki, E.M., 2017. Emerging anabolic agents in the treatment of osteoporosis. Expert Opin. Emerg. Drugs 22, 247–257. https://doi.org/10.1080/14728214.2017.1362389

Luxenburg, C., Geblinger, D., Klein, E., Anderson, K., Hanein, D., Geiger, B., Addadi, L., 2007. The Architecture of the Adhesive Apparatus of Cultured Osteoclasts: From Podosome Formation to Sealing Zone Assembly. PLOS ONE 2, e179. https://doi.org/10.1371/journal.pone.0000179

Ma, W., Yang, L., He, L., 2018. Overview of the detection methods for equilibrium dissociation constant KD of drug-receptor interaction. J. Pharm. Anal. 8, 147. https://doi.org/10.1016/j.jpha.2018.05.001

MacLean, B., Tomazela, D.M., Shulman, N., Chambers, M., Finney, G.L., Frewen, B., Kern, R., Tabb, D.L., Liebler, D.C., MacCoss, M.J., 2010. Skyline: an open source document editor for creating and analyzing targeted proteomics experiments. Bioinformatics 26, 966–968. https://doi.org/10.1093/bioinformatics/btq054

Madan, B., McDonald, M.J., Foxa, G.E., Diegel, C.R., Williams, B.O., Virshup, D.M., 2018. Bone loss from Wnt inhibition mitigated by concurrent alendronate therapy. Bone Res. 6, 1–10. https://doi.org/10.1038/s41413-018-0017-8

Manolagas, S.C., 2000. Birth and death of bone cells: basic regulatory mechanisms and implications for the pathogenesis and treatment of osteoporosis. Endocr. Rev. 21, 115–137. https://doi.org/10.1210/edrv.21.2.0395

Marieb, E.N., Hoehn, K., 2012. Chapter 6 - Bones and Skeletal Tissues, in: Human Anatomy and Physiology (Eight Edition). Pearson Bejamin Cummings, San Francisco, pp. 176–182.

Matsuo, K., Galson, D.L., Zhao, C., Peng, L., Laplace, C., Wang, K.Z.Q., Bachler, M.A., Amano, H., Aburatani, H., Ishikawa, H., Wagner, E.F., 2004. Nuclear factor of activated T-cells (NFAT) rescues osteoclastogenesis in precursors lacking c-Fos. J. Biol. Chem. 279, 26475–26480. https://doi.org/10.1074/jbc.M313973200

McClung, M.R., 2017. Sclerostin antibodies in osteoporosis: latest evidence and therapeutic potential: Ther. Adv. Musculoskelet. Dis. https://doi.org/10.1177/1759720X17726744

McClung, M.R., Miller, P.D., Papapoulos, S.E., 2018. Osteoporosis, in: Primer on the Metabolic Bone Diseases and Disorders of Mineral Metabolism. John Wiley & Sons, Ltd, pp. 393–397. https://doi.org/10.1002/9781119266594.ch49

McNamara, L.M., Van der Linden, J.C., Weinans, H., Prendergast, P.J., 2006. Stress-concentrating effect of resorption lacunae in trabecular bone. J. Biomech. 39, 734–741. https://doi.org/10.1016/j.jbiomech.2004.12.027

Menaa, C., Reddy, S.V., Kurihara, N., Maeda, H., Anderson, D., Cundy, T., Cornish, J., Singer, F.R., Bruder, J.M., Roodman, G.D., 2000. Enhanced RANK ligand expression and responsivity of bone marrow cells in Paget's disease of bone. J. Clin. Invest. 105, 1833–1838. https://doi.org/10.1172/JCI9133

Millán, J.L., Narisawa, S., Lemire, I., Loisel, T.P., Boileau, G., Leonard, P., Gramatikova, S., Terkeltaub, R., Camacho, N.P., McKee, M.D., Crine, P., Whyte, M.P., 2008. Enzyme replacement therapy for murine hypophosphatasia. J. Bone Miner. Res. Off. J. Am. Soc. Bone Miner. Res. 23, 777–787. https://doi.org/10.1359/jbmr.071213

Miller, S.C., de Saint-Georges, L., Bowman, B.M., Jee, W.S., 1989. Bone lining cells: structure and function. Scanning Microsc. 3, 953–960; discussion 960-961.

Mills, B.G., Singer, F.R., 1976. Nuclear inclusions in Paget's disease of bone. Science 194, 201–202. https://doi.org/10.1126/science.959849

Mirza, F.S., Padhi, I.D., Raisz, L.G., Lorenzo, J.A., 2010. Serum Sclerostin Levels Negatively Correlate with Parathyroid Hormone Levels and Free Estrogen Index in Postmenopausal Women. J. Clin. Endocrinol. Metab. 95, 1991–1997. https://doi.org/10.1210/jc.2009-2283

Miyamoto, T., 2006. The dendritic cell-specific transmembrane protein DC-STAMP is essential for osteoclast fusion and osteoclast bone-resorbing activity. Mod. Rheumatol. 16, 341–342. https://doi.org/10.1007/s10165-006-0524-0

Mödder, U.I., Roforth, M.M., Hoey, K., McCready, L.K., Peterson, J.M., Monroe, D.G., Oursler, M.J., Khosla, S., 2011. Effects of estrogen on osteoprogenitor cells and cytokines/bone-regulatory factors in postmenopausal women. Bone 49, 202–207. https://doi.org/10.1016/j.bone.2011.04.015

Moester, M.J.C., Papapoulos, S.E., Löwik, C.W.G.M., van Bezooijen, R.L., 2010. Sclerostin: current knowledge and future perspectives. Calcif. Tissue Int. 87, 99–107. https://doi.org/10.1007/s00223-010-9372-1

Mori, S., Burr, D.B., 1993. Increased intracortical remodeling following fatigue damage. Bone 14, 103–109. https://doi.org/10.1016/8756-3282(93)90235-3

Moritz, B., Stracke, J.O., 2017. Assessment of disulfide and hinge modifications in monoclonal antibodies. Electrophoresis 38, 769–785. https://doi.org/10.1002/elps.201600425

Mullard, A., 2019. FDA approves first-in-class osteoporosis drug. Nat. Rev. Drug Discov. 18, 411–411. https://doi.org/10.1038/d41573-019-00083-y

Munns, C.F., Shaw, N., Kiely, M., Specker, B.L., Thacher, T.D., Ozono, K., Michigami, T., Tiosano, D., Mughal, M.Z., Mäkitie, O., Ramos-Abad, L., Ward, L., DiMeglio, L.A., Atapattu, N., Cassinelli, H., Braegger, C., Pettifor, J.M., Seth, A., Idris, H.W., Bhatia, V., Fu, J., Goldberg, G., Sävendahl, L., Khadgawat, R., Pludowski, P., Maddock, J., Hyppönen, E., Oduwole, A., Frew, E., Aguiar, M., Tulchinsky, T., Butler, G., Högler, W., 2016. Global Consensus Recommendations on Prevention and Management of Nutritional Rickets. J. Clin. Endocrinol. Metab. 101, 394–415. https://doi.org/10.1210/jc.2015-2175

Murray, J.E., Laurieri, N., Delgoda, R., 2017. Chapter 24 - Proteins, in: Badal, S., Delgoda, Rupika (Eds.), Pharmacognosy. Academic Press, Boston, pp. 477–494. https://doi.org/10.1016/B978-0-12-802104-0.00024-X

Nakashima, K., de Crombrugghe, B., 2003. Transcriptional mechanisms in osteoblast differentiation and bone formation. Trends Genet. TIG 19, 458–466. https://doi.org/10.1016/S0168-9525(03)00176-8

Nampei, A., Hashimoto, J., Hayashida, K., Tsuboi, H., Shi, K., Tsuji, I., Miyashita, H., Yamada, T., Matsukawa, N., Matsumoto, M., Morimoto, S., Ogihara, T., Ochi, T., Yoshikawa, H., 2004. Matrix extracellular phosphoglycoprotein (MEPE) is highly expressed in osteocytes in human bone. J. Bone Miner. Metab. 22, 176–184. https://doi.org/10.1007/s00774-003-0468-9

Need, A.G., O'Loughlin, P.D., Morris, H.A., Coates, P.S., Horowitz, M., Nordin, B.E.C., 2008. Vitamin D metabolites and calcium absorption in severe vitamin D deficiency. J. Bone Miner. Res. Off. J. Am. Soc. Bone Miner. Res. 23, 1859–1863. https://doi.org/10.1359/jbmr.080607

Nesbitt, S.A., Horton, M.A., 1997. Trafficking of Matrix Collagens Through Bone-Resorbing Osteoclasts. Science 276, 266–269. https://doi.org/10.1126/science.276.5310.266

Niehrs, C., 2012. The complex world of WNT receptor signalling. Nat. Rev. Mol. Cell Biol. 13, 767–779. https://doi.org/10.1038/nrm3470

NIH Consensus Development Panel on Osteoporosis Prevention, Diagnosis, and Therapy, 2001. Osteoporosis prevention, diagnosis, and therapy. JAMA 285, 785–795. https://doi.org/10.1001/jama.285.6.785

Nilsson, O., Marino, R., De Luca, F., Phillip, M., Baron, J., 2005. Endocrine Regulation of the Growth Plate. Horm. Res. Paediatr. 64, 157–165. https://doi.org/10.1159/000088791

Nishioka, T., Tomatsu, S., Gutierrez, M.A., Miyamoto, K., Trandafirescu, G.G., Lopez, P.L.C., Grubb, J.H., Kanai, R., Kobayashi, H., Yamaguchi, S., Gottesman, G.S., Cahill, R., Noguchi, A., Sly, W.S., 2006. Enhancement of drug delivery to bone: characterization of human tissue-nonspecific alkaline phosphatase tagged with an acidic oligopeptide. Mol. Genet. Metab. 88, 244–255. https://doi.org/10.1016/j.ymgme.2006.02.012

Nusse, R., Clevers, H., 2017. Wnt/β-Catenin Signaling, Disease, and Emerging Therapeutic Modalities. Cell 169, 985–999. https://doi.org/10.1016/j.cell.2017.05.016

Øie, S., Tozer, T.N., 1979. Effect of altered plasma protein binding on apparent volume of distribution. J. Pharm. Sci. 68, 1203–1205. https://doi.org/10.1002/jps.2600680948

Ominsky, M.S., Libanati, C., Niu, Q.-T., Boyce, R.W., Kostenuik, P.J., Wagman, R.B., Baron, R., Dempster, D.W., 2015. Sustained Modeling-Based Bone Formation During Adulthood in Cynomolgus Monkeys May Contribute to Continuous BMD Gains With Denosumab. J. Bone Miner. Res. Off. J. Am. Soc. Bone Miner. Res. 30, 1280–1289. https://doi.org/10.1002/jbmr.2480

Ominsky, M.S., Niu, Q.-T., Li, C., Li, X., Ke, H.Z., 2014. Tissue-level mechanisms responsible for the increase in bone formation and bone volume by sclerostin antibody. J. Bone Miner. Res. Off. J. Am. Soc. Bone Miner. Res. 29, 1424–1430. https://doi.org/10.1002/jbmr.2152

Ominsky, M.S., Vlasseros, F., Jolette, J., Smith, S.Y., Stouch, B., Doellgast, G., Gong, J., Gao, Y., Cao, J., Graham, K., Tipton, B., Cai, J., Deshpande, R., Zhou, L., Hale, M.D., Lightwood, D.J., Henry, A.J., Popplewell, A.G., Moore, A.R., Robinson, M.K., Lacey, D.L., Simonet, W.S., Paszty, C., 2010. Two doses of sclerostin antibody in cynomolgus monkeys increases bone formation, bone mineral density, and bone strength. J. Bone Miner. Res. 25, 948–959. https://doi.org/10.1002/jbmr.14

Ornitz, D.M., 2005. FGF signaling in the developing endochondral skeleton. Cytokine Growth Factor Rev., Fibroblast Growth Factors 16, 205–213. https://doi.org/10.1016/j.cytogfr.2005.02.003

Orriss, I.R., Taylor, S.E.B., Arnett, T.R., 2012. Rat Osteoblast Cultures, in: Helfrich, M.H., Ralston, S.H. (Eds.), Bone Research Protocols, Methods in Molecular Biology. Humana Press, Totowa, NJ, pp. 31–41. https://doi.org/10.1007/978-1-61779-415-5_3

Oursler, M.J., Cortese, C., Keeting, P., Anderson, M.A., Bonde, S.K., Riggs, B.L., Spelsberg, T.C., 1991. Modulation of transforming growth factor-beta production in normal human osteoblast-like cells by 17 beta-estradiol and parathyroid hormone. Endocrinology 129, 3313–3320. https://doi.org/10.1210/endo-129-6-3313

Parfitt, A.M., 2002. Targeted and nontargeted bone remodeling: relationship to basic multicellular unit origination and progression. Bone 30, 5–7. https://doi.org/10.1016/s8756-3282(01)00642-1

Parfitt, A.M., 2000. The mechanism of coupling: a role for the vasculature. Bone 26, 319–323. https://doi.org/10.1016/S8756-3282(00)80937-0

Parfitt, A.M., 1994. Osteonal and hemi-osteonal remodeling: the spatial and temporal framework for signal traffic in adult human bone. J. Cell. Biochem. 55, 273–286. https://doi.org/10.1002/jcb.240550303

Partington, G.A., Fuller, K., Chambers, T.J., Pondel, M., 2004. Mitf-PU.1 interactions with the tartrate-resistant acid phosphatase gene promoter during osteoclast differentiation. Bone 34, 237–245. https://doi.org/10.1016/j.bone.2003.11.010

Peel, N., 2009. Bone remodelling and disorders of bone metabolism. Surg. Oxf. 27, 70–74. https://doi.org/10.1016/j.mpsur.2008.12.007

Peters, R., Harris, T., 2018. Advances and innovations in haemophilia treatment. Nat. Rev. Drug Discov. 17, 493–508. https://doi.org/10.1038/nrd.2018.70

Petsch, D., 2000. Endotoxin removal from protein solutions. J. Biotechnol. 76, 97–119. https://doi.org/10.1016/S0168-1656(99)00185-6

Pettifor, J.M., Thandrayen, K., Thacher, T.D., 2018. Chapter 67 - Vitamin D Deficiency and Nutritional Rickets in Children, in: Feldman, D. (Ed.), Vitamin D (Fourth Edition). Academic Press, pp. 179–201. https://doi.org/10.1016/B978-0-12-809963-6.00067-5

Pietruschka, G., 1958. [Further information on marble bones (Albers-Schonberg disease) with remarks on differential diagnosis]. Klin Monbl Augenheilkd Augenarztl Fortbild 132, 509–525.

Piters, E., Culha, C., Moester, M., Van Bezooijen, R., Adriaensen, D., Mueller, T., Weidauer, S., Jennes, K., de Freitas, F., Löwik, C., Timmermans, J.-P., Van Hul, W., Papapoulos, S., 2010. First missense mutation in the SOST gene causing sclerosteosis by loss of sclerostin function. Hum. Mutat. 31, E1526–E1543. https://doi.org/10.1002/humu.21274

Plotkin, L.I., 2014. Apoptotic osteocytes and the control of targeted bone resorption. Curr. Osteoporos. Rep. 12, 121–126. https://doi.org/10.1007/s11914-014-0194-3

Plotkin, L.I., Bellido, T., 2013. Beyond gap junctions: Connexin43 and bone cell signaling. Bone 52, 157–166. https://doi.org/10.1016/j.bone.2012.09.030

Poole, K.E.S., van Bezooijen, R.L., Loveridge, N., Hamersma, H., Papapoulos, S.E., Löwik, C.W., Reeve, J., 2005. Sclerostin is a delayed secreted product of osteocytes that inhibits bone formation. FASEB J. 19, 1842–1844. https://doi.org/10.1096/fj.05-4221fje

Qin, A., Cheng, T.S., Pavlos, N.J., Lin, Z., Dai, K.R., Zheng, M.H., 2012. V-ATPases in osteoclasts: structure, function and potential inhibitors of bone resorption. Int. J. Biochem. Cell Biol. 44, 1422–1435. https://doi.org/10.1016/j.biocel.2012.05.014

Qing, H., Bonewald, L.F., 2009. Osteocyte remodeling of the perilacunar and pericanalicular matrix. Int. J. Oral Sci. 1, 59–65. https://doi.org/10.4248/ijos.09019

Qu, Q., Perälä-Heape, M., Kapanen, A., Dahllund, J., Salo, J., Väänänen, H.K., Härkönen, P., 1998. Estrogen enhances differentiation of osteoblasts in mouse bone marrow culture. Bone 22, 201–209. https://doi.org/10.1016/s8756-3282(97)00276-7

Raggatt, L.J., Partridge, N.C., 2010. Cellular and Molecular Mechanisms of Bone Remodeling. J. Biol. Chem. 285, 25103–25108. https://doi.org/10.1074/jbc.R109.041087

Rath, T., Baker, K., Dumont, J.A., Peters, R.T., Jiang, H., Qiao, S.-W., Lencer, W.I., Pierce, G.F., Blumberg, R.S., 2015. Fc-fusion proteins and FcRn: structural insights for longer-lasting and more effective therapeutics. Crit. Rev. Biotechnol. 35, 235–254. https://doi.org/10.3109/07388551.2013.834293

Raubenheimer, E., Miniggio, H., Lemmer, L., van Heerden, W., 2017. The Role of Bone Remodelling in Maintaining and Restoring Bone Health: an Overview. Clin. Rev. Bone Miner. Metab. 15, 90–97. https://doi.org/10.1007/s12018-017-9230-z

Rebel, A., Malkani, K., Baslé, M., Bregeon, Ch., 1976. Nuclear Inclusions in Osteoclasts in Paget's Bone Disease, in: Nielsen, S.P., Hjørting-Hansen, E. (Eds.), Calcified Tissues 1975: Proceedings of the XIth European Symposium on Calcified Tissues. Springer, Berlin, Heidelberg, pp. 113–116. https://doi.org/10.1007/978-3-662-29272-3_16

Ren, Y., Han, X., Ho, S.P., Harris, S.E., Cao, Z., Economides, A.N., Qin, C., Ke, H., Liu, M., Feng, J.Q., 2015. Removal of SOST or blocking its product sclerostin rescues defects in the periodontitis mouse model. FASEB J. Off. Publ. Fed. Am. Soc. Exp. Biol. 29, 2702–2711. https://doi.org/10.1096/fj.14-265496

Reynolds, T., de Zafra, C., Kim, A., Gelzleichter, T.R., 2013. Chapter 1 - Overview of Biopharmaceuticals and Comparison with Small-molecule Drug Development, in: Plitnick, L.M., Herzyk, D.J. (Eds.), Nonclinical Development of Novel Biologics, Biosimilars, Vaccines and Specialty Biologics. Academic Press, San Diego, pp. 3–33. https://doi.org/10.1016/B978-0-12-394810-6.00001-0

Riihonen, R., Supuran, C.T., Parkkila, S., Pastorekova, S., Väänänen, H.K., Laitala-Leinonen, T., 2007. Membrane-bound carbonic anhydrases in osteoclasts. Bone 40, 1021–1031. https://doi.org/10.1016/j.bone.2006.11.028

Robert, F., Bierau, H., Rossi, M., Agugiaro, D., Soranzo, T., Broly, H., Mitchell-Logean, C., 2009. Degradation of an Fc-fusion recombinant protein by host cell proteases: Identification of a CHO cathepsin D protease. Biotechnol. Bioeng. 104, 1132–1141. https://doi.org/10.1002/bit.22494

Robey, P.G., Fedarko, N.S., Hefferan, T.E., Bianco, P., Vetter, U.K., Grzesik, W., Friedenstein, A., Van der Pluijm, G., Mintz, K.P., Young, M.F., 1993. Structure and molecular regulation of bone matrix proteins. J. Bone Miner. Res. Off. J. Am. Soc. Bone Miner. Res. 8 Suppl 2, S483-487. https://doi.org/10.1002/jbmr.5650081310

Robling, A.G., Bonewald, L.F., 2020. The Osteocyte: New Insights. Annu. Rev. Physiol. 82, 485–506. https://doi.org/10.1146/annurev-physiol-021119-034332

Robling, A.G., Castillo, A.B., Turner, C.H., 2006. Biomechanical and molecular regulation of bone remodeling. Annu. Rev. Biomed. Eng. 8, 455–498. https://doi.org/10.1146/annurev.bioeng.8.061505.095721

Robling, A.G., Niziolek, P.J., Baldridge, L.A., Condon, K.W., Allen, M.R., Alam, I., Mantila, S.M., Gluhak-Heinrich, J., Bellido, T.M., Harris, S.E., Turner, C.H., 2008. Mechanical Stimulation of Bone in Vivo Reduces Osteocyte Expression of Sost/Sclerostin. J. Biol. Chem. 283, 5866–5875. https://doi.org/10.1074/jbc.M705092200

Roforth, M.M., Fujita, K., McGregor, U.I., Kirmani, S., McCready, L.K., Peterson, J.M., Drake, M.T., Monroe, D.G., Khosla, S., 2014. Effects of age on bone mRNA levels of sclerostin and other genes relevant to bone metabolism in humans. Bone 59, 1–6. https://doi.org/10.1016/j.bone.2013.10.019

Rogers, L.D., Overall, C.M., 2013. Proteolytic Post-translational Modification of Proteins: Proteomic Tools and Methodology. Mol. Cell. Proteomics MCP 12, 3532–3542. https://doi.org/10.1074/mcp.M113.031310

Roschger, P., Paschalis, E.P., Fratzl, P., Klaushofer, K., 2008. Bone mineralization density distribution in health and disease. Bone 42, 456–466. https://doi.org/10.1016/j.bone.2007.10.021

Rudd, P.M., Dwek, R.A., 1997. Glycosylation: Heterogeneity and the 3D Structure of Proteins. Crit. Rev. Biochem. Mol. Biol. 32, 1–100. https://doi.org/10.3109/10409239709085144

Ruff, C.B., Hayes, W.C., 1982. Subperiosteal expansion and cortical remodeling of the human femur and tibia with aging. Science 217, 945–948. https://doi.org/10.1126/science.7112107

Russell, W.M.S., Burch, R.L., 1959. The principles of humane experimental technique. Methuen.

Salbach-Hirsch, J., Samsonov, S.A., Hintze, V., Hofbauer, C., Picke, A.-K., Rauner, M., Gehrcke, J.-P., Moeller, S., Schnabelrauch, M., Scharnweber, D., Pisabarro, M.T., Hofbauer, L.C., 2015. Structural and functional insights into sclerostin-glycosaminoglycan interactions in bone. Biomaterials 67, 335–345. https://doi.org/10.1016/j.biomaterials.2015.07.021

Samee, N., Geoffroy, V., Marty, C., Schiltz, C., Vieux-Rochas, M., Levi, G., de Vernejoul, M.-C., 2008. Dlx5, a positive regulator of osteoblastogenesis, is essential for osteoblast-osteoclast coupling. Am. J. Pathol. 173, 773–780. https://doi.org/10.2353/ajpath.2008.080243

Santos, A., Bakker, A.D., Klein-Nulend, J., 2009. The role of osteocytes in bone mechanotransduction. Osteoporos. Int. 20, 1027–1031. https://doi.org/10.1007/s00198-009-0858-5

Sayers, E.W., Agarwala, R., Bolton, E.E., Brister, J.R., Canese, K., Clark, K., Connor, R., Fiorini, N., Funk, K., Hefferon, T., Holmes, J.B., Kim, S., Kimchi, A., Kitts, P.A., Lathrop, S., Lu, Z., Madden, T.L., Marchler-Bauer, A., Phan, L., Schneider, V.A., Schoch, C.L., Pruitt, K.D., Ostell, J., 2019. Database resources of the National Center for Biotechnology Information. Nucleic Acids Res. 47, D23–D28. https://doi.org/10.1093/nar/gky1069

Schaffler, M.B., Cheung, W.-Y., Majeska, R., Kennedy, O., 2014. Osteocytes: master orchestrators of bone. Calcif. Tissue Int. 94, 5–24. https://doi.org/10.1007/s00223-013-9790-y

Scheuermann, T.H., Padrick, S.B., Gardner, K.H., Brautigam, C.A., 2016. On the acquisition and analysis of microscale thermophoresis data. Anal. Biochem. 496, 79–93. https://doi.org/10.1016/j.ab.2015.12.013

Schneider, C.A., Rasband, W.S., Eliceiri, K.W., 2012. NIH Image to ImageJ: 25 years of image analysis. Nat. Methods 9, 671–675. https://doi.org/10.1038/nmeth.2089

Schwarze, U., Dobsak, T., Gruber, R., Bookstein, F., 2019. Anatomical similarity between the Sost-knockout mouse and sclerosteosis in humans. Anat. Rec. Hoboken NJ 2007. https://doi.org/10.1002/ar.24318

Seeman, E., 2013. Age- and menopause-related bone loss compromise cortical and trabecular microstructure. J. Gerontol. A. Biol. Sci. Med. Sci. 68, 1218–1225. https://doi.org/10.1093/gerona/glt071

Seeman, E., 2009. Bone modeling and remodeling. Crit. Rev. Eukaryot. Gene Expr. 19, 219–233. https://doi.org/10.1615/critreveukargeneexpr.v19.i3.40

Seeman, E., 2008. Chapter 1 - Modeling and Remodeling: The Cellular Machinery Responsible for the Gain and Loss of Bone's Material and Structural Strength, in: Bilezikian, J.P., Raisz, L.G., Martin, T.J. (Eds.), Principles of Bone Biology (Third Edition). Academic Press, San Diego, pp. 1–28. https://doi.org/10.1016/B978-0-12-373884-4.00023-9

Semënov, M., Tamai, K., He, X., 2005. SOST Is a Ligand for LRP5/LRP6 and a Wnt Signaling Inhibitor. J. Biol. Chem. 280, 26770–26775. https://doi.org/10.1074/jbc.M504308200

Semenov, M.V., He, X., 2006. LRP5 Mutations Linked to High Bone Mass Diseases Cause Reduced LRP5 Binding and Inhibition by SOST. J. Biol. Chem. 281, 38276–38284. https://doi.org/10.1074/jbc.M609509200

Shah, M., Kola, B., Bataveljic, A., Arnett, T.R., Viollet, B., Saxon, L., Korbonits, M., Chenu, C., 2010. AMP-activated protein kinase (AMPK) activation regulates in vitro bone formation and bone mass. Bone 47, 309–319. https://doi.org/10.1016/j.bone.2010.04.596

Shah, M., Maroof, A., Gikas, P., Mittal, G., Keen, R., Baeten, D., Shaw, S., Roberts, S.J., 2020. Dual neutralisation of IL-17F and IL-17A with bimekizumab blocks inflammation-driven osteogenic differentiation of human periosteal cells. RMD Open 6, e001306. https://doi.org/10.1136/rmdopen-2020-001306

Shahnazari, M., Dwyer, D., Chu, V., Asuncion, F., Stolina, M., Ominsky, M., Kostenuik, P., Halloran, B., 2012a. Bone turnover markers in peripheral blood and marrow plasma reflect trabecular bone loss but not endocortical expansion in aging mice. Bone 50, 628–637. https://doi.org/10.1016/j.bone.2011.11.010

Shahnazari, M., Wronski, T., Chu, V., Williams, A., Leeper, A., Stolina, M., Ke, H.Z., Halloran, B., 2012b. Early Response of Bone Marrow Osteoprogenitors to Skeletal Unloading and Sclerostin Antibody. Calcif. Tissue Int. 91, 50–58. https://doi.org/10.1007/s00223-012-9610-9

Shapiro, J.R., Burn, V.E., Chipman, S.D., Jacobs, J.B., Schloo, B., Reid, L., Larsen, N., Louis, F., 1989. Pulmonary hypoplasia and osteogenesis imperfecta type II with defective synthesis of alpha I(1) procollagen. Bone 10, 165–171. https://doi.org/10.1016/8756-3282(89)90049-5

Sheffield, W.P., Eltringham-Smith, L.J., Bhakta, V., 2018. Fusion to Human Serum Albumin Extends the Circulatory Half-Life and Duration of Antithrombotic Action of the Kunitz Protease Inhibitor Domain of Protease Nexin 2. Cell. Physiol. Biochem. 45, 772–782. https://doi.org/10.1159/000487168

Shimamoto, G., Gegg, C., Boone, T., Queva, C., 2012. Peptibodies: A flexible alternative format to antibodies. mAbs 4, 586–591. https://doi.org/10.4161/mabs.21024

Shin, D.-E., Ahn, T.-K., Kim, J.-W., Oh, C.-H., Choi, S., 2018. Testosterone and Male Osteoporosis. Clin. Rev. Bone Miner. Metab. 16, 49–56. https://doi.org/10.1007/s12018-018-9245-0

Simonet, W.S., Lacey, D.L., Dunstan, C.R., Kelley, M., Chang, M.S., Lüthy, R., Nguyen, H.Q., Wooden, S., Bennett, L., Boone, T., Shimamoto, G., DeRose, M., Elliott, R., Colombero, A., Tan, H.L., Trail, G., Sullivan, J., Davy, E., Bucay, N., Renshaw-Gegg, L., Hughes, T.M., Hill, D., Pattison, W., Campbell, P., Sander, S., Van, G., Tarpley, J., Derby, P., Lee, R., Boyle, W.J., 1997. Osteoprotegerin: a novel secreted protein involved in the regulation of bone density. Cell 89, 309–319. https://doi.org/10.1016/s0092-8674(00)80209-3

Sims, N.A., Martin, T.J., 2015. Coupling Signals between the Osteoclast and Osteoblast: How are Messages Transmitted between These Temporary Visitors to the Bone Surface? Front. Endocrinol. 6. https://doi.org/10.3389/fendo.2015.00041

Sims, N.A., Martin, T.J., Quinn, J.M.W., 2016. Chapter 10 - Coupling: The Influences of Immune and Bone Cells, in: Lorenzo, J., Horowitz, M.C., Choi, Y., Takayanagi, H., Schett, G. (Eds.), Osteoimmunology (Second Edition). Academic Press, San Diego, pp. 169–185. https://doi.org/10.1016/B978-0-12-800571-2.00010-4

Sinha, K.M., Zhou, X., 2013. Genetic and molecular control of Osterix in skeletal formation. J. Cell. Biochem. 114, 975–984. https://doi.org/10.1002/jcb.24439

Smith, D.A., Beaumont, K., Maurer, T.S., Di, L., 2015. Volume of Distribution in Drug Design: Miniperspective. J. Med. Chem. 58, 5691–5698. https://doi.org/10.1021/acs.jmedchem.5b00201

Smith, S.M., Wastney, M.E., O'Brien, K.O., Morukov, B.V., Larina, I.M., Abrams, S.A., Davis-Street, J.E., Oganov, V., Shackelford, L.C., 2005. Bone markers, calcium metabolism, and calcium kinetics during extended-duration space flight on the mir space station. J. Bone Miner. Res. 20, 208–218. https://doi.org/10.1359/JBMR.041105

Sobacchi, C., Schulz, A., Coxon, F.P., Villa, A., Helfrich, M.H., 2013. Osteopetrosis: genetics, treatment and new insights into osteoclast function. Nat. Rev. Endocrinol. 9, 522–536. https://doi.org/10.1038/nrendo.2013.137

Sockolosky, J.T., Kivimäe, S., Szoka, F.C., 2014. Fusion of a Short Peptide that Binds Immunoglobulin G to a Recombinant Protein Substantially Increases Its Plasma Half-Life in Mice. PLOS ONE 9, e102566. https://doi.org/10.1371/journal.pone.0102566

Soltanoff, C.S., Yang, S., Chen, W., Li, Y.-P., 2009. Signaling Networks that Control the Lineage Commitment and Differentiation of Bone Cells. Crit. Rev. Eukaryot. Gene Expr. 19, 1–46. https://doi.org/10.1615/CritRevEukarGeneExpr.v19.i1.10

Somerville, J.M., Aspden, R.M., Armour, K.E., Armour, K.J., Reid, D.M., 2004. Growth of C57Bl/6 Mice and the Material and Mechanical Properties of Cortical Bone from the Tibia. Calcif. Tissue Int. 74, 469–475. https://doi.org/10.1007/s00223-003-0101-x

Sroga, G.E., Vashishth, D., 2012. Effects of bone matrix proteins on fracture and fragility in osteoporosis. Curr. Osteoporos. Rep. 10, 141–150. https://doi.org/10.1007/s11914-012-0103-6

Stark, Z., Savarirayan, R., 2009. Osteopetrosis. Orphanet J. Rare Dis. 4, 5. https://doi.org/10.1186/1750-1172-4-5

Stein, S.A., Witkop, C., Hill, S., Fallon, M.D., Viernstein, L., Gucer, G., McKeever, P., Long, D., Altman, J., Miller, N.R., Teitelbaum, S.L., Schlesinger, S., 1983. Sclerosteosis: neurogenetic and pathophysiologic analysis of an American kinship. Neurology 33, 267–277.

Steinitz, M., 2000. Quantitation of the Blocking Effect of Tween 20 and Bovine Serum Albumin in ELISA Microwells. Anal. Biochem. 282, 232–238. https://doi.org/10.1006/abio.2000.4602

Stout, S.D., Brunsden, B.S., Hildebolt, C.F., Commean, P.K., Smith, K.E., Tappen, N.C., 1999. Computer-assisted 3D reconstruction of serial sections of cortical bone to determine the 3D structure of osteons. Calcif. Tissue Int. 65, 280–284. https://doi.org/10.1007/s002239900699

Strohl, W.R., 2018. Current progress in innovative engineered antibodies. Protein Cell 9, 86–120. https://doi.org/10.1007/s13238-017-0457-8

Strohl, W.R., 2015. Fusion Proteins for Half-Life Extension of Biologics as a Strategy to Make Biobetters. BioDrugs 29, 215–239. https://doi.org/10.1007/s40259-015-0133-6

Suda, T., Takahashi, N., Udagawa, N., Jimi, E., Gillespie, M.T., Martin, T.J., 1999. Modulation of osteoclast differentiation and function by the new members of the tumor necrosis factor receptor and ligand families. Endocr. Rev. 20, 345–357. https://doi.org/10.1210/edrv.20.3.0367

Sugiura, Y., Yasuhara, T., 1975. Sclerosteosis. A case report. J Bone Jt. Surg Am 57, 273–277.

Sun, W., Zheng, W., Simeonov, A., 2017. Drug discovery and development for rare genetic disorders. Am. J. Med. Genet. A. 173, 2307–2322. https://doi.org/10.1002/ajmg.a.38326

Sunters, A., Thomas, D.P., Yeudall, W.A., Grigoriadis, A.E., 2004. Accelerated Cell Cycle Progression in Osteoblasts Overexpressing the c-fos Proto-oncogene INDUCTION OF CYCLIN A AND ENHANCED CDK2 ACTIVITY. J. Biol. Chem. 279, 9882–9891. https://doi.org/10.1074/jbc.M310184200

Sutherland, M.K., Geoghegan, J.C., Yu, C., Turcott, E., Skonier, J.E., Winkler, D.G., Latham, J.A., 2004. Sclerostin promotes the apoptosis of human osteoblastic cells: a novel regulation of bone formation. Bone 35, 828–835. https://doi.org/10.1016/j.bone.2004.05.023

Suzuki, S., Annaka, H., Konno, S., Kumagai, I., Asano, R., 2018. Engineering the hinge region of human IgG1 Fc-fused bispecific antibodies to improve fragmentation resistance. Sci. Rep. 8, 17253. https://doi.org/10.1038/s41598-018-35489-y

Tacconi, P., Ferrigno, P., Cocco, L., Cannas, A., Tamburini, G., Bergonzi, P., Giagheddu, M., 1998. Sclerosteosis: report of a case in a black African man. Clin Genet 53, 497–501.

Takata, S., Yasui, N., 2001. Disuse osteoporosis. J. Med. Investig. JMI 48, 147–156.

Takayanagi, H., Kim, S., Koga, T., Nishina, H., Isshiki, M., Yoshida, H., Saiura, A., Isobe, M., Yokochi, T., Inoue, J., Wagner, E.F., Mak, T.W., Kodama, T., Taniguchi, T., 2002. Induction and activation of the transcription factor NFATc1 (NFAT2) integrate RANKL signaling in terminal differentiation of osteoclasts. Dev. Cell 3, 889–901. https://doi.org/10.1016/s1534-5807(02)00369-6

Tambuyzer, E., Vandendriessche, B., Austin, C.P., Brooks, P.J., Larsson, K., Miller Needleman, K.I., Valentine, J., Davies, K., Groft, S.C., Preti, R., Oprea, T.I., Prunotto, M., 2020. Therapies for rare diseases: therapeutic modalities, progress and challenges ahead. Nat. Rev. Drug Discov. 19, 93–111. https://doi.org/10.1038/s41573-019-0049-9

Tannenbaum, J., Bennett, B.T., 2015. Russell and Burch's 3Rs Then and Now: The Need for Clarity in Definition and Purpose. J. Am. Assoc. Lab. Anim. Sci. JAALAS 54, 120–132.

Taylor, S., Ominsky, M.S., Hu, R., Pacheco, E., He, Y.D., Brown, D.L., Aguirre, J.I., Wronski, T.J., Buntich, S., Afshari, C.A., Pyrah, I., Nioi, P., Boyce, R.W., 2016. Time-dependent cellular and transcriptional changes in the osteoblast lineage associated with sclerostin antibody treatment in ovariectomized rats. Bone 84, 148–159. https://doi.org/10.1016/j.bone.2015.12.013

Taylor, S.E.B., Shah, M., Orriss, I.R., 2014. Generation of rodent and human osteoblasts. BoneKEy Rep. 3, 585. https://doi.org/10.1038/bonekey.2014.80

Teitelbaum, S.L., 2007. Osteoclasts: What Do They Do and How Do They Do It? Am. J. Pathol. 170, 427–435. https://doi.org/10.2353/ajpath.2007.060834

Teitelbaum, S.L., 2000. Bone resorption by osteoclasts. Science 289, 1504–1508. https://doi.org/10.1126/science.289.5484.1504

ten Dijke, P., Krause, C., de Gorter, D.J.J., Löwik, C.W.G.M., van Bezooijen, R.L., 2008. Osteocyte-Derived Sclerostin Inhibits Bone Formation: Its Role in Bone Morphogenetic Protein and Wnt Signaling. J. Bone Amp Jt. Surg. 90, 31–35.

Thompson, W.R., Modla, S., Grindel, B.J., Czymmek, K.J., Kirn-Safran, C.B., Wang, L., Duncan, R.L., Farach-Carson, M.C., 2011. Perlecan/Hspg2 deficiency alters the pericellular space of the lacunocanalicular system surrounding osteocytic processes in cortical bone. J. Bone Miner. Res. Off. J. Am. Soc. Bone Miner. Res. 26, 618–629. https://doi.org/10.1002/jbmr.236

Tobeiha, M., Moghadasian, M.H., Amin, N., Jafarnejad, S., 2020. RANKL/RANK/OPG Pathway: A Mechanism Involved in Exercise-Induced Bone Remodeling. BioMed Res. Int. 2020. https://doi.org/10.1155/2020/6910312

Towbin, H., Staehelin, T., Gordon, J., 1979. Electrophoretic transfer of proteins from polyacrylamide gels to nitrocellulose sheets: procedure and some applications. Proc. Natl. Acad. Sci. 76, 4350–4354. https://doi.org/10.1073/pnas.76.9.4350

Truswell, A.S., 1958. Osteopetrosis with syndactyly. J. Bone Joint Surg. Br. 40-B, 208–218. https://doi.org/10.1302/0301-620X.40B2.208

Tu, X., Delgado-Calle, J., Condon, K.W., Maycas, M., Zhang, H., Carlesso, N., Taketo, M.M., Burr, D.B., Plotkin, L.I., Bellido, T., 2015. Osteocytes mediate the anabolic actions of canonical Wnt/β-catenin signaling in bone. Proc. Natl. Acad. Sci. 112, E478–E486. https://doi.org/10.1073/pnas.1409857112

Tu, X., Rhee, Y., Condon, K., Bivi, N., Allen, M.R., Dwyer, D., Stolina, M., Turner, C.H., Robling, A.G., Plotkin, L.I., Bellido, T., 2012. Sost downregulation and local Wnt signaling are required for the osteogenic response to mechanical loading. Bone 50, 209–217. https://doi.org/10.1016/j.bone.2011.10.025

Ubaidus, S., Li, M., Sultana, S., de Freitas, P.H.L., Oda, K., Maeda, T., Takagi, R., Amizuka, N., 2009. FGF23 is mainly synthesized by osteocytes in the regularly distributed osteocytic lacunar canalicular system established after physiological bone remodeling. J. Electron Microsc. (Tokyo) 58, 381–392. https://doi.org/10.1093/jmicro/dfp032

van Bezooijen, R.L., ten Dijke, P., Papapoulos, S.E., Löwik, C.W.G.M., 2005. SOST/sclerostin, an osteocyte-derived negative regulator of bone formation. Cytokine Growth Factor Rev. 16, 319–327. https://doi.org/10.1016/j.cytogfr.2005.02.005

van Buchem, F.S.P., Hadders, H.N., Ubbens, R., 1955. An Uncommon Familial Systemic Disease of the Skeleton: Hyperostosis Corticalis Generalisata Familiaris. Acta Radiol. os-44, 109–120. https://doi.org/10.1177/028418515504400203

van Buchem, F.S.P. van, Prick, J.J.G., Jaspar, H.H.J., 1976. Hyperostosis Corticalis Generalisata Familiaris (Van Buchem's Disease). Excerpta Medica.

Van Hul, W., Balemans, W., Van Hul, E., Dikkers, F.G., Obee, H., Stokroos, R.J., Hildering, P., Vanhoenacker, F., Van Camp, G., Willems, P.J., 1998. Van Buchem disease (hyperostosis corticalis generalisata) maps to chromosome 17q12-q21. Am. J. Hum. Genet. 62, 391–399. https://doi.org/10.1086/301721

van Lierop, A.H., Appelman-Dijkstra, N.M., Papapoulos, S.E., 2017. Sclerostin deficiency in humans. Bone 96, 51–62. https://doi.org/10.1016/j.bone.2016.10.010

van Lierop, A.H., Hamdy, N.A., Hamersma, H., van Bezooijen, R.L., Power, J., Loveridge, N., Papapoulos, S.E., 2011. Patients with sclerosteosis and disease carriers: Human models of the effect of sclerostin on bone turnover. J. Bone Miner. Res. 26, 2804–2811. https://doi.org/10.1002/jbmr.474

Vasikaran, S., Eastell, R., Bruyère, O., Foldes, A.J., Garnero, P., Griesmacher, A., McClung, M., Morris, H.A., Silverman, S., Trenti, T., Wahl, D.A., Cooper, C., Kanis, J.A., IOF-IFCC Bone Marker Standards Working Group, 2011. Markers of bone turnover for the prediction of fracture risk and monitoring

of osteoporosis treatment: a need for international reference standards. Osteoporos. Int. J. Establ. Result Coop. Eur. Found. Osteoporos. Natl. Osteoporos. Found. USA 22, 391–420. https://doi.org/10.1007/s00198-010-1501-1

Verborgt, O., Gibson, G.J., Schaffler, M.B., 2000. Loss of osteocyte integrity in association with microdamage and bone remodeling after fatigue in vivo. J. Bone Miner. Res. Off. J. Am. Soc. Bone Miner. Res. 15, 60–67. https://doi.org/10.1359/jbmr.2000.15.1.60

Veverka, V., Henry, A.J., Slocombe, P.M., Ventom, A., Mulloy, B., Muskett, F.W., Muzylak, M., Greenslade, K., Moore, A., Zhang, L., Gong, J., Qian, X., Paszty, C., Taylor, R.J., Robinson, M.K., Carr, M.D., 2009. Characterization of the Structural Features and Interactions of Sclerostin. J. Biol. Chem. 284, 10890–10900. https://doi.org/10.1074/jbc.M807994200

Vitale, M.G., Matsumoto, H., Kessler, M.W., Hoffmann, W., Roye, D.P., 2007. Osteogenesis imperfecta: determining the demographics and the predictors of death from an inpatient population. J. Pediatr. Orthop. 27, 228–232. https://doi.org/10.1097/BPO.0b013e31803179e2

Vortkamp, A., Lee, K., Lanske, B., Segre, G.V., Kronenberg, H.M., Tabin, C.J., 1996. Regulation of rate of cartilage differentiation by Indian hedgehog and PTH-related protein. Science 273, 613–622. https://doi.org/10.1126/science.273.5275.613

Wang, D., Christensen, K., Chawla, K., Xiao, G., Krebsbach, P.H., Franceschi, R.T., 1999. Isolation and Characterization of MC3T3-E1 Preosteoblast Subclones with Distinct In Vitro and In Vivo Differentiation/Mineralization Potential. J. Bone Miner. Res. 14, 893–903. https://doi.org/10.1359/jbmr.1999.14.6.893

Wang, L., Wang, Y., Han, Y., Henderson, S.C., Majeska, R.J., Weinbaum, S., Schaffler, M.B., 2005. In situ measurement of solute transport in the bone lacunar-canalicular system. Proc. Natl. Acad. Sci. U. S. A. 102, 11911–11916. https://doi.org/10.1073/pnas.0505193102

Wang, Z.Q., Ovitt, C., Grigoriadis, A.E., Möhle-Steinlein, U., Rüther, U., Wagner, E.F., 1992. Bone and haematopoietic defects in mice lacking c-fos. Nature 360, 741–745. https://doi.org/10.1038/360741a0

Wehmeyer, C., Frank, S., Beckmann, D., Böttcher, M., Cromme, C., König, U., Fennen, M., Held, A., Paruzel, P., Hartmann, C., Stratis, A., Korb-Pap, A., Kamradt, T., Kramer, I., Berg, W. van den, Kneissel, M., Pap, T., Dankbar, B., 2016. Sclerostin inhibition promotes TNF-dependent inflammatory joint destruction. Sci. Transl. Med. 8, 330ra35-330ra35. https://doi.org/10.1126/scitranslmed.aac4351

Weidauer, S.E., Schmieder, P., Beerbaum, M., Schmitz, W., Oschkinat, H., Mueller, T.D., 2009. NMR structure of the Wnt modulator protein Sclerostin. Biochem. Biophys. Res. Commun. 380, 160–165. https://doi.org/10.1016/j.bbrc.2009.01.062

Wein, M.N., 2017. Bone Lining Cells: Normal Physiology and Role in Response to Anabolic Osteoporosis Treatments. Curr. Mol. Biol. Rep. 3, 79–84. https://doi.org/10.1007/s40610-017-0062-x

Weinstein, R.S., Jilka, R.L., Parfitt, A.M., Manolagas, S.C., 1998. Inhibition of osteoblastogenesis and promotion of apoptosis of osteoblasts and osteocytes by glucocorticoids. Potential mechanisms of their deleterious effects on bone. J. Clin. Invest. 102, 274–282. https://doi.org/10.1172/JCI2799

Werle, M., Bernkop-Schnürch, A., 2006. Strategies to improve plasma half life time of peptide and protein drugs. Amino Acids 30, 351–367. https://doi.org/10.1007/s00726-005-0289-3

Wesenbeeck, L.V., Cleiren, E., Gram, J., Beals, R.K., Bénichou, O., Scopelliti, D., Key, L., Renton, T., Bartels, C., Gong, Y., Warman, M.L., Vernejoul, M.-C. de, Bollerslev, J., Hul, W.V., 2003. Six Novel Missense Mutations in the LDL Receptor-Related Protein 5 (LRP5) Gene in Different Conditions with an Increased Bone Density. Am. J. Hum. Genet. 72, 763–771. https://doi.org/10.1086/368277

Whyte, M.P., Greenberg, C.R., Salman, N.J., Bober, M.B., McAlister, W.H., Wenkert, D., Van Sickle, B.J., Simmons, J.H., Edgar, T.S., Bauer, M.L., Hamdan, M.A., Bishop, N., Lutz, R.E., McGinn, M., Craig, S., Moore, J.N., Taylor, J.W., Cleveland, R.H., Cranley, W.R., Lim, R., Thacher, T.D., Mayhew, J.E., Downs, M., Millán, J.L., Skrinar, A.M., Crine, P., Landy, H., 2012. Enzyme-replacement therapy in life-threatening hypophosphatasia. N. Engl. J. Med. 366, 904–913. https://doi.org/10.1056/NEJMoa1106173

Wienken, C.J., Baaske, P., Rothbauer, U., Braun, D., Duhr, S., 2010. Protein-binding assays in biological liquids using microscale thermophoresis. Nat. Commun. 1, 1–7. https://doi.org/10.1038/ncomms1093

Wijenayaka, A.R., Kogawa, M., Lim, H.P., Bonewald, L.F., Findlay, D.M., Atkins, G.J., 2011. Sclerostin Stimulates Osteocyte Support of Osteoclast Activity by a RANKL-Dependent Pathway. PLOS ONE 6, e25900. https://doi.org/10.1371/journal.pone.0025900

Wilson, S.R., Peters, C., Saftig, P., Brömme, D., 2009. Cathepsin K Activity-dependent Regulation of Osteoclast Actin Ring Formation and Bone Resorption. J. Biol. Chem. 284, 2584–2592. https://doi.org/10.1074/jbc.M805280200

Winkler, D.G., Sutherland, M.K., Geoghegan, J.C., Yu, C., Hayes, T., Skonier, J.E., Shpektor, D., Jonas, M., Kovacevich, B.R., Staehling-Hampton, K., Appleby, M., Brunkow, M.E., Latham, J.A., 2003. Osteocyte control of bone formation via sclerostin, a novel BMP antagonist. EMBO J. 22, 6267–6276. https://doi.org/10.1093/emboj/cdg599

Wittig, N.K., Laugesen, M., Birkbak, M.E., Bach-Gansmo, F.L., Pacureanu, A., Bruns, S., Wendelboe, M.H., Brüel, A., Sørensen, H.O., Thomsen, J.S., Birkedal, H., 2019. Canalicular Junctions in the Osteocyte Lacuno-Canalicular Network of Cortical Bone. ACS Nano 13, 6421–6430. https://doi.org/10.1021/acsnano.8b08478

Wu, B., Sun, Y.-N., 2014. Pharmacokinetics of Peptide-Fc fusion proteins. J. Pharm. Sci. 103, 53–64. https://doi.org/10.1002/jps.23783

Xiao, Y., Isaacs, S.N., 2012. Enzyme-Linked Immunosorbent Assay (ELISA) and Blocking with Bovine Serum Albumin (BSA) - Not all BSAs are alike. J. Immunol. Methods 384, 148–151. https://doi.org/10.1016/j.jim.2012.06.009

Xiong, J., Piemontese, M., Onal, M., Campbell, J., Goellner, J.J., Dusevich, V., Bonewald, L., Manolagas, S.C., O'Brien, C.A., 2015. Osteocytes, not Osteoblasts or Lining Cells, are the Main Source of the RANKL Required for Osteoclast Formation in Remodeling Bone. PloS One 10, e0138189. https://doi.org/10.1371/journal.pone.0138189

Yamaguchi, A., Komori, T., Suda, T., 2000. Regulation of osteoblast differentiation mediated by bone morphogenetic proteins, hedgehogs, and Cbfa1. Endocr. Rev. 21, 393–411. https://doi.org/10.1210/edrv.21.4.0403

Yang, Y.-S., Xie, J., Wang, D., Kim, J.-M., Tai, P.W.L., Gravallese, E., Gao, G., Shim, J.-H., 2019. Bone-targeting AAV-mediated silencing of Schnurri-3 prevents bone loss in osteoporosis. Nat. Commun. 10, 2958. https://doi.org/10.1038/s41467-019-10809-6

Yavropoulou, M.P., Yovos, J.G., 2008. Osteoclastogenesis--current knowledge and future perspectives. J. Musculoskelet. Neuronal Interact. 8, 204–216.

Yellowley, C.E., Li, Z., Zhou, Z., Jacobs, C.R., Donahue, H.J., 2000. Functional gap junctions between osteocytic and osteoblastic cells. J. Bone Miner. Res. Off. J. Am. Soc. Bone Miner. Res. 15, 209–217. https://doi.org/10.1359/jbmr.2000.15.2.209

Young, M.F., Kerr, J.M., Ibaraki, K., Heegaard, A.M., Robey, P.G., 1992. Structure, expression, and regulation of the major noncollagenous matrix proteins of bone. Clin. Orthop. 275–294.

Yuan, F.-L., Xu, M.-H., Li, X., Xinlong, H., Fang, W., Dong, J., 2016. The Roles of Acidosis in Osteoclast Biology. Front. Physiol. 7. https://doi.org/10.3389/fphys.2016.00222

Zaidi, M., 2007. Skeletal remodeling in health and disease. Nat. Med. 13, 791–801. https://doi.org/10.1038/nm1593

Zapata, A., Amemiya, C.T., 2000. Phylogeny of Lower Vertebrates and Their Immunological Structures, in: Du Pasquier, L., Litman, G.W. (Eds.), Origin and Evolution of the Vertebrate Immune System, Current Topics in Microbiology and Immunology. Springer, Berlin, Heidelberg, pp. 67–107. https://doi.org/10.1007/978-3-642-59674-2_5

Zebaze, R.M.D., Jones, A., Knackstedt, M., Maalouf, G., Seeman, E., 2007. Construction of the femoral neck during growth determines its strength in old age. J. Bone Miner. Res. 22, 1055–1061. https://doi.org/10.1359/jbmr.070329

Zhang, D., Park, B.M., Kang, M., Nam, H., Kim, E.J., Bae, C., Lim, S.K., 2016. The systemic effects of sclerostin overexpression using ΦC31 integrase in mice. Biochem. Biophys. Res. Commun. 472, 471–476. https://doi.org/10.1016/j.bbrc.2016.01.178

Zhang, K., Barragan-Adjemian, C., Ye, L., Kotha, S., Dallas, M., Lu, Y., Zhao, S., Harris, M., Harris, S.E., Feng, J.Q., Bonewald, L.F., 2006. E11/gp38 selective expression in osteocytes: regulation by mechanical strain and role in dendrite elongation. Mol. Cell. Biol. 26, 4539–4552. https://doi.org/10.1128/MCB.02120-05

Zhang, Y., Xie, R.-L., Croce, C.M., Stein, J.L., Lian, J.B., van Wijnen, A.J., Stein, G.S., 2011. A program of microRNAs controls osteogenic lineage progression by targeting transcription factor Runx2. Proc. Natl. Acad. Sci. U. S. A. 108, 9863–9868. https://doi.org/10.1073/pnas.1018493108

Zhao, C., Irie, N., Takada, Y., Shimoda, K., Miyamoto, T., Nishiwaki, T., Suda, T., Matsuo, K., 2006. Bidirectional ephrinB2-EphB4 signaling controls bone homeostasis. Cell Metab. 4, 111–121. https://doi.org/10.1016/j.cmet.2006.05.012

Zhu, D., Mackenzie, N.C.W., Millán, J.L., Farquharson, C., MacRae, V.E., 2011. The Appearance and Modulation of Osteocyte Marker Expression during Calcification of Vascular Smooth Muscle Cells. PLOS ONE 6, e19595. https://doi.org/10.1371/journal.pone.0019595

Research Ethics Committee

Project Title	**Can exogenous sclerostin mitigate the excessive bone formation associated with sclerosteosis?**
Project Number	**REC001-19**
Researcher / Principal Investigator	**Mr TJ Dreyer**

DIissertation / Thesis submitted for	**Doctoral**

Supervisor	**Prof V Naidoo**

APPROVED	Date:	**2019-07-09**
CHAIRMAN: UP Research Ethics Committee	Signature:	

Office of the Chairman: Research Ethics Committee
Room 2-24, Pathology Building, Onderstepoort
University of Pretoria, Private Bag X04
Onderstepoort 0110, South Africa
Tel +27 (0)12 529 8052
Email
www.up.ac.za

Fakulteit Veeartsenykunde
Lefapha la Diseanse tša Bongakadiruiwa

UCB Celltech

Dear Members of AEC,

I can confirm that UCB UK has been issued by the UK Home Office with an Establishment License under Section 2C of the Animals (Scientific Procedures) Act 1986. That states: -

 UCB

216 Bath Rd

Slough

Berks

SL1 4EN

is granted license to carry on an undertaking involving the application of regulated procedures to protected animals.

This document includes the persons responsible for compliance, care and welfare of the animals and the training and competency of any persons carrying out procedures.

A project license has also been granted to carry out the described work, this had been through full ethical review both internally by an Ethical Review Board that includes a veterinary surgeon, experienced scientists, statisticians and a lay person, and also externally by the UK Home Office.

Yours Sincerely

Tania Boden

Head of Animal Facilities.